Absorbance Modulation Optical Lithography: Simulating the Performance of an Adaptable Absorbance Mask in the Near-Field.

John Foulkes

A thesis presented for the degree of
Doctor of Philosophy
In
Electrical and Electronic Engineering
at the
University of Canterbury,
Christchurch, New Zealand.

December 2010

ABSTRACT

The challenge for lithography today is to continue the reduction of feature size whilst facing severe theoretical and practical limitations. In 2006 Rajesh Menon and Hank Smith proposed a new lithography system named absorbance modulation optical lithography (AMOL) [Menon 2006]. AMOL proposed replacing the normal metal mask of a lithography system with an absorbance modulation layer (AML), made from a photochromic material. This allows, through the competition between two incident wavelengths, the creation of an adaptive absorbance mask. The AML allows intimate contact to an underlying resist and hence the optical near-field may be used to create sub-diffraction limited exposures. The aim of this thesis is to model AMOL and demonstrate the abilities and the limits of the system, particularly focusing on sub-diffraction limited imaging.

This thesis describes the construction of a vector electromagnetic simulation to explore the idea and performance of AMOL, and an exploration of the ability of AMOL to propagate sub-diffraction limited images into a photoresist. A finite element method (FEM) model was constructed to simulate the formation of apertures in the AML and light transmission through the system. Three major areas of interest were explored in this thesis; the effect of polarisation on imaging, using a plasmonic reflector layers (PRLs) to improve the depth of focus (DOF), and introducing a superlens to AMOL.

Investigations of polarisation demonstrated strong preference for a transverse magnetic (TM) polarised exposing wavelength for near-field exposures. Associated with polarisation, and supporting work with absorbance gratings, the importance of the material parameters of the AML in allowing sub-diffraction limited exposures was discussed. It was also noted that, in common with all near-field systems, the depth of focus (DOF) was poor, worse than comparable metal systems. This thesis also demonstrates that the introduction of a PRL can improve the DOF and process latitude for resist thicknesses

up to 60 nm and, although performance was reduced when using a silver PRL, the substantial improvements to the DOF and process latitude make a PRL valuable for an AMOL system.

This thesis also models the superlens to an AMOL system, which theoretically allows propagation of the image in the near-field. It is demonstrated that the superlens can project an AMOL image into an underlying resist, but that this image is degraded, especially for thick and non-ideal superlenses. The superlens does have a second useful effect, as it can act as a dichroic filter; decreasing the intensity ratio in the resist by a factor of ten, overcoming issues of resist sensitivity. The superlens can allow image projection and filtering with AMOL, however improvements to the available superlens materials or changes to the AML will be needed to avoid image deterioration.

This thesis has developed the first full-vector model of an absorbance modulation optical lithography (AMOL) system. This model has been used to increase the understanding of the complex effects that go into the creation of sub-diffraction limited features with AMOL. In particular the model has been used to investigate polarisation, PRLs and superlenses in AMOL. This thesis demonstrates the ability of AMOL to create narrow apertures and sub-diffraction limited exposures in a photoresist, and describes the limitations of AMOL, including material parameters and DOF. AMOL is a new and interesting lithography technique; this thesis simulates the abilities and challenges of sub-diffraction lithography using an AMOL system.

PREFACE

This dissertation describes research undertaken in the Department of Electrical and Computer Engineering at the University of Canterbury between March 2007 and December 2010. I thank my supervisor, Professor Richard Blaikie for his suggestion of this topic of research and his continuous support of my work. The course of this thesis has been an interesting journey, combining the difficulties involved in creating and verifying a computer simulation of a novel lithography technique with the on-going challenges of near-field lithography.

Aspects of the work described in this dissertation have been published as follows:

Foulkes, JE & Blaikie, RJ 2009, 'Influence of polarization on absorbance modulated subwavelength grating structures', *Journal of Vacuum Science & Technology B*, vol. 27, no. 6, pp. 2941-6.

Foulkes, J & Blaikie, R 2008, 'Finite Element Simulation of Absorbance Modulation Optical Lithography', Melbourne, Australia: 2008, *Proceedings International Conference on Nanoscience and Nanotechnology (ICONN 2008),* Feb 25-29 2008, pp184-187

Aspects of the work described in this dissertation have been presented at the following conferences:

Oral Presentations:

Foulkes, J & Blaikie, R, 2010, 'Improved performance in Absorbance Modulation Optical Lithography using a Plasmonic Reflector Layer' *International Conference on Nanoscience and Nanotechnology (ICONN 2010)* 22- 26th February 2010

Foulkes, J.E. and Blaikie, R.J. (2009) 'Finite-element simulation of absorbance modulation optical lithography'. *4th International Conference on Advanced Materials and Nanotechnology* (AMN-4), Dunedin, New Zealand, 8-12 Feb 2009

Foulkes, J & Blaikie, R 2008, 'Finite Element Simulation of Absorbance Modulation Optical Lithography', Melbourne, Australia: 2008, *International Conference on Nanoscience and Nanotechnology (ICONN 2008),* Feb 25-29 2008, pp184-187

Poster Presentations:

Foulkes, J.E. and Blaikie, R.J. (2009) 'Influence of polarization on absorbance modulated sub-wavelength grating structures'*, 53rd International Conference on Electron, Ion, and Photon Beam Technology and Nanofabrication (EIPBN)*, 26-29 May 2009. Marco Island, FL, USA

Aspects of the work described in this dissertation have been presented through the following seminars and talks:

Foulkes J & Blaikie, R, 'Absorbance Modulation Optical Lithography with Plasmonic Reflectors', *Presentation to the NanoLab users group*, University of Canterbury, March 2010

Foulkes J & Blaikie, R, 2009, 'Drawing at the Nanoscale' *Departmental Seminar*, Department of Electrical and Computer Engineering, University of Canterbury, 29 May 2009

Foulkes J & Blaikie, R, 2008, 'The challenges of nanometer resolution', *IET- Present around the world competition,* University of Canterbury August 2008

Foulkes J, Moore, C & Blaikie, R, Finite Element Modeling with COMSOL, *MacDiarmid Student Symposium 2009*, Wellington, NZ, 4th-7th November 2008

PREFACE

Foulkes J & Blaikie, R, 'Optical Lithography with a photochromic material', *Presentation to the NanoStructures Laboratory Group*, Massachusetts Institute of Technology, 2007

ACKNOWLEDGEMENTS

Firstly I would like to thank my supervisor Professor Richard Blaikie for his support and guidance to my research over the course of this thesis. I would also like to acknowledge Rajesh Menon and Hank Smith for introducing the idea of AMOL and allowing me to visit MIT and discuss AMOL at the beginning of my research.

This thesis was undertaken at the Department of Electrical and Computer Engineering at the University of Canterbury and I would like to thank the department and all of the associated staff and students for their support. I would also like to thank the University of Canterbury Doctoral Scholarship for financial support of my thesis studies.

A special thanks to my fellow students who have shared in the battles of producing this thesis, in particular the other students in the lithography area: Mikkel Schøler, Ciaran Moore, Prateek Mehrotra and postdocs Trey Holzwarth and Matt Arnold. Your support, and the discussions at group meetings made my thesis better and the journey more interesting. Thank you also Mikkel, Ciaran and Prateek, along with David Kim, Jannah Ibrahim and, earlier, Jessica Chai for making the A217 office a relaxed but pleasant working environment; not forgetting those people who shared the slightly more haphazard arrangements in A219. Mikkel has shared both offices with me and has been a continuing presence during my thesis; I thank him for sharing the experience, for the many lunches at Tandoori Palace and stimulating discussions. I would also like to thank members of the wider MacDiarmid Institute, particularly those at the University of Canterbury, for exposing me to the many different areas encompassed by the phrase nanotechnology.

I would like to thank all those people that provided pleasant distractions during the years of my thesis research and my friends. I would like to thank my friends outside of the department who have allowed me to enjoy the wider world whilst completing my thesis, as well as the many flatmates who have supported me at home. In particular I thank

Andrew, Clare and Laura for lunchtime discussions at university, about research and other things.

Finally I would like to thank my family who have supported me throughout my thesis, and in my life and education leading up to my thesis; my grandparents, my parents Donald and Christeen, and my sisters Anne and Emma and my niece Kate. Your support, encouragement and patience enabled me to complete this thesis.

TABLE OF CONTENTS

TABLE OF CONTENTS

LIST OF FIGURES

LIST OF FIGURES

LIST OF TABLES

ACRONYMS AND ABBREVIATIONS

AMOL	Absorbance Modulation Optical lithography
AML	Absorbance Modulation Layer
ArF	Argon-Fluoride Laser
CEL	Contrast Enhancement Layer
DE	Differential Equation
DFT	Discrete Fourier Transform
DOF	Depth of Focus
EBL	Electron Beam Lithography
ENFOL	Enhanced Near-Field Optical Lithography
EUV	Extreme Ultraviolet Lithography
FDTD	Finite Difference Time Domain
FEM	Finite Element Method
FTIR	Frustrated Total Internal Reflectance
FWHM	Full Width at Half Maximum
ITRS	The International Technology Roadmap For Semiconductors
i/j	Imaginary Unit
LSF	Line Spread Function
NA	Numerical Aperture
NILS	Normalised Image Log Slope
OPC	Optical Proximity Correction
PML	Perfectly Matched Layer
PRL	Plasmonic Reflector Layer
PMEA	poly[4-[2-(methacryloyloxy)ethyl] azobenzene]
RET	Resolution Enhancement Techniques
RCWA	Rigorous Coupled Wave Analysis
STED	Stimulated Emission Depletion Microscopy
SERS	Surface Enhanced Raman Spectroscopy
SP	Surface Plasmon

SPECL	Surface Plasmon Enhanced Contact Lithography
TE	Transverse Electric
TM	Transverse Magnetic
VF	Variational Form

Chapter 1

INTRODUCTION

1.1 MOTIVATION

Lithography is of central importance to the construction of any small features, with particular relevance to the semiconductor industry. Advancements in lithography allow new generations of improved microchips and improved development processes. If it is desired to continue the exponential increase in computing power of the last forty years then lithographic improvements will be necessary.

The constant technological development in lithography engineering has led to considerable variety in and complexity of the techniques used to pattern at scales from micrometers down to nanometers. In this thesis a lithography technique involving the optical near-field and the use of an absorbance-modulated mask are the primary focus, investigating and characterising these techniques through modeling and exploring the possibilities for improving their performance. The techniques developed here are not mainstream industrial techniques, but promise interesting advantages when considering the obstacles facing lithography's ongoing development, alongside the possibility to explore the details of how light may be confined to form sub-wavelength features.

1.2 LITHOGRAPHY

From the early days of the integrated circuit and the microchip there has been ongoing demand for greater number of transistors on each chip. Lithography – the art and engineering challenge of patterning integrated circuits – has been a central mechanism allowing technological improvement through a reduction in feature size. The industry-

created requirement to increase the functionality of devices whilst reducing size, failure rate and cost and improving yield has led to intensive efforts to scale the feature sizes of integrated circuits to smaller dimensions. The continued development of optical lithography technologies [Lin 2006, Fay 2002] has enabled these goals to be achieved and optical lithography has remained the mainstream method for integrated chip production since the inception of the industry. In the past when it has been assumed that a feature size limit was reached, new developments and techniques have allowed the further reduction of feature sizes from the micrometer range to current integrated circuits with critical dimensions of less than 40 nm.

Although early optical lithography techniques began as optical printing, involving masks in contact or close proximity (Fig 1.1) the general industry trend has been towards optical projection lithography as this reduces the difficulties with mask contamination [Ronse 2006]. The basic structure of a projection system used for optical lithography takes the light from the laser source, passes it through a beam expander, before it impinges on a mask. The light pattern is then focussed by an objective/projection lens onto a photoresist layer on the wafer, as shown in Fig 1.2. In order to improve the image resulting from the lithography system adjustments may be made to each of the components: different photoresist selection may allow for improved selectivity, improved construction of the lenses and masks can decrease the presence of defects and a more ideal light source can reduce secondary effects like dispersion. After the image has been transferred into the photoresist a development of the photoresist must take place to produce the desired feature, the details of this process will depend heavily on the nature of the resist used as well as the quality of the transferred image.

1.2.1 PROJECTION LITHOGRAPHY

The overall effectiveness of a lithography system may be judged against a number of criteria, including the maximum achievable resolution, the ability to position a series of lithographic exposures accurately (overlay), line edge roughness and the cost effectiveness of the system being looked at. The cost effectiveness is the most important industry

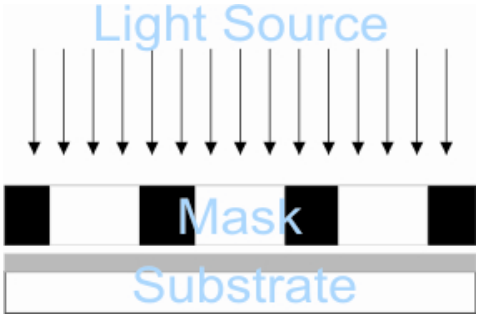

Figure 1.1 Schematic of a proximity optical lithography process

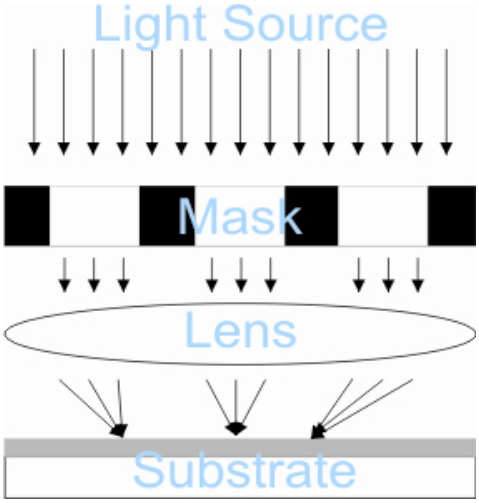

Figure 1.2 Schematic of a projection optical lithography process

requirement and combines a variety of factors including maximum throughput, exposure speed, availability and expense of required materials and the ability to produce on a large scale. The lithographic effectiveness may be represented by the resolution of the system, which Mack defines as the smallest feature that can be reproduced with adequate control [Mack 2007]. The maximum resolution achievable by any optical lithography system is inherently important because it sets the smallest possible linewidths that can be drawn using the particular lithographical processes and hence the maximum number of transistors in any given area.

The resolution of a given projection optical lithography system may be related to the wavelength, λ and numerical aperture, NA of the system by the Rayleigh equation

$$R = k_1 \frac{\lambda}{NA} \tag{1.1}$$

where k_1 is the merit factor of the lithography system [Mack 2007]. This equation arises from a definition of loss in resolution as the point at which two point spread functions are brought together such that the peak of one overlaps the first diffractive order of the second. A second important measurement parameter is the depth of focus (DOF – also known as depth of field), for a projection system this is a measure of the depth for which an adequate focus for imaging can be achieved in the resist. For a grating of equally spaced lines this may be approximated by the relation

$$DOF = k_2 \frac{\lambda}{NA^2}, \tag{1.2}$$

where k_2 is a system constant, although this expression requires several caveats and may be of limited accuracy [Mack 2007]. It is desirable to produce a smaller resolution and larger DOF; it may be seen from Eqs 1.1 and 1.2 that by decreasing either k_1, λ or increasing NA a smaller and hence improved resolution may be achieved. However reducing λ or increasing NA causes a reduction in the DOF and hence more difficult development process and smaller process latitude.

The reduction of wavelength in order to achieve improved resolution has led from the use of the g-line of a mercury lamp at 436nm in the 1980's to the use of lasers such as Argon-Fluoride (ArF) at 193 nm in current production systems (Fig 1.3). Although continued reduction of the wavelength used in the optical system would result in improved resolution capabilities numerous challenges have arisen. A change in wavelength requires each section of the optical lithography system to be redesigned; a new photoresist absorbing at the wavelength must be chosen and the lens materials must be carefully selected to avoid absorption and overheating.

This system overhaul required to change wavelength is both expensive and complex and the alternative of improving the resolution through either increasing the numerical aperture or decreasing the merit factor of the system can be preferable. Currently attempts to produce a functioning system with a wavelength of 157 nm (F_2 laser) or below have been unsuccessful due to absorption and birefringence problems with lens materials

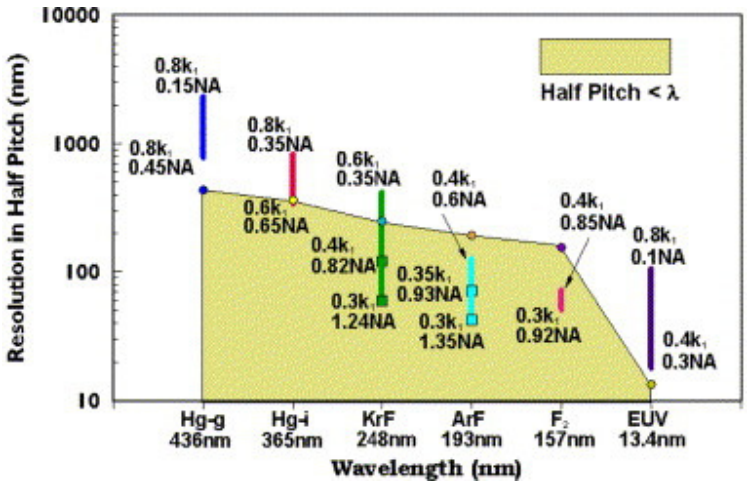

Figure 1.3 Evolution of projection optical lithography from 436 nm, 0.15 NA, 0.8 k_1 to 193 nm immersion. The vertical bars represent the performance limits achieved with each technology; the shaded region represents the half wavelength limit [Lin 2006].

and too much absorbance in resists [Lin 2006]. This has forced research into improving the performance of material parameters [Sanders 2010] and resolution enhancement techniques (RET) [Mack 2007, Trouiller 2006] at 193 nm. Alongside the introduction of new experimental techniques the increasing use of simulations and computational methods has enabled the testing of new ideas and a greater understanding of the processes taking place [Mack 2006, Cole 2001, Mack 2001].

The numerical aperture of the system is a measure of the 'light gathering ability' of the lens in the lithography system, it is a product of the refractive index (n) and the angular semi-aperture (θ_0) in the object space;

$$NA = n \times sin(\theta_0). \tag{1.3}$$

Through complex lens design and material choice the numerical aperture of the system may be increased, however because of the square in Eq 1.2 this can lead to a large and undesirable reduction in DOF. A major breakthrough in NA improvement was made with the implementation of immersion lithography [French 2009, Ronse 2009, Bratton 2006] in which the volume between the lens and the wafer is filled with a fluid with higher refractive index than air (e.g water) that will act to increase the NA of the lens; this is particularly impressive given that the lithography system is moving rapidly to

sweep across the wafer, and the engineering of such systems now needs a strong understanding of hydraulics and fluid dynamics in additional to the optical design.

The final component of the resolution equation is the merit factor, k_1, of the optical lithography system. This is used to describe the effects of changing system parameters and features, such as the resist process, resolution enhancement techniques (RET) or optical proximity correction (OPC) [Mack 2007]. There is an extensive selection of techniques which have been investigated to lower the k_1 of a lithography system such as phase shifting masks, off-axis illumination and polarization [Ronse 2006]. Each of these requires additional machinery, understanding and process steps, however the demand for resolution improvement continues to encourage further developments in these areas [Pease 2008]. The k_1 value has a theoretical limit for dense half-pitch gratings of 0.25, although the manufacturable limit may be higher [Lee 2009]. With current technologies already requiring reduction from ~0.5 to ~0.30 further improvements are even more challenging.

1.2.2 CURRENT LITHOGRAPHY SYSTEMS

The International Technology Roadmap For Semiconductors (ITRS) is a industry led group whose main aim is to "present industry-wide consensus on the 'best current estimate' of the industry's research and development needs out to a 15-year horizon" [ITRS 2009]. The 2009 roadmap outlined the current technology involved in creating 45 nm half-pitch DRAM, using a 193 nm wavelength from an ArF laser with water immersion, a k_1 value 0.28-0.31 and making use of a variety of corrective techniques including OPC. Thus using Eq 1.1

$$\text{Resolution} = k_1 * \frac{\lambda}{\text{NA}} \approx 0.31 * \frac{193}{1.35} = 44\text{nm}, \tag{1.4}$$

with a reducing DOF for a single layer resist of

$$DOF = k_2 * \frac{\lambda}{\text{NA}^2} \approx 1 * \frac{193}{1.35^2} = 105\text{nm}, \tag{1.5}$$

where more complex resist structures allow a $DOF \approx 160$ nm. The engineering skill needed to reach this limit is extraordinary [Sanders 2010], and if the progression of

Moore's law [Moore 1998] is to continue then so must further improvements, the ITRS report notes that no proven optical technique exists below 22 nm, $\sim\lambda/9$ for the 193 nm wavelength. The struggle for further improvement and the complex nature current optical projection lithography systems (Fig 1.4) has also inspired a search for alternative techniques that can improve the resolution and match the speed of current projection lithography.

1.3 ALTERNATIVE TECHNIQUES

Given the technological obstacles facing optical projection lithography and the demand for improved resolution in lithography systems there has been a huge development of alternative ideas and variations which have the potential to improve resolution capabilities [Saavedra 2010, Smith 2009, Pease 2008, Bratton 2006]. These alternative techniques make some adjustment to the system so that the effect of light diffraction (which leads to loss of resolution) is largely reduced and the projection lithography equation (Eq 1.1) no longer applies, thus allowing the potential of further resolution improvement. This is accomplished in many ways: by removing light from the system, such as nanoimprint lithography [Guo 2007]; using a second stage to improve resolution, such as self-assembly lithography [Stoykovich 2007] and double patterning [Lee 2009, Mack 2008]; creating a non-linearity such as multi-photon absorption (MAP) [Fischer 2010, Li 2009, Ogawa 2009]; by placing the mask very close to or in contact with the photoresist such as enhanced near-field optical lithography (ENFOL) [McNab 2001, Alkaisi 1999] and absorbance modulation optical lithography (AMOL) [Menon 2007]; or by developing systems working at much smaller wavelengths such as x-ray [Silvermann 1997], extreme ultraviolet (EUV) [Kumar 2007] and electron beam lithography (EBL) [Viece 2000]. However each of these techniques faces serious obstacles to compete in effectiveness with the well-developed projection optical lithography systems and to convince the industry to make the large investments required to further their development.

Figure 1.4 ASML Twinscan XT:1950i scanner, a modern day lithography machine capable of imaging >140 wafers per hour. The illuminator (source), lenses, photomask and stage (substrate) are labeled [French 2009]

The techniques of double patterning and self-assembly lithography give options to extend the reach of current technologies. For instance double patterning (possibly followed by triple and/or quadruple patterning) allows the same optical lithography techniques to be used but requires additional process steps, either extra development and re-exposure or protection of the first exposure; these additional steps increase the time taken for the fabrication process as well as the importance of accurate alignment. Similarly self-assembly lithography processes increase the complexity of the lithographical systems because the operation of the introduced self-assembly compounds and their relation with the lithographical systems must be well understood. The advantage of these methods, that they build upon previous optical lithography methods, is also partially shared by the small wavelength methods.

The small wavelength methods (x-ray, EUV and EBL) take advantage of their much smaller wavelengths to avoid diffraction effects; this will allow better resolution [Stulen 1999] but two major problems exist. Firstly there is a materials problems: at short

wavelengths it is no longer possible to design refractive lenses due to absorption, hence reflective mirrors must be used and although advances have been made this remains problematic; alongside this are mask and resist problems [Wurm 2009]. Secondly it has proven difficult to develop high power, high resolution, sources, for this reason EBL has remained a single beam, non-masked lithography which is inherently slow, well below the speed required for large scale manufacture (but widely used for laboratory and small scale work) and research has focused on developing improved power sources at EUV. Each of these techniques have strong performance possibilities which has encouraged large investment and research, however the discussed obstacles remain before they can take over from projection lithography systems.

Another alternative technique to overcome the diffraction limit problem is to make use of the optical near-field. Projection lithography works with propagating light at large distances and hence undergoes diffraction after passing through, say a narrow aperture (Fig 1.5a), but continues to propagate (hopefully towards a lens). If the aperture is narrower than $\lambda/2$ it may be shown that an evanescent field is produced in the region just behind the aperture and that these evanescent waves contain the complete spatial information but decay exponentially (Fig 1.5b). It was shown [McNab 2001] that non-

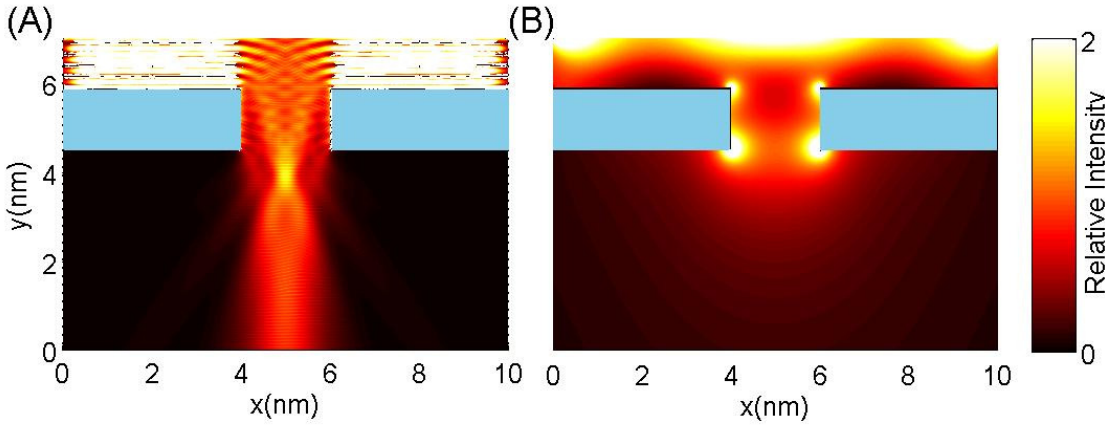

Figure 1.5 Intensity of light passing through a metal ($\epsilon_r = -4.4 - 18j$) aperture (width= 2 nm) with wavelength (a) 0.5 nm and (b) 8 nm. At the short wavelength the light propagates with the diffractive orders visible, however the long wavelength only shows an evanescent field as the aperture is too narrow.

diffraction limited lithographical systems are possible in this region, although the decay is dependent on spatial frequency and hence non-uniform and the exponential nature of the decay requires that the mask and photoresist are placed as close together as possible, leading to contact issues and contamination problems.

Combining the optical near-field with a technique to control and reduce the exposure size would allow non-diffraction limited lithography and have been explored by techniques such as beam-pen lithography [Huo 2010] in which a gold covered polymer tip is used to guide light to a narrow aperture. Instead of requiring the fabrication of such a system or the creation of a similar near-field source it would be much preferable to use far-field sources as these are commonly available and simple to use. An implementation of this idea was suggested by Hell [Hell 2004, Hell 2003] following on from work in stimulated emission depletion microscopy (STED) involving two competing incident wavelengths with a third input used to 'freeze' the final form when desired. Although this idea was not directly used it inspired a series of related non-linear far-field enabled near-field systems which may enable nanoscale lithography with visible light sources [Fourkas 2010]. These include two-color excitation/deactivation photolithography [Scott 2009] and absorbance modulation optical lithography (AMOL). AMOL combined the possibilities of using the optical near-field and double patterning without multiple development stages [Menon 2007] through the use absorbance modulation layer (AML) as a mask. AMOL is an exciting idea because it proposes access to the advantages of both of these alternative techniques as well as remaining within the technological area of projection lithography and it is the subject of the majority of this thesis.

1.4 COMPUTATIONAL LITHOGRAPHY

The ability to simulate and test new lithography ideas and adaptations to current designs is now an essential part of lithography [Cole 2001, Mack 2001]. Before the early 1970's there was limited need to create complex models of lithography systems, with rules of thumb and trial and error sufficient to increase resolving capabilities. However, with the ongoing drive to reduce feature size continuing the needs to validate and improve the

theoretical understanding of each section of lithographical systems and the need for lithographers to be able to test improvements [Mack 2006] it has since been necessary to develop ever more complex computational methods to explain the interactions between light, chemicals, fluids and movements taking place.

The Dill papers [Dill 1975, Dill 1975a, Dill 1975b] introduced a linear model for photo-resist exposure and development and mark the start of the computational lithography. Since these early models many more assumptions have been removed, for instance; high NA systems requiring vector models to replace scalar models, small dimensions requiring differentiation between polarizations, and stochastic modeling to determine and reduce variations and improve process latitude. For modern systems every part of the lithography process is relentlessly optimized, either with complex models or through simulations; the difference between the mask pattern and the images formed has led to optical proximity correction (OPC) in which the mask is adjusted to create an improved image; the illumination can similarly be adjusted to optimize performance. Computational simulation is a mainstay of the lithography industry today; its performance in areas of research, optimization and understanding has allowed the improvements in resolution seen today [Mack 2006, Cole 2001, Mack 2001]. Of course, there must always be a combination of the computational work with experimental results, allowing each method to push the other forward and encourage new ideas.

1.5 AIMS OF THIS THESIS

This thesis examines the performance of AMOL through the development and use of a finite element method (FEM) model to explore the relationships between the AMOL material parameters and the input settings. The aim of this thesis is first to explore and characterise this new and promising optical lithography system and explore how the performance of AMOL may be improved or degraded through the introduction of techniques that have been successful in related near-field technologies. This greater understanding of AMOL is unavailable from solely experimental research and will be able to offer direction to following AMOL experimental work.

This thesis begins with a review of the development of modeling in lithography leading towards the creation of a model of a photochromic system. This chapter is followed by the presentation of background material introducing AMOL and surface plasmon. After the background in introduced the next two chapters introduce the modeling of photochromic layers and resists and validate the FEM modeling of Maxwell's equations, describing the transmission of light in an optical system. The FEM model of the AMOL system is described and validated in full in the fifth chapter completing the model development stage. The later chapters explore the interaction of AMOL with known near-field effects: Chapter 6 examines how polarisation affects transmission, Chapter 7 examines how a plasmonic reflector can aid the transmission of an image into a resist layer for an AMOL exposure and Chapter 8 explores superlensing in an AMOL system and if a dichroic filtering is seen. The final chapter outlines the conclusions made in the thesis and ideas for the further development of AMOL.

1.6 PUBLICATIONS

Aspects of this thesis have been published or presented as follows:

Early modeling work was presented at The International Conference on Nanoscience and Nanotechnology (ICONN) 2008 through an oral presentation and published in refereed conference proceedings,

Foulkes, J & Blaikie, R 2008, 'Finite Element Simulation of Absorbance Modulation Optical Lithography', Melbourne, Australia: 2008, *Proceedings International Conference on Nanoscience and Nanotechnology (ICONN 2008),* Feb 25-29 2008, pp184-187.

The work on the influence on polarisation on AMOL presented in Chapter 6 was presented at the 53rd International Conference on Electron, Ion Photon Beam Nanofabrication and Technology through a poster and was published in the Journal of Vacuum Science and Technology,

1.6 PUBLICATIONS

Foulkes, JE & Blaikie, RJ 2009, 'Influence of polarization on absorbance modulated subwavelength grating structures', *Journal of Vacuum Science & Technology B*, vol. 27, no. 6, pp. 2941-6.

The work on influence on the impact of the introduction of a PRL on AMOL presented in Chapter 7 was presented at the International Conference on Nanoscience and Nanotechnology (ICONN 2008), through an oral presentation and the work on the interfacing of AMOL with a superlens in Chapter 8 has been accepted for oral presentation at the 5th International Conference on Advanced Materials and Nanotechnology (AMN-5). In addition it is planned that a journal article combining the work of these two papers describing the interface of AMOL with plasmonic materials will be submitted in early 2011.

Chapter 2

BACKGROUND

2.1 INTRODUCTION

The system of AMOL introduced by papers published in late 2006 and 2007 by Rajesh Menon and Hank Smith at MIT [Menon 2006, Menon 2007] described an optical lithography system using a photochromic azobenzene polymer named PMEA (poly[4-[2-(methacryloyloxy)ethyl] azobenzene]) to create a mask and was broadly related to the microscopy technique of STED [Hell 1994]. The system would involve a thin layer of photoresist spun directly on top of a photoresist. The absorption of this layer could then be changed because of its photochromic nature; a beam at one wavelength, λ_1 could create a transparent state and a second wavelength, λ_2, could create an opaque state. By combining an exposure pattern of λ_1 and λ_2 a full pattern could be created consisting of high and low absorbance states, thus an adaptive mask would be formed and because the photochromic material is completely reversible a second pattern may be exposed after the first without additional development steps being required.

In order for an AMOL system to be modelled or fabricated there are a series of key requirements that must be achieved, both for material and experimental set up. Most importantly a photochromic layer with appropriate absorbance characteristics, fabrication potential, and sensitivity at suitable wavelengths must be found. AMOL also requires a system which can combine two wavelengths into a useful arrangement which is incident on the photoresist; here the Lloyd's mirror set up is introduced, however a zone-plate array system has also been described [Tsai 2008]. A near-field lithography system, such as AMOL, will struggle to image into a deep resist and it is important to try and extend this distance to allow for easier fabrication, here surface plasmon are sug-

gested as a suitable approach. This chapter outlines the development of AMOL, beginning with STED microscopy and photochromic layers. It then presents background information regarding surface plasmons and describes the metrics used to clarify imaging performance in this thesis.

2.1.1 STIMULATED EMISSION DEPLETION MICROSCOPY

Stimulated emission depletion microscopy (STED) is a microscopy technique that makes use of two incident wavelengths and fluorescent molecules that was initially claimed to be able to improve resolution by a factor of 4.5 [Hell 1994], as shown in Fig 2.1. One wavelength is used to excite fluorescence in the molecules, as this is the information of interest; however STED then uses a second wavelength with a ring spatial pattern to suppress fluorescence in the area surrounding the point of interest and hence allow a smaller region to be examined. This technique has demonstrated resolution down to 5.8nm, a factor of 133 improvement on the responsible wavelength [Rittweger 2009], with an example improvement shown in Fig 2.2. Taking this idea and applying it to lithography is an attractive option as Hell has suggested [Hell 2004, Hell 2003]. The major difference between this method and a lithography system based upon it is the interchange of the fluorescent molecules with some other light-dependent medium, such as a photochromic layer.

2.1.2 PHOTOCHROMES

Photochromism may be defined as a reversible absorbance spectra change induced by the irradiation of a material by light (Fig 2.3). Organic photochromic compounds have been observed since the 19th century [Fritzsche 1867], however it was not until the 1940's that research into photochromism developed significantly, particularly for use in ophthalmic lenses [Crano 1996]. Since this time there has been a huge amount of research into different aspects of photochromism and related phenomena [Ercole 2010], including the kinetics, surface patterning [Barrett 2007] and induced birefringence and dichroism [Delaire 2000]. There is a large range of different functionalities for which

2.1 INTRODUCTION

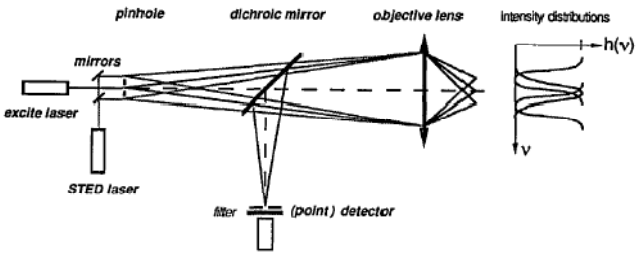

Figure 2.1 Principles of a STED fluorescence scanning microscope. An excitation beam and two offset STED beams are focused into the object for excitation and stimulated emission, respectively. The spontaneously emitted light is recorded in a (point) detector. [Hell 1994]

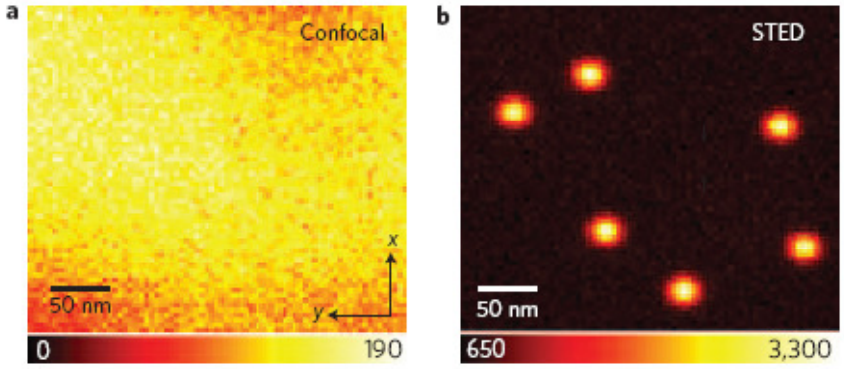

Figure 2.2 Comparison the same crystal sections measured with (a) Confocal and (b) STED microscopy of densely packed nitrogen vacancy centres in diamond [Rittweger 2009]

photochromic materials have shown possible use [Bouas-Laurent 2001, Wilson 1984], including optical data recording [Kawata 2000, Pederson 2000], optical data processing, actinometry and optical switching [Yager 2006, Sasaki 1997]. Photochromism may also have secondary effects alongside the changing colour; the refractive index, the metal ion capture, electron capture, and the shape and size of the polymers and solids have been shown to change, alongside other bulk material properties [Kumar 1989].

There is a large range of molecules which exhibit some form of photochromism, including spiropyrans, chromenes, fulgides and azobenzenes and the kinetics and chemical pathways of these photochromes vary [Bouas-Laurent 2001]. In this work the focus is placed on a generic photochrome based on an azobenzene. Photochromism in azobenzene is caused by the incident light causing a change in the cis-trans isomerisation (Fig

2.4) of the molecule [Yamashita 1962, Barrett 1995]. The photochromism in azobenzene can affect not only the absorbance but also the viscosity, solubility, pH and surface structure among other parameters [Norikane 2004, Kumar 1989] depending on the attached functional groups. The first experimental work in AMOL used an azobenzene (PMEA) photochromic layer as this operated at suitable wavelengths $\lambda{\sim}400-500nm$ and the absorbance change was adequate to allow pattern generation. For a lithography system it is desirable that the masking layer has large differentiation between opaque and transparent regions, this requires the absorbance change of the photochrome to be as large as possible.

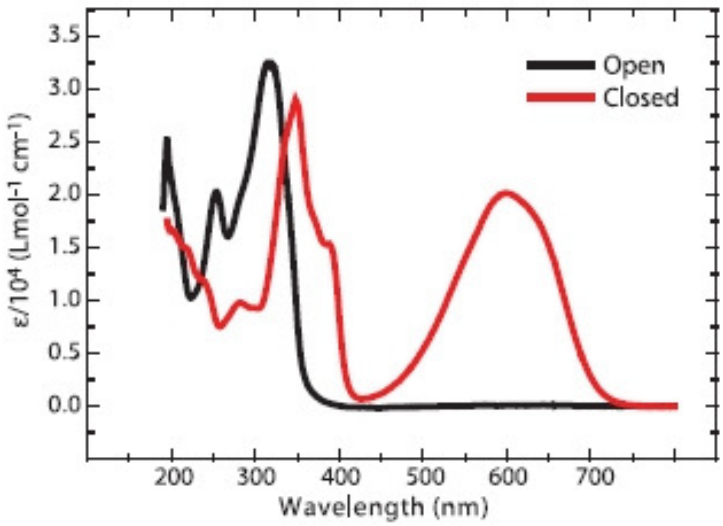

Figure 2.3 Changing absorption spectra in a photochromatic material [Andrew 2009]

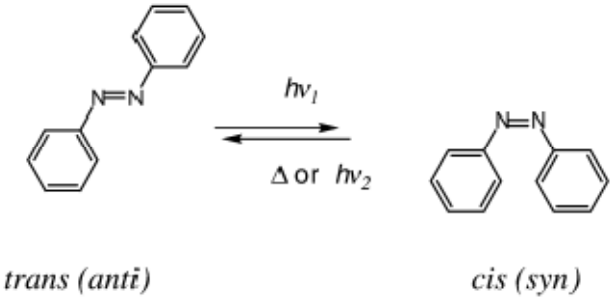

Figure 2.4 Isomerization of azo-compound causing photochromatic effect [Bouas-Laurent 2001], $h\nu_1$ and $h\nu_2$ represent the conversions by light and Δ the thermal constant.

2.1.3 ABSORBANCE MODULATION OPTICAL LITHOGRAPHY – PROGRESS TO DATE

Menon and Smith proposed and began basic steps towards making use of the photochromic effect in optical lithography [Menon 2006]. The suggested system, shown schematically in Fig 2.5, involved a layer of the photochromic material placed above a layer of photoresist on the substrate. Through careful selection of the pattern and intensity of the incident wavelengths, λ_1 and λ_2, a transparent spot may be created in the photochromic layer, allowing λ_1 to pass through and expose the underlying photoresist. By extension a complex pattern may be formed in the photoresist by a series of serial exposures, shown in Fig 2.5. Thus the AMOL layer may be used as an adaptable masking layer, with the adaptation controlled by optical sources which could be placed in the far-field. A theoretical of improvement in resolution to $\lambda/13$ was proposed [Menon 2006].

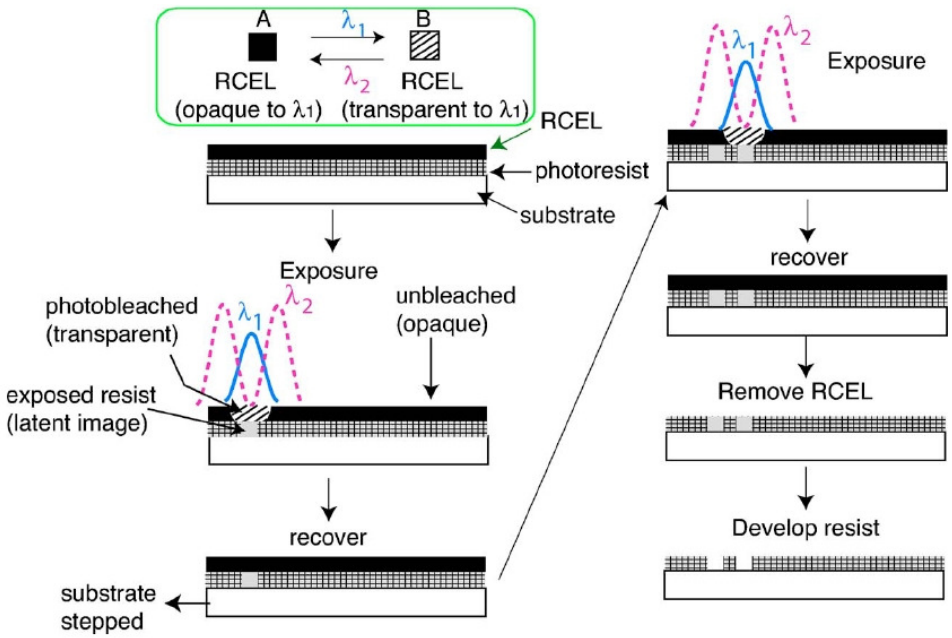

Figure 2.5 Schematic of the AMOL procedure showing a single exposure using two standing waves and the ability to perform multiple exposure steps [Menon 2006]

A following paper [Menon 2007] detailed an experimental exploration of AMOL (Fig 2.6). Using a Lloyd's mirror [Born 1999] set-up (Fig 2.7), a standing wave in λ_2 (532 nm) was created at the surface of the photochromatic layer to provide the changing intensity ratios between the two wavelengths; a constant intensity of λ_1

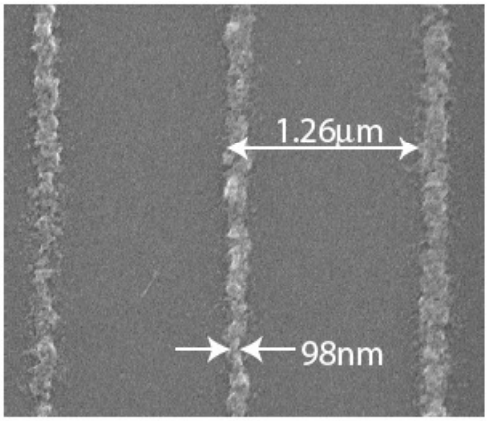

Figure 2.6 Scanning electron micrographs of lines exposed in negative resist by AMOL system showing average linewidth of 117 nm. [Menon 2007]

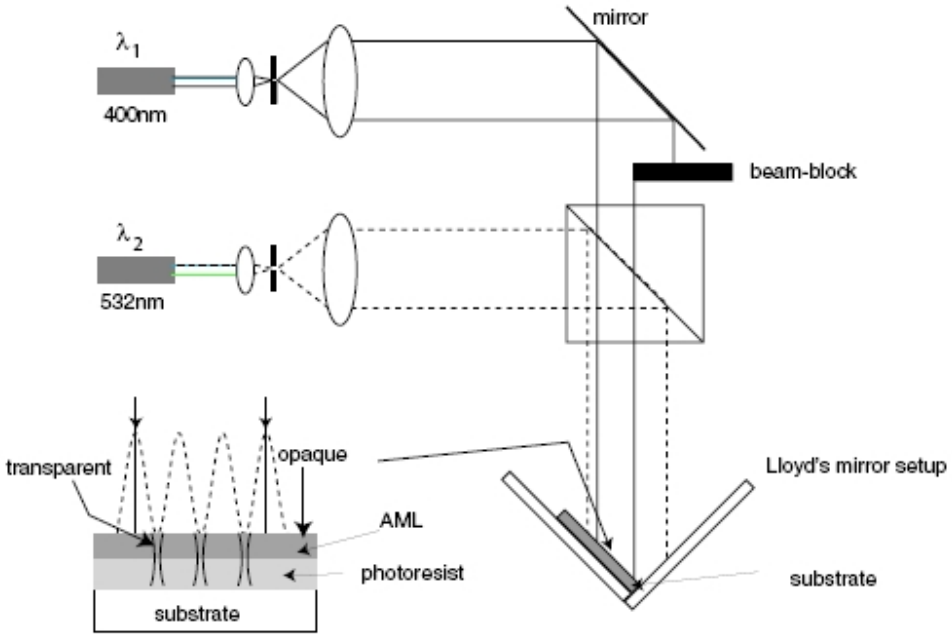

Figure 2.7 Schematic of the Lloyd's mirror configuration able to create a modulated $\boldsymbol{\lambda_2}$ and plane-wave incident $\boldsymbol{\lambda_1}$ [Menon 2007]

(400 nm) was then also directed onto the layer. Lines of varying widths were created, with a smallest linewidth of 100nm; this limitation was attributed to the thickness of the photoresist. A third paper experimentally demonstrated that multiple exposures could be made using the AMOL system and these could produce spatial frequency multiplication in the exposure pattern; decreasing the period of the grating below the wavelength [Tsai 2007], this verification of the double exposure capabilities demonstrates how AMOL is able to offer improved resolution even though a small duty cycle may be used for a single exposure.

In 2009 a further paper presented the same AMOL system with an alternative photochromic material with wider separation of λ_1 and λ_2 [Andrew 2009]. Later work by the same group has researched the interaction of AMOL with zone-plate array lithography [Tsai 2008] and the possibilities for microscopy with AMOL [Tsai 2010]. Zone-plate arrays offer a method to create desirable waveforms in both λ_1 and λ_2 concurrently using diffractive elements, whilst the opportunity to use AMOL for microscopy uses the confinement provided by an AML to resolve smaller particles.

2.1.4 ADVANTAGES OF AMOL

AMOL has the potential to create sub-diffraction limited patterns in the photoresist layer without the use of a rigid mask, alleviating the need to design and manufacture a mask, removing the need to consider the contamination of the mask as well as reducing the need for the tight control of the spatial distances required for conventional near-field imaging. These advantages provide a useful technique to access the non-diffraction limited near-field using far-field optics, providing an opportunity to improve resolving capability. Secondly the maskless nature of AMOL allows for quick prototyping of circuit designs as making a mask is often a considerable expense and may also allow for inexpensive surface patterning. However in order to be able to make use of these advantages further understanding is needed of the AMOL process. One particular focus is the resolution limits and process latitudes of an AMOL system and how these can be improved or affected by system adjustments. The nature of sub-diffraction limited imaging

requires operation using the near-field, hence the incorporation of near-field phenomena, such as surface plasmons to improve performance will be required to enhance the AMOL resolution.

2.2 SURFACE PLASMONS

2.2.1 INTRODUCTION

Many of the intrinsic properties of a metal are caused by the presence of the conduction electrons unbound to the metallic atoms; the interaction of these electrons with electromagnetic oscillation at optical frequencies has some particularly interesting effects [Zakharian 2007, Pitarke 2005, Maier 2005]. Particular interest is placed on the generation of surface charge oscillations on metals with loosely held electrons (Fig 2.8a), known as surface plasmons, as these oscillations are not limited by the wavelength of light, but rather by the electrons' confinement to the metal surface. Surface plasmons effects have been demonstrated using silver, gold and aluminium as well as other metamaterials, but there is work to find suitable plasmonic metals for different situations [West 2010]. Particular focus has been placed on areas including the combination of surface plasmon effects with circuitry [Ozbay 2006] and surface enhanced raman spectroscopy (SERS) which uses surface plasmons to allow improved measurement [Campion 1998]. The ability to break the diffraction limit as well as bridge the gap between light and circuitry has lead to a large amount of research in different areas of plasmonics.

2.2.2 COUPLING TO SURFACE PLASMONS

In order that light may induce surface plasmons on a planar metal dielectric interface the light must supply the appropriate momentum and energy to the conduction electrons. The nature of the plasmonics creates a requirement that the momentum of the light must be greater than the free-space momentum of the light [Barnes 2003, Novotny 2006], hence a simple air-metal interface will not induce surface plasmons (Fig 2.8b). Fortunately this momentum gap may be bridged by evanescent fields, for instance by a narrow

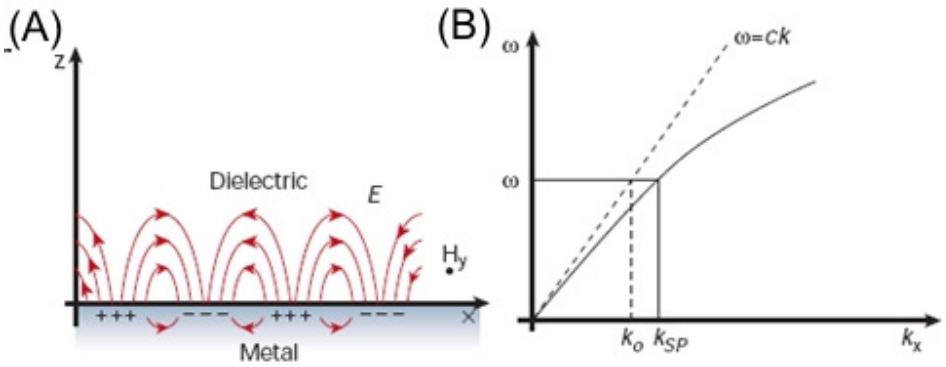

Figure 2.8 Surface plasmon generation showing (a) generation of electric fields at the interface which create surface plasmons and (b) the dispersion curve showing the mismatch between the light line and surface plasmon [Barnes 2003].

grating or frustrated total internal reflectance (FTIR), of course the evanescent nature of these fields require the dimensions to be small. Surface plasmons generated by subwavelength apertures or small particles are able to couple to surface plasmons and able to confine them locally [Novotny 2006], whereas surface plasmons in waveguides may be propagated ~100 μm or more [Barnes 2003]. This difference is based upon the electric fields; when they are uniform a propagating surface plasmon is created, if however the fields are heavily concentrated there is interference between the surface plasmon excitations and localisation occurs [Kawata 2001].

The generation of localized surface plasmons on a metal interface is very dependent on the geometries involved, as the evanescent decay of the field reduces in impact at long distances and also, at short distances it has been noted that there is a decrease in performance, perhaps due to coupling between the probe and sample [Novotny 2006]. However these properties have the possibility of leading to new lithography techniques [Smith 2009]. The generation of surface plasmons with transverse magnetic (TM) polarised light has been shown to assist in some lithography work, including improving process latitude [Arnold 2007] and is responsible for silver superlensing effects [Pendry 2000]. There are opportunities to combine near-field lithography with surface plasmons, through plasmonic metal layers which may allow improved performance. Previous surface plasmon work has been successfully modeled using a variety of techniques

including finite element methods (FEM) and finite difference time domain (FDTD) [Barnes 2009]. The interaction of such a layer with an AMOL system is different, as there is only a simple absorbance mask, yet may show improved performance.

2.3 MEASUREMENT METRICS

In order to quantify and compare the performance of an optical lithography system a series of metrics need to be used that reflect the important features of the lithography system. Unfortunately this is a difficult problem as there are a number of criteria of an intensity profile in a resist layer that are important in an image formation. In the case of AMOL neither the normal metrics, or a comparison between the desired and transmitted image provide clear answers, as there is not a perfect replication to be compared to as there would be in a system with a set mask and there is only an absorbance contrast in the mask rather. In this thesis a number of metrics are used to reflect the performance of lithography systems, with the choice of metric explained for each case; here the follwing metrics are considered: contrast, full width half maximum (FWHM), and normalised image log slope (NILS) to indicate the suitability of a particular grating and the depth of focus (DOF) to indicate depth that an image has propagated into the resist.

2.3.1 CONTRAST

One of the simplest methods to measure the quality of an intensity waveform is to compare the difference between the maximum and minimum value of the intensity. The Michelson Contrast, V is defined as the ration of the difference and sum of the intensity minimum and maximum in the intensity profile;

$$V = Contrast = \frac{I_{max} - I_{min}}{I_{max} + I_{min}}, \tag{2.1}$$

[Michelson 1927] where I_{max} and I_{min} are the maximum and minimum intensities of that profile. This contrast is similar to contrast measured used in photography where the difference between the light and dark areas of a photo shows the range of light sensitivity. Although a useful metric in many cases where a periodic, 50% duty-cycle,

rectangular grating is being examined, the contrast does not always adequately reflect the performance of a lithography system as it does not adjust to alternative patterns and does not examine the most important section of the intensity waveform, the steepness of the intensity waveform around the imaging limit [Mack 2007]. Considering AMOL gratings it can provide some indication of performance but the lack of deep nulls in the intensity waveforms can cause unnecessarily large variation.

2.3.2 FULL WIDTH AT HALF MAXIMUM

Instead of measuring the relative change in intensity the FWHM relates to the breadth of the intensity waveform, with a smaller FWHM being desirable because it suggests a narrow peak. Shown in Fig 2.9 the FWHM is the horizontal distance between the two points at half the maximum intensity (I_{max}) in the intensity waveform. This metric is very useful for AMOL type gratings as it allows the size of the intensity waveform to be measured and compared to the period of the standing wave in λ_2, and in AMOL the aperture size should be less than the grating size in order to image small features. Similar to contrast a DC offset present in the intensity waveform will affect the FWHM as the half maximum point may not reflect the shape of the central feature.

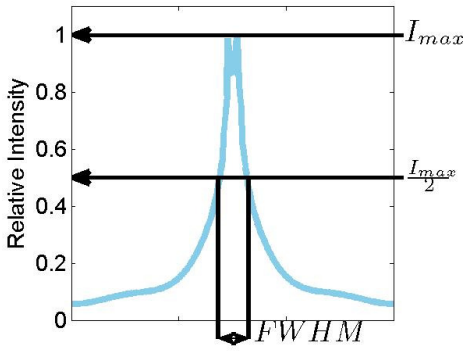

Figure 2.9 Demonstration of the I_{max} and $I_{max}/2$ points used to calculate the FWHM by finding the distance between the two points where the intensity waveform crosses $I_{max}/2$.

2.3.3 NORMALISED INTENSITY LOG-SLOPE

NILS is an alternative measure introduced by Mack that measures the slope of the intensity waveform at the desired width so that a steeper, thus more desirable intensity transition gives a larger NILS value [Mack 2007]. To make the metric more resistant to intensity and period it is normalised by intensity and linewidth (w), and may be written as

$$NILS = w\frac{1}{I}\left(\frac{dI}{dx}\right)\Big|_{x=\pm\frac{w}{2}} = \frac{w\big(dln(I)\big)}{(dx)}\Big|_{x=\pm\frac{w}{2}}. \tag{2.2}$$

NILS is particularly useful as a metric because it allows the determination of the potential for a given intensity waveform to create a useful feature in a resist and is less affected by background intensity limits. In an AMOL system there is no straightforward choice of w as there would be with a fixed mask, hence w becomes a parameter that must be chosen. In this work w has been taken as 50 nm unless otherwise specified as this suggests the reasonably narrow features desired.

2.3.4 DEPTH OF FOCUS

The image intensity at the AML/resist interface is important to the potential imaging power of the system, however for this to be transferred into the resist effectively the intensity waveform must remain well shaped throughout the thickness of resist used.

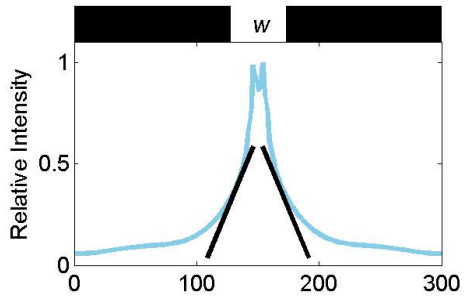

Figure 2.10 Demonstration of the NILS metric showing slopes of the intensity waveforms measured at the desired linewidth, w to be used in Eq 2.2.

This is of particular importance for evanescent features because they decay with propagation, especially the higher spatial frequencies. In projection lithography DOF measures the distance in a resist that the lens is able to focus the image [Mack 2007], here a similar idea is used where the DOF is the distance before the intensity waveform quality drops below a desired level. This metric is found by calculating the above metrics at increasing depth into the resist layer until they no longer meet the desired quality level. The change of FWHM with propagation depth into a resist can also provide insight into the change of the intensity profile.

2.4 CONCLUSIONS

This chapter has introduced the historical development of AMOL and explained some of the methods that have inspired its development including STED and photochromic materials. The outline of AMOL presents the current development and the potential advantages of such a system. However it is also noted that there are obstacles for any near-field lithography system, particularly in achieving adequate depth of focus and surface plasmons are introduced as a potential way to partially alleviate these issues. The following three chapters introduce the modeling work used in this thesis, first by presenting scalar models for photochromes and AMOL before presenting the development of a vector model of AMOL.

Chapter 3

MODELING OF PHOTOCHROMATIC LAYERS

3.1 INTRODUCTION

In this chapter the background information that enables a model of a photoresist system for lithography to be developed is presented. First an introduction is made to the previous modeling of photochromic layers, such as contrast enhancement layers (CELs) used in lithography, which leads into the scalar modeling of AMOL by Menon [Menon 2007]. Following an overview of Menon's modeling the additional complexity introduced by Warner's [Warner 2009] work, extending this model for the AMOL system to include some analytical solutions and aperture formation is examined. Finally the vector approach to light propagation, Maxwell's equations, is introduced and related to the scalar work.

3.2 MODELING TECHNIQUES

It is possible to model light propagation by both scalar and vector techniques. Historically simplicity, lack of computation and speed has encouraged a wide range of scalar techniques to be developed to explore light propagation, reflection, refraction and some aspects of diffraction. However even simple cases may lead to situations not able to be fully explained by scalar methods. Here scalar methods to examine photo-lithographical and photochromic techniques are introduced and explained before Maxwell's Equations are used to introduce the same problems in vector form.

3.3 MODELING OF PHOTORESISTS

In the initial work on optical lithography there was little modeling of the processes occurring in the systems, instead experimental evidence and rules of thumb were widely used. As increasingly complex systems were developed to meet the continuing demands for performance improvement increased interest was placed on solidifying the understanding of photoresist kinetics. Seminal papers providing models for a set of scalar equation systems behind the kinetics were introduced by Dill [Dill 1975], with later work both adding to these initial techniques and exploring new technological developments [Cole 2001, Mack 2001].

3.3.1 DILL EQUATIONS

In 1975 Frederick Dill and coauthors published a series of papers [Dill 1975, Dill 1975a, Dill 1975b] looking to improve the quantitative science behind optical lithography, with a particular focus on the modeling of a positive photoresist. Dill posited a model based on four measurable parameters which could be used to calculate the response of a positive photoresist to exposure and then the post-exposure development. Here a brief review of this development is given before this model is extended for a photochromic material.

Dill [Dill 75a] presents photoresists as materials with three components, a base resin as the carrying liquid, a photoactive compound (inhibitor) to react with the incident light and solvents to allow application to a surface. The model is built based on the assumptions that: optical scattering is small so that the material may be fully described optically by an index of refraction and absorption coefficient; that the photoactive compound creates a significant change in absorption; and the photoactive compound's sensitivity is proportional to the local exposure intensity and a semi-infinite layer of photoresist is present.

The Beer-Lambert law describes the optical absorption of light, intensity I, passing through a distance, x, as

3.3 MODELING OF PHOTORESISTS

$$\frac{dI}{dx} = -I \sum a_i m_i, \tag{3.1}$$

where a_i and m_i represent the *i*th component of the molar absorption coefficient and molar concentration respectively for some absorbing species in the material [Lakowicz 1999, Strong 1952]. Deviations from Beer's law exist in a number of cases, for example aggregation of the particles in solution, non-modeled absorbers, scattering, fluoresence and saturation at high densities however these are ignored here. Assuming there are three absorptive components of the system, the inhibitor, the base resin and the reaction products (numbered as 1, 2 and 3 respectively) and knowing the initial inhibitor and resin concentrations m_{10} and m_{20} respectively, Dill writes the rate of change of the intensity, $I(x,t)$ as

$$\frac{\partial I(x,t)}{\partial x} = -I[m_1(x,t)\{\alpha_1 - \alpha_3\} + \alpha_2 m_{20} + \alpha_3 m_{10}], \tag{3.2}$$

and the rate at which the inhibitor is converted into reaction products is given by

$$\frac{\partial m_1(x,t)}{\partial x} = -I(x,t) m_1(x,t) C \tag{3.3}$$

where C is the fractional decay rate of inhibitor per unit intensity (shown schematically in Fig 3.1). Dill then simplifies the presentation of these equations by normalizing them with respect to the initial inhibitor concentration,

$$M(x,t) = \frac{m_1(x,t)}{m_{10}}, \tag{3.4}$$

and introducing parameters A, B and C, defined as

$$A = (\alpha_1 - \alpha_3) m_{10}, \tag{3.5}$$

$$B = (\alpha_2 m_{20} - \alpha_3 m_{10}), \tag{3.6}$$

$$C = C, \tag{3.7}$$

allowing Eqs 3.2 and 3.3 to be rewritten as

$$\frac{\partial I(x,t)}{\partial x} = -I(x,t)[AM(x,t) + B], \tag{3.8}$$

and

$$\frac{\partial M(x,t)}{\partial x} = -I(x,t) M(x,t) C. \tag{3.9}$$

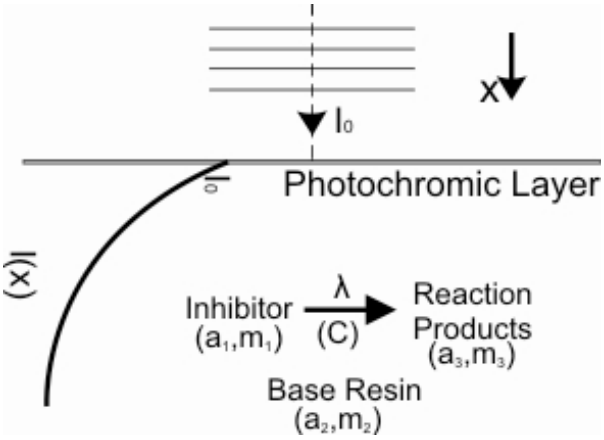

Figure 3.1 Schematic of the interactions taking place in a photoresist layer, as described by Dill's equations. The incident intensity, $I(x)$ decays due to three components, the inhibitor, reaction products and base resin, with the inhibitor transformed into reaction products with fractional efficiency C.

These equations are subject to the initial conditions that the initial concentration is all in the inhibitor state with an initial intensity profile reflecting this, and boundary conditions that set the initial intensity at the photoresist surface as $I_0(x,t)$. It was later shown that an exact solution could be derived from these equations and conditions [Babu 1986], resulting in a closed form for the intensity of

$$I(x,t) = I_0 \frac{[A(1-M) - BlnM]}{\{A[1-e^{-I_0 Ct}] + BCI_0 t\}}. \tag{3.10}$$

where M could be found by solving

$$\int_{g(t)}^{M} \frac{\partial y}{y\{a(1-y) - B\,ln\,y\}} = x, \tag{3.11}$$

where the lower limit, $g(t)$, is the solution of Eq. 3.11 for $x = 0$.

The developed expression allows the calculation of the intensity at any depth into the photoresist, from this equation a complete characterisation of a resist can be derived using the three constants, A, B and C with a fourth relation describing the resist development rate. Dill then shows how these may be related to measurable optical properties based on the transmittance, $T(t)$ of a thin film sample;

$$A = \left(\frac{1}{d}\right)\ln\left[\frac{T(\infty)}{T(0)}\right],$$
$$B = -\left(\frac{1}{d}\right)\ln[T(\infty)], \tag{3.12}$$
$$C = \frac{A+B}{AI_0T(0)\{1-T(0)\}}\frac{dT(0)}{dt},$$

thus allowing an equation describing the full kinetics to be derived from a transmittance test. The three parameters A, B and C may now be defined as the ratio between the initial and final transmittance, the transmission when no inhibitor remains and the fractional decay of inhibitor per unit intensity, respectively. Dill also described a model for the development of a photoresist [Dill 1975b], but this is not considered here.

3.3.2 CONTRAST ENHANCEMENT LAYERS (CEL)

Griffing [Griffing 1985, Grifing 1983] introduced a thin photobleachable contrast enhancement layer placed directly above the photoresist in a lithography system to enable imaging improvement. The CEL layer improves the contrast achieved in the photoresist because it absorbs part of the light passing through it; in the centre of the exposure the CEL will become completely transparent and allow an image to form but at the edges of the exposure the light intensity is reduced and the CEL will absorb this light thus protecting the unexposed photoresist below (Fig 3.2). This introduced non-linearity in the system enables a narrowing of the image in the resist. It has also been demonstrated that materials with non-linear photobleaching characteristics may be used [Hofer 1984].

Beginning with Dill's model for a positive photoresist it has been shown that an extension to the analytical solution may be made for the case of a CEL [Babu 1988, Oldham 1987, Diamond 1986]. In the general case, for a non-linear CEL layer, Dill's A parameter may be rewritten as

$$A_{eff} = \alpha M_c + \beta, \tag{3.13}$$

where $\alpha = 0$ for a linear CEL layer. In the linear case this may be developed [Babu 1985] as in the case of the positive photoresist, giving Eq 3.10. However, considering

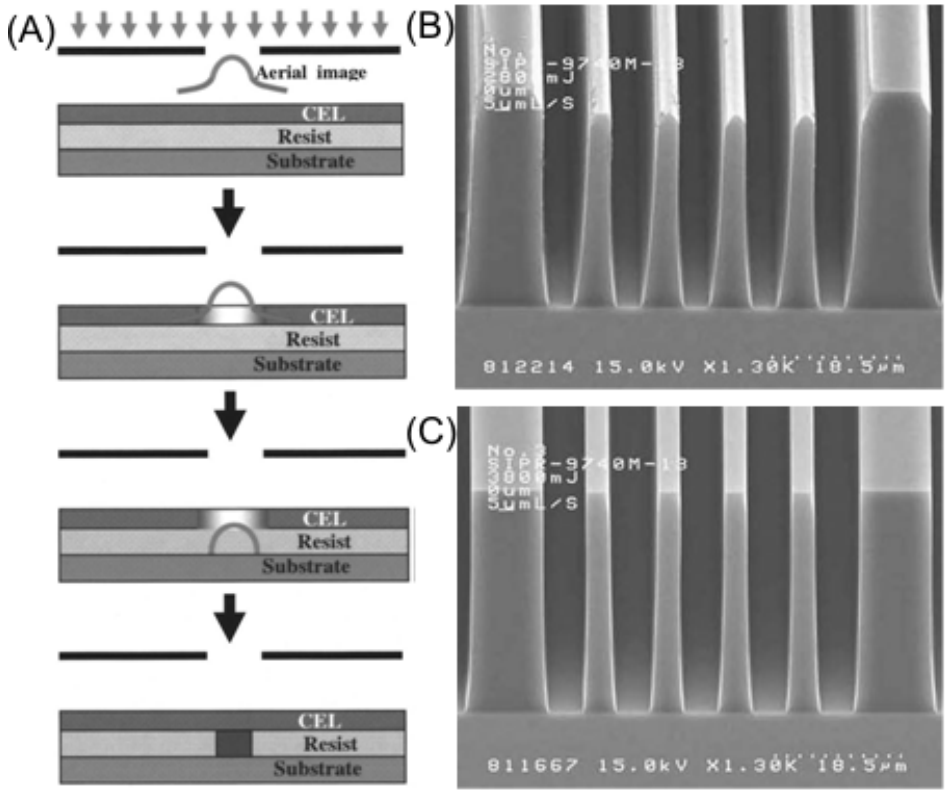

Figure 3.2 Actions of a contrast enhancement layer (CEL) showing (a) reduction of edges of exposure profile through CEL placed above resist [Kim 2007]. Demonstrating imaging performance without (b) and with (c) a CEL being used to fabricate 5μm grating with 350-450 nm wavelength [Flack 2004].

the photoresist beneath the CEL, the initial conditions have changed as the incident intensity is now dependent on the CEL layer's absorption;

$$I(0,x,t) = I_{CEL}(l,x,t), \tag{3.14}$$

where l is the depth of the CEL. [Babu 1988] shows this does not restrict the ability to solve the equations of the photoresist analytically.

The performance of CELs has been demonstrated both experimentally and through simulation [Flack 2004, Ito 1991, White 1986, O'Toole 1985] to allow improved resolution and some improvement in process latitude as the absorbance reduces changes due to intensity variation. This is pertinent to an AMOL system because it demonstrates how an absorbance layer may be used in a lithography system to improve resolution and that

interfacing photobleaching layers and resist is possible. However CELs are primarily able to improve the edge sharpness of exposures, without a second wavelength or additional non-linearity the photo-bleachable layer cannot create an image resolved beneath the diffraction limit. The problems which have faced CEL also shadow those which may face AMOL, with material parameter requirements becoming increasingly difficult [French 2009], although theoretically improvement remains possible at shorter wavelengths [Kim 2007].

3.4 MODELING OF AMOL PHOTOCHROMIC LAYERS

Scalar analytical solutions for two-wavelength exposure into photochromic layers have also been developed, with many closely related to Dill's methods; the implementation of the photo-kinetic reaction used in this work and how the appropriate values have been derived are presented here. This overview will begin by examining the modeling of photochromic layers before concentration on the solution for photochromic apertures presented by Menon [Menon 2006] and discuss the areas in which further research is warranted. The later development of an analytical solution by Warner [Warner 2009] will also be reviewed and explained before the model used in this thesis is outlined.

3.4.1 PHOTOCHROMIC MODELING

Photochromic effects and related phenomena have been of interest for various disciplines for a number of years and hence a great body of work has been published; in particular a focus has been placed on explaining the kinetics behind different photochromic materials. Research has been performed in several different areas, from investigating the chemical reactions and associated rate constants of simple and complicated systems [Ottavi 1998] to showing the possibility for complex dynamical systems to form [Borderie 1992] and non-linear absorption [Corbett 2008].

The effects that incident light may cause in chemical systems have also been modeled for various interesting systems including photodeformation of cantilevers [Corbett 2008,

Corbett 2007] (including some investigation of polarisation [Corbett 2008]) and surface relief formation [Bublitz 2001]. Concentrating on photochromic layers a number of studies have created models using first order kinetics for azobenzene [Serra 2008, Mechau 2005, Statman 2003]. The central difference between this modeling and an AMOL system is that there are two, competing wavelengths creating an aperture; this area has also been analytically modeled for some cases [Warner 2009, Menon 2006, Dantsker 1998, Dantsker 1994]. In this work an explanation of the model used for the simulation is made from combining the work of Menon [Menon 2006] and Warner [Warner 2009], focusing on using both wavelengths to understand the steady-state solution in two dimensions (the third being infinite in extent)

3.4.2 MENON'S MODEL

Menon examines the case of a thin layer of photochromic material where the focus is on the overall performance of the layer; a photokinetic factor is used to account for the depth of the film so knowledge of characteristics inside the layer is not possible using this method. The differential equations developed in this method are able to be numerically solved by a simple ODE solver.

Menon [Menon 2006] begins by considering a photochromic system with two states; a low absorbing state, *A*, and a high absorbing state, *B*, then the absorbance, α, of a given wavelength, say λ_1, in the photochromic layer is the sum of the absorbance of each of the species in the layer. A diagram showing the axis and dimensions used is given in Fig 3.3. The absorbance of the species is the product of its concentration and its ability to absorb at the particular wavelength;

$$\bar{\alpha}_1 = (\alpha_{1A} + \alpha_{1B})l = (\varepsilon_{1A}[A] + \varepsilon_{1B}[B])l \tag{3.15}$$

where ε_{1A} is the decadic molar absorption coefficient of state A for wavelength λ_1, $[A]$ is the concentration of state A and l the thickness of the photochromic layer (here $\bar{\alpha}_1$ is used to represent the absorbance through a sample and α the absorbance per unit length). A similar expression may be written for the absorbance of λ_2 ,

$$\bar{\alpha}_2 = (\alpha_{2A} + \alpha_{2B})l = (\varepsilon_{2A}[A] + \varepsilon_{2B}[B])l \tag{3.16}$$

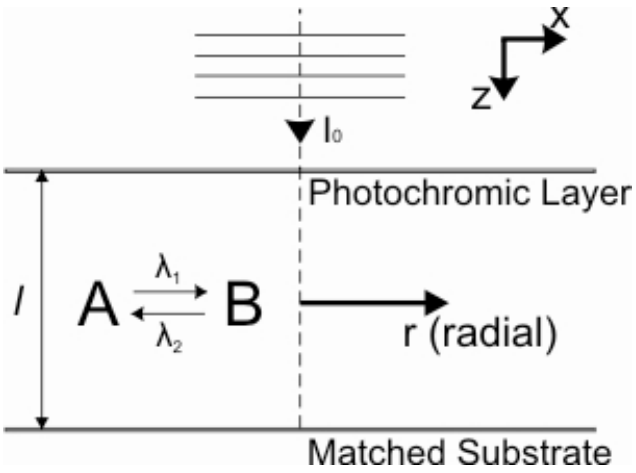

Figure 3.3 Showing the system used for the analytical analyses of AMOL. The axes are as x and z, with radial length r, measured from the center of the exposure. The input intensity is I_0, the depth of the photochromic layer is l, with a matched substrate below the resist removing all reflections.

and the expression may be extended to include any number of absorbing species present. Any light incident on the material will be partially absorbed by each state.

Menon introduces an expression for the fraction of incident light absorbed throughout the photochromic layer in terms of the incident intensity, I_{01},

$$f_1(r,t) = \frac{I_{01}(r)}{l}\left[1 - 10^{-\bar{\alpha}_1(r,t)}\right], \tag{3.17}$$

however only part of this fraction then contributes to the conversion between the states. For example the fraction converted from state A to B by λ_1 is given by

$$f_1(r,t) = \frac{I_{01}(r)}{l}\left[1 - 10^{-\bar{\alpha}_1(r,t)}\right]\frac{\alpha_{1A}(r,t)}{\bar{\alpha}_1(r,t)}, \tag{3.18}$$

whence he defines the photokinetic factor as

$$F_1 = \left[1 - 10^{-\bar{\alpha}_1(r,t)}\right]\frac{1}{\bar{\alpha}_1(r,t)}. \tag{3.19}$$

The change in the concentration of either of the species with time can now be written as the sum of the fraction of incident light effecting a transformation multiplied by how efficient each transformation is; a thermal coefficient, k_{BA} is also required as one state is more thermally stable (in the presented case the opaque state is more stable);

$$-\frac{d[A]}{dt} = \phi_{1AB}\frac{I_{01}}{l}F_1\alpha_{1A} + \phi_{2AB}\frac{I_{02}}{l}F_2\alpha_{2A} - k_{BA}[B] - \phi_{1BA}\frac{I_{01}}{l}F_1\alpha_{1B} - \phi_{2BA}\frac{I_{02}}{l}F_2\alpha_{2B}, \tag{3.20}$$

where ϕ_{1ij} represents the quantum efficiency of the transformation from state i to state j. For any given system $[B]$ may be expressed as the difference between the initial concentration (assuming that this was all in one state, $[A]_0$) and the current $[A]$,

$$[A]_0 = [A] + [B]. \tag{3.21}$$

and hence, with Eqs 3.20 and 3.19 an expression of the concentration fraction may be formulated as

$$-\frac{d[A]}{dt} = [(\phi_{1AB}\epsilon_{1A} + \phi_{1BA}\epsilon_{1B})I_{01}F_1 + (\phi_{2AB}\epsilon_{2A} + \phi_{2BA}\epsilon_{2B})I_{02}F_{2+}k_{BA}] \times [A] - [\phi_{1BA}\epsilon_{1B}I_{01}F_1 + \phi_{2BA}\epsilon_{2B}I_{02}F_2 + k_{BA}] \times [A]_0. \tag{3.22}$$

Menon solved this form numerically and demonstrated the ability of the AMOL system to compress a given point spread function (Fig 3.4), thus improving resolution. Whilst this approach calculates an absorption level for the light passing through the resist, it does not examine the change in absorbance levels inside the resist (with distance z) or how the aperture shape in the AML affects the propagation of light.

3.4.3 WARNER'S MODEL

Warner and Blaikie [Warner 2009] examined the same problem of two incident wavelengths driving a photochromic layer, with the focus on the change in intensity with depth and time. In particular they examined the formation of narrow profiles and the dynamics of the equilibrium states formed based on the rate constants of the processes and demonstrated the profiles of the light intensity with depth into the photoresist, which was not possible with Menon's approach.

Warner assumes that there are no thermal or back reactions involved in the process, thus the population obeys the dynamics

$$\frac{\partial n}{\partial t} = -\phi_{1AB}\Gamma_A I_1 n + (1-n)\phi_{2BA}\Gamma_B I_2, \tag{3.23}$$

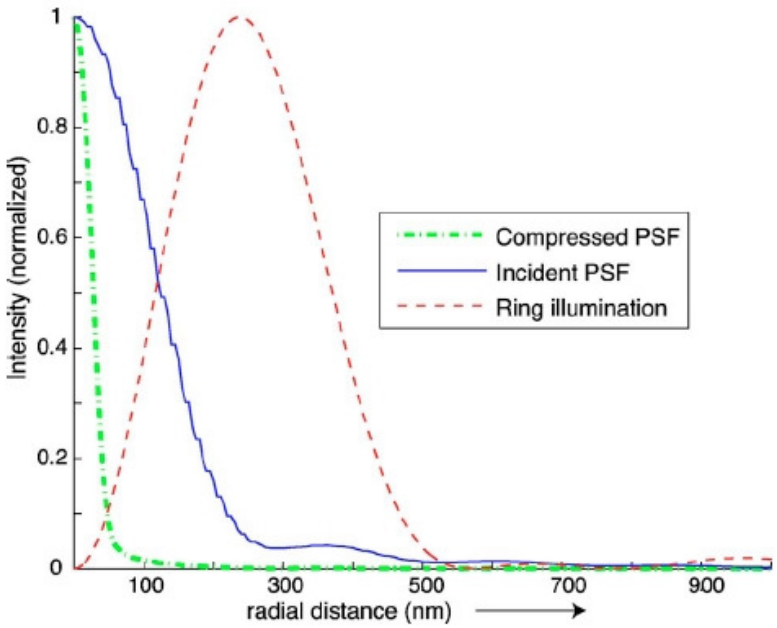

Figure 3.4 Compression of the PSF achieved by AMOL system showing the ring illumination of λ_2, the incident PSF of λ_1 and the compressed PSF after transmission through the AML [Menon 2006].

where the population n is expressed as the fraction of photochromes in state A (opaque), Γ_{A} and Γ_B are the absorption cross sections of each species and ϕ_{1ij} the quantum efficiency of the transformation from state i to state j (the symbol η_1 was used [Warner 2009] but has been changed to match [Menon 2006], also additional subscripts have been added to the model to allow later extension). The introduction of the constants

$$w_{1AB} = \phi_{1AB}\Gamma_A I_1(0), \tag{3.24}$$

$$w_{2AB} = \phi_{2BA}\Gamma_B I_2(0), \tag{3.25}$$

and the intensity ratio

$$\mathcal{I}_i(z,t) = \frac{I_i(z,t)}{I_i(0)}, \qquad i = 1,2 \tag{3.26}$$

allows the dynamics to be rewritten as

$$\frac{\partial n}{\partial t} = -w_{1AB}\mathcal{I}_1 n + w_{2BA}\mathcal{I}_2(1-n). \tag{3.27}$$

Warner considers the equilibrium intensity distribution (no further change in n)

$$n = \frac{w_{2\mathrm{BA}}\mathcal{I}_2}{w_{1\mathrm{AB}}\mathcal{I}_1 + w_{2\mathrm{BA}}\mathcal{I}_2} \tag{3.28}$$

and combines this with the decay in intensity as defined by Beer's law (Eq 3.1)

$$\frac{d\mathcal{I}_1}{dz} = -n\frac{\mathcal{I}_1}{d_{B1}}, \tag{3.29}$$

and

$$\frac{d\mathcal{I}_2}{dz} = -(1-n)\frac{\mathcal{I}_2}{d_{B2}}, \tag{3.30}$$

for λ_1 and λ_2 respectively, where d_{Bi} represents the Beer length of wavelength i, which characterizes the absorption of wavelength i if it was the only species present [Warner 2009]. This leads to equilibrium equations for the change in intensity with depth,

$$\frac{\partial\mathcal{I}_1}{\partial u} = -\frac{w_{2BA}}{d_1}\frac{\mathcal{I}_1\mathcal{I}_2}{w_{1AB}\mathcal{I}_1 + w_{2BA}\mathcal{I}_2} \tag{3.31}$$

and similarly for the second wavelength, where the lengths have been reduced by a constant a, such that $z = au$ and $d_{Bi} = ad_i$. By combining Eq 3.31 with the equivalent equilibrium equation for λ_2 and introducing the constant, w, it may be shown that

$$\frac{\partial\mathcal{I}_2}{\partial u} = \frac{w_{1\mathrm{AB}}d_1}{w_{2\mathrm{BA}}d_2} \times \frac{\partial\mathcal{I}_1}{\partial u} = w \times \frac{\partial\mathcal{I}_1}{\partial u} \tag{3.32}$$

which may then be integrated using initial conditions at the front surface (for instance $\mathcal{I}_1 = \mathcal{I}_2 = 1$ at $u = 0$) to get a connection between the two wavelengths at equilibrium with changing depth,

$$\mathcal{I}_2(u) = 1 - w[1 - \mathcal{I}_1(u)]. \tag{3.33}$$

A second relation between the two intensities fractions can be created by eliminating n from Eqs 3.29 and 3.30 giving

$$\frac{d}{du}ln\left(\mathcal{I}_1^{d_1}\mathcal{I}_2^{d_2}\right) = -1 \tag{3.34}$$

Combining Eqs 3.33 and 3.34 allows a closed form for the intensity fraction at equilibrium to be calculated,

$$\frac{w_{1AB}d_1}{w_{2BA}d_2} \times \mathcal{I}_1^{\frac{d_1+d_2}{d_2}} + \left(1 - \frac{w_{1AB}d_1}{w_{2BA}d_2}\right) \times \mathcal{I}_1^{\frac{d_1}{d_2}} = e^{\frac{-u}{d_2}}. \tag{3.35}$$

From this set of equations a number of useful conclusions are drawn on the comparative decay of each wavelength, the emergence of narrow profiles in such systems (Fig 3.5), and the dynamics of the intensity distributions in the photoresist layers. It is, however, still a scalar method and when situations involving diffusion and/or sub-wavelength features exist it will not be able to fully characterise the system.

3.4.4 FURTHER MODEL CHANGES

A complete photochromic system needs to include the complete kinetics; the reverse transformation by each incident wavelength and the effect of the thermal constant. It is also necessary to compare the methods reviewed here and note any differences in the absorbance measured and other photochromic and material parameters.

Considering the problem of including all the basic system dynamics in Warner's model, examining Eq 3.20 there are three components which must be added to Eq 3.23, representing the two reverse reactions and the thermal constant, creating the equation

$$\frac{\partial n}{\partial t} = -\phi_{1AB}\Gamma_A I_1 n + (1-n)\phi_{2BA}\Gamma_B I_2 + (1-n)\phi_{1BA}\Gamma_B I_1 - \phi_{2AB}\Gamma_A I_2 n + k_{nBA}(1-n). \tag{3.36}$$

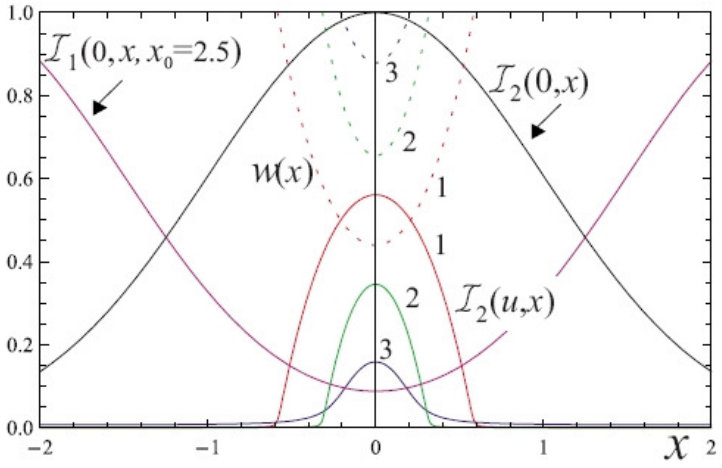

Figure 3.5 Demonstration of aperture formation in transverse direction x in an AML photochromic system showing the relative incident intensities, $\mathcal{I}_1(0), \mathcal{I}_2(0)$, and for three different cases (1,2,3) the $\mathcal{I}_2$ at 8 Beer lengths and the incident intensity ratio $w(x)$ (axis restricted to between 0 and 1). [Warner 2009]

Then considering the photostationary state where there is no further change in n, the fraction remaining in state A may be expressed;

$$\frac{\partial n}{\partial t} = 0 \rightarrow n = \frac{\phi_{1BA}\Gamma_1 I_1 + \phi_{2BA}\Gamma_2 I_2 + k_{BA}}{(\phi_{1AB} + \phi_{1BA})\Gamma_1 I_1 + (\phi_{2AB} + \phi_{2BA})\Gamma_2 I_2 + k_{nBA}} \tag{3.37}$$

from which the fraction in the second state (B) may simply calculated by $1 - n$, which is a differential equation including all the basic kinetics of the problem in the stationary state. The additional complexity introduced in this equation removes the opportunity to use the same analytical method which was used previously, although this equation may be solved quickly numerically.

3.4.5 MODEL UNITS

Having completed the derivation of the underlying kinetics of the photochromic reaction the various parameters must be related to each other. Equation 3.15 expressed the absorbance as a product of the concentration of states A and B and now the problem is expressed in terms of the fraction of photochromes in each state. An equivalent form of Eq 3.15 may be rewritten using the maximum absorbance of each state (α_{iMax}) and the fraction of photochromes in each state;

$$\begin{aligned} \alpha_1 &= \alpha_{1A} + \alpha_{1B} = (\varepsilon_{1A}[A] + \varepsilon_{1B}[B]) \\ &= n \times \alpha_{A1Max} + (1 - n) \times \alpha_{B1Max} \end{aligned} \tag{3.38}$$

where α_{A1Max} may be calculated by [Warner 2009]

$$\alpha_{A1Max} = \frac{1}{d_{A1}} = \rho\Gamma_1 \tag{3.39}$$

where $d_{A1}$is the Beer length of state 1 in isolation and ρ the number density of chromophores.

Given the determination of an equation determining the kinetics of the photochromic system appropriate constant values for the system now need to be calculated. This is complicated by the variation in expressions used in absorption laws. The Beer-Lambert law may be expressed as

$$ln\frac{I_0}{I} = \Gamma ml, \tag{3.40}$$

where m is the number of molecules per unit volume and l the distance [Lakowicz 1999] or in the alternative form,

$$log\frac{I_0}{I} = \varepsilon cl, \tag{3.41}$$

where $\varepsilon[mol^{-1}m^2]$ is the decadic molar absorption coefficient and $c[molm^{-3}]$ the concentration. Further, as discussed by [Cardarelli 2008] there may be different units used depending on the particular context or field (e.g. cm and/or litres). Converting between these forms is achieved by relating Eqs 3.40 and 3.41, taking into account the different logarithmic forms and using Avagadro's constant ($N_A = 6.02 \times 10^{23}$) to adjust from concentration to number of molecules per unit volume;

$$\Gamma_{ij} = 2.303\frac{\varepsilon c}{m} = 3.8243 \times 10^{-24}\varepsilon_{ij}. \tag{3.42}$$

The model systems of Menon [Menon 2007] and Warner [Warner 2009] are closely related, with the introduction of the photokinetic factor (Eq 3.19) by [Menon 2007] allowing the kinetics to be expressed as a function of the incident wavelength alone and expressing values for a thickness, l, whereas [Warner 2009] uses a relative intensity $\mathcal{I}_i$ specified at each depth ($0 < z < l$) of the photochromic layer allowing information about the changes taking place in this layer to be extracted. Here the relations have been detailed to allow a model with kinetics similar to Warner's to be complete and to be compared to the model and experimental results of Menon. The next section will detail how a vector model can be set up which will allow the previous scalar modeling work to be repeated and allow the investigation of several, very interesting and relevant phenomena to be investigated fully.

3.5 MAXWELL'S EQUATIONS

Maxwell's Equations may be used to explain the underlying propagation of electromagnetic waves through media and can be expressed in the form;

$$\nabla \times \boldsymbol{E} = -\frac{\partial \boldsymbol{B}}{\partial t}, \tag{3.43}$$

$$\nabla \times \boldsymbol{H} = \boldsymbol{J} + \frac{\partial \boldsymbol{D}}{\partial t}, \tag{3.44}$$

$$\nabla \cdot \boldsymbol{D} = \rho_v\,, \tag{3.45}$$

$$\nabla \cdot \boldsymbol{B} = 0, \tag{3.46}$$

where $\boldsymbol{E}$ and $\boldsymbol{B}$ represent the electric and magnetic fields respectively, $\boldsymbol{J}$ is the current density, ρ_v is the volume charge density and where auxiliary equations relationships can be defined to connect the fields dependent on the medium.

Through these equations a study of lithographical and photochromic systems is possible as the propagation of light and its interaction with materials may be explained completely, thus allowing a vector model to be developed when linked with numerical methods to solve the created system. Here an introduction is made to the links and relationships between the scalar models discussed above and Maxwell's equations.

3.6 INTENSITY IN RESIST FROM MAXWELL'S EQUATIONS

The effect of incident light in a light absorbing medium, such as a photochromic layer or photoresist, is proportional to the intensity of the incident light, I $[W/m^2]$. This relationship may be explained through Maxwell's equations, which also allow the definition of various useful parameters. The derivation begins by taking Maxwell's equations and subtracting the dot product with $\boldsymbol{H}$ of Eq 3.43 from the dot product of $\boldsymbol{E}$ with Eq 3.44 to give

$$\boldsymbol{E} \cdot \nabla \times \boldsymbol{H} - \boldsymbol{H} \cdot \nabla \times \boldsymbol{E} = \boldsymbol{E} \cdot \frac{\partial \boldsymbol{D}}{\partial t} + \boldsymbol{H} \cdot \frac{\partial \boldsymbol{B}}{\partial t} + \boldsymbol{E} \cdot \boldsymbol{J}. \tag{3.47}$$

Using vector identities the equation may be stated as

$$-\nabla \cdot (\boldsymbol{E} \times \boldsymbol{H}) = \boldsymbol{E} \cdot \frac{\partial \boldsymbol{D}}{\partial t} + \boldsymbol{H} \cdot \frac{\partial \boldsymbol{B}}{\partial t} + \boldsymbol{E} \cdot \boldsymbol{J} \tag{3.48}$$

and taking the integral of this equation about a volume, V, bounded by a closed surface, S and unit outward normal, $\boldsymbol{n}$ (Fig 3.6) produces

$$-\int_S (\boldsymbol{E} \times \boldsymbol{H}) \cdot \boldsymbol{n}\, dS = \int_V \left[\boldsymbol{E} \cdot \frac{\partial \boldsymbol{D}}{\partial t} + \boldsymbol{H} \cdot \frac{\partial \boldsymbol{B}}{\partial t}\right] dV + \int_V (\boldsymbol{E} \cdot \boldsymbol{J})\, dV, \tag{3.49}$$

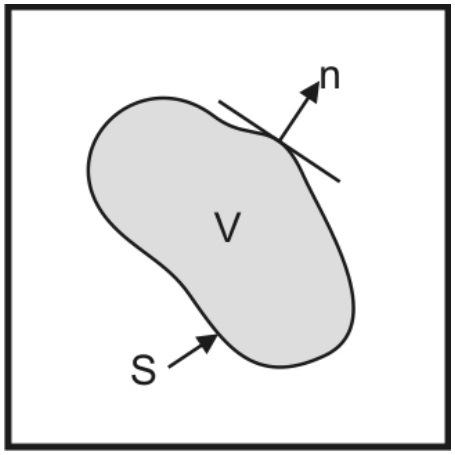

Figure 3.6 Schematic demonstrating the volume, V, surface, S and unit outward normal, n

which is known as Poynting's theorem of energy conservation and may be interpreted as the energy balance of the electromagnetic problem [Mack 2007]. The LHS represents the change of energy within the volume (the amount of energy flowing into the system), the first of the RHS integrals represents the energy contained in the electric and magnetic fields and the second RHS integral represents the work done by the field inside the volume, work either on charges or on atoms (absorption).

To establish a relation between this equation and the light intensity a definition for the intensity of light, I (alternatively known as irradiance) is taken as the magnitude of the time averaged Poynting vector [Mack 2007], where the Poynting vector,

$$\boldsymbol{S} = (\boldsymbol{E} \times \boldsymbol{H}), \tag{3.50}$$

is seen on the LHS of Eq 3.49. As described in Eq 3.49 this is a measure of the flow of energy density in the system. Regarding the absorbance of light by a medium the $\boldsymbol{E} \cdot \boldsymbol{J}$ integral term from Eq 3.49 may be considered as the intensity of light, as this is the portion of the energy which is absorbed by the system; and therefore the portion that has an effect on the material. In a solely absorbing material (such as a photoresist) the absorbance of the system may be related to σ from Eq A.9 and hence the expression for the absorbed intensity may be written as

$$I_{absorbed} = \boldsymbol{E} \cdot \boldsymbol{J} = \sigma |\boldsymbol{E}|^2. \tag{3.51}$$

The Poynting vector produces the same relation for the total intensity passing through the photoresist (as opposed to only the absorbed intensity), however a different, larger, constant is present as the total intensity is measured compared to only the absorbed intensity; the difference may be corrected later, for example though the consideration of the proportion of light absorbed. Considering a time-harmonic electric field, $\boldsymbol{E}(P,t)$ is represented by the phasor $\boldsymbol{U}(P)$ at time, *t* and point, *P*

$$\boldsymbol{E}(P,t) = \boldsymbol{A}(P)\cos\big(wt + \phi(P)\big) = Re\big[\boldsymbol{U}(P)e^{iwt}\big], \tag{3.52}$$

where

$$\boldsymbol{U}(P) = \boldsymbol{A}(P)e^{\mathrm{i}\phi(P)}. \tag{3.53}$$

A similar form may be written for the magnetic field $\boldsymbol{H}(P,t)$, represented by the phasor $\boldsymbol{V}(P)$.

In the phasor form it is possible to expand and simplify the Poynting vector and the intensity may be expressed as [Mack 2007]

$$I = \frac{1}{2}|Re(\boldsymbol{U} \times \boldsymbol{V}^*)|. \tag{3.54}$$

where **V*** implies the complex conjugate of **V**. For the case of an isotropic medium the components of plane wave may be related by ϵ and μ; for the case of such a plane wave travelling in the z direction this may be written as

$$E_y = -\sqrt{\frac{\mu}{\varepsilon}}H_x \; and \; E_x = \sqrt{\frac{\mu}{\varepsilon}}H_y, \tag{3.55}$$

and substituting these into Eq 3.54 gives

$$\begin{aligned} I &= \frac{1}{2}Re\big(U_x V_y^* + U_y V_x^*\big) \\ &= \frac{1}{2}Re\left[\sqrt{\frac{\varepsilon}{\mu}}\big(U_x U_x^* + U_y U_y^*\big)\right] = \frac{1}{2}Re\left(\sqrt{\frac{\varepsilon}{\mu}}\right)|\boldsymbol{U}|^2, \end{aligned} \tag{3.56}$$

which may be rewritten, using Eqs 3.52 and 3.53,

$$I = \frac{1}{2}Re\left(\sqrt{\frac{\varepsilon}{\mu}}\right)|\boldsymbol{E}|^2, \tag{3.57}$$

which, as earlier claimed, has the same form to Eq 3.51. In many imaging cases only the relative intensity is of concern and thus the constant multiplier may be ignored (because

the incident intensity can be tuned in the manufacturing process without changing the system performance). In the case of the photochromic system discussed here the absolute intensity is important as the system is affected by the incident intensity and also the competition between the two wavelengths to form an aperture and tuning the intensity of either wavelength will affect the aperture formation and the exposure.

3.7 VECTOR AND SCALAR MODELING

In this chapter first scalar then vector methods for modeling photochromic materials have been discussed however this thesis will use vector methods to explore the abilities of AMOL. This is because only a vector interpretation of Maxwell's equations can properly account for the propagation of light in the near field, or when features approach the wavelength as they will in AMOL. For instance, consider a normally incident plane wave approaching a 10nm aperture in a metal grating, the light propagating through the aperture would be strongly attenuated due to the narrowness of the aperture and the effects of the metal side walls, after passing through the grating a diffraction would be expected of the high spatial frequency components. Whilst a suitable vector model based on Maxwell's equations coupled with sufficient computing power is able to model these effects completely, the scalar methods discussed here would not.

The scalar methods discussed here have no ability to take into account the fields in the system, or any boundary conditions and each essentially creates a two dimensional result by combining a series of unconnected one dimensional cross sections. Whilst the results from these methods are still very useful, and often much easier to obtain their accuracy is questionable when considering the sub-wavelength features discussed here. Even if full scalar diffraction theory [Born 1999] is used, which accounts for much of the diffraction taking place, it remains impossible, due to assumptions made in the formulation of the theory, to fully model polarisation and high frequency effects [Ciocci 2009, Born 1999, Yuan 1993, Smith 1993]. Although the scalar methods detailed here offer easy analyses of the basic AMOL process in order to properly characterise the operation

of the system for small apertures it is necessary to implement some form of vector model.

3.8 CONCLUSIONS

This chapter began by explaining the development of scalar mathematical modeling of photoresists before extending this to include work by Menon and Warner on photochromic systems. The results shown in the published work demonstrates the potential of the AMOL system as a lithography technique. This introduction highlighted the abilities of these methods to provide useful results in some cases; however incompleteness in these methods was also briefly examined as were the limitations of relying on the scalar treatments provided. To overcome these problems a vector model was proposed and Maxwell's Equations were introduced, along with an explanation of the connections between the scalar models and Maxwell's Equations. The next chapter will extend this discussion by examining how Maxwell's Equations may be solved through numerical methods.

Chapter 4

MODELING METHODS

4.1 MOTIVATION

In the preceding chapter analytical solutions for AMOL type problems and the short-comings of scalar methods in comparison to vector methods were discussed. In this chapter vector modeling methods are introduced that will allow the solving of Maxwell's equations and thus the characterisation of the propagation of light through the AMOL system. A review of possible modeling techniques is given, before reasoning for the choice of FEM. This is followed by an introduction to how the FEM method operates and how Maxwell's equations can be represented in a suitable form, a simple example with an analytical solution is used to validate the technique. Finally the methods used to implement the AMOL system using the FEM are detailed, in particular the use of MATLAB/COMSOL and how two wavelengths and the photochromic layer were implemented.

4.2 MODELING TECHNIQUES

It is possible to analyze an AMOL type system of using vector based electromagnetic wave propagation with a number of modeling techniques; each of these techniques having positive and negative aspects and the choice of method is largely dependent on the particular problem being analysed and availability. Here four methods are briefly considered: finite difference time domain (FDTD) analysis, rigorous coupled wave analysis (RCWA), the PROLITH simulator and the finite element method (FEM).

4.2.1 FINITE DIFFERENCE TIME DOMAIN (FDTD)

FDTD was the first technique developed which worked by discretising differential equations through creating a grid in the geometric plane. It was first popularized in electromagnetics by a seminal paper by Yee [Yee 1966] and has since been continuously developed to adapt to a range of later developments. FDTD has several advantages as a numerical method [Taflove 2000]; it avoids the creation of a memory-intensive linear algebra equation, handles time changing materials easily and provides a systematic approach to problems. The Yee algorithm discretises the problem by looking at a unit cube in which each E field is surrounded by four H fields and vice versa, the propagation of time is then recorded in a two step process in each time step, first the E-fields are calculated based on the H-fields, then the H-fields are updated based on the just calculated E fields, thus providing a simple technique to model Maxwell's equations. It can be more difficult to effectively model dispersive materials in FDTD as it is not a frequency-based numerical method and the flexibility in choosing the mesh design is limited. However FDTD is a simple method to work with and has been widely and successfully used in electromagnetics and lithography modeling.

4.2.2 RIGOROUS COUPLED WAVE ANALYSIS

Rigorous couple wave analysis (RCWA) has been used to analyse the interaction of light with various grating systems [Gaylord 1985, Moharam 1981] and multilayer structures [Lee 2004]. The method discretises the grating into a series of domains and then solves the wave equation from Maxwell's laws in each domain, finally matching the fields at the boundaries to complete the analysis. This allows for diffraction effects and modulated conduction/absorption structures to be investigated through the summation of any diffractive orders created in the system. Although RCWA has been shown to be a valuable technique for explaining diffraction by gratings the nature of a two wavelength system with variable absorbance modulation such as AMOL would introduce additional complexity due to the changing absorbance with time and the absorbance grating height, as would introducing a multilayer stack.

4.2.3 POSITIVE RESIST OPTICAL LITHOGRAPHY (PROLITH)

The positive resist optical lithography (PROLITH) simulator [KLATencor 2010] is a commercially available simulation for lithography, able to implement models of optical projection, contact and proximity lithographies as well as new features such as double patterning and some new lithography techniques such as EUV. The ability to model the complete process from exposure to feature formation (based on the Dill Equations (Eq 3.11) but fully developed to the latest developments, RCWA and FDTD techniques) has created a very strong tool for lithographic simulations, including stochastic effects. However the use of the two wavelength illumination and the introduction of an AML create new and novel problems that may not be able to be implemented easily in the commercial software package; modeling software designed for broader problems would allow more flexibility in the design of a model as well as enable greater understanding of the propagation of light in the layers, in particular regarding the evanescent fields. Also when new ideas are incorporated there is no guarantee that these will be suitable for the PROLITH system.

4.2.4 FINITE ELEMENT METHOD (FEM)

FEM turns a system of differential equations into a set of algebraic equations through the recasting of the equation problem as an error minimisation followed by the division of the domain into a set of small elements with constant parameters. This allows the calculation of the solution, at a single frequency per simulation, and is suited to complex and/or changing domains as well as variation within domains. FEM is computationally intensive with regards to the required memory because the created algebraic elements must all be stored in a large matrix; it is also a mathematically complicated method and thus is not as easily developed as FDTD and is more difficult to run time-dependent simulations in FEM. However FEM has been well developed in recent years as is able to cope with a large array of problems and situations. FEM is particularly good when considering frequency specific materials and complex geometries and material inhomogeneities [Davidson 2010] and has been successfully applied to many electromagnetic problems.

4.2.5 CHOICE OF METHOD

In this work FEM was chosen as the simulation tool to be used to develop a full vector model of the AMOL process due to the strengths of FEM in handling dispersive media and inhomogeneities like those present in the AMOL layer. FEM has also been demonstrated to be very effective in previous mask simulations [Burger 2005]. It was decided to be appropriate to initially consider only the steady state solution, assuming this could be achieved within a reasonable time period. It was felt that FEM could suitably handle the dual wavelength nature of the simulation through multiple, concurrent simulations and that the flexibility in material and geometry parameters would allow new ideas to be easily tested. In particular it was decided that a commercial FEM software, COMSOL multiphysics [COMSOL] be used as this offered the advantage of a confirmed and tested FEM package to work from as well as being able to interface to a MATLAB [Mathworks] environment to allow more complex simulations to be run and for automated testing routines.

4.3 FINITE ELEMENT METHOD MODELING

FEM [Pepper 2006, Jin 2002, Henwood 1996] was pioneered in structural problems in Civil Engineering, particularly solid mechanics but has since been developed to be a strong tool in solving a broad range of differential equations (DEs) based problems. Although progress was initially limited by available computational power available and the large memory resources required growth in these technologies has allowed manageable access to problems in structural dynamics, thermodynamics and fluids as well as electromagnetics. FEM has become widely used in electromagnetic simulations [Webb 1995] and in various optical [Anderson 2009, Cummer 2006] and lithographic systems [Fikri 2003, Tejeda 1998] even given the computational power required for large domains. Here FEM is introduced, describing the background technique before creating an example problem in electromagnetics. Mention is also made of the errors involved and in the use of COMSOL Multiphysics, the commercial FEM software package used in this thesis, in tandem with Matlab.

4.3.1 INTRODUCTION TO THE FINITE ELEMENT METHOD

The FEM involves the rewriting of the differential equations and associated boundary conditions in the form of a power function, or variational form (VF). It may then be shown that minimising the VF through the appropriate choice for the dependent variables is equivalent to solving the original equations. This process is simplified by dividing the domain of interest into small areas (finite elements) and assuming constant parameters for each of these elements. The introduction of the finite elements allows the functional equation to be rewritten in matrix form;

$$Ku = f \tag{4.1}$$

where K and f are known and u the solution vector. This set of linear equations may be solved algebraically, through Gaussian elimination or by an alternative, more computationally efficient method. The mathematical background of the method, including the appropriate boundary conditions is included in Appendix B.

4.3.2 LIGHT PROPAGATION IN FEM

Here the required techniques for the solution of wave propagation problems using FEM analysis are outlined. This begins by considering Maxwell's equations and converting these into variational form, then looking at the required boundary conditions before introducing COMSOL's techniques. Restating Maxwell's equations (Eqs 3.42-3.45) in phasor form,

$$\nabla \times \boldsymbol{H} = \boldsymbol{J} + j\omega \boldsymbol{D} = \sigma \boldsymbol{E} + j\omega\varepsilon \boldsymbol{E} \tag{4.2}$$

$$\nabla \times \boldsymbol{E} = -j\omega\mu \boldsymbol{H}, \tag{4.3}$$

with the fields in time-harmonic form

$$\boldsymbol{E}(x,y,z,t) = \mathrm{Re}\{\boldsymbol{E}(x,y,z)\mathrm{e}^{j\omega t}\} \text{ and} \tag{4.4}$$

$$\boldsymbol{H}(x,y,z,t) = \mathrm{Re}\{\boldsymbol{H}(x,y,z)e^{j\omega t}\}. \tag{4.5}$$

Where, for non-magnetic and isotropic media the auxiliary equations can be specified as

$$\boldsymbol{D} = \epsilon \boldsymbol{E}, \tag{4.6}$$

$$\boldsymbol{B} = \mu \boldsymbol{H}, \tag{4.7}$$

where ϵ, μ are known as the permittivity and permeability respectively [Born 1999] and given that $\boldsymbol{J}$ may be expressed as

$$\boldsymbol{J} = \sigma \boldsymbol{E}, \tag{4.8}$$

where σ is the electrical conductivity where only a conduction current density is present.

Taking the cross product of the two equations and cancelling one of the field vectors allows the formation of a Helmholtz-type equation of each field, producing for $\boldsymbol{E}$,

$$\nabla \times \frac{1}{\mu} \nabla \times \boldsymbol{E} - \omega^2 \tilde{\varepsilon}_c \boldsymbol{E} = 0, \tag{4.9}$$

where

$$\tilde{\varepsilon} = \varepsilon - j\frac{\sigma}{\omega} \text{ and} \tag{4.10}$$

$$\omega = \frac{k_0}{\sqrt{\epsilon_0 \mu_0}}. \tag{4.11}$$

Looking at a TE polarised wave the field equation may be simplified as only the $E_{\mathbf{z}}$ component is present,

$$\nabla \cdot \frac{1}{\mu_r} \nabla E_{\mathbf{z}} - {k_0}^2 \tilde{\varepsilon}_{rz} E_{\mathbf{z}} = 0, \tag{4.12}$$

where $\tilde{\varepsilon}_{rz}$ represents the relative permittivity in z. The TM case is similarly found and may be given by the substitution of

$$E_{\mathbf{z}} = -H_{\mathbf{z}} \; and \; \mu \leftrightarrows \varepsilon \, . \tag{4.13}$$

Expanding the gradient function in Eq 4.12,

$$\frac{\partial}{\partial x}\frac{1}{\mu_r}\frac{\partial E_{\mathbf{z}}}{\partial x} + \frac{\partial}{\partial y}\frac{1}{\mu_r}\frac{\partial E_{\mathbf{z}}}{\partial y} - {k_0}^2 \tilde{\varepsilon}_{rz} E_{\mathbf{z}} = 0. \tag{4.14}$$

which may be rewritten in variational form,

$$\iint_{\mathrm{R}} \left[\frac{1}{\mu_r}(-\nabla \times v)_y(-j\omega\mu H_{\mathbf{z}}) + \frac{1}{\mu_r}(\nabla \times v)_x\big((j\omega\mu H_{\mathbf{z}})\big) - \varepsilon_0 \mu_0 \omega^2 \tilde{\varepsilon}_{rz} E_{\mathbf{z}} v\right] \mathrm{dA}. \tag{4.15}$$

The coefficient form of the ODE as given by COMSOL is represented as

$$\nabla \cdot (-c\nabla \boldsymbol{u} - \alpha \boldsymbol{u} + \gamma) + a\boldsymbol{u} + \beta \cdot \nabla \boldsymbol{u} = f, \tag{4.16}$$

comparing this to Eq 4.12 leads to the selection of the parameters as

$$c = \frac{1}{\mu} \; and \; a = {k_0}^2 \tilde{\varepsilon}_{rz} \tag{4.17}$$

to form the desired equation in COMSOL. Alternatively the equation may be specified in variational form or an alternative weak-form, indeed this is the case for the COMSOL preset harmonic propagation mode which may be related back to Eq 4.15.

4.4 A SIMPLE EXAMPLE – DIELECTRIC BOUNDARY

Here the simple problem of a normally-incident plane wave on a dielectric boundary is used to validate the COMSOL FEM model and to analyze the error in the model through a comparison to the analytical solution. The analytical solution to the problem is outlined in Appendix C which derives the expected result for the reflected and transmitted amplitudes (C.12 and C.13 respectively)

4.4.1 ANALYTICAL SOLUTION

Selecting appropriate material parameters (as defined in Fig C.1) allows the calculation of the reflected and transmitted magnitudes, choosing for instance

$$n_\alpha = 1, n_\beta = 2 \;\; and \;\; A_\perp = 1 \tag{4.18}$$

results in

$$R_\perp = {}^{-1}/_{3} \; and \; T_\perp = {}^{2}/_{3}. \tag{4.19}$$

Substituting these results into the formula for E_z^I (Eq C.2 – Eq C.4) and updating the direction vector, which is now being parallel to the y axis, the resulting waves can be calculated in both regions,

$$\begin{aligned} E_z^\alpha = E_z^I + E_z^R &= e^{-ik_1 y} - \frac{1}{3} e^{ik_1 y} \\ &= e^{-ik_1 y}\left[1 - \frac{1}{3} e^{2ik_1 y}\right] \\ &= e^{-ik_1 y}\left[1 - \left[\frac{1}{3}\cos(2k_1 y) + i\frac{1}{3}\sin(2k_1 y)\right]\right] \end{aligned} \tag{4.20}$$

$$E_z^\beta = T_\perp e^{-ik_2 y} = \frac{2}{3} e^{-ik_2 y}. \tag{4.21}$$

The intensity is calculated as the square of the electric field strength (Eq 3.59) so that

$$I_z^1 = |E_z^\alpha|^2 \; and \; I_z^2 = \left|E_z^\beta\right|^2 = \frac{4}{9}, \tag{4.22}$$

which can be calculated and a line-section plot along the *y*-axis shows the result, Fig 4.1. As expected the result is a standing wave about the incident intensity ($A_\perp = 1$) in region α due to the reflected wave and constant magnitude in region β as there is only a transmitted wave present.

4.4.2 COMSOL SIMULATION

The COMSOL simulation is based on the in-plane hybrid-mode wave application mode with harmonic propagation which models the wave propagation techniques introduced in Section 4.3.2. The simulation of a dielectric boundary could be performed in 1-D due to symmetries however 2-D has been used so that better comparison may be made with 0.4, later simulations of gratings and more complicated features. The simulation, Fig 4.2, has

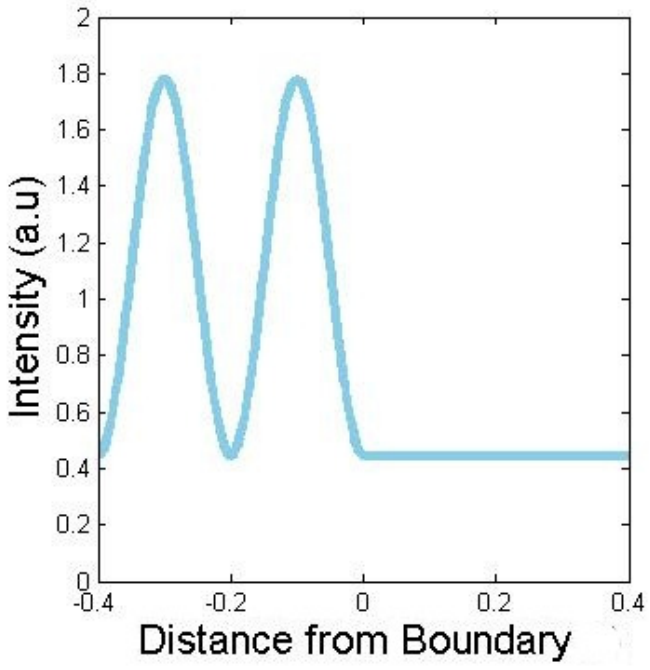

Figure 4.1 Cross section along y-axis of the analytical solution for the Electric Field Intensity of a dielectric boundary at $y = 0$, between regions of with refractive indexes $n_\alpha = 1$ and $n_\beta = 2$.

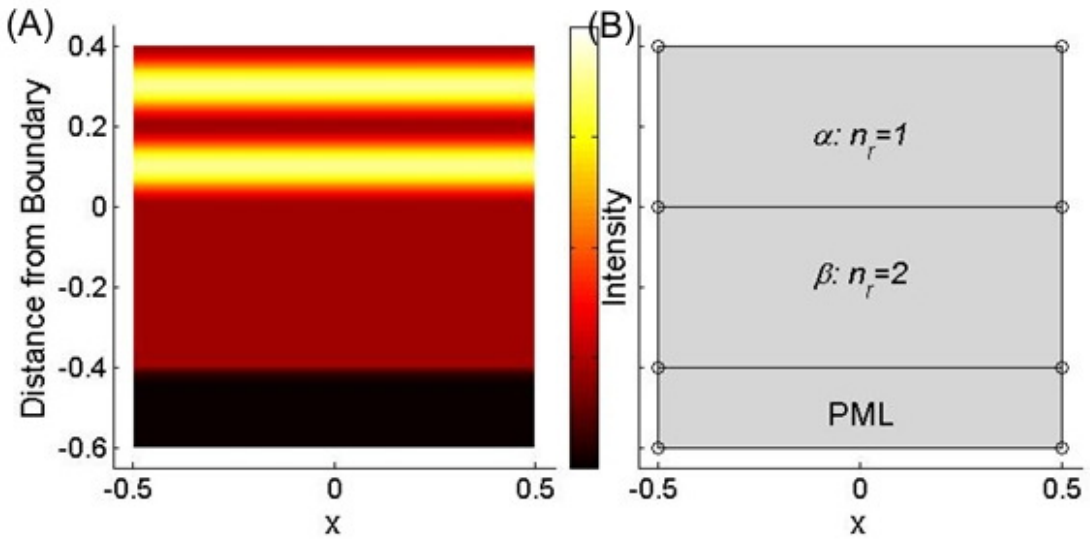

Figure 4.2 COMSOL simulation diagram showing (a) a sample intensity plot and (b) a description of the geometry used.

had the dimensions normalized so that the domain is a unit square and the wavelength is the domain has then been divided vertically into three sections; 0.4 with refractive index, $n_r = 1$, 0.4 with refractive index, $n_r = 2$ and 0.2 with refractive index, $n_r = 2$ as a perfectly matched layer (PML).

The external boundaries on the left and right have periodic boundary conditions, suggesting an infinite dielectric layer so as to avoid any boundary effects; the bottom boundary is specified as a scattering boundary, thus with the PML allowing the second medium to appear semi-infinite. The top boundary is also specified as a scattering boundary condition, but with a source field in z specified as either a unit electric field or a magnitude $1/Z_0$ magnetic field, where Z_0 is the impedance of free space ($Z_0 \approx 376.73$) so that the same initial electric field intensity is present for both polarisations. This boundary setting means any reflected wave will be ignored, allowing the first medium to also be semi-infinite. The PML used for the bottom layer is added as an additional (but non-real) layer and uses the default COMSOL settings. The removal of any reflections from the PML/model boundary demonstrated the effectiveness of the

matching and no difficulties were found in implementing the PML in this thesis, due to generous PML depths being used and evanescent decay of many of the fields.

4.4.3 COMSOL ACCURACY

The accuracy of a FEM simulation will depend on the size of the finite elements used in the simulations, in particular for electromagnetic wave simulations the number of finite elements per wavelength is important to consider, with around five elements per wavelength required for reasonable accuracy [Jin 2002]. Here the simple dielectric boundary system is examined to gain an understanding of the system accuracy. Fig 4.3 demonstrates graphically the improvement of the COMSOL simulation working from a coarse mesh (65 elements) where serious errors are seen to a finer mesh (968 elements) where the difference between the analytical and COMSOL solutions is only slightly visible at the plotted scale.

To be able to understand this improvement in accuracy the number of elements is related to a measure of size compared with wavelength (as changing the wavelength used will significantly affect the accuracy). By measuring the number of elements covering the area of a square with side length of a wavelength it is found that the 65 element mesh (Fig 4.4) has 10.4 elements/wavelength^2, as opposed to 591 elements/wavelength^2 for the 3694 element mesh (this may be calculated by multiplying the number of elements by 0.4^2) such as is shown in Fig 4.4. In this case the two-norm;

$$norm(error) = \sqrt{\sum_{k=1}^{n} |error_k|^2}, \tag{4.23}$$

is used to measure the error between the two solutions as it is proportional to the total error along a line measurement, in this case line traces measured at steps of 0.001 along vertical lines parallel to the y-axis. Measuring eleven lines evenly spaced along the x-axis and taking the largest value, normally occurring at the edges of the simulated domain (the error here is increased due to the nature of the periodic boundary conditions) returns a useful result to work with.

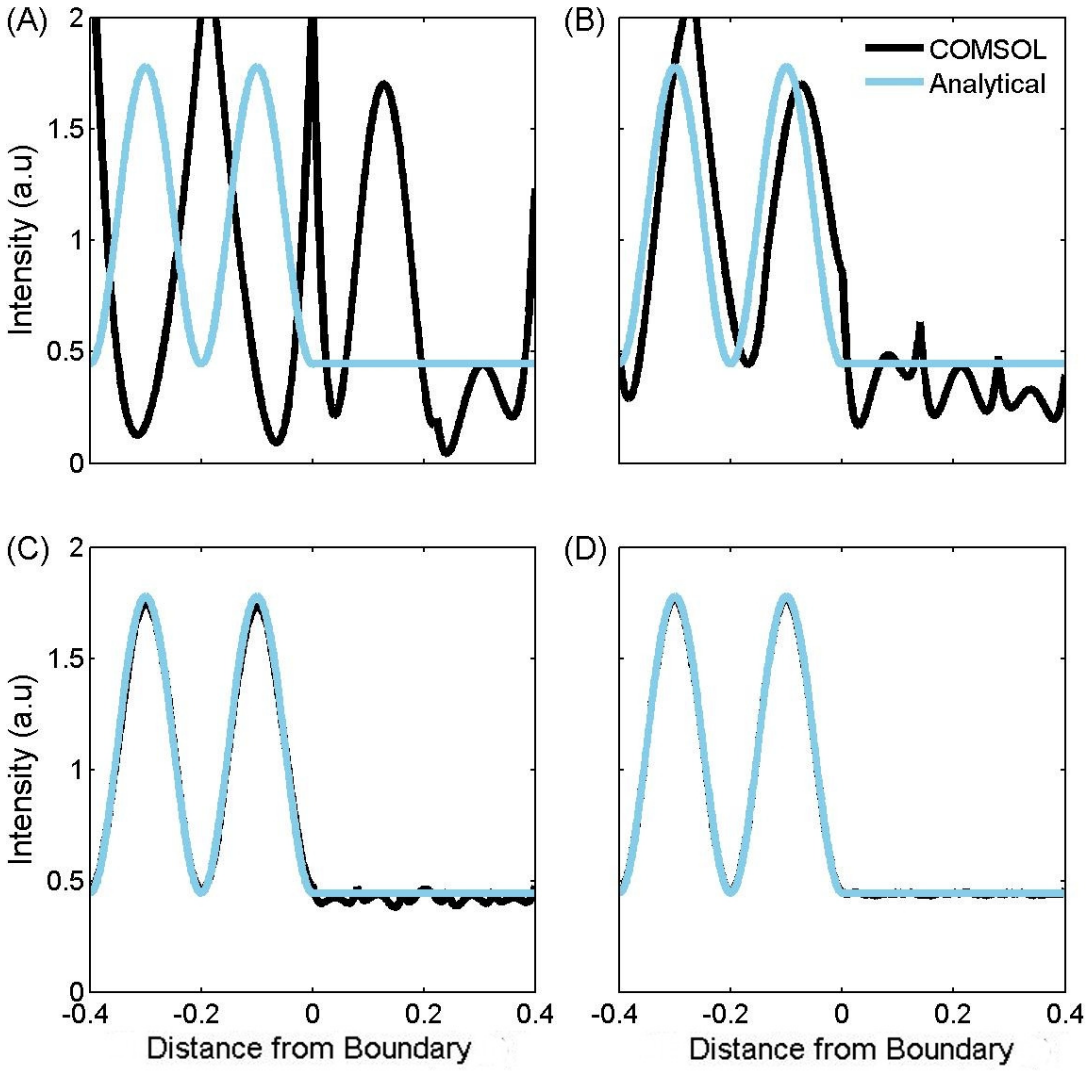

Figure 4.3 Comparison of analytical solution (light blue) and COMSOL solution (black) to the dielectric boundary problem with (a) 65 elements, (b) 159 elements, (c) 470 elements and (d) 968 elements

As expected, the error reduces with increases in the number of elements with a logarithmic relationship scale as shown in Fig 4.5 where the error is seen to reduce by five orders of magnitude as the number of elements per wavelength increases from ten to approximately 5000. An additional understanding of the size of this error may be gained by comparing it to a relative error. Consider an error magnitude of 0.1% of the incident value (0.001) in the simulation results (calculated as above this is an error of $10^{-1.55}$), an

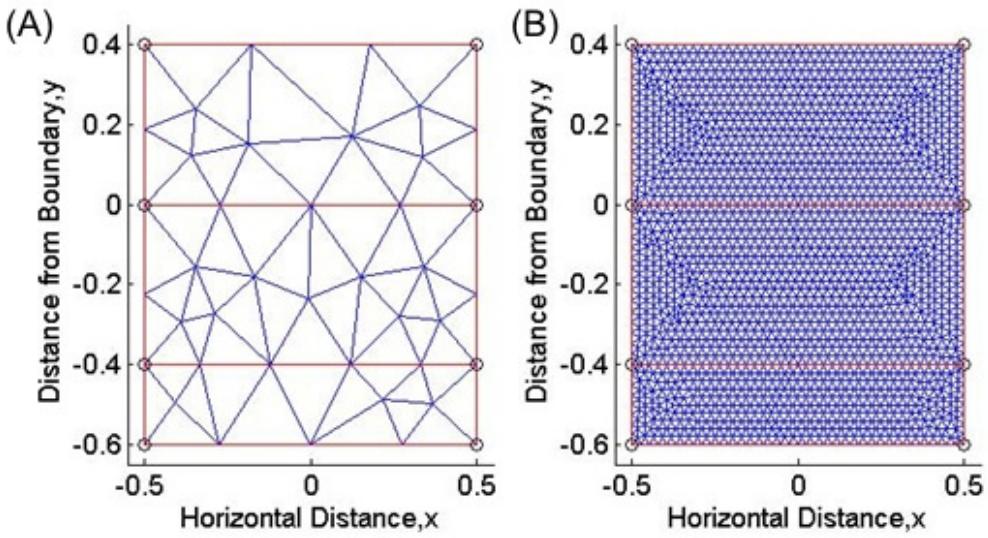

Figure 4.4 (a) Coarse (65 elements) and (b) fine (3694 elements) COMSOL meshes for the domain of the simple dielectric boundary problem.

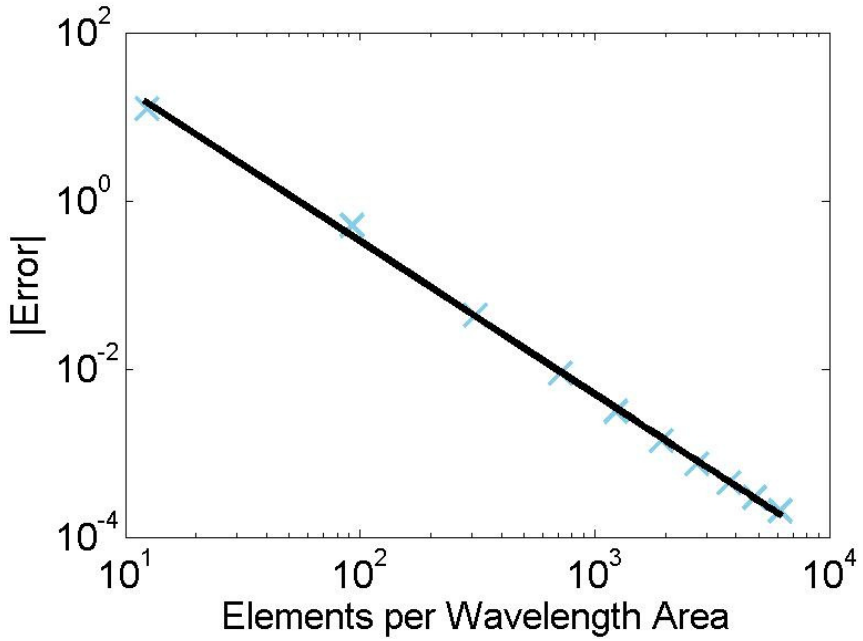

Figure 4.5 Log axis plot of the Norm of the error between the analytical and COMSOL solutions plotted against the number of elements per wavelength area, a best fit line is also plotted.

The results of this comparison between the analytical and COMSOL solution to a simple electromagnetic wave harmonic propagation problem have allowed validation of the performance of a COMSOL FEM model in solving this and related problems. It has also allowed an examination of the relationship between the error and mesh size in the FEM simulation which will be valuable in judging the performance of later simulations and the mesh sizes required for the AMOL simulations.

4.5 CONCLUSIONS

In this chapter the method of solving the vector methods discussed in the previous chapter was outlined, beginning with a brief discussion of the various techniques available before expanding on the choice of FEM and an explanation of the operation of FEM. This was followed by the linking of the FEM to the particular problem of solving Maxwell's equations which relate directly to problems concerning the propagation of light in media. Finally the case of a layered dielectric medium was used to investigate the performance of a COMSOL FEM model in comparison to a known analytical solution. This found that 0.1% and 0.01% accuracies could be achieved with greater than 310 and greater than 1100 elements per unit wavelength area. This example validates the initial modeling and gives an approximation to the accuracy of the solution achieved in later simulations. This chapter has successfully introduced the techniques required for solving vector based light propagation systems, now this approach needs to be introduced to the AMOL system which has the additional complications of an AML with absorbance dependant on the incident ratios and two incident wavelengths of light.

Chapter 5

FEM MODELING OF AMOL

5.1 INTRODUCTION

In this chapter the development of the previous two chapters is combined; recognizing the limitations of the scalar approach to the characterisation of the AMOL system a full-wave FEM model is built, using COMSOL, to model such a system. Here the model used is introduced, with particular focus on the complications involved in allowing for the competition in the AMOL layer between two wavelengths of light in a FEM system and how these are managed through interfacing with MATLAB. This system is then used to replicate the predictions of the analytical solutions proposed by Menon [Menon 2007] and Warner [Warner 2009], in particular showing that for incidence of plane waves there is very good agreement, however, when apertures are formed there are complications that are not accounted for in a scalar model.

5.2 AMOL MODEL IN MATLAB

The principles of the FEM and the dynamics of photochromic materials have been described mathematically earlier. Here COMSOL is used to perform the FEM analysis and the photochromic reaction kinetics of the AMOL layer are inserted into the COMSOL model. Because it allows both this substitution to be performed easily and the ability to run multiple simulations with different parameters the COMSOL/MATLAB interface has been used. In general an initial simulation has been created using the COMSOL interface, to make use of the automatic settings and usability, with this model then being exported and saved in a MATLAB structure for later use. Here the generic model is described, with particular focus on the choice of settings and how various

parameters are controlled. Then the operation of the model is described, with care taken to explain how the kinetics of the photochromic layer are modeled, a flow chart of the operation of the model is given in Fig 5.1 and selected code of the important features may be found in Appendix D.

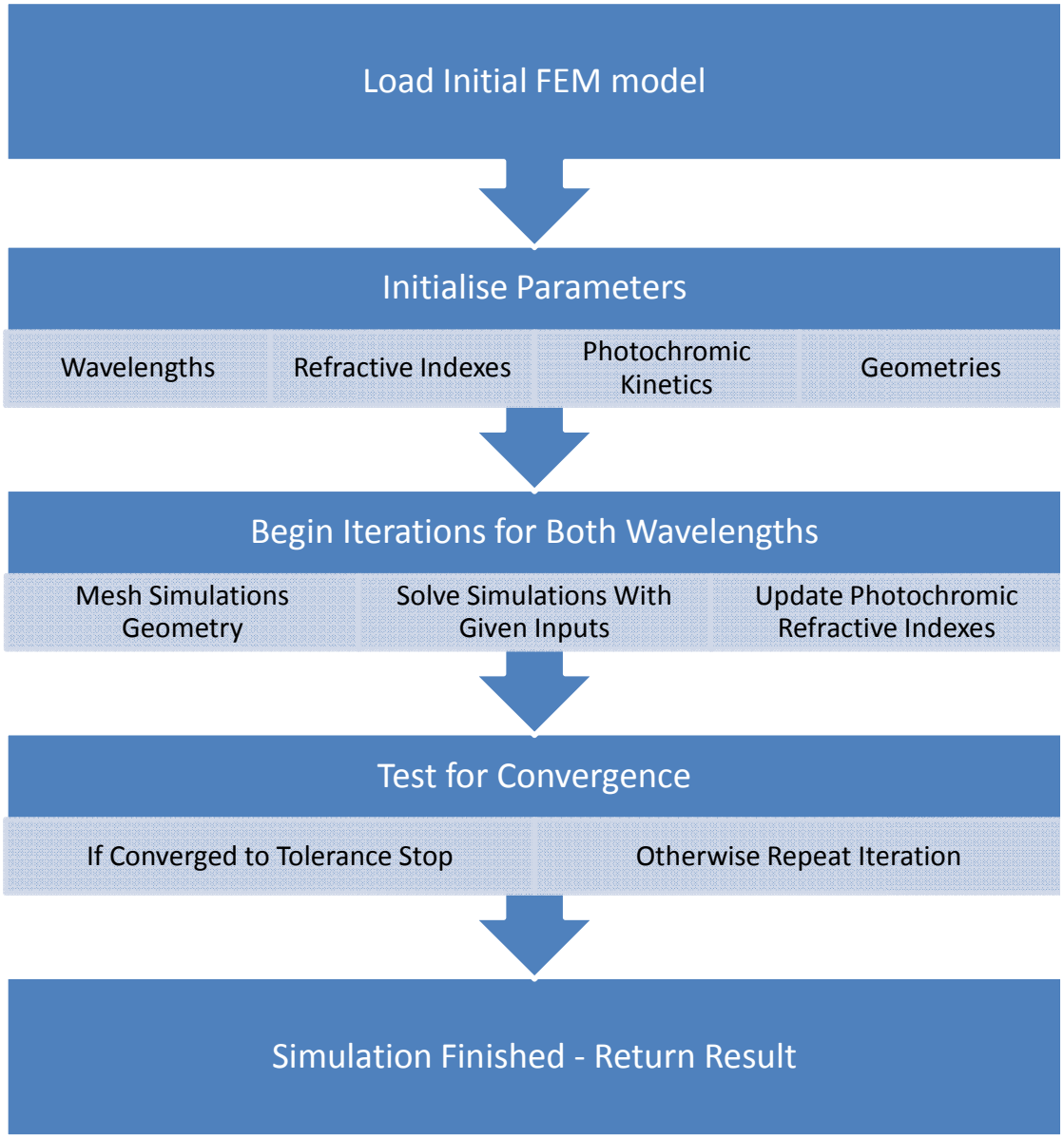

Figure 5.1 Chart showing operation of code to perform the simulation of a photochromic layer in a FEM system.

5.2.1 SETTING UP THE COMSOL MODEL

The initial simulation structure is developed in the COMSOL graphic user interface; this enables the background equation systems, geometries and program features to be created semi-automatically. Although a similar system could have been created through the MATLAB interface the additional support of the COMSOL interface ensures a sound basis for the simulation and enables quick experiments and adaptations to be made. This is partially reliant on COMSOL's accuracy, however COMSOL benefits from frequent updates and wide use and validation has been performed on the models used. For simplicity the same geometry and has been used for both wavelengths considered, similar boundary conditions have been used except when variation is required due to different incident waveforms.

GEOMETRY

The generic model geometry built in this thesis (Fig 5.2) has a rectangular domain which varies in height and width but is generally in the region of hundreds of nanometers; although a dimensionless form could have been used this is the scale where lithography operates and material parameters vary widely with dimensions and hence it was not thought useful. The geometry is viewed as a vertical cross section of a resist stack on a wafer, with light incident from the top of the geometry and a substrate being the final layer. Depending on the simulation the rectangular domain is divided into two or more different regions, representing different materials, where the base layer is always a PML to model a thick, absorbing, substrate.

BOUNDARY SETTINGS

The boundaries of the simulation are defined as periodic on the left and right sides, envisioning an infinite layer in the $x - z$ plane, which represents a reasonable assumption as many current chip features, such as gratings, extend over large dimensions and this method reduces the domain size greatly; however edge effects will alter results for finite gratings. Depending on the incident waveforms the periodic conditions may

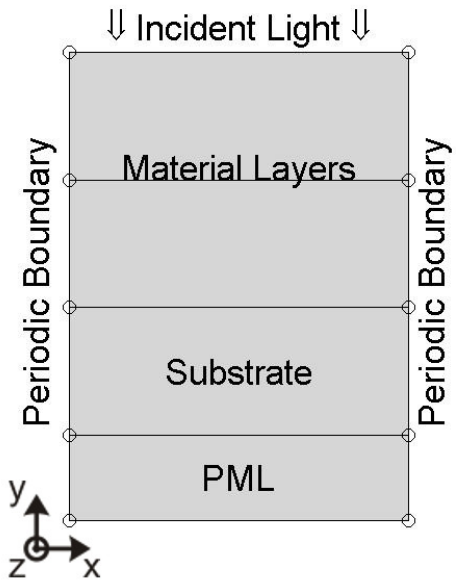

Figure 5.2 Schematic diagram showing the geometry and boundary conditions of the generic simulation. The substrate and PML were present in all simulations, however a variety of material layers were used, including an AML and photoresist and possibly a plasmonic layer or air spacer layer.

change between periodicity and anti-periodicity in order to allow a correct match (e.g. a plane wave would have periodic conditions, whereas a one period of a sinusoidal intensity waveform would have anti-periodicity – consider the underlying sinusoid). In this work only normal incidence is considered, if oblique incidence was of interest then Floquet periodicity would likely be used, with the phase change between boundaries dependent on the refractive index of the layer.

As explained in the geometry section a PML is used to model the substrate, and a scattering boundary condition with no incident wave is used at the external boundary of this to further reduce any reflections. Similar to the model of the dielectric stack the incident field is specified as either a TE or TM or combined incident field specified on a scattering boundary condition. The scattering boundary condition models the incidence of a coherent plane wave, from say a laser source, as an intensity level is set and then a standing wave from the reflection is able to form without affecting the intensity level. In this formulation of the model there is complete control over the incident angle and

power for both wavelengths. Example code for setting this incident wave is included in Appendix D. The incident light can be specified as a sum of plane waves at the top surface with free choice of amplitude and direction. This allows the incident wave to be easily specified as that from a Lloyd's mirror arrangement involving two waves interfering from opposite angles.

5.2.2 EXPORTING TO MATLAB

After the AMOL geometry and system has been set out in COMSOL it is then exported into MATLAB to allow greater control over the simulation and for automating operation. The FEM is represented in MATLAB as a structure which lists the relevant equations, geometries, variables and parameters; in MATLAB the FEM structures for both wavelengths are combined in a cell matrix and then this file is saved to allow it to be easily loaded in the future. When the file is loaded later care must be taken that all required variables are set to appropriate values for the simulation, otherwise they remain at the initial levels.

5.2.3 PHOTOCHROMIC LAYER IN MATLAB

The kinetics of the photochromic reaction require knowing the intensity of both wavelengths involved in the simulation at each point in the photochromic layer, furthermore the absorbance pattern of this layer will change with the change of intensity caused by the change in absorbance. To handle this situation an assumption is made that a stable photochromic state formed in a small time period; the simulation may then be repeated multiple times updating the absorbance in the AMOL layer based upon the incident intensities until the change between resulting photochromic states is less than a given tolerance.

The two simulation models described above are used to enable this process in MATLAB, for the first iteration of the simulations an opaque absorbance matrix is assumed for both wavelengths. The absorbance is set by creating an array of the refrac-

tive index in the photochromic layer for each simulation (this array is manually set to opaque for the first iteration), which is set as a global variable so that it may be referenced throughout the simulation. The absorbance values of the photochromic layer are then set as a function of the co-ordinates in the xy plane, with an additional specifier to differentiate in the case of different absorbances for each wavelength. This function interpolates from the refractive index array to allow an approximation of the absorbance to be made for any point in the photochromic layer.

The calculation of the refractive index at each point in the photochromic layer requires knowledge of the light intensities, thus after the first iteration these must be calculated. This is achieved through the construction of the refractive index array as a rectangular grid with regular spacing (taken at 1 nm generally-this is limited by an increase in time required to interpolate a larger array and the limit in accuracy is the mesh of the simulation), the co-ordinates of this grid may then be used to interpolate the light intensity (normE_rfweh^2) for both wavelengths in the photochromic layer. Once the light intensity of both wavelengths has been calculated it must be converted into a corresponding refractive index, as described in Chapter 3. This calculation is held in a separate function to allow simple modification of the parameters used and any assumption, such as a constant refractive index.

5.2.4 CHANGING PARAMETERS IN MATLAB

Throughout the exploration of the AMOL system various parameters of the system must be altered so that appropriate simulations may be performed. Primarily adjustments are made to the geometry being used, the incident waveforms, or the material parameters of the simulation. The location of the setting in the FEM structure depends on the parameter being changed; the geometry has a separate part of the FEM structure to itself, the primary parameters are located in a variables structure and the material parameters and definitions are defined inside the FEM equation variables.

First considering the geometry; the COMSOL scripts must be used to generate a geometry structure that is consistent with the COMSOL requirements; in this work this consists of a set of rectangular regions, where each of these regions then requires an appropriate set of equations. The straightforward way of ensuring that the model remains consistent is to maintain a number of regions the same as the initial simulation, reducing the complexity in making the changes. With this practice the geometry width and height dimensions can be changed by creating a new geometry and substituting it. The variables structures inside the FEM structure contain large variable lists; when a variable is changed the specific COMSOL variable name must be used and then code allows the variable list to be searched and updated appropriately (it should be noted that many variables are specified as tensors and hence may require multiple updates in the structure).

5.2.5 SOLVING AMOL IN MATLAB

The solution of a complete AMOL system model may now be found using the COMSOL FEM model with the created MATLAB functions and environment. Assuming an initial geometry has already been created a generic simulation would begin by reloading this basic structure for both wavelengths and setting initial properties such as the wavelength values, refractive indexes of all layers (including an initial setting for the refractive index of the photochromic layer), model dimensions and incident waveforms and photochromic reaction kinetics; the simulation parameters such as the tolerance and maximum iterations must also be set. Once all the parameters are set the iterations may begin, repeatedly meshing and solving the model for both wavelengths until the refractive index in the photochromic layer changes by less than the pre-defined tolerance level and hence the solution is returned. Figure 5.3 demonstrates the formation of an aperture for a representative case, with a funnel shape forming within a few apertures before slowly widening as increased λ_1 propagates through it. The rapid decrease in difference between consecutive iterations is shown in the log plot in Fig 5.3d.

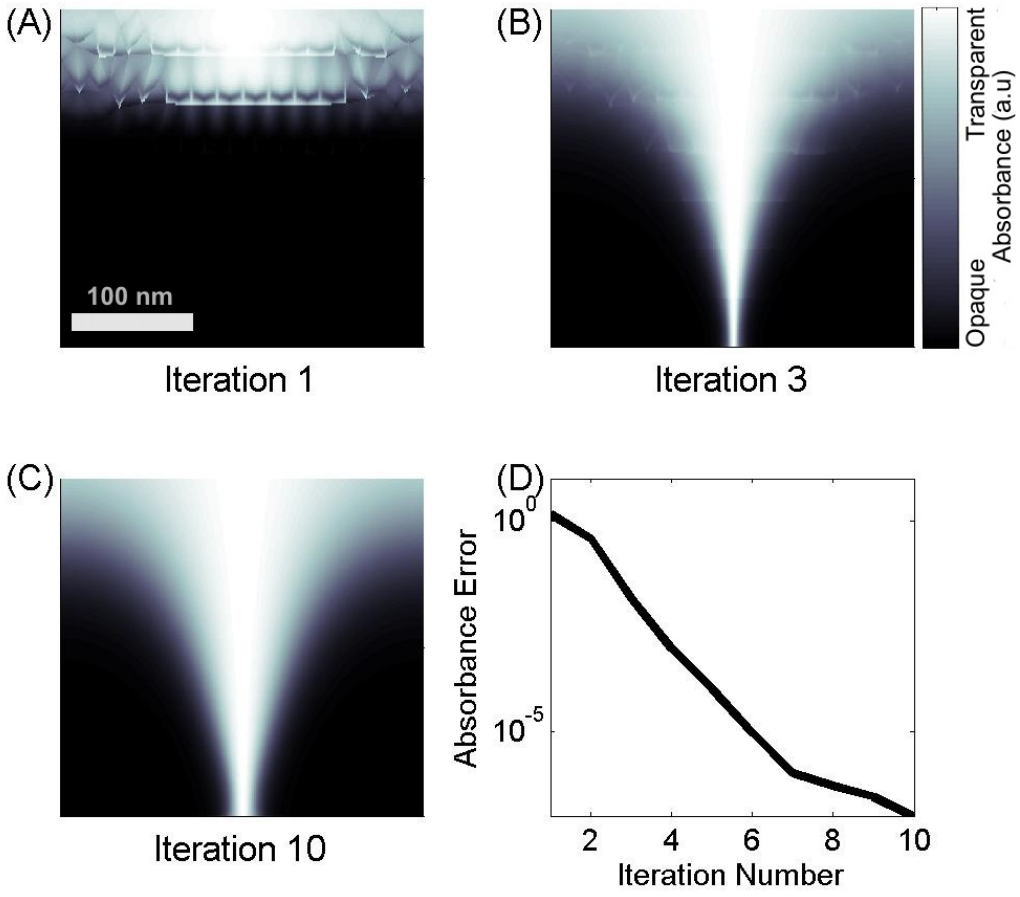

Figure 5.3 Absorbance pattern in the AML at iteration number (a) 1, (b) 3 and (c) 10, with the measured change in absorbance plotted in (d).

5.3 PLANE WAVE INCIDENCE IN AMOL

Warner and Blaikie [Warner 2009] introduced an analytical model for an AMOL type system which was described in Chapter 3 (Section 3.4.3); here the results of this analytical system are matched to the results produced to the presented FEM AMOL model for normally incident plane waves (i.e. no grating) where the scalar approach is valid. Taking the closed form of the intensity fraction at equilibrium (Eq 3.34) a figure may be drawn showing the decay of light intensity ($\mathcal{I}_1, \mathcal{I}_2$) with normalized depth (u), reproduced in Fig 5.4. The figure shows the weaker beam asymptote to zero whereas the

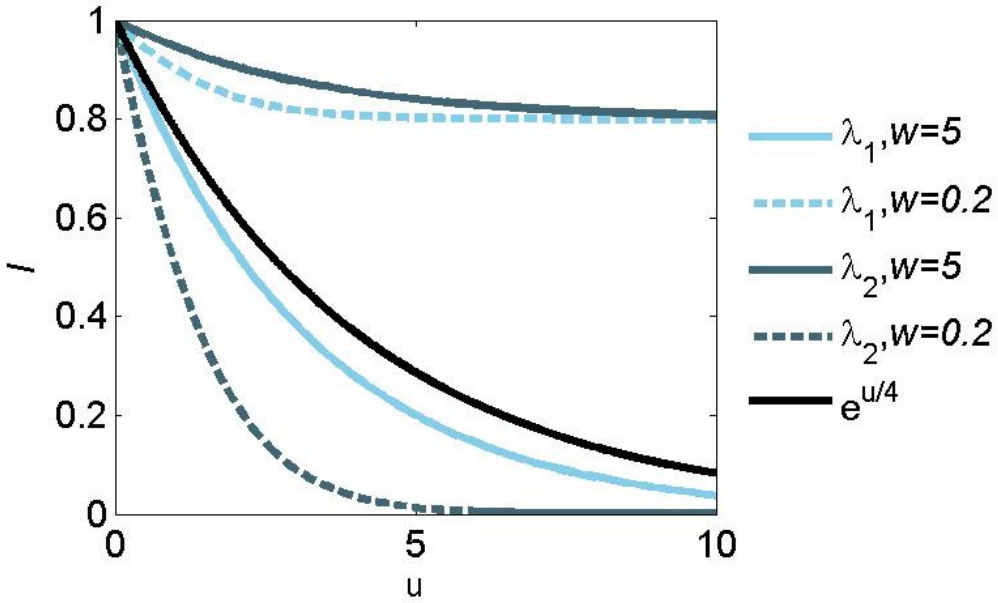

Figure 5.4 Reproduction from Warner showing the decay of reduced light intensity for colours 1 and 2 against reduced depth u into a dye layer with $d_1 = 3$, $d_2 = 1$ and effective intensity ratios (w) 0.2 and 0.5 [Warner 2009]

stronger beam asymptotes to $1 - \frac{1}{w}$ if w > 1 or $1 - w$ if w < 1, where the decay constant is dominated by the weaker beam. Thus, considering a standing wave pattern of one beam and a plane wave incidence of a second beam the beam at the nulls of the standing wave may have almost no decay whereas the beam at the peaks will have a strong decay, thus allowing the formation of an aperture.

The FEM model of the system can replicate this graph by adjusting it so that only the AMOL layer and PML layer are present, hence modeling an infinite depth of photochromic layer. Here the PML permittivity will also be related to the relative intensities, although this is a change from the normal use it seems to allow minimal reflections. The input waves are set as plane waves with a unit electric field vector perpendicular to the plane of incidence. The system parameters are adjusted such both incident wavelengths are plane waves at 400 nm (because the Beer lengths are set independently and no reflections or diffraction effects are present the wavelength selected does not alter the results of the simulation) and the dynamics of the model reflect that of Warner's analyti-

cal form where state A is the initial state and opaque and each wavelength only causes isomerisation of one state, where the transparency is set by the ratio w. The geometry and boundary settings of the model are shown in Fig 5.5.

The COMSOL simulation used a Beer's length of 40 nm for λ_2 with the Beer's length of λ_1 being a third of this. Assuming a real refractive index (n) of 1.6, this corresponded to an imaginary refractive index (κ), of between 0 and 0.27 for λ_1 and between 0 and 0.80 for λ_2. Figure 5.6 shows the results of the COMSOL simulation matched against appropriately scaled plots using the analytical solution which demonstrates very good agreement between the solutions for this resolution. There is some difference between the results seen with greater magnification, likely due to some reflections in the COMSOL model. This helps to further validate the COMSOL model as well as giving confidence in the modeling of the AMOL layer. However in the development of AMOL and for this thesis the more interesting feature is the ability to control the formation of apertures in the AMOL layer, thus using it as an adaptive mask.

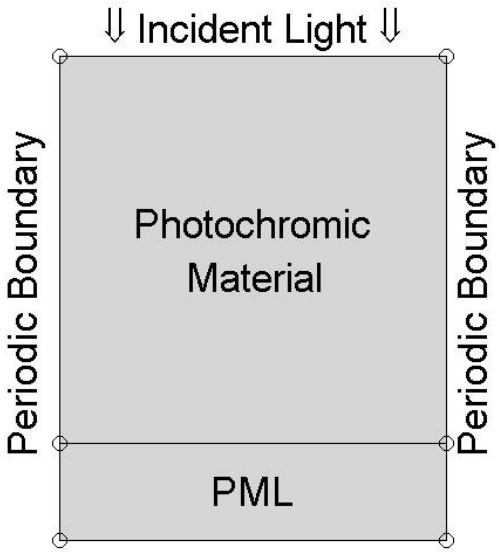

Figure 5.5 Schematic diagram showing the geometry and boundary conditions of the simulation of an infinite photochromic material. The absence of any substrate layer means no reflections are modeled.

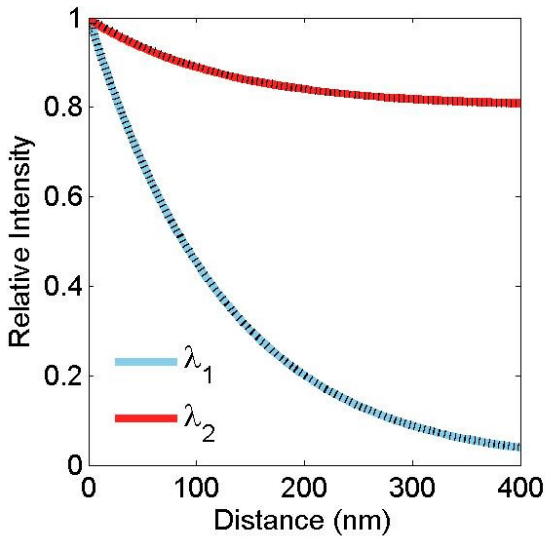

Figure 5.6 Comparison of analytical results (coloured solid lines) and COMSOL/MATLAB simulation (black dashed lines) over 400 nm for two plane wave incidence on an infinite AMOL material with no discernable difference seen at this magnification. The Beer length has been defined as 40 nm for $\boldsymbol{\lambda_2}$, with the Beer length of $\boldsymbol{\lambda_1}$ a third of this.

5.4 PHOTOCHROMIC APERTURE FORMATION

Warner also investigated the case of aperture formation [Warner 2009]; the same model has been used to replicate his work in COMSOL, and Fig 5.7 shows the incident waveforms, the relative incident intensities and the intensity reduction of λ_2 at a distance of eight Beer lengths into an AMOL layer. Careful note is made that the relative incident intensity plot is only partially visible and that the intensity reduction of λ_2 is shown, not the intensity waveform of λ_2. Here a different aperture formation method is used, in which one incident waveform is a standing wave (Intensity $\propto \sin^2 x$) and the other a plane wave (Fig 5.8). This system has a similar ability to create a narrow aperture but is experimentally easier to set-up as the peaks and troughs of the two waves do not need to be aligned.

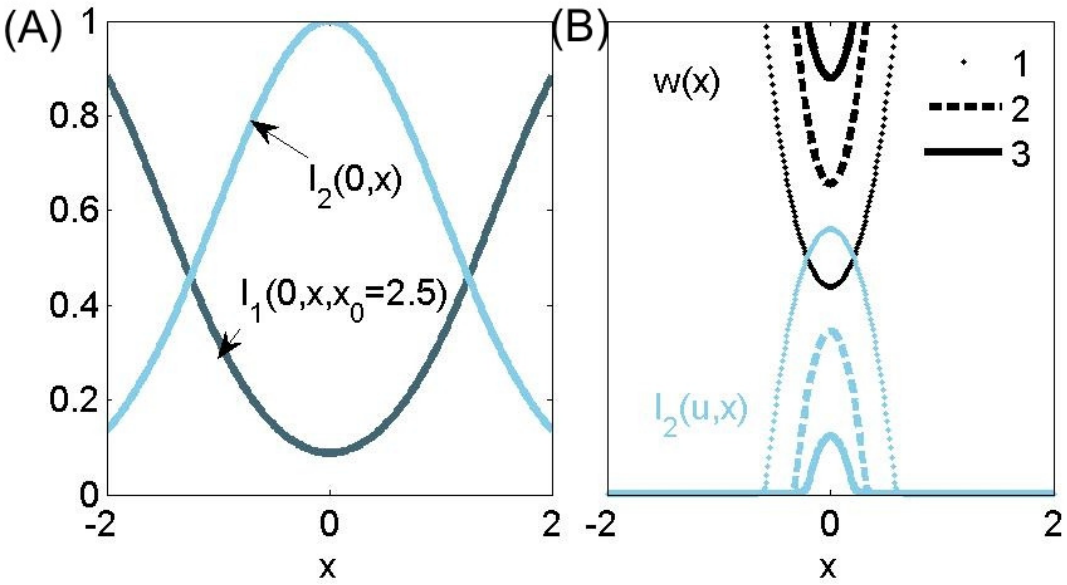

Figure 5.7 Reproduction from Warner showing (a) Incident intensities for both wavelengths and (b) relative intensities at input, $w(x)$ and I_2 intensities at 8 Beer lengths into an infinite photochromic layer for three cases (x_0, w_0); 1, (2.5, 5), 2, (2.5,10) and 3(3.1, 40), where $\pm x_0$ are the peak positions of the I_1 Gaussian profiles [Warner 2009, split into two figures].

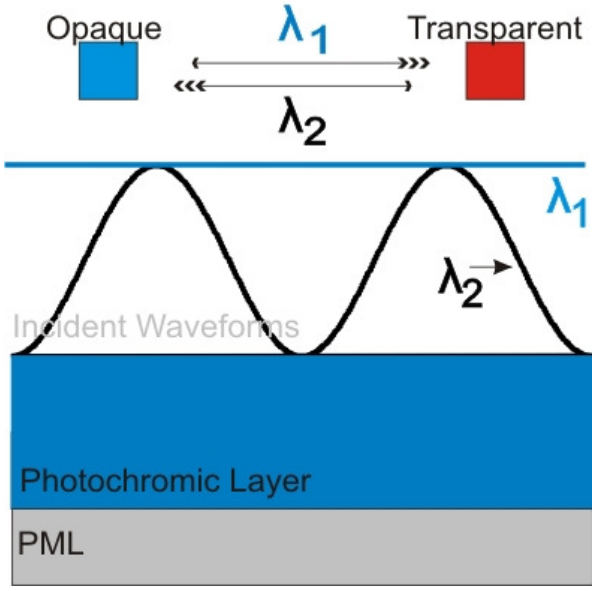

Figure 5.8 Schematic diagram of FEM simulation used to create aperture profiles in an infinite photochromic layer showing the incident wavelengths, photochromic layer and PML.

5.4 PHOTOCHROMIC APERTURE FORMATION

The first simulations here use the same model as in the plane wave incidence, with only the incident waveforms changed to the required forms, including the ability to choose polarity. It was also necessary to change the periodic conditions (to anti-periodicity) for the standing wave when imaging a single aperture due to symmetrical concerns. A Beer length of 50 nm was used for both wavelengths with the characteristic intensity ratio, w_0, set to one; this resulted in a possible imaginary refractive index (κ), of between 0 and 0.64 for both wavelengths where the real part was assumed constant at 1.6. A large-period grating of 2000 nm pitch was the first investigated to validate the comparison between Warner's analytical solution and the COMSOL model. The results, demonstrated graphically in Figs 5.9 and 5.10 for TE and TM cases respectively, show reasonable agreement between the models. When the intensity waveform of λ_2 found by COMSOL are overlaid by those calculated exactly no difference is seen at the shown resolution for the TE case, however there are already noticeable difference for the TM polarisation, showing the importance of considering the effect of polarisation for these gratings.

There are however both system constraints and properties of electromagnetic radiation that show shortcomings in the analytical solution. As noted previously the analytical solution used here only accounts for two of the possible five photochromic reactions (ignoring the thermal constant and the cross-reactions of both species (e.g. λ_2 being absorbed by state 2) as well as any background absorption. In the exploration of this narrow aperture formation it was also clear that the reflections of the substrate will alter the solution, particularly with no background absorbance present. The analytical model is created through the assumption of an infinite depth of AML, in reality this layer will be finite and need to rest on some substrate. Whilst the FEM model is able to represent this situation by using a PML the performance can vary, particularly with period. If a physical AML is considered it would be possible to use a matched substrate but this could only exactly match for one of the incident wavelengths, thus standing waves in the AMOL are important to consider.

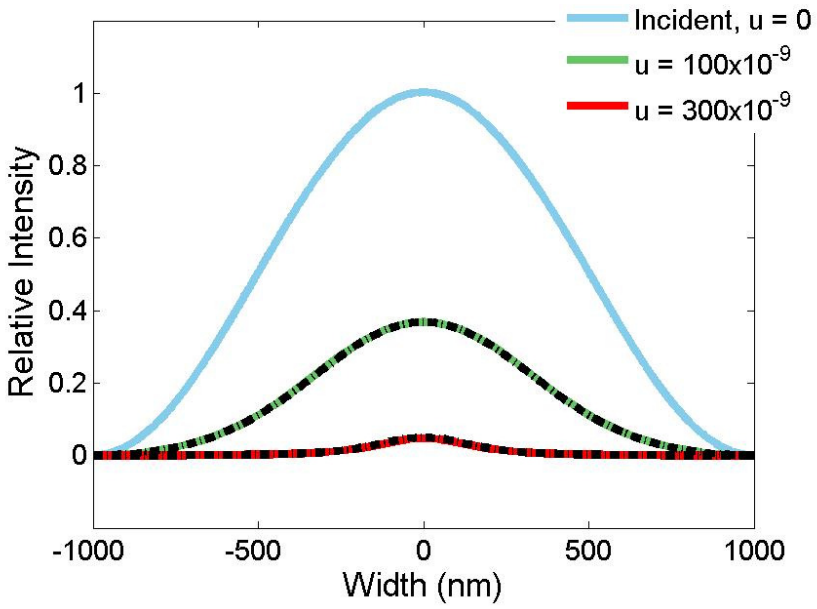

Figure 5.9 Aperture formation of a photochromic system for TE case with a Beer length of 50 nm using the FEM model (coloured) with analytical solutions overlaid in dashed black lines showing strong agreement. Here *u* is the depth (in nm) into the photochromic layer.

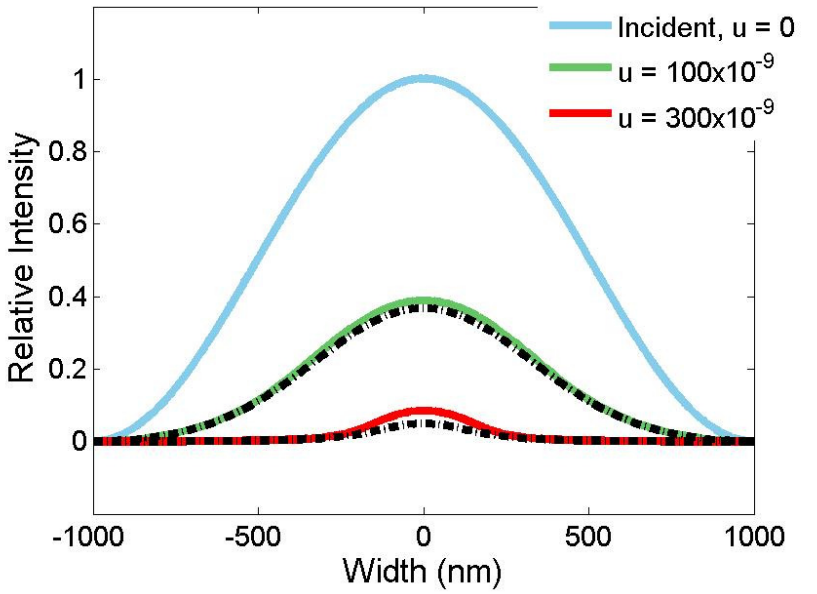

Figure 5.10 Aperture formation of a photochromic system for TE case using the FEM model (coloured) with analytical solutions overlaid in dashed black lines showing some agreement. The effect of polarisation is noted as there is increased transmission in the TM case, and hence disagreement with the scalar methods. Here *u* is the depth (in nm) into the photochromic layer.

5.4 PHOTOCHROMIC APERTURE FORMATION

Finally the analytical model does not account for the diffractive effects of light when the aperture period approaches the wavelength, which is shown to be important in Fig 5.11. Here the analytical model and COMSOL results are compared for a 250 nm period structure in which the differences are due to the shortcomings of the analytical model. The FEM model clearly shows Talbot effects (periodic repetition of the image) [Teng 2008, Latimer 1992] and the increasing impact of differences in polarisation for smaller period gratings, Fig 5.11b, whereas the analytical solution does not change from the large-period case.

These differences in the transmission of light due to polarisation are driven by the inherent problems in focusing light through an aperture with dimensions approaching, and less than, the size of its wavelength. This is particularly pronounced in the case of the absorbance aperture because the confinement is due only to an absorbance change – in the case of a metal grating it is not possible for the field to propagate in the metal

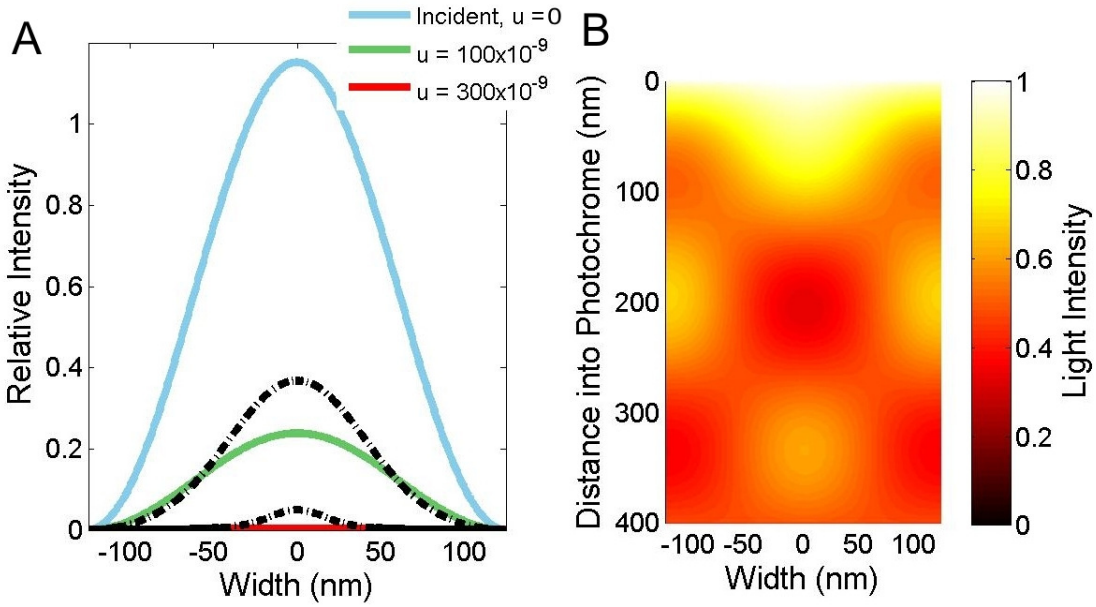

Figure 5.11 (a) Comparison of FEM and analytical aperture formation of a photochromic system for TE case where the aperture size is narrower than the wavelength. (b) Talbot effect seen in the λ_1 intensity in the photochromic layer from the FEM system. This is present because there is only a short aperture created before an approximately constant absorbance is seen due to absorbance of λ_2.

regions and hence the grating boundaries are clearly defined and a narrow aperture may be achieved. The absorbance aperture allows some propagation (although with more loss) outside the desired channel, and hence a broadening of the incident beam is possible, particularly for a TE polarised incident wavelength.

5.5 MODELING AN AMOL SYSTEM

Having validated the FEM model created with COMSOL against an analytical model and isolated some of the areas which the FEM model may improve the understanding of an AMOL system the full AMOL simulation model is now constructed. Here the dynamics used are outlined, drawing from Chapter 3, as are parameters drawn from research which are then used to describe the settings used for the initial model.

5.5.1 SYSTEM EQUATIONS AND PARAMETERS

Here the equation system used and the values selected are explained, the development begins by restating the model which combines elements from [Menon 2006] and [Warner 2009], in the majority the values presented in [Menon 2006] have been used as they are measured from a photoresist but the dynamics and variables have been transferred into Warner's naming convention with the addition of appropriate extra terms for the absorbance between species (Eq 3.36);

$$n = \frac{\phi_{1BA}\Gamma_1 I_1 + \phi_{2BA}\Gamma_2 I_2 + k_{BA}}{(\phi_{1AB} + \phi_{1BA})\Gamma_1 I_1 + (\phi_{2AB} + \phi_{2BA})\Gamma_2 I_2 + k_{nBA}}. \tag{5.1}$$

The values of the constants in this equation may be related to those presented in graphical form (Fig 5.12) by Menon [Menon 2007] through the relations defined in Section [3.4.5]. Following research by Holzwarth [Holzwarth 2010] the parameters have been adjusted (with the model made to fitting the measured curves). It is thought these changes account for the fact that it is not possible to reach complete saturation in either state (an implicit assumption in the data); the ϵ_{1a}: ϵ_{1b} ratio must hence be increased and the power used appears to be 1.7 mW due to the area of the photodetector not being accounted for. The final parameters used for Eq 5.1 are listed in Table 5.1 along with the original and adjusted values.

5.5 MODELING AN AMOL SYSTEM

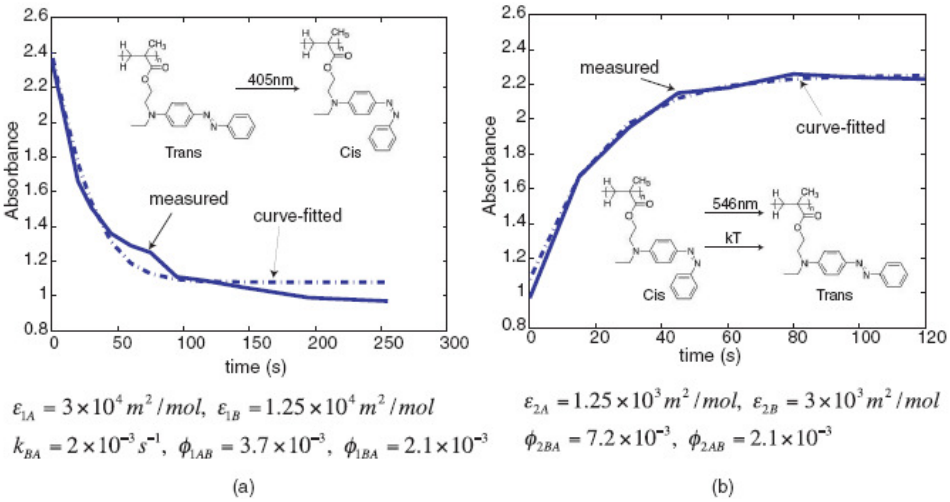

Figure 5.12 Absorbance (at 405 nm) measured as a function of time, when a 200 nm photochromic layer was illuminated by (a) 1.2 mW/cm^2 at 405 nm, and subsequently by (b) 20 mW/cm^2 at 546 nm. The experimental data (solid) are overlaid with the simulation (dashed), which enables the extraction of the photochromic parameters listed beneath the diagram. [Menon 2007]

	Menon [Menon 2007]	[Holzwarth] [Holzwarth 2010]	Warner Equivalent	Warner Value
$\epsilon_{1A}\ [m^2mol^{-1}]$	3×10^4	3×10^4	$\Gamma_{1A}\ [m^2]$	1.15×10^{-19}
$\epsilon_{1B}[m^2mol^{-1}]$	1.25×10^4	0.7×10^4	$\Gamma_{1B}[m^2]$	2.68×10^{-20}
$\epsilon_{2A}[m^2mol^{-1}]$	1.25×10^3	.	$\Gamma_{2A}[m^2]$	4.78×10^{-21}
$\epsilon_{2B}[m^2mol^{-1}]$	3×10^3	.	$\Gamma_{2B}[m^2]$	1.15×10^{-20}
$k_{BA}[s^{-1}]$	2×10^{-3}	8.5×10^{-3}	k_{nBA}	8.5×10^{-3}
ϕ_{1AB}	3.7×10^{-3}	28.5×10^{-3}		28.5×10^{-3}
ϕ_{1BA}	2.1×10^{-3}	24.5×10^{-3}		24.5×10^{-3}
ϕ_{2AB}	7.2×10^{-3}	.		7.2×10^{-3}
ϕ_{2BA}	2.1×10^{-3}	.		2.1×10^{-3}
A_{conc} [M]	unknown		ρ_{conc} [M]	0.395
-	-	-	$n_{assumed}$	1.6

Table 5.1 Parameter values calculated for AMOL, based on values published by Menon [Menon 2007] and measured by Holzwarth [Holzwarth 2010] with conversions into units from Warner [Warner 2009].

5.5.2 VALIDATION WITH MENON MODEL

Here a brief demonstration is made of the agreement between the modeling of Menon and the FEM model. The Menon model uses the photochromic factor to overcome the problem of the depth of the AMOL layer, and assumes a constant absorbance in the layer, which allows for a simple comparison to measured results. The FEM model is able to replicate the results of Figs 5.12a and 5.12b by comparing the intensity incident on a modeled photochromic layer with the intensity 200 nm into the photochromic layer, thus allowing the calculation of the absorbance through that depth (Eq 3.1). As the FEM model only looks at the stationary state only the initial and final absorbance can be calculated.

The FEM model used a 1000 nm thick photochromic layer which was 400 nm wide with a 100 nm PML base; a plane-wave of either λ_1 or λ_2 or both was specified on the top surface, matching Fig 5.5. To match the results of Fig 5.12 two simulations were run, the first with λ_1 and λ_2 set to incident intensities of 1.7 mW and 0 mW respectively and the second with incident intensities of 0.0001 mW and 20 mW respectively (here λ_1 is non zero as the absorbance of λ_1 is the measured quantity). Fig 5.13 shows the decay in intensity with depth for the two simulations, from which the intensity at 200 nm may be recorded. Then using the inverse of Eq 3.1;

$$\bar{\alpha} = \log_{10}\left(\frac{I_{200\,nm}}{I_{incident}}\right)$$

the absorbances in the states may be calculated as 1.17 and 2.23 respectively which are in good agreement with Menon's results.

5.6 FULL COMSOL MODEL

To model the AMOL system including the photochromic layer several new layers were introduced to the simulation of the photochromic layer, although the overall structure remains similar (Fig 5.14). An air-gap is created above the layer to represent the distance of the laser from the AMOL system and allow the effect of surface reflections to be

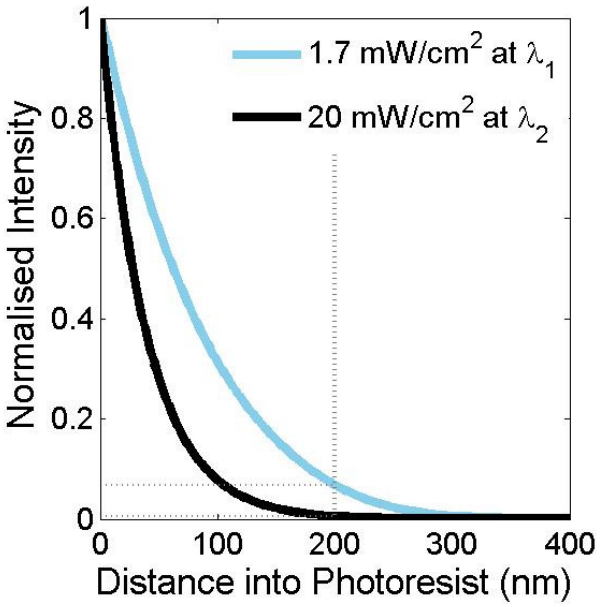

Figure 5.13 Normalised Intensity with distance into the photoresist from the FEM model of a photochromic layer. The dotted lines show the intensity at 200 nm, as used for the comparison with an analytical solution. The intercepts are at normalised intensities of 0.067 and 0.0058.

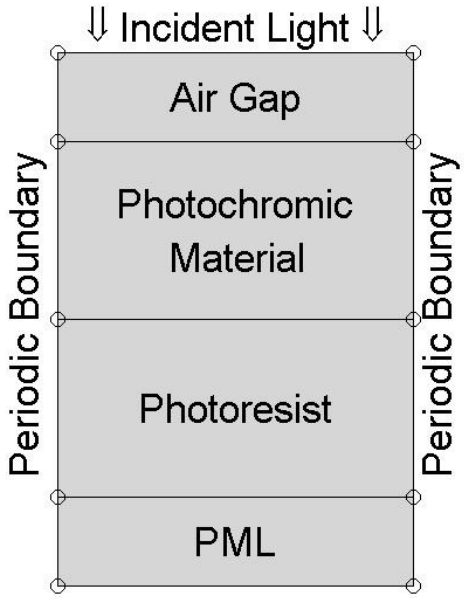

Figure 5.14 Schematic diagram showing the geometry and boundary conditions of the simulation of for the initial full AMOL system.

accounted for (this layer is 100 nm thick). The photochromic layer is 200 nm thick and modelled as described above, it is placed on 200 nm of absorbing photoresist ($n = 1.6 - 0.05j$) at both wavelengths (similar to values specified by industry [Microchemicals 2010]. This photoresist is deep enough to observe the propagation of near-field waves from an aperture without increasing the computational power needed.

As with the aperture formation in the photochromic layer the incident fields are set to a plane wave for λ_1 and a standing wave for λ_2. With an appropriate choice of the relative intensities at each of these wavelengths it is possible to demonstrate image formation in the underlying resist. A typical result, Fig 5.15, presents the shape of the aperture in the photochromic layer as a grayscale colour scheme and the λ_1 intensity in the photoresist in a red/orange colour scheme. Here a large period grating is shown in TM polarisation for demonstration and although there is clear confinement of λ_1 in the photoresist created by the photochromic layer the exposure is quite broad.

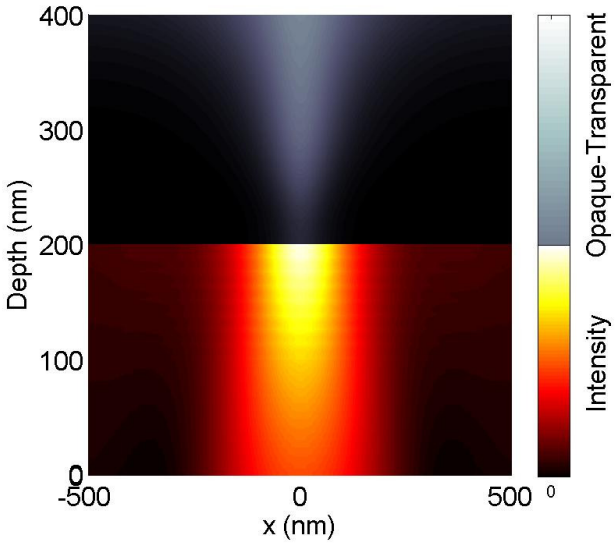

Figure 5.15 Typical simulation result, showing only absorbance in the photochromic layer and the intensity of $\boldsymbol{\lambda_1}$ in the photoresist. This simulation has a relatively large 1000 nm period and hence the propagation into the resist is strong.

5.7 DIFFERENCES USING A VECTOR MODEL

The FEM model developed in his thesis is able to solve Maxwell's equations which include effects such as diffraction and polarisation which are overlooked in many scalar approaches, these are particularly important for the case of narrow apertures such as those created by AMOL. An initial simulation of an AMOL system (Fig 5.16a and b) which creates a narrow aperture in the AML layer for TE and TM polarisations clearly demonstrates the variation of the resulting light transmission due to polarisation. To study these differences more completely the case of a simple rectangular grating, of varying period, will be considered to allow comparison between the effects found in metal and absorbance gratings. Then the FEM model will extend the study to the apertures created in an AMOL system and relate these to the effects seen in the rectangular gratings. The results of these simulations will be reported in Chapter 6.

5.8 CONCLUSIONS

In this chapter the modeling of the AMOL system undertaken in the thesis has been completely described through linking the ideas developed in the previous chapters on the

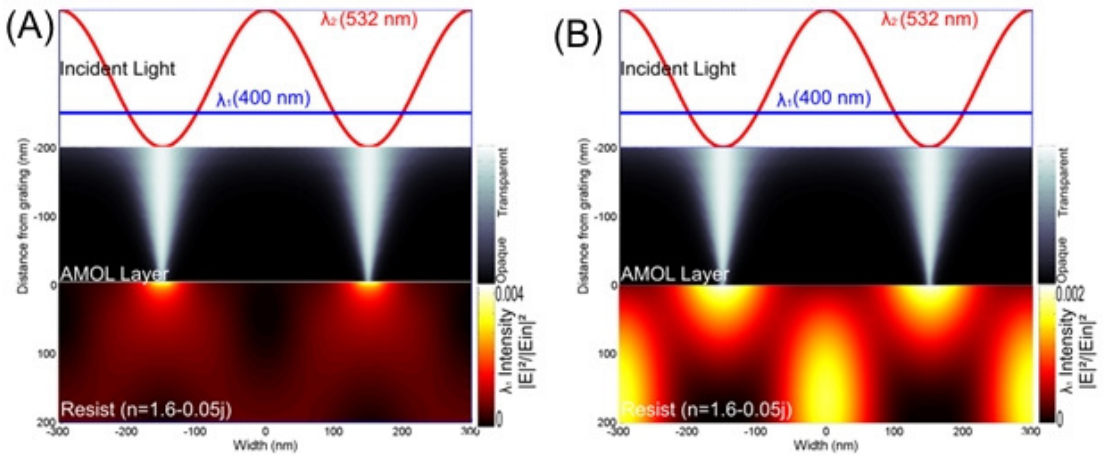

Figure 5.16 FEM simulation of (a)TM and (b)TE polarized $\boldsymbol{\lambda_1}$ light showing the absorbance in the AML (above the line at $y = 0$) and the light intensity propagated into the resist (below the line at $y = 0$) at an input intensity ratio $I(\lambda_2)/I(\lambda_1) = 1.35$. The standing-wave and plane-wave illumination schemes at λ_2 and λ_1, respectively, are shown schematically at the top of each figure.

modeling of photochromic systems and the FEM. The description of the techniques used in COMSOL and MATLAB to allow the creation of the AMOL model were described and compared to results derived analytically. Further experimental and analytical results were then used to further verify the model and enable the calculation of suitable parameters for the initial simulations. The creation of this model has overcome the difficulties of working with multiple wavelengths in a FEM system and is able to explore the complex effects of considering Maxwell's equations in lithographical systems, thus providing a strong tool for further research. With the completion of the model it is now possible to explore the characteristics of the AMOL system; in particular focus is placed on the performance with regard to sub-wavelength apertures and relating an AMOL system to plasmonic effects.

Chapter 6

POLARISATION EFFECTS

6.1 INTRODUCTION

Absorbance modulation optical lithography (AMOL) involves the use of a photochromic absorbance modulation layer (AML) that has a reversible transition between states transparent and opaque to the photoresist-exposing wavelength. During the AMOL patterning process an equilibrium is reached where a particular absorbance pattern has formed in the AML. As there is no material change in this layer, there instead being an isomerisation of the photochromic molecules, this refractive index pattern is predominantly a modulated absorbance pattern although small refractive index changes may occur. When the incident fields are a standing wave in λ_2 and a normally-incident plane wave in λ_1 various sized absorbance modulated apertures may be formed in the AML; depending on the nature of the incident light and the aperture size this may allow sub-wavelength imaging. In this chapter the FEM vector modeling approach is used to allow the effect of the polarisation of the incident wavelengths, unobservable in scalar methods, to be observed.

In order to gain insights into the fundamental polarisation-dependent, vector field AMOL imaging processes simplified absorbance gratings are investigated first as these relate to the ability of an absorbance modulated layer to act as a near-field mask. These results are compared to previously published results for metal and dielectric gratings. The simplifications used allow for compact analytical techniques to be applied and general trends to be established before the introduction of the more complex AMOL patterns. The FEM modeling is then benchmarked against the analytical results, with the differences discussed, before full AMOL simulations are presented to allow detailed

characterisation of the effects of polarisation to take place. Finally it is found that for grating-like structures polarisation control of both the exposing and aperture-defining wavelengths are also critical in achieving deep sub-wavelength resolution, with the key finding that, whilst transverse-electric (TE) polarisation is required to provide a deep null in the standing-wave interference pattern at λ_2, transverse-magnetic (TM) polarisation provides better contrast and depth of field for the exposing wavelength (λ_1).

6.2 POLARISATION

Given any electromagnetic plane wave propagating in a material, as described by Maxwell's equations (Eqs 3.42 and 3.45), it is possible to decompose this plane wave as the summation of two orthogonally polarised plane waves. The freedom of choice in selecting these two new plane waves allows a simplification to be made by selecting the magnetic and electric fields in directions parallel to the axes. This common separation creates TE and TM polarisations (defined in Fig 6.1), where, for a wave propagating in the $y-z$ plane, they consist of (E_x, H_y, H_z) and (H_x, E_y, E_z) respectively (TE and TM polarisation may also be referred to as *s*-polarised and *p*-polarised respectively). Furthermore, taking the expanded form of Maxwell's equations it is possible to simplify the system, taking for example the TE case, H_x, E_y and E_z are set to 0 and the equations system reduces to three equations;

$$\frac{\partial E_x}{\partial z} = ik\mu H_y \tag{6.1}$$

$$\frac{\partial E_x}{\partial y} = ik\mu H_z, \qquad and \tag{6.2}$$

$$\frac{\partial H_y}{\partial z} - \frac{\partial H_z}{\partial x} = ik\epsilon E_x. \tag{6.3}$$

Along with providing the opportunity for easier analysis for some situations, different results may be produced in lithographical systems due to the polarisation used. Polarisation has been demonstrated to be an important feature in lithographic imaging in projection lithography where TE polarised light provides better images due to better overlap in interference lithography [Mack 2007]; differences have also been seen in

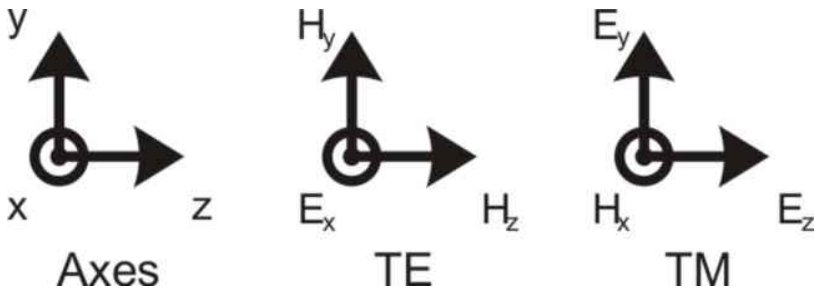

Figure 6.1 The axes used in this work and the separation of the electric and magnetic fields for TE and TM polarisation.

near-field lithography [McNab 2000, Melville 2006] where TM polarisation generally exhibits better contrast.

6.3 GRATING MODELING

To improve the understanding of the effect that an absorbance grating structure will have on the formation and propagation of light intensity profiles a very simplistic version of the AMOL system is modeled, involving a two-dimensional (2D) grating created through the incidence of a standing wave interference pattern in λ_2 and a plane wave at normal incidence in λ_1 (Fig 6.2). Before using the full FEM model to examine this system an analytical analysis of idealised absorbance-modulated gratings has been performed. This allows the essential features of AMOL-like imaging through sub-wavelength apertures to be examined, and image contrast beneath absorbance-modulated gratings being compared with that below metal or dielectric gratings.

In previous work investigating sub-wavelength propagation of light through grating-like structures Rytov [Rytov 1956] has shown an analytical calculation method for determining field profiles inside gratings for both TE and TM polarisations and this method is used here to provide analytical results for comparison with FEM simulations. Further modeling for metal [McNab 2000] and dielectric [Pilozzi 1996, Bockelmann 1991] grating structures has taken place to improve the understanding of light transmission and the effects of polarisation in such gratings.

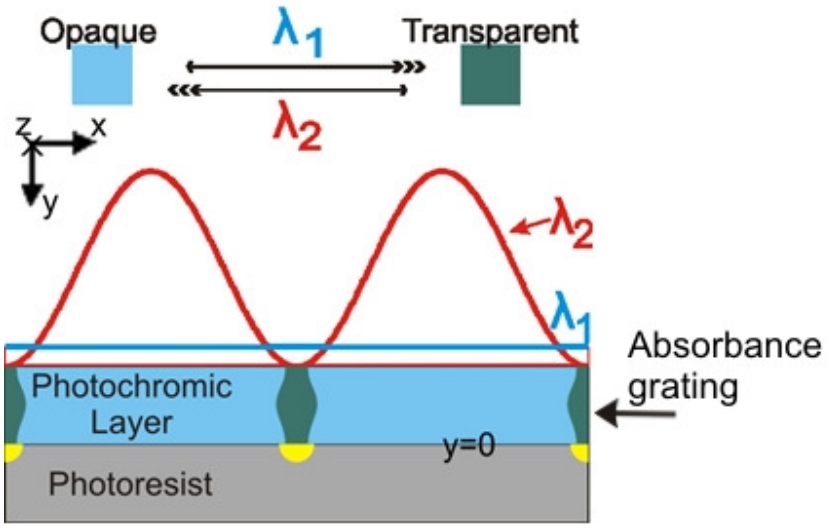

Figure 6.2 Schematic diagram of the AMOL process being modeled

Gratings, slit apertures and surface relief features have been heavily researched because of their applications in a range of areas including imaging, optics, spectral analysis and the subtle physics involved. Several alternative analytic and numerical techniques have been used in previous work examining sub-wavelength grating structures including effective medium theory [Lalanne 1997], rigorous coupled wave analysis [Moharam 1995, Moharam 1986, Gaylord 1985], FDTD analysis [Garcia 2007] and multiple multipole techniques [Novotny 1994]. Comparison is made to the results from some of this work and this analysis is extended through FEM modeling using COMSOL in order to capture the behavior of the optical fields beneath the gratings (i.e. in the underlying photoresist) that the Rytov analysis does not give us. There is limited research on absorption gratings, although Baird discusses a sinusoidal grating case using RCWA [Baird 1983]. Here the full AMOL FEM model is used to investigate the effects of the polarisation on forming absorbance gratings of the type produced in the two-wavelength AMOL process and the effect of polarisation of light on the production of absorbance modulated patterns.

6.3.1 RYTOV MODELLING

A model of the Rytov system was created in which the grating geometry, real and imaginary grating refractive indexes and the input fields could be altered (Fig 6.3). Rytov's analytical technique [Rytov 1956] proceeds by determining that, for fine sub-wavelength gratings of infinite extent in the propagation direction, an effective index of refraction can be calculated for the entire grating. This may then be substituted into a set of equations and boundary conditions which are solutions to Maxwell's equations, with the equations separated based on light polarisation.

For example, for the TE polarization of light the electric field intensity E_x, the magnetic field intensity in the y-direction H_y and the magnetic field intensity in the z-direction H_z in one section of the grating $(0 \leq z \leq a)$ with $\epsilon_r = \epsilon_1$, $\mu_r = \mu_1$ are given by solutions periodic in z, with period d;

$$E_x = U(z)e^{-ik_0 ny}, \tag{6.4}$$

$$H_y = V(z)e^{-ik_0 ny}, \tag{6.5}$$

$$H_z = W(z)e^{-ik_0 ny}, \tag{6.6}$$

where U, V and W are the field intensity profiles at any point given by $y = y_0$;

$$U(z) = Acos(\alpha_1 z) + Bsin(\alpha_1 z), \tag{6.7}$$

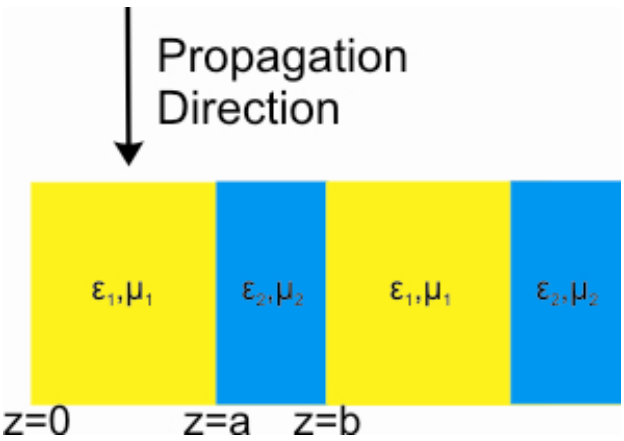

Figure 6.3 Analytic grating model demonstrating the model geometry, variables and coordinate system with infinite extent in the third dimension.

$$V(z) = -\frac{\alpha_1}{ik_0 n\mu}\big(Asin(\alpha_1 z) - Bcos(\alpha_1 z)\big), \tag{6.8}$$

$$W(z) = \frac{n}{\mu}\big(Acos(\alpha_1 z) + Bsin(\alpha_1 z)\big), \tag{6.9}$$

respectively, where

$$\alpha_1 = k_0\sqrt{n_1^2 - n^2} \tag{6.10}$$

with n being the effective refractive index of the grating,

$$k_0 = \frac{2\pi}{\lambda}, \tag{6.11}$$

$$n_1^2 = \epsilon_1\mu_1, \tag{6.12}$$

with similar expressions for α_2 and n_2 and for the second grating section [Rytov 1956]. Imposing the required boundary conditions allows the formulation of an expression with n as the only variable (implicit in the expressions for α_1 and α_2),

$$\frac{\alpha_2}{\mu_2}tan\left(\frac{\alpha_2 b}{2}\right) = -\frac{\alpha_1}{\mu_1}tan\left(\frac{\alpha_1 a}{2}\right). \tag{6.13}$$

Once Eq 6.13 has been solved for n the value may be substituted back into Eq 6.10 to determine α_1 and α_2 for the intensity profile equations (Eqs 6.7 to 6.9). Then, by applying periodic boundary conditions to determine the amplitude coefficients A, B, C and D the full shape of the propagating intensity profile within the grating can be calculated. Similar analyses for the case of TM polarisation produces the result

$$\frac{\alpha_2}{\epsilon_2}tan\left(\frac{\alpha_2 b}{2}\right) = -\frac{\alpha_1}{\epsilon_1}tan\left(\frac{\alpha_1 a}{2}\right), \tag{6.14}$$

which is also be solved for n and substituted back into the TM field profiles (which are equivalent to the TE field profiles with the change of $\boldsymbol{H}$, $\boldsymbol{E}$, ε, μ *to* $\boldsymbol{E}$, $-\boldsymbol{H}$, μ, ε) to produce the desired intensity profiles.

As an example consider a grating of 50% duty cycle and 80 nm pitch with 436 nm TE polarised light propagating inside. Let the grating consist of a dielectric material ($\epsilon_1 = 4$) for region 1 ($0 \leq z \leq 40\,nm$) and an air gap ($\epsilon_2 = 1$) for region 2 ($40\,nm \leq z \leq 80\,nm$), with this pattern being repeated infinitely along the z direction. Thus the parameters for from Eqs 6.11 and 6.12 may be calculated as

$$k = \frac{2\pi}{436 \times 10^{-9}}\ [m^{-1}], \qquad n_1^2 = 4\ and\ \ n_2^2 = 1. \tag{6.15}$$

Substituting these parameter values into Eqs 6.13 and 6.14 and solving numerically returns a value of n of 1.6007. Substituting this value into Eq 6.10 determines α_1 as $17.3 \times 10^6 m^{-1}$ and similarly α_2 is determined to be $i18.0 \times 10^6 m^{-1}$. If these values are substituted into the intensity profile equations (Eqs 6.7 to 6.9) there remain four unknown parameters, A, B, C and D which represent the magnitudes of the solutions.

To solve for these unknowns the boundary conditions may be used, as, in any system, the boundary conditions must hold for the result to be appropriate. This means that for the periodic system of electromagnetic waves the tangential field components E_x and H_y are required to be continuous at the boundaries between sections ($0, a$ and b). Applying these conditions and selecting the value of one of the coefficients allows the calculation of all of the resulting waveforms (as expected the absolute magnitude of the intensity profile may vary depending on the choice of this coefficient, or correspondingly on the incident intensity).

For example selecting $A = 1$, sets the intensity of U, at $z = 0$ to 1, from which values for the other parameters may be found; $B = 1.30, C = 1$ and $D = i0.9554$. The formulation of the intensity profile of the entire grating is shown in Fig 6.4 with region 1 ($0 \leq z \leq 40\ nm$) described by

$$U(z) = 1 \times cos(\alpha_1 z) + 1.3 \times sin(\alpha_1 z), \tag{6.16}$$

$$V(z) = -\frac{\alpha_1}{ik_0 n\mu_1}\big(1sin(\alpha_1 z) - 1.3cos(\alpha_1 z)\big)_{,,} \tag{6.17}$$

$$W(z) = \frac{1.6}{\mu_1}\big(1cos(\alpha_1 z) + 1.3sin(\alpha_1 z)\big), \tag{6.18}$$

and region 2 ($40\ nm \leq z \leq 80\ nm$) by

$$U(z) = 1 \times cos(\alpha_2 z) + i0.95 \times sin(\alpha_2 z), \tag{6.19}$$

$$V(z) = -\frac{\alpha_1}{ik_0 n\mu_1}\big(1sin(\alpha_2 z) — i0.95cos(\alpha_2 z)\big), \tag{6.20}$$

$$W(z) = \frac{1.6}{\mu_1}\big(1cos(\alpha_2 z) + i0.95sin(\alpha_2 z)\big). \tag{6.21}$$

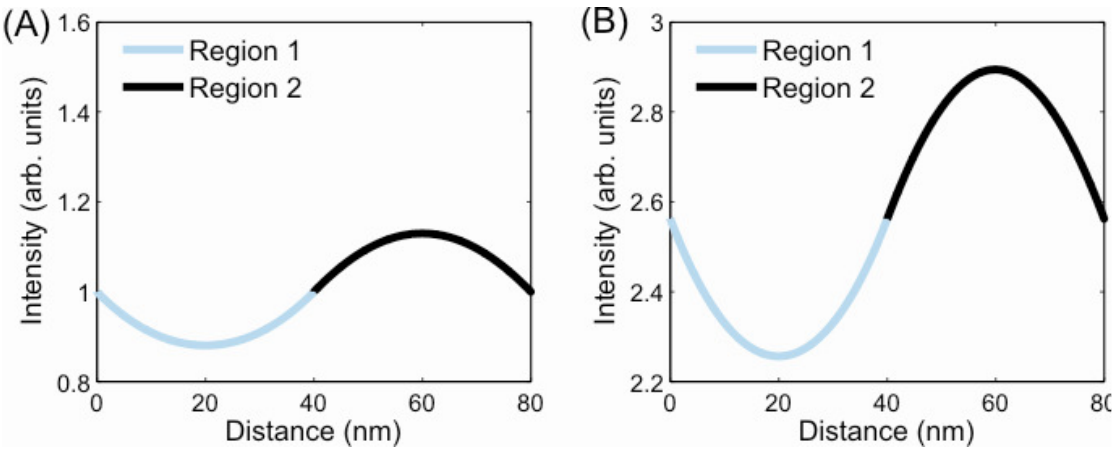

Figure 6.4 Plots showing the intensity profiles predicted by a Rytov Analysis for (a) E_x and (b) H_z for transmission in an 80 nm grating consisting of a dielectric (Region 1, $\varepsilon = 4$) and an air gap (Region 2, $\varepsilon = 1$) and wavelength of 436 nm. The absolute value of the intensity is arbitrarily chosen but allows fair comparison between (a) and (b).

Thus the Rytov analysis allows the construction of intensity profiles for any sized grating with metal, dielectric or absorbance parameters and, with minimal change a similar analysis for TM polarisation. As an infinite grating is used the propagation of the intensity pattern through the grating and any associated magnitude reduction is not accounted for; instead a nominal magnitude may be selected for one of the values, but this does not detract from the results.

6.3.2 FEM MODELING

A complimentary model of the Rytov system was created using FEM to create a similar, simplified 2D grating structure. This was undertaken for two purposes: firstly, it allowed the accuracy and validity of the FEM models to be tested by comparison with the analytical Rytov results for the fields inside the grating structures; and, secondly, it allowed the fields beneath the gratings (i.e. the fields in the underlying photoresist) to be determined, which is not possible with the Rytov analysis as this relies on the assumption that the gratings are of infinite extent. The FEM model also uses an air-gap above the grating which determines the reflectivity of the grating, and providing a measure of

the absolute field intensity in the grating, whereas the Rytov result can be scaled to the desired height, in the cases shown here to match FEM results.

The FEM model, shown in Fig 6.5, includes a grating with limited height (200 nm was used in this case), with an air-gap above the grating and a photoresist modeled below the grating, such that it more closely represents the true AMOL set up. The FEM model also required boundary conditions; periodic conditions were used on the sides parallel to the gratings and PMLs were placed at the ends of the model geometry to reduce any standing wave effects. The input wave was able to be specified as either TE or TM polarised wave incident at the top of the model geometry. FEM modeling was performed for this type of system in idealised gratings with fixed dielectric properties, exposed to λ_1 only; and for systems with more realistic AMOL-like gratings formed by the competition between a TE-polarised standing wave at λ_2 (to produced a deep null) and normal-incidence plane-wave illumination at λ_1 (for either TE or TM polarisation).

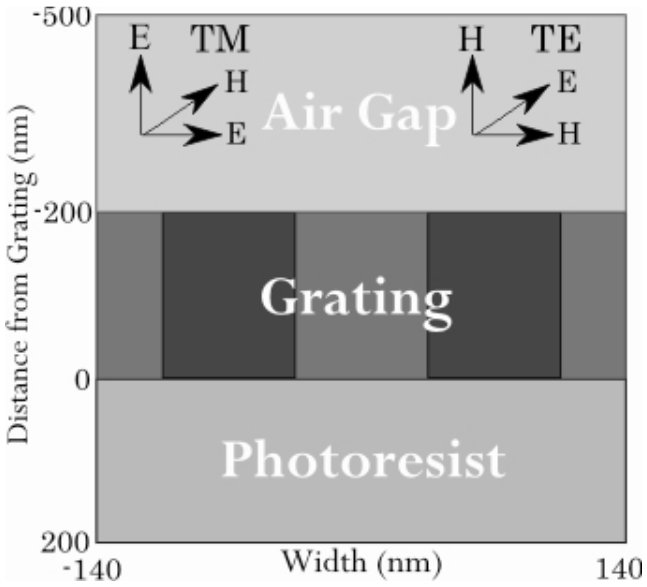

Figure 6.5 FEM grating model showing air gap, grating and photoresist layers for a 140 nm period grating; illuminated from above with λ_1 polarised as TE or TM as shown at the top of the diagram

6.4 FIELD PROFILES INSIDE GRATINGS

The FEM modeling of the idealised gratings has been validated by comparing cross-sections of intensity profiles taken in the middle of the gratings with Rytov analytical solutions, and results for 80-nm period gratings are shown in Fig 6.6; the two techniques show very good agreement (FEM and Rytov results are overlaid in Fig 6.6, and no discernable difference is present at this magnification) for sub-wavelength gratings. However, as the grating period approaches the order of the wavelength the difference between the Rytov and FEM models increases due to the approximations of the Rytov model becoming less applicable. To clarify this point, in the Rytov model an assumption of a sub-wavelength grating is used to allow an effective index (n) of propagation to be defined across the entire period; this can only be applicable when the grating is narrow enough such that each grating region strongly affects the other and as the grating period is increased this becomes less realistic. Fig 6.7 demonstrates the increasing error as the grating period is increased for both metal and dielectric cases. As any errors introduced have a much larger effect on the Rytov model for simulations of gratings larger than half the wavelength the FEM simulations are accepted as the more accurate solutions.

Simulations were performed for three general cases with 80 nm, 50% duty cycle gratings of air ($\varepsilon_r = 1$) and; chromium (a, $\varepsilon_r = -13.24 - 14.62i$), dielectric (b, $\varepsilon_r = 4$) and a strong absorber (c, $\varepsilon_r = 1 - 3i$) as shown in Fig 6.6. The intensities in the metal grating resemble those shown by McNab [McNab 2000], where there is very good confinement of the light in the air gaps for TM polarisation and very little transmission of TE polarised light through the grating. For the dielectric case strong confinement is shown in the low dielectric constant region for the TM polarisation whereas for the TE polarisation there is a reversal so that there is greater intensity in the higher dielectric constant region, which is similar to Bockelmann's results [Bockelmann 1991]. It is however, important to note that the TE case has far less contrast than TM polarisation and lacks the steep transition at the boundary, which makes it less suitable for imaging purposes. The absorbance-modulated grating (Fig 6.6c) also shows high contrast and good field

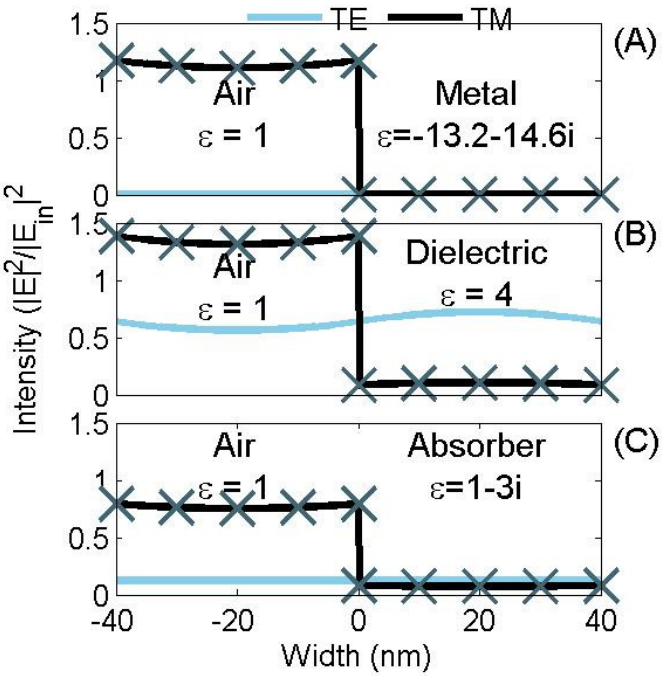

Figure 6.6 Light intensity relative to input field inside 50% duty cycle, 80 nm pitch gratings for TM and TE polarised light at 436 nm for (a) Metal (Nichrome), (b) dielectric and (c) strongly absorbing gratings with FEM simulation. The crosses mark TM results of the Rytov model results for the same cases.

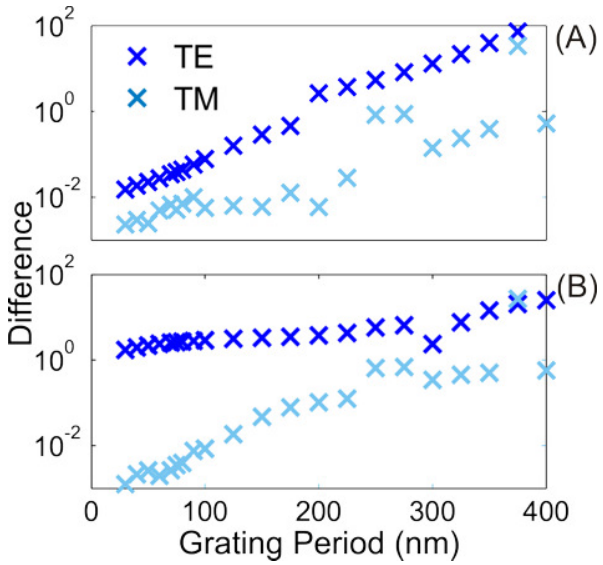

Figure 6.7 Two-norm of the difference between the waveform calculated by the FEM and Rytov models of (a) metal and (b) absorbing gratings as the grating period is increased. The incident wavelength is 436 nm. The apparent poor agreement in TE polarisation is due to a disagreement in field strength rather than waveform profile, suggesting that the relative field strengths are incorrect in the Rytov model..

confinement for TM polarisation, with very low intensity for TE polarisation. This is because, like the dielectric grating case, the fields prefer to be guided into the absorber for TE illumination but now they are strongly attenuated (as in the metal case).

By considering the effects of the boundary conditions at the edges of the gratings for the TE and TM polarisation cases the explanation of the very different intensity profiles becomes clearer. Considering first the metallic grating for the TE case, there is an x-directed electric field (E_x) only, which is parallel to the grating and hence there is only a tangential electric field at the grating boundary. These fields must be continuous, otherwise an electric field would be induced between them, equalising them. In the case of the TM polarisation there is no E_x component and the E_z component is acting perpendicular to the gratings; the boundary conditions for a normal electric field require a constant electric flux density (D) which allows a discontinuity in the electric field, as seen in step change at the boundary (0 nm) in the resulting plots. The same general boundary conditions apply for the dielectric and absorbing boundary conditions, but due to the nature of the mediums the effect is reduced. This is because the difference in permittivity, and hence field transmission, between the two grating media is reduced; two consequences of this are that the discontinuity may be reduced size and there is noticeable transmission of the TE polarisation and of fields in the absorber/dielectric material.

In an AMOL type system the absorbance change will depend on the photochromic material used in the AML, which is subject not only to absorbance change requirements but also other material parameter requirements and the need to be easily applied. Figure 6.8 demonstrates the effect of changing absorbance profile. The abrupt change at the boundary remains, however the difference in transmission between the air and absorbing dielectric regions decreases with absorbance, as the cost of transmission in the absorbing medium is reduced. Clearly the larger the change of absorbance achieved the easier it will be to create a useful mask from a photochromic layer.

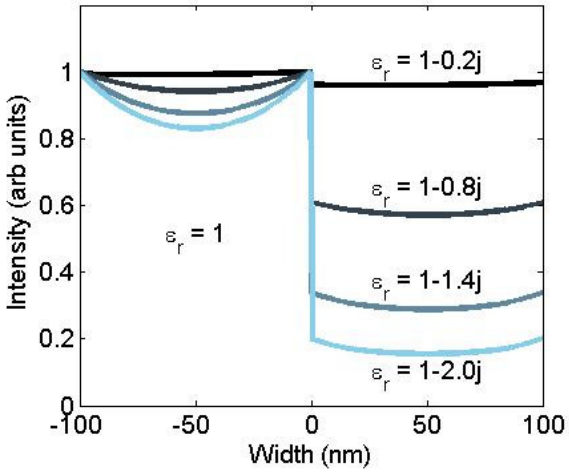

Figure 6.8 Grating waveforms for a 200 nm period, 50% duty-cycle grating between air ($\epsilon_r = 1$) and an increasing absorbing medium.

6.4.1 EFFECT OF GRATING PERIOD

Although the results presented here concentrate on transmission through sub-wavelength features it is important to note that significant changes occur as the grating period is increased, in particular the performance of the TE polarised light improves markedly and the relationship between TM and TE polarised light does not stay constant. As shown in Fig 6.9, which compares metal and dielectric gratings which are sub-wavelength (200 nm), wavelength scale (400 nm) and multi-wavelength (2000 nm) using the FEM model, the TM polarisation maintains a reasonably constant profile with a slowly increasing magnitude up to the 400 nm grating. The TE polarisation shows far greater increase in magnitude, from being much more poorly transmitted than the TM polarisation to being transmitted many times more strongly with a period near that of the incident waveform. Finally as the period is increased past the incident wavelength the magnitudes of the TE and TM polarisations converge and additional features are created, such as the oscillations seen in the air gap in Fig 6.9c. The differences noted can be explained by considering the increasing period of the gratings and noting that this will reduce the impact of the boundary conditions. Although the TE polarised waveforms remain continuous at the boundary as the period increases this does not restrict the ability of the field to propagate through the grating as it did for narrow apertures.

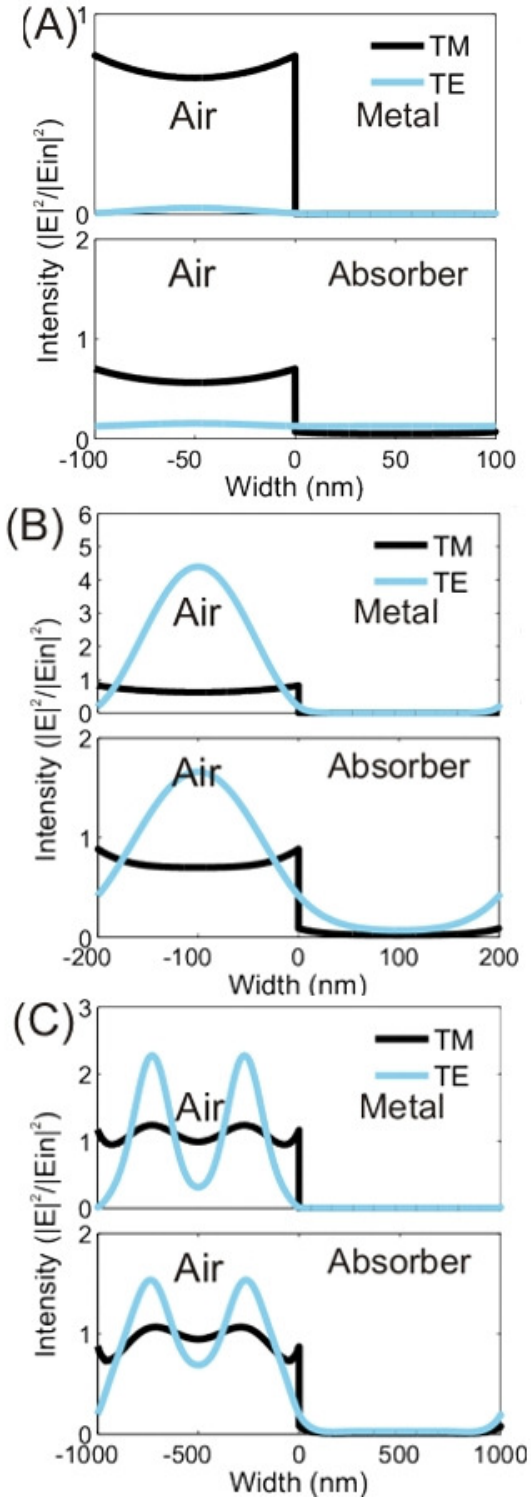

Figure 6.9 Comparison of metal (ε_r = -13.24 − 14.62i) and absorbance ($\varepsilon_r = 1 - 3i$) gratings as the period increases past the incident wavelength. Grating images are shown at (a) 200 nm, (b) 400 nm and (c) 2000 nm, with an incident wavelength of 436 nm.

6.4.2 EFFECT OF GRATING DUTY CYCLE

The duty cycle, or portion of the grating period allowing light through, is also a variable of the absorbance gratings. There is particular relevance for investigating the effect of changing the duty cycle here because an AMOL absorbance grating will have an adjustable duty cycle based upon the incident intensities, and this duty cycle will normally be less than 50% for near-field exposures. Here the FEM grating model is used to investigate the influence that changing the grating cycles has, shown in Fig 6.10 for an absorbance grating. As the low absorbing ($\epsilon_r = 1$) portion of the grating is increased from 25% to 75% of the period there is greater overall transmission through the grating, since at low duty cycles the narrower low absorbing aperture forces more of the field into the high absorbing ($\epsilon_r = 1 - 2i$) region. The relative intensity difference in the intensity waveforms between the high and low absorbing regions remains reasonably constant as the duty-cycle reduces, which is a good result as this suggest that narrow, sub-wavelength apertures will still allow good differentiation between transparent and opaque areas, but longer exposure times will be required.

6.5 MODELING BENEATH GRATINGS

The intensity profiles inside the grating provide good insight into the effectiveness in confining the light to a certain part of each of the structures; in the case of an AMOL system it is also very important to consider how the light is transmitted into the underlying materials and photoresist. Analytical and simulation tools can once again be used to investigate these physics. Here analytical wave propagation and a series of FEM simulations of the idealised gratings are used to calculate intensity profiles for the electric field strength at different depths below the grating. This work provides an improved understanding of propagation of the λ_1 intensity profiles beneath gratings and, particularly for the evanescent waves created by the sub-diffraction limited gratings, offers insight and understanding to the impact of using an AML as an adaptive mask as opposed to the common metal masks. Again, the effects of polarisation on these changes are the focus of this part of the thesis.

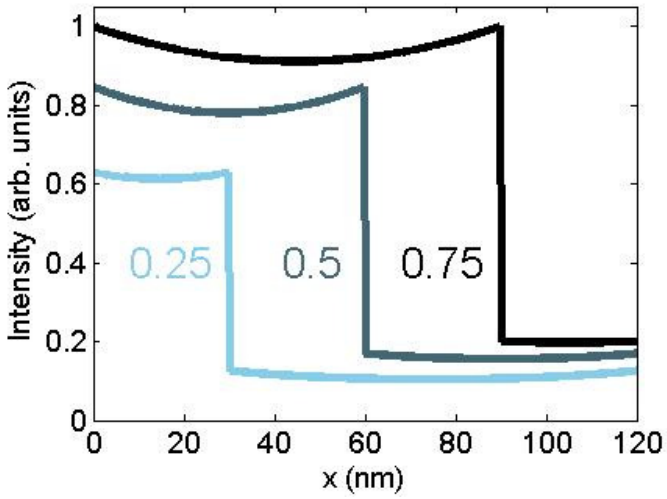

Figure 6.10 Intensity waveforms for a 120 nm period absorbance grating ($\varepsilon_r = 1 - 2i$, right hand side) when the portion which is less absorbing ($\varepsilon = 1$, left hand side) increases from 25% – 50% – 75%.

6.5.1 ANALYTICAL MODELLING

The analytical techniques developed by Rytov are only valid for the case of propagation inside gratings, hence a new technique must be introduced to model the propagation beneath the gratings. Fortunately the propagation of electromagnetic plane waves can be derived for the case of isotropic materials (e.g. the photoresist and substrate beneath the AMOL layer). To begin consider the solution to the wave equations expressed as a phasor as introduced previously (Eq 3.55), $\boldsymbol{U}(P)$, at any point, P,

$$\boldsymbol{U}(P) = \boldsymbol{A}(P)e^{i\phi(P)} \tag{6.22}$$

where $\boldsymbol{A}$ is the amplitude and ϕ the phase. This may be related back to the sinusoidal representation, $\boldsymbol{E}(P,t)$ at any time, t, by

$$\boldsymbol{E}(P,t) = \boldsymbol{A}(P)\cos\big(\omega t + \phi(P)\big) = Re\big[\boldsymbol{U}(P)e^{i\omega t}\big]. \tag{6.23}$$

Considering here a plane wave propagating in an arbitrary direction described by,

$$\boldsymbol{U}(P) = Ae^{-i\boldsymbol{k}\cdot\boldsymbol{r}} \tag{6.24}$$

where $\boldsymbol{k}$ is a vector of the propagation constants, $\boldsymbol{r}$ is the position vector and any phase offset has been ignored. In Cartesian coordinates this may be expressed as

$$\boldsymbol{U}(x,y,z) = Ae^{-ik(\alpha x+\beta y+\gamma z)} \tag{6.25}$$

where α, β and γ are the direction cosines of propagation, describing the angles between the axis and the direction of propagation. The direction cosines are not independent, as the combined magnitude must be 1, and may be related through

$$\beta = \sqrt{1-\alpha^2-\gamma^2}; \tag{6.26}$$

this allows Eq 6.25 to be rewritten with the propagation term separated,

$$\boldsymbol{U}(x,y,z) = Ae^{ik(\alpha x+\gamma z)}e^{ik\beta y} = Ae^{ik(\alpha x+\gamma z)}e^{ik\sqrt{1-\alpha^2-\gamma^2}y}. \tag{6.27}$$

The phasor representation may also use spatial frequencies to describe the plane wave [Goodman 2005]; these relate directly to the direction cosines as

$$\begin{gathered}\alpha = \lambda f_x, \\ \gamma = \lambda f_z, \qquad and \\ \beta = \sqrt{1-(\lambda f_x)^2-(\lambda f_z)^2} = \lambda\sqrt{1/\lambda^2-(f_x)^2-(f_z)^2},\end{gathered} \tag{6.28}$$

so that Eq 6.25 may be updated to give,

$$\boldsymbol{U}(x,y,z) = Ae^{i2\pi(f_x x+f_z z)}e^{i2\pi\sqrt{1/\lambda^2-{f_x}^2-{f_z}^2}y}. \tag{6.29}$$

This transformation is useful because the plane wave has been expressed as a function of its spatial frequency, this may now be combined with the ability of Fourier analysis to represent any given signal as the sum of a series of plane waves at specific frequencies. A signal may then be propagated in the frequency domain through the application of Eq 6.29, allowing the waveform to be calculated at a series of distances from the initial waveform. To clarify the process further, consider a 2D field of interest, $\boldsymbol{U}$, in the x,z plane, the 2D Fourier transform of this field is given by [Mack 2007]

$$\boldsymbol{T}(f_x,f_z;y) = \iint \boldsymbol{U}(x,z,y)e^{-i2\pi(f_x x+f_z z)}dxdz = \Im\big(\boldsymbol{U}(x,z,y)\big) \tag{6.30}$$

and similarly the inverse transform, defined as

$$\boldsymbol{U}(x,z,y) = \iint \boldsymbol{T}(f_x,f_z;y)e^{i2\pi(f_x x+f_z z)}df_x df_z = \Im^{-1}\big(\boldsymbol{T}(f_x,f_z;y)\big) \tag{6.31}$$

Taking an initial waveform on the plane at $y = y_0$ the signal at any future plane $y = y_1$ may be calculated as

$$\boldsymbol{U}(x,z,y) = \Im^{-1}\left\{ \boldsymbol{T}(f_x, f_z; y_0) e^{i2\pi\sqrt{\frac{1}{\lambda}-{f_x}^2-{f_z}^2}\,y} \right\} \tag{6.32}$$

Thus by taking the Fourier transform of the initial waveform at y_0 using Eq 6.30 and then applying Eq 6.32 with the desired distance, y, and finally taking the inverse transform (Eq 6.31) of the resulting signal the propagated wave is calculated.

The modeling of the propagation of the electromagnetic fields beneath sub-wavelength gratings requires particular features of the system to be taken into account. Firstly, regarding propagation in the *y* direction, the propagation is given by the β term of Eq 6.28 and in the case of high spatial frequencies, as created by sub-wavelength gratings,

$$\sqrt{{f_x}^2 + {f_z}^2} > \frac{1}{\lambda}, \tag{6.33}$$

an imaginary value is returned and the propagation term becomes an exponential decay, describing an evanescent wave. Thus transmission of a signal through an isotropic material may be considered as the operation of a simple low-pass filter on the intensity profile. In the case of near-field imaging there may be no propagating wave, hence the evanescent wave is of primary importance. A second feature arises in the computation due to the use of the Discrete Fourier Transform (DFT), this introduces a summation of terms instead of the integration but more importantly there is also a frequency cutoff due to a limit in the number of signal points used. It is important to note that there are simplifying assumptions in this method, in particular it does not take into account any edge effects created by the end of the grating and hence errors are expected.

6.5.2 FIELD PROFILES BENEATH GRATINGS

The FEM model that was briefly described in Section 6.3.2 allowed calculation of intensity profiles beneath gratings without significant changes to the model (a larger photoresist region was used to reduce the effect of any possible reflections from the PML). The resulting intensity profiles are shown in Fig 6.11 for two different 80 nm period gratings – one a metal grating and the other an absorbance grating. Here only the plots of the TM-polarised field are shown as this is transmitted more effectively by all

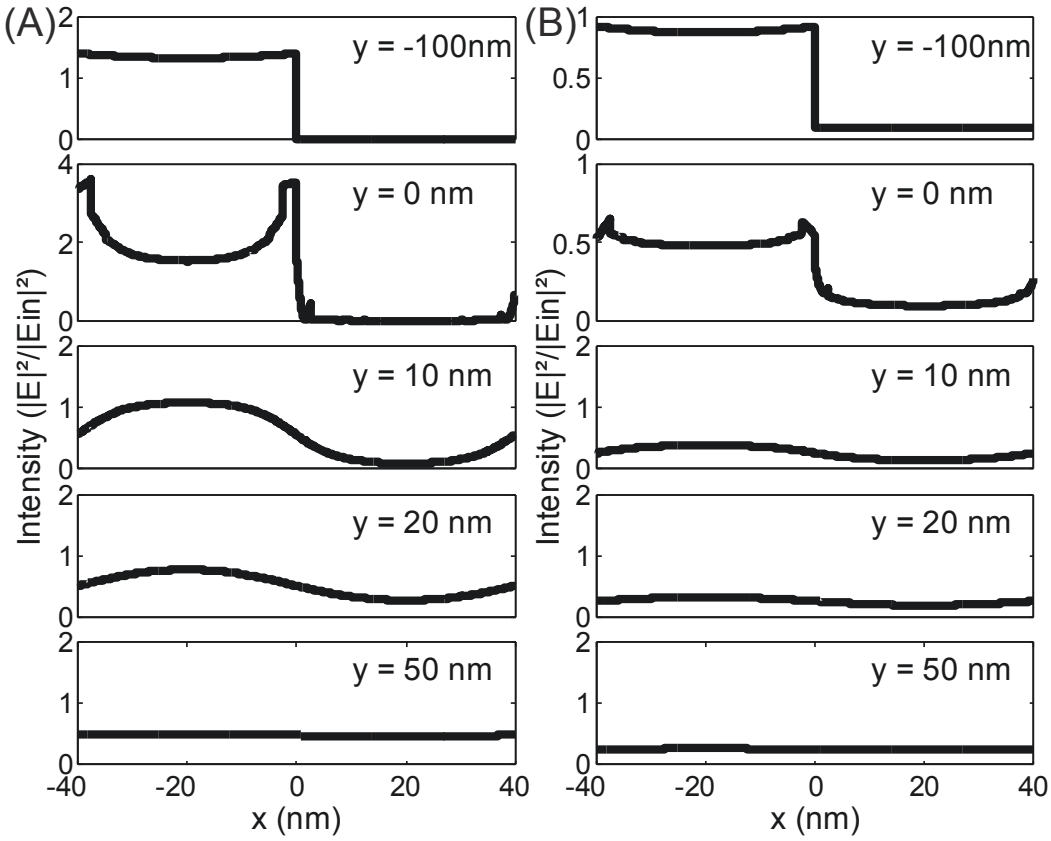

Figure 6.11 Light intensity after passing through (a) metal and (b) absorbance gratings with 80 nm period and 50% duty cycle, as calculated using FEM simulations. Horizontal intensity profiles are taken inside the grating, at the exit, 20 nm, and 50 nm beneath the grating.

sub-wavelength gratings considered. Beginning by considering the metal grating (Fig 6.11a), which is in general agreement with that presented by McNab [McNab 2000], the strong confinement of TM polarised light outside the metal region inside the masks is combined with sharp peaks at the bottom edges of the grating (y = 0). The intensity peaks are not present in the field transmitted in the grating and hence it can be assumed that they are caused by the step change in material properties at the boundary between the grating and the photoresist. This feature quickly reduces, due to the evanescent decay of the high spatial frequencies so that by 10 nm beneath the grating a steep sided cross section remains, which slowly reduces in contrast as the distance from the grating increases.

The absorbance grating case (Fig 6.11b) shows some important differences in the propagation beneath the grating when compared with the metal grating. Although the sharp peaks are again seen at the bottom edges of the grating these are no longer as pronounced, nor do they extend above the internal grating intensity levels as they did in the metal grating case, hence there is an initial loss of contrast moving from the grating into the resist. This effect, combined with the lower overall magnitude leads to a less steep profile and to a faster reduction in the contrast in the transmitted intensity profiles. Importantly, however, the light intensity remains well confined beneath the lower refractive index material until the region of 20 - 40 nm beneath the grating.

In comparing the numerical FEM results and the analytical results it is clear that the effects caused by the sharp material change at the base of the grating cannot be over-looked in order to get a good approximation; Fig 6.12a shows large differences between the FEM results and those extrapolated using the analytical techniques. It seems that, in particular, it is the formation of the sharp peaks at the edges of the grating which cause improvement in the waveform's propagation as these peaks help to emphasise the region with improved transmission. If, instead of the Rytov approximation, the waveform at the base of the grating calculated by the FEM method is used, a much improved agreement is seen between the two techniques, Fig 6.12b. As expected, the remaining error is likely due to high frequency components in the signal being lost in the Fourier transform and approximations in the FEM profiles due to the large peaks at the base of the grating. This displays the loss of accuracy through necessary assumptions made using analytical methods to consider the propagation of Maxwell's equations.

6.5.3 CONTRAST BENEATH GRATINGS

To further understand of the behaviour of the light after transmission through gratings the contrast (V) and depth of focus (DOF) were calculated following McNab [McNab 2000], as they provide simple measurements of the performance of regular, periodic gratings in defining features in an optical lithography system. In Fig 6.13 the contrast of the horizontal cross section is calculated for the first 100 nm beneath example gratings:

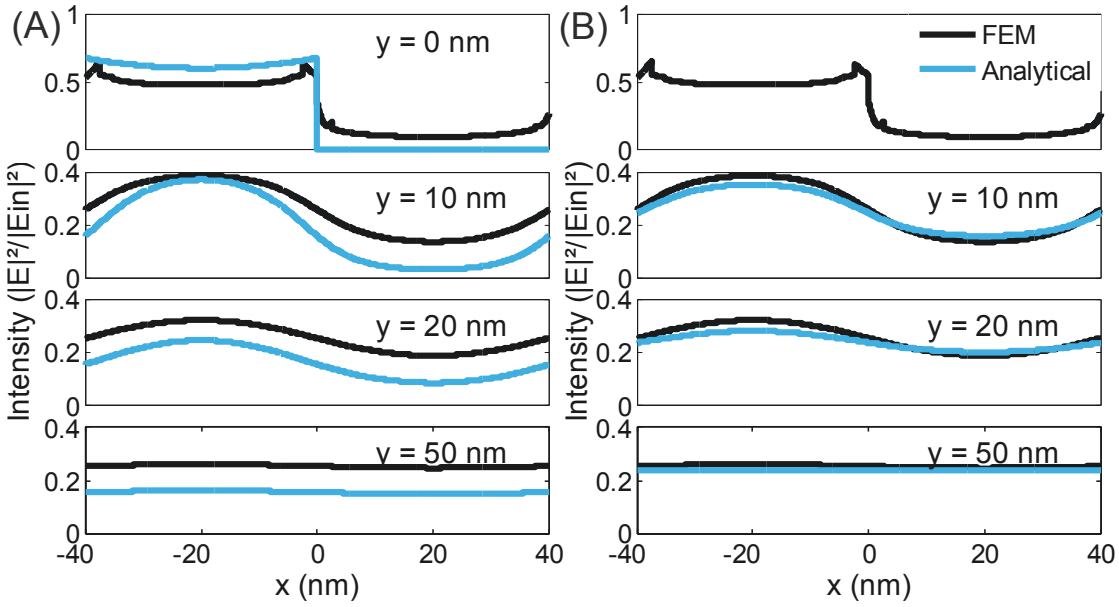

Figure 6.12 Comparison of FEM and analytical methods for modeling the propagation of electromagnetic fields beneath waveforms; (a) is based on a Rytov grating and (b) on the FEM calculated field profile at the base of the grating.

metal gratings and absorbance-modulated gratings are compared, and plots for two different grating periods (200 nm and 20 nm are shown). These show that absorbance gratings demonstrate much better contrast for TM polarised light than for TE polarisation at these sub-wavelength dimensions but neither polarisation is as effective as the metal gratings. As the grating period reduces from 200 nm (Fig 6.13a) to 20 nm (Fig 6.13b) there is noticeable degradation of the initial TE contrast (TE contrast is effectively zero for the 20 nm period grating), whereas the initial TM contrast remains reasonably constant; but, as expected, there is a large shortening of the high contrast region. This shortening is due to the presence of higher spatial frequencies in the evanescent (sub-wavelength) modes that are transmitted as the period reduces, which have correspondingly shorter evanescent decay lengths in the underlying resist.

In the DOF plot shown in Fig 6.14, which measures the distance into the resist at which the contrast falls below 0.5 for the absorbance-modulated gratings, the shortening of the

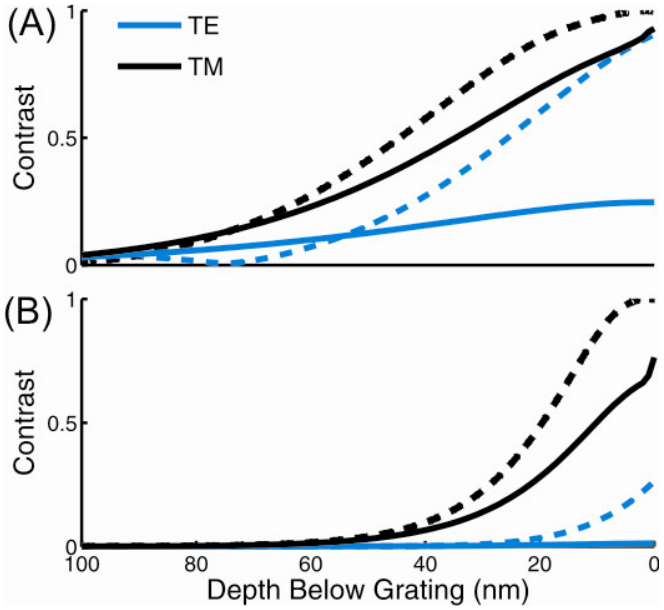

Figure 6.13 Contrast as a function of depth below the grating for (a) 200 nm and (b) 20 nm period gratings. Solid and dashed lines represent absorbing and metal gratings respectively.

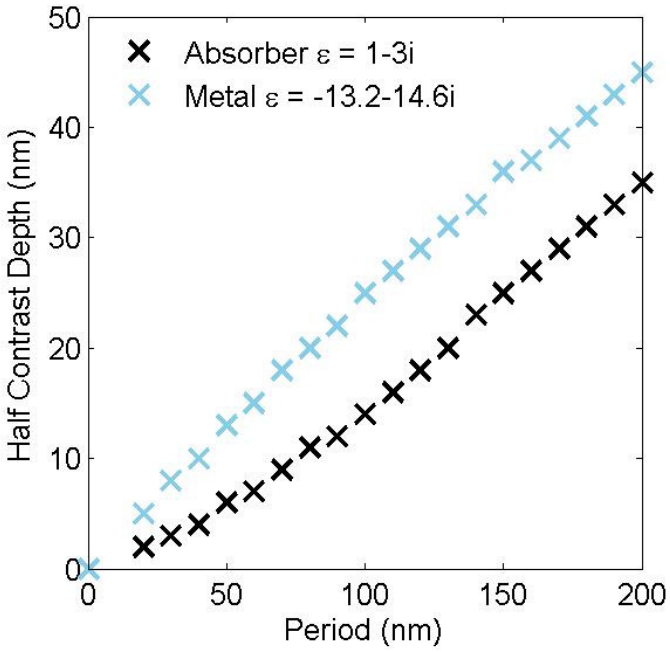

Figure 6.14 Plot of the contrast depth of focus FEM simulations of 50% duty cycle absorbance-modulated and metal gratings as the period is increased from 0 to 200 nm.

high contrast region is clearly demonstrated. This means that if there was going to be an attempt to transfer this image into a resist layer then the effective depth of that resist would need to be on the order of 5 nm, less than half of that required in the metal case. This can partially be explained by the poor nulls which are achieved behind the opaque regions in exposures using absorbance gratings, due to there being propagation, albeit attenuated, through the opaque sections of the gratings and offsetting for this base intensity may improve the measure. However the performance is still poor, as is the case for all near-field systems due to the exponential decay of the signal and this is a problem that must be addressed in order to allow the possibility of useable sub-diffraction limited exposures. In order to be feasible this type of system will require some form of contrast enhancement and propagation in the resist layer. There have been some developments in this area, for example a plasmonic reflector layer may be used, and this matter is explored in depth in Chapter 7.

In conclusion the nature of sub-wavelength absorbance gratings has been examined and the response is similar to that of similar sized metallic gratings, although with much lower transmittance efficiency. Inside the grating there is markedly better transmittance of TM polarised light due to interactions between the in-plane electric field and the grating edges. This is continued beneath the grating where TM polarised light propagates much further than similarly guided TE polarised light. This clearly suggests that absorbance gratings using TM polarised light are more feasible for lithographic system in the near-field, but contrast enhancement may be needed to ensure adequate DOF for fabrication.

6.6 LIGHT PROFILES BENEATH AMOL GRATINGS

The study of transmission through absorbance gratings may be extended to include gratings created through AMOL or related techniques. Here a full FEM model of the AMOL system is used to investigate the impacts of polarisation on transmission through absorbance-modulated apertures. This introduces further difficulties because the transmission of light through the aperture and the size and structure of the aperture are both

dependent on the incident intensity in both wavelengths, with scalar analytical modeling indicating that the ultimate resolution is determined by the ratio of the incident intensities, $I(\lambda_2)/I(\lambda_1)$ [Menon 2007]. The scalar results, which have been validated against the FEM model for large aperture systems (Section 6.3) are compared with full vector simulations for narrow apertures, together with a study of how polarization affects contrast and DOF.

The simulations involved a standing wave (300 nm period) in λ_2 at 532 nm and a plane wave of λ_1 at 400 nm incident into a 200 nm thick AML placed on a 400 nm thick resist layer (representing resist plus bottom anti-reflection layers, as exposure into a 400 nm thick resist layer is not expected). TE polarization was used for the standing wave in λ_2 in all cases, as otherwise a deep null cannot be formed, as shown in Fig 6.15b. This may be explained by considering the field diagrams of the two situations (Fig 6.15a) in which the TE case will always lead to complete overlap of the electric field vectors, however the TM case allows partial overlap and creates a residual field, meaning that the minimum will fluctuate and a deep null cannot be achieved at all angles.

With the intensity and polarisation of the standing wave at λ_2 thus fixed the effects of changing the intensity and polarization of the plane wave at λ_1 were studied. The resist was modelled with refractive index of $n_R = 1.6 - 0.05i$. The AML had a refractive index which varied between $n_{1,o} = 1.6 - 1.6i$ in the opaque state to $n_{1,t} = 1.6 - 0.2i$ in the transparent state for λ_1 and $n_2 = 1.6 - 0.05i$ in both states for λ_2; the transition between these states being based upon competing reactions driven by the intensities of λ_1 and λ_2 [Andrew 2009]. The quantum efficiencies used for λ_1 were $\phi_{1AB} = 1.4\times10^{-5}$ and $\phi_{1BA} = 3\times10^{-9}$ for the forward and reverse reactions respectively and for λ_2 $\phi_{2BA} = 3.5\times10^{-5}$ and $\phi_{2AB} = 4\times10^{-9}$ were used; the thermal rate constant was $k_{BA} = 2\times10^{-8}s^{-1}$.

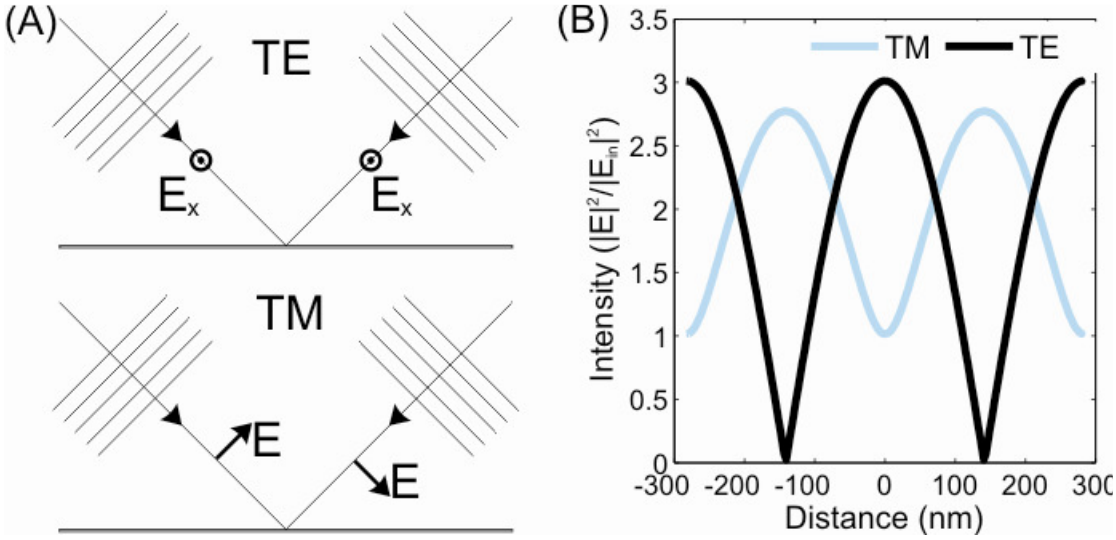

Figure 6.15 Comparison of standing waves formed by TE and TM polarisations, with (a) showing electric field diagram and (b) demonstrating the difference in intensity profile when the angle is 20^0.

As shown in Figs 6.16 and 6.17 for TE and TM polarised λ_1 respectively, it was possible to create patterns in the absorbance region such that a very narrow aperture was created at the base of the AML for either polarization of λ_1. This does not, however allow the transmission of similar sized beam at λ_1 because the shape of the absorbance aperture (narrowing with depth) and the transmittance of significant intensities of λ_1 through the partially-opaque regions in the AML enables the transmission of a beam wider than the measured aperture, for both TE and TM polarisation. The resulting intensity profiles in the resist layers are significantly different for the two polarizations, with the TE profile being broader than that for TM illumination, as expected from the study of idealized grating structures in the previous sections (Figs 6.18 and 6.19).

It is further noted that although the AML aperture shapes are very similar the confinement of the TE illumination is poor and, as will be discussed later, this lack of confinement leads to the inability of the AMOL system to create narrow apertures using TE polarised λ_1. It can also be seen in Fig 6.16 that there is significant pattern inversion

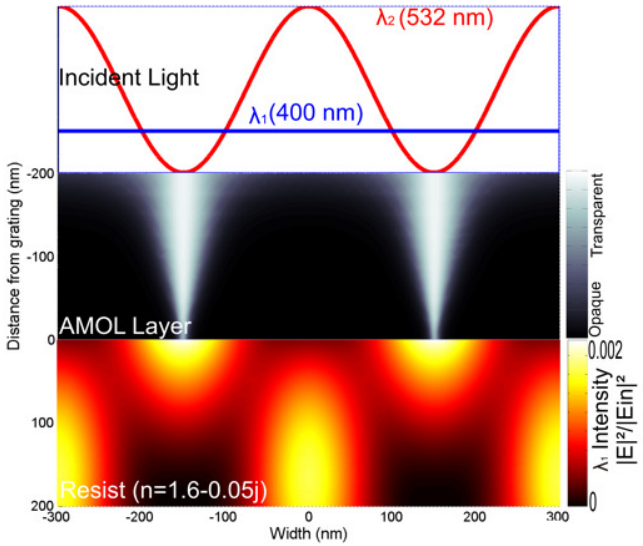

Figure 6.16 FEM simulation of TE polarized $\boldsymbol{\lambda_1}$ light showing the absorbance in the AML (above the line at $\boldsymbol{y = 0}$) and the light intensity propagated into the resist (below the line at $\boldsymbol{y = 0}$) at an input intensity ratio $\boldsymbol{I(\lambda_2)/I(\lambda_1) = 1.35}$. The standing-wave and plane-wave illumination schemes at $\boldsymbol{\lambda_2}$ and $\boldsymbol{\lambda_1}$, respectively, are shown schematically at the top of the figure.

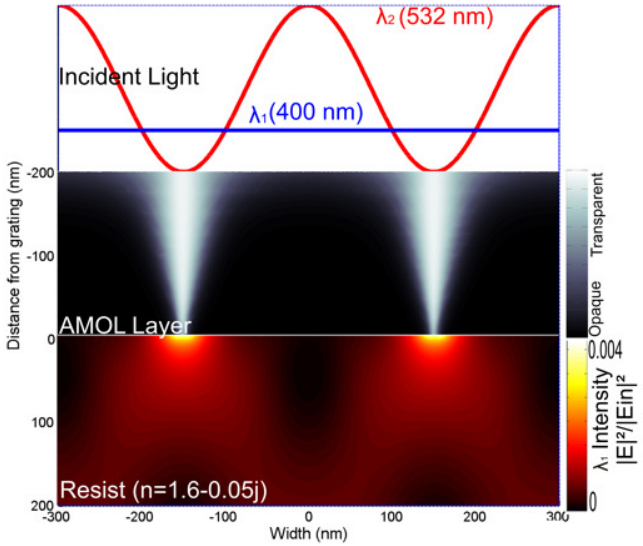

Figure 6.17 FEM simulation of TM polarized λ_1 light showing the absorbance in the AML (above the line at $y = 0$) and the light intensity propagated into the resist (below the line at $y = 0$) at an input intensity ratio $I(\lambda_2)/I(\lambda_1) = 1.35$. The standing-wave and plane-wave illumination schemes at λ_2 and λ_1, respectively, are shown schematically at the top of the figure.

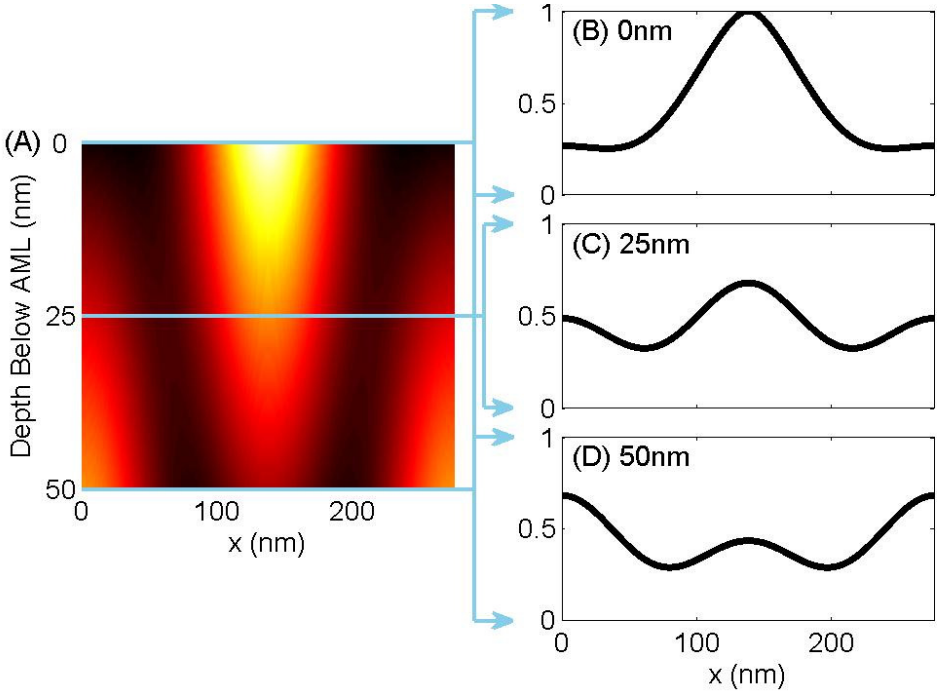

Figure 6.18 (a) $\lambda_1$intensity in the first 50 nm of resist for TE polarised light with an input intensity ratio $I(\lambda_2)/I(\lambda_1) = 1.35$. Intensity profiles are shown at (b) 0 nm, (c) 25 nm and (d) 50 nm below the AML.

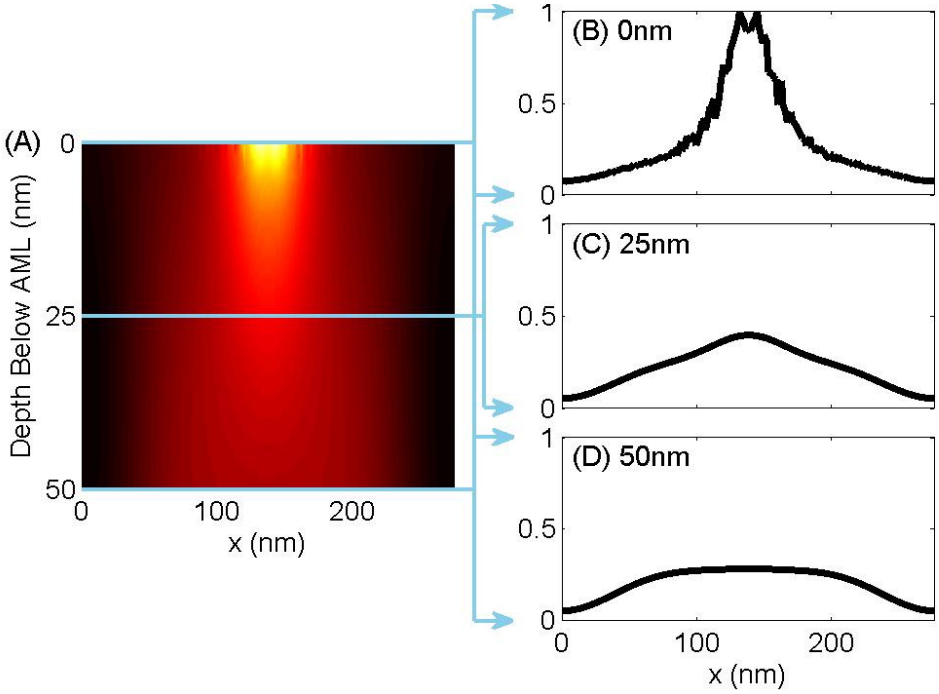

Figure 6.19 (a) λ_1 intensity in the first 50 nm of resist for TM polarised light with an input intensity ratio $I(\lambda_2)/I(\lambda_1) = 1.35$. Intensity profiles are shown at (b) 0 nm, (c) 25 nm and (d) 50 nm below the AML.

(Talbot effect) close to the AML/resist interface for TE illumination, which is highly undesirable because this leads to a reversal of the intensity profile and hence complete loss of the image. This is clearly shown by the intensity profiles in Fig 6.19 in which the central peak is quickly obscured by the increasing intensity of the sidelobes. This effect was not present in the previous study of idealized gratings as these concentrated on sub-half-wavelength period gratings; but it is evident with the 300-nm grating period used here, chosen to approximate the apertures used in the previous scalar analysis of the AMOL process [Menon 2006]. The AMOL system using TM polarised light (Figs 6.16 and 6.18) also shows some pattern inversion, however it is much weaker and further from the AMOL layer due to the narrowness of the intensity waveform at the AML/resist interface. It is also noted that the intensity maximum in the resist is greater with TM incident light.

For the AMOL process the period of the grating at λ_2 is not the resolution-determining factor, as multiple exposures will be used to create dense patterns—rather it is the linewidth of the apertures in the AML layer, and hence the intensity profiles formed beneath them, which will ultimately limit the resolution. This was studied as a function of the intensity ratio $I(\lambda_2)/I(\lambda_1)$ using the systems described in section 6.6 and shown in Figs. 6.16 and 6.17. The FWHM of the AML absorbance aperture, (Fig 6.20a) shows a decreasing trend with $I(\lambda_2)/I(\lambda_1)$ whereas the FWHMs of the intensity profiles in λ_1 just beneath the AML reach a minimum before increasing again (Fig 6.20b). This is contrary to the monotonic decrease predicted by the scalar modeling of [Menon 2007] and can be explained by considering the transmission of λ_1 through the absorbance aperture; when the aperture reaches a narrow size at which there is only a small difference between the amount of light able to pass through the aperture and the amount of light able to pass through the opaque region surrounding it and light cannot be arbitrarily confined to a narrow aperture in an absorbance modulated medium, hence the transmitted peak broadens and the λ_1 FWHM increases. The minimum FWHM achievable is affected by the interplay of factors including the system geometry, light polarizations, parameters of the AML (especially the thermal constant and absorbance range) and the absolute input intensities.

The effect of polarisation can also be seen in Fig 6.20 where the use of TM polarised λ_1 is able to give a smaller FWHM than a similar TE polarised incident beam for small aperture widths. This allows the generation of a 50 nm FWHM for TM polarised λ_1 compared to a minimum of 95 nm FWHM for TE polarised λ_1, thus the TM polarisation is allowing far better confinement in the photoresist. Investigating the propagation of λ_1 in the photoresist beneath the AML reveals further differences between the TE and TM propagation. Figure 6.21 shows the contrast and DOF performance of each polarisation; for TM polarisation the contrast remains high as the aperture size is decreased, which is due to both a deeper null and higher peak intensity in the intensity profile at the AML/resist interface compared to the TE-polarisation case.

The decrease of contrast with increasing input intensity ratio is also much slower for the TM polarization and the DOF also improves. For a λ_1 transmission FWHM of 100 nm the DOF of the TM polarisation is ~90 nm as compared to ~40 nm for the TE polarisation; the higher DOF of the TM polarisation demonstrates that this is transmitted more

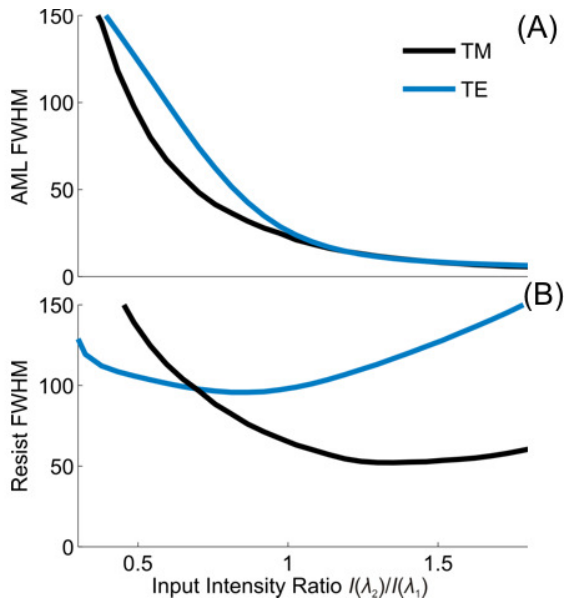

Figure 6.20 The FWHM of (a) the AMOL aperture and (b) the λ_1 intensity profile at the base of the AML in the FEM simulation as the input intensity ratio $I(\lambda_2)/I(\lambda_1)$ is varied to change the aperture size.

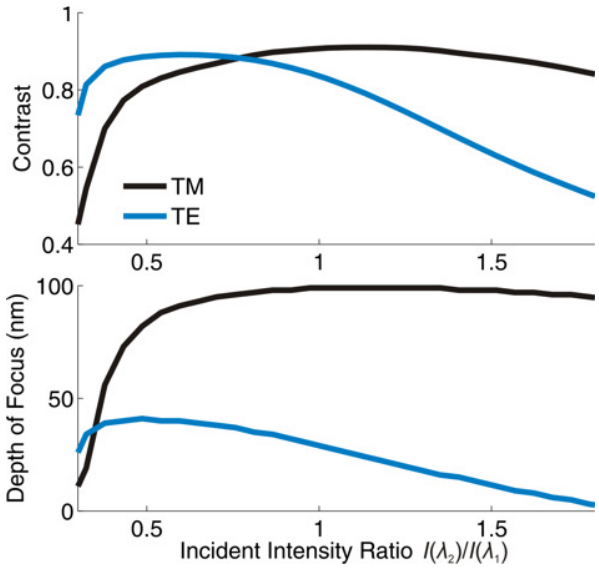

Figure 6.21 The (a) contrast and (b) DOF of TM and TE polarised λ_1 as the input intensity ratio $I(\lambda_2)/I(\lambda_1)$ is varied to change the aperture size.

effectively into the photoresist layer for lithography use. The importance to any lithographical process of transmitting a high contrast image combined with the results discussed above suggest strongly that a TM polarised λ_1 transmission will outperform a TE polarised incident field for sub-wavelength apertures.

6.7 EFFECT OF CHANGING PERIOD

It is also informative to investigate the effect of the period of the λ_2 standing wave in the creation of the intensity waveform in the resist. The FEM simulation is set up to model a Lloyd's mirror which enables a minimum period of $\lambda_2/2$, however smaller periods can be achieved, in the model, by reducing the designed λ_2 without changing how it interacts with the photochromic layer and therefore without influence on the results; this allows exploration of the effect of reducing the AMOL system period. Fig 6.22 shows a graph of the results from simulations between 50 and 300 nm for TE and TM polarisations using the intensity ratio which gave the smallest FWHM for the 300nm grating ($I(\lambda_2)/I(\lambda_1)$ =1.35).

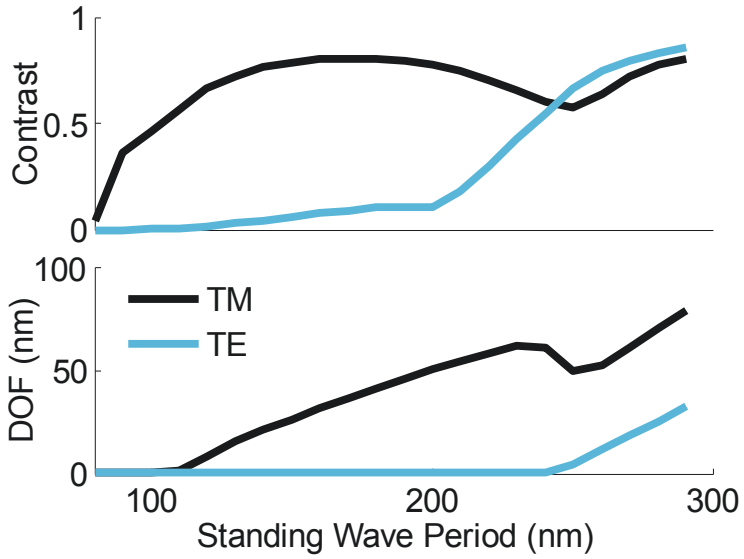

Figure 6.22 Comparison of the (a) contrast and (b) DOF for TE and TM polarised transmission performance as the period of the λ_2 standing wave in the AMOL system is changed.

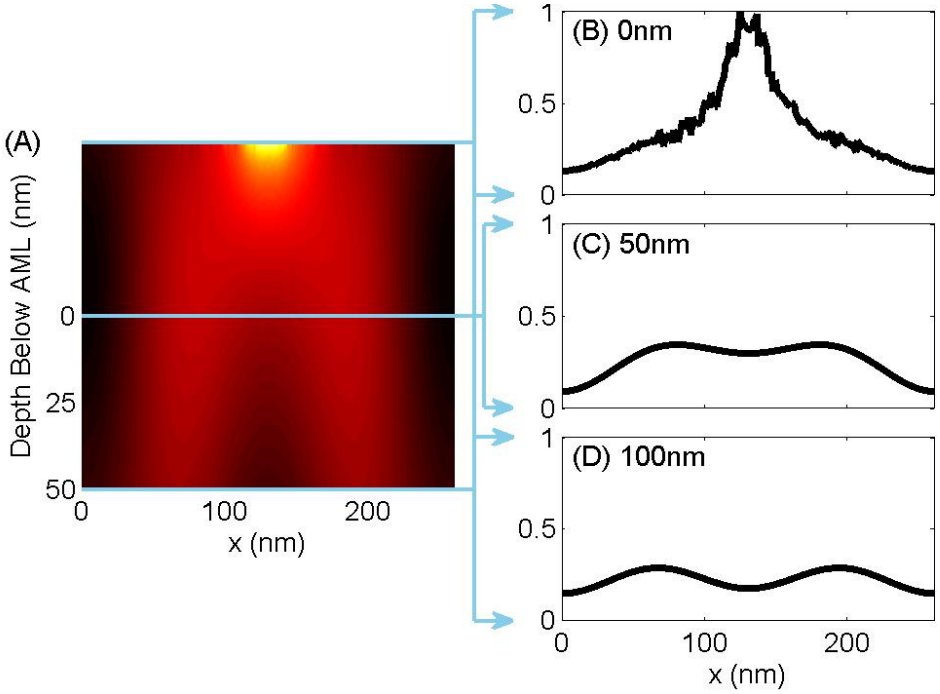

Figure 6.23 (a) λ_1 intensity in the first 50 nm of resist for TM polarised light with intensity profiles shown at (b) 0 nm, (c) 25 nm and (d) 50 nm below the AML demonstrating a frequency doubling effect.

It can be seen that the TM polarisation gives superior contrast for periods beneath 250 nm and larger DOF for all periods measured periods. A DOF of above 50 nm was achievable with a 200 nm period standing wave in λ_2. For both contrast and DOF an interesting effect is seen in the graph near a period of 260 nm. This is caused by a frequency doubling effect occurring at approximately the half wavelength dimension (400 nm free-space wavelength, medium refractive index ~1.6), which causes the two separate peaks to quickly form in the resist rather than a single peak (Fig 6.23); this leads to a wider peak and an increase in high order spatial frequencies, hence giving shorter decay lengths.

Figure 6.24 demonstrates the change in λ_1 intensity profiles as the period increases, demonstrating clearly the improved performance of TM polarisation at smaller periods and showing the reduction of intensity passing through the gratings, but with narrower and steeper peaks. Figure 6.24c demonstrates that at larger periods and aperture sizes the performance of the TE polarisation may exceed TM, although even at larger periods if a narrow aperture is present TM polarised λ_1 would be expected be more confined to the aperture than TE polarised. This improved confinement is negated by the increased intensity and better intensity profile shape of the TE polarised λ_1.

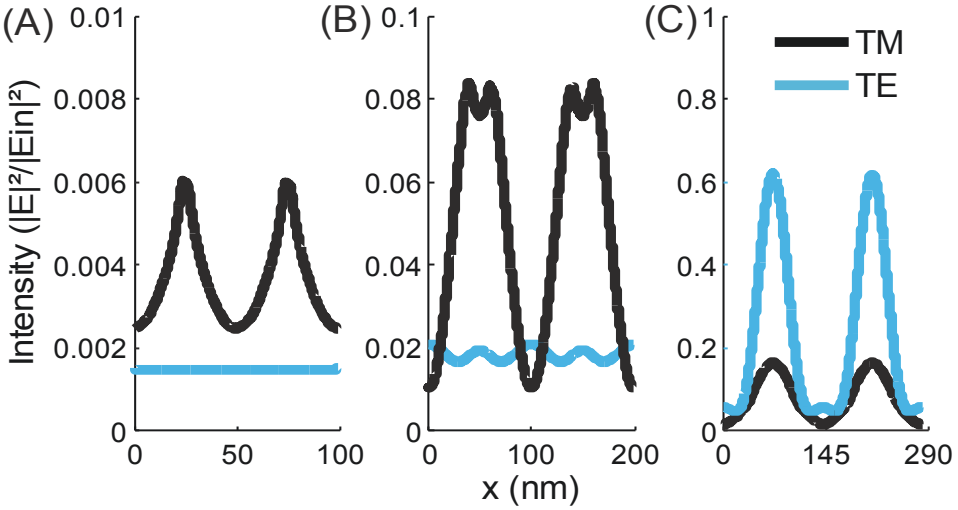

Figure 6.24 Comparison of the intensity waveforms produced by TM and TE polarised λ_1 when the period of the λ_2 standing wave is (a) 100 nm, (b) 200 nm and (c) 290 nm.

6.8 EFFECT OF CHANGING DUTY CYCLE

The duty cycle was shown to have an effect on the grating model so here a similar analysis is made of the AMOL system. The duty cycle of the AMOL system can be controlled by the intensity of the λ_2 standing wave as a larger intensity will narrow the gap through which λ_1 can penetrate (changing the intensity ratio). To place a quantitative value on the duty cycle the FWHM of the intensity profile in the resist was used, with the results shown in Fig 6.25a. A large reduction in the intensity is seen as the duty cycle is reduced as the AML becomes more absorbing and the transition from transparent to opaque regions more abrupt, also the top of the profile becomes more square with steeper sides as the light is more confined in the transparent region. Alternatively the FWHM of the absorbance profile at the bottom of the AML may be used; this is smaller than the FWHM of the resist layer as λ_1 will not be perfectly confined to the transparent regions. Figure 6.25b demonstrates this and the results are similar to those of Fig 6.25a.

6.9 FORMATION OF NARROW APERTURES

The preceding results have used material parameters that have been chosen so as to be able to create and characterise apertures much narrower than the λ_1 wavelength. Howev-

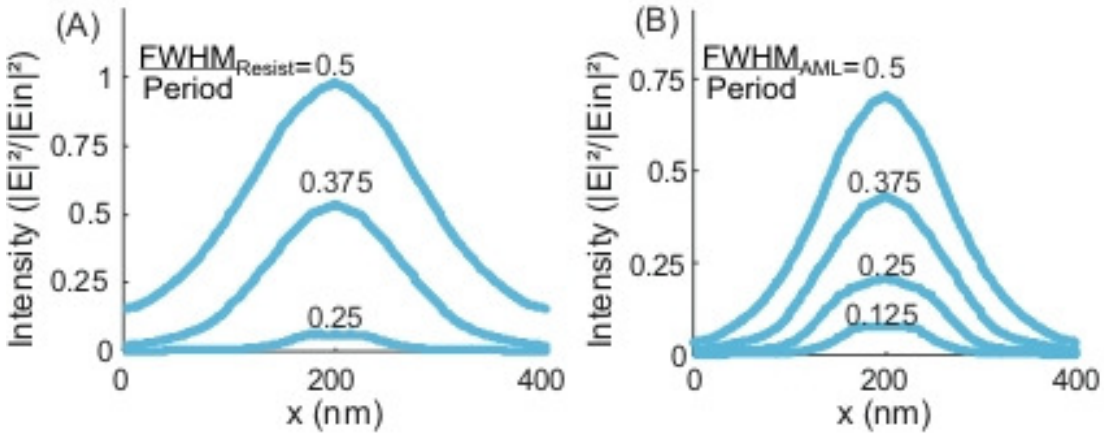

Figure 6.25 Showing the effect of reducing the duty cycle for TM polarised light, as measured by the FWHM of the (a) resist intensity waveform and the (b) base of the AML, for a 400 nm AMOL system.

er, the material parameters of the photochromic layer have a large effect on the ability of the AMOL system to form these narrow apertures. If suitable absorbance modulation cannot be achieved, or the distinction between the opaque and transparent regions is not large enough it can become difficult to create the desired narrow apertures. This is expected from the results in Section 0 where the field profiles for a range of absorbance gratings were compared, showing reduced performance with reduced absorbance range. Here results (Figs 6.26 and 6.27) are presented looking at the effects of the concentration of photochromes (ρ) and the thermal constant (k_{nBA}) using the FEM model with the parameter values described in Section 5.5.1, an intensity ratio $I(\lambda_2)/I(\lambda_1)$ of 5 was used, however the results generalise.

When the concentration of photochromes is increased the maximum absorbance in the layer increases, due to there being more absorbing particles; this reduces the efficiency of the grating in transmitting λ_1 but also helps to ensure that the opaque regions are more effective barriers. As shown in Fig 6.26 this leads to an increase in contrast, as $I_{\min}$ has been significantly reduced, this reduced transmission of λ_1 through the opaque regions also leads to a narrower FWHM as the transition from opaque to transparent becomes more abrupt but the transparent region can still transmit a suitable intensity profile until the overall absorbance becomes too strong. The minimum FWHM will occur between these two points, as shown in Fig 6.26 where the minimum FWHM of 24nm occurs at ~1.2M (as opposed to the ~0.4M used in experimental work, which is the maximum concentration of PMEA achievable). The drawback to increasing the chromophore density is the increased absorption, this reduces the efficiency of the AMOL system, so that for the case of the TE polarisation in Fig 6.26 when the FWHM has been reduced to below 100 nm there is a very large reduction in the maximum intensity incident on the resist.

The second simulations investigated how a change in the thermal constant effected the formation of a narrow aperture. Figure 6.27 shows the thermal constant having a large effect until any further improvement becomes limited below a thermal constant rate of

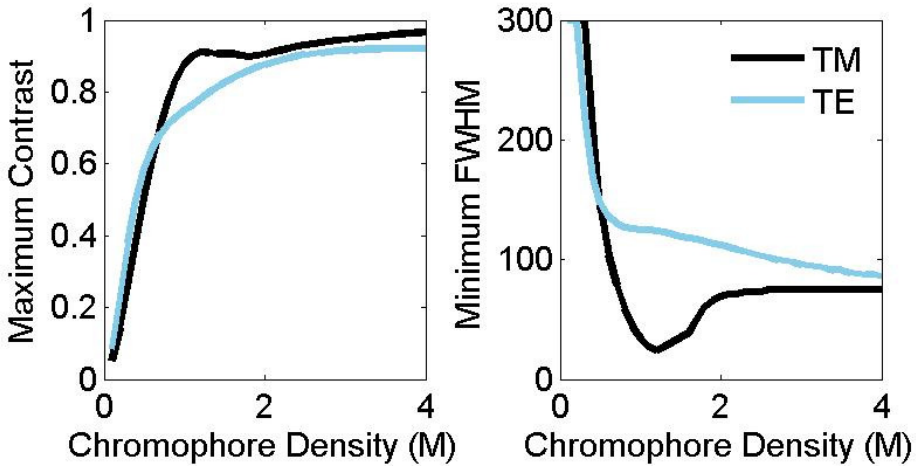

Figure 6.26 (a) Maximum Contrast and (b) Minimum FWHM achieved in an AMOL system with changing chromophore density. A minimum FWHM of 24nm is achieved (thermal constant 8.5×10^{-9} to remove any thermal effect).

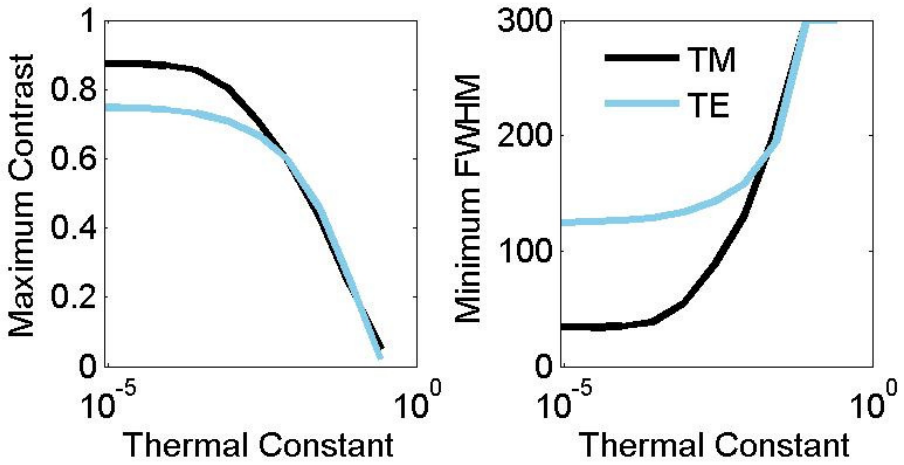

Figure 6.27 (a) Maximum Contrast and (b) Minimum FWHM achieved in an AMOL system with changing thermal constant density. Limited further improvement in performance is seen when the thermal constant is reduced below $2 \times 10^{-4}\ s^{-1}$.

$\sim 2 \times 10^{-4}\ s^{-1}$. This rate is much less than that used in the earliest work, $\sim 2 \times 10^{-3}\ s^{-1}$ [Menon 2007] and explains why better results were found using a compound with thermal constant $< 3 \times 10^{-6}\ s^{-1}$ [Andrew 2009]. This effect of thermal constant was discussed using a simple model by Andrew who showed that a large thermal constant limits the level of transparency achievable for the aperture, hence reducing the peak intensity in the resist; there is also less reaction against λ_1 making the AML more

transparent [Andrew 2009]. The full FEM model also demonstrated that even with no thermal rate constant other material parameters, such as photochrome density, will limit resolution, shown by the lack of further improvement as the thermal constant is reduced below $\sim 2 \times 10^{-4}\ s^{-1}$. In all cases improved performance was seen for the TM polarisation, with TE polarised λ_1 either unable to create narrow apertures, or only shown to do so with very limited transmitted intensity.

6.10 CONCLUSIONS

Analytical analysis and FEM simulations have been carried out for the first time to explore the effects of introducing polarised light into sub-wavelength absorbance-modulated gratings. These demonstrate the importance of considering the polarisation of light being used and show that TM polarisation at λ_1 is better transmitted and better confined through such geometries. The comparisons made to metal and dielectric gratings show reduced efficiency of transmission and some loss in contrast for both polarisations, however there is still considerable contrast achieved and reasonable propagation of the transmitted light into the photoresist to depths approaching 40 nm for gratings with sub-100 nm periods.

The FEM modeling of the AMOL process also provided an example of the importance of polarisation as the TM polarised light gave more effective light intensity patterns in the underlying photoresist than the TE polarised light, which demonstrated reduced contrast and DOF. Thus the introduction of TM polarised λ_1 to the AMOL system may enable improved performance to be achieved compared to the already impressive experimental results reported using TE polarization at both wavelengths [Andrew 2009]. The importance of material and operational parameters including the period, duty-cycle, thermal constant and photochromes concentration to an AMOL system creating narrow TE and TM apertures has also been shown. It has been demonstrated that, given suitable material parameters an AMOL system is capable of sub-wavelength exposures, however it was also demonstrated that these exposures are poorly transmitted into resist, losing contrast within the first 10 nm for 50 nm grating exposures. To allow AMOL to allow

reasonably consistent fabrication at these dimensions large improvements are needed to this DOF, including the introduction of techniques such as surface plasmons.

Chapter 7

PLASMONIC REFLECTOR LAYERS

7.1 MOTIVATION

It is highly desirable to improve the ability of AMOL systems to transmit features deeper into an underlying resist, with intensity, contrast and image confinement maintained; this allows for improved process latitude and improved reliability in manufacturing. The decay in contrast with depth is particularly severe for the basic AMOL process modeled previously because the imaging is taking place in the near-field; this contains the high order spatial information but decays exponentially with distance from the AML.

Similar problems faced previous work in near field systems [Fang 2003, Blaikie 2002]. Here particular note is taken of previous work in which the performance of a near-field optical lithography system using metal masks placed in conformal contact with photoresist enhanced near field optical lithography (ENFOL) [Blaikie 2002, Alkaisi 1999] was considerably improved through the introduction of a plasmonic layer [Blaikie 2004] placed beneath the resist. This introduced layer acts as a reflective layer which enhances the confinement and transmission of the light intensity profile in the resist [Arnold 2007, Arnold 2006]. The question posed here is to see if this can also be effective in improving contrast and depth of focus (DOF) in AMOL, or do the reflections from an underlying plasmonic layer disrupt the equilibrium between the competing light sources in the AML so that any gain is diminished?

In this chapter a plasmonic reflector layer (PRL) is introduced to the previously studied AMOL system (Fig 7.1) and the effects on the system performance and the transmission into an underlying photoresist are investigated. Particular importance is placed on the

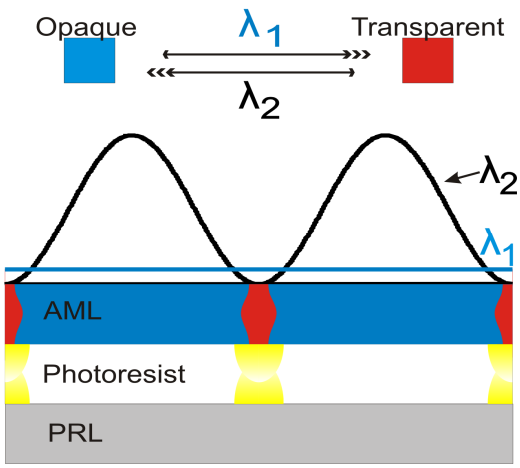

Figure 7.1 Schematic of the AMOL process being modeled including plasmonic reflector layer (PRL).

ability of the PRL to extend the DOF of the AMOL lithographic system whilst maintaining deep sub-wavelength resolution. The interaction of an absorbance mask with a plasmonic system is an area which had not previously been explored.

7.2 DEPTH OF FOCUS

As mentioned in Section 2.3.4 the DOF of a lithography system is an important system parameter that measures the depth of photoresist into which an image may be effectively transmitted, it can be defined as the "range of focus that can be tolerated, before the image quality is degraded beyond usefulness" [Mack 2007]. A general expression for DOF of a projection system was given in Eq 1.2. The requirement for a reasonable DOF places constraints on the lens/substrate distance, control of focus in the exposure tool and the thickness and smoothness of the resist. For example, the 22 nm node calls for resist depths < 66 nm [ITRS 2009], which approaches those achieved in near-field imaging systems

In the case of evanescent exposures or near-field systems the mask and resist layer are in close or conformal contact and are the same size so no focusing takes place, however the fields are non-propagating in the resist. Hence an analogous measure of DOF is made which measures the propagation of the image into the photoresist before the image

quality is degraded beyond “usefulness”. It is important to increase this DOF for similar reasons to having DOF for projection lithography, as working with thinner resists increases the difficultly of later manufacturing stages.

7.3 PLASMONIC REFLECTOR LAYERS

It was noted by McNab that an interesting effect, the enhancement of the image in the region above a planar superlens, was occurring in an evanescent exposure; this effect was termed surface plasmon enhanced contact lithography (SPECL) [McNab 2004]. This was in disagreement with the conventional wisdom which suggested that performance of a resist is maximized with a non-reflecting substrate (for the case of propagating exposures this removes any standing wave effects). The reported results for using silver as a plasmonic reflector (Fig 7.2) demonstrated clear improvement in the maintenance of linewidth with depth into a resist sandwiched between the mask and the planar silver layer when compared to the perfectly matched case.

A more thorough exploration of the SPECL effect was reported by Arnold [Arnold 2006] in which some of the parameter space affecting the imaging performance was explored. The principles of the SPECL effect are interpreted through the coupling of the electric fields generated by the mask to surface plasmons (SPs) on the surface of the PRL; the improved fields can then be explained by a consideration of the interference of these two fields, with partial compensation for any phase decay due to the variation of reflection with spatial frequency. Arnold used a figure of merit for the lithographical performance of

$$Figure\ of\ Merit = Contrast \times DOF^2, \tag{7.1}$$

to demonstrate, through FEM modeling of a contact lithography system with a metal mask, that for small distances there was improvement up to a factor of ten when a silver PRL was added. The permittivity required of the PRL was also reported, showing the ability of silver to produce improved performance in an approximate range of 300-400 nm. It was shown that the geometry of the grating, in particular the opaque portion of the grating period (grating absorber width) had a noticeable effect on the performance

of the SPECL system; smaller grating absorber widths required a closer PRL, which may be explained by the difficulties in achieving a balance of the high spatial frequency components. Figure 7.3 shows a replication of the metal grating system discussed by Arnold [Arnold 2006] in COMSOL, with the resulting graphics appearing to be in agreement with the published results.

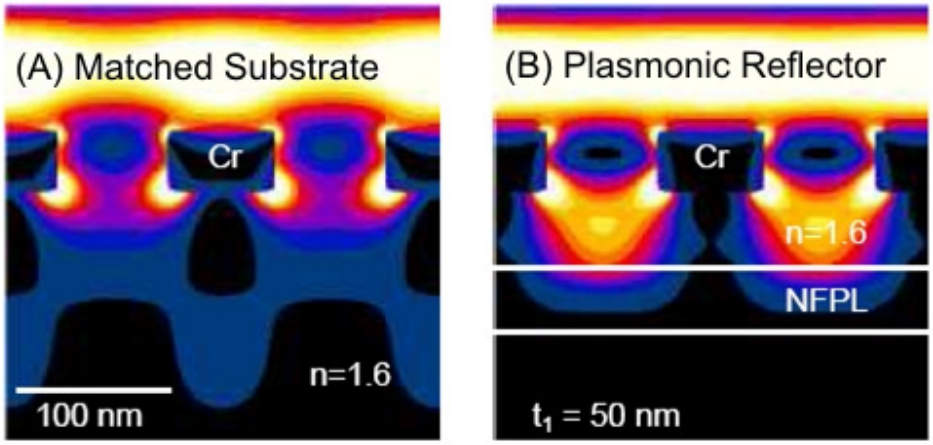

Figure 7.2 Comparison of an ENFOL system with and without a near-field plasmonic layer (NFPL) demonstrating improved confinement in resist. Intensity profiles for 140 nm period Cr gratings illuminated at 365 nm with (a) an index matched substrate and (b) a silver NFPL. [McNab 2004]

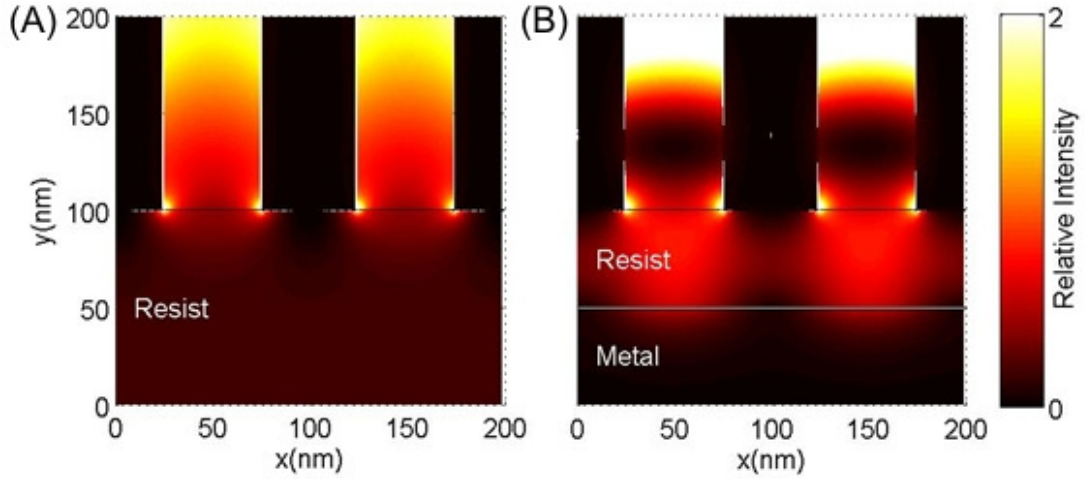

Figure 7.3 COMSOL simulation of Photoresist exposures for rectangular metal gratings without (a) and with (b) a plasmonic reflector layer. The gratings are 50% duty-cycle, 100 nm period gratings, modeled at 400 nm with 50 nm of photoresist ($n = 1.6 - 0.05j$, $\epsilon_r = 2.5575 - 0.16j$) and either a matched layer or plasmonic layer ($\epsilon_r = -2.5575 - 0.16j$), both semi-infinite. The grating material has permittivity of $\epsilon_r = 4.4 - 18j$ and 1.

7.3 PLASMONIC REFLECTOR LAYERS

A second paper by Arnold [Arnold 2007] expanded on SPECL idea and presented a thorough mathematical description of the phenomena, describing the possibility of improvements in sub-wavelength near-field images through the use of plasmonic slabs. It was shown mathematically that the interference between the fields propagating in the photoresist, a forward field from the masking layer and a reflected field from the PRL, may create a more tightly confined near-field image, as opposed to the poor image that would normally be expected due to standing wave effects (Fig 7.4).

The system modeled by Arnold is a periodic absorber placed at a distance d above an imaging region (resist) with a PRL placed directly beneath the photoresist (the direction of propagation is defined as x, and the lateral direction as y). Using this model the fields in the photoresist ($0 < x < d$) are calculated based on a known object field, described as $H(d, y)$, with variation of the photoresist depth (d) and the reflectivity of the reflector layer. It is reported that vertical image uniformity (improved confinement in y) is optimized when the symmetry plane (X) of the fields in the photoresist lies exactly between the mask and the reflector ($X = d/2$); it is however, noted that the dependence of the reflection on spatial frequency suggests perfect image reproduction to be unlikely.

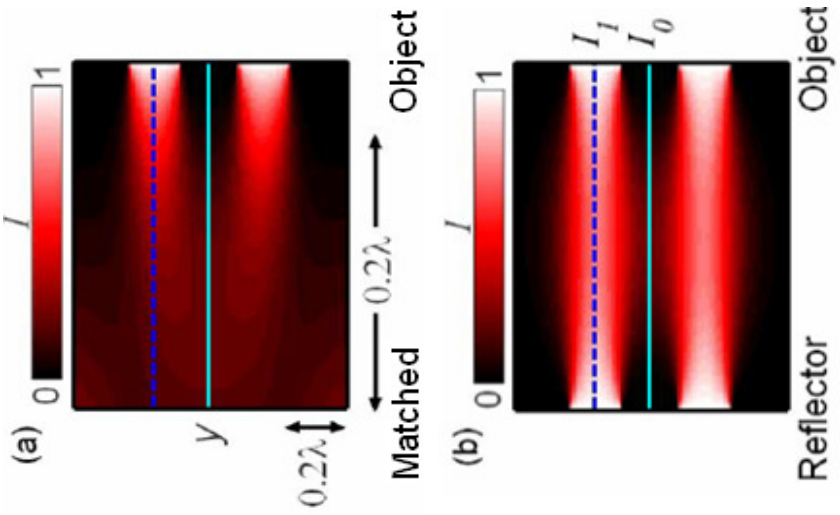

Figure 7.4 A demonstration of the impact of plasmonic reflector layers by Arnold. The image geometry is in two-dimensions, the third being invariant. A hypothetical (but representative) image with no reflection is shown in (a) and with reflection (b). [Arnold 2007]

Arnold also reports that a reflecting layer, as described above may be implemented by a plasmonic metal reflector ($Re\{\varepsilon_r\} < 0$) although the change in reflectance levels may affect the performance of the layer; this matches the previous work which demonstrated the performance of silver in the wavelength range 300-400 nm. The description and explanation of the use of a plasmonic metal as a suitable reflector layer relies on the use of only the complex permittivity of the silver layer, rather than a physical explanation as used previously and this allows the calculation of the most and least suitable cases; it is shown that the case $Re\{\varepsilon_{r,prl}\} = Re\{-\varepsilon_{resist}\}$ becomes the optimum reflectivity at high spatial frequencies. There is some divergence of optimum response for low spatial frequencies; a reasonable compromise for this is shown to be limiting d to a quarter wavelength, although this restricts the resist depth.

It is desirable to avoid high spatial dispersion with a PRL as this will have a negative effect on an image because the different spatial frequencies of the image will lose their phase; for this reason the PRL performs better than a high index reflector (normal reflector/absorber etc). Reducing dispersion also suggests avoiding the surface plasmon region, where

$$\beta = k_0 \sqrt{\frac{\varepsilon_{r,prl}\varepsilon_{resist}}{\varepsilon_{r,prl} + \varepsilon_{resist}}}, \tag{7.2}$$

as behaviour here would be unstable due to rapidly changing reflections depending on spatial frequency. However, so long as the surface plasmon resonance frequency region is avoided improvement is possible, particularly if there are dominant spatial frequencies present.

Comparing the free-space case ($r = 0$) to the presence of a reflector beneath the photo-resist Arnold found a significant reduction in the maximum line spread function (LSF) over the photoresist region for certain photoresist depths [Arnold 2007]. The LSF is a function representing the light intensity field from a single infinitesimal slit, and thus a smaller LSF relates to a narrower image and is related to the DOF. In particular, for the optimum case, $Re\{\varepsilon_{r,prl}\} = Re\{-\varepsilon_{resist}\}$ improvement is possible with thicknesses in the range $\lambda/8 < d < \lambda/4$, outside this range the effect is reduced and possibly detrimen-

tal (where $d > \lambda/4$ this is due to low frequency effects and intensity decay and for $d < \lambda/8$ due to added dispersion due to proximity). In an AMOL system a second wavelength, λ_2 is present; a similar interaction can be expected to occur to the standing wave in λ_2 and this has some relation to the interferometric imaging discussion [Arnold 2007] where two plane waves incident at equal and opposite angles of incidence are shown to be affected by the PRL. Although, as λ_2 is commonly propagating wave in the AMOL system, standing wave features are to be expected from the increased reflection.

In summary, the idea of a PRL has been introduced to improve the DOF, or the transmission of an image into a resist. This is achieved by the high spatial frequency components in the transmitted light intensity (TM polarised) exciting surface plasmons at the photoresist/plasmonic metal boundary. The interference between these surface plasmons and incident light creates a plane of symmetry inside the photoresist which improves the image confinement in the lateral direction; system geometry, spatial frequency dispersion, imperfect reflection and losses in the photoresist all have further effects on the system. The ability of the developed PRL system to improve a two-wavelength AMOL system will be explored here, so that the desirable image produced by AMOL may be transmitted deeper into an underlying resist.

7.4 PRL IN ABSORBANCE SYSTEMS

The central point of difference between the use of PRL in an AMOL system and previous PRL work is that the metal mask has been removed and replaced with a layer of photochromic material (the AML); the interaction of the two incident wavelengths with the photochromic layer creates an absorbance profile and with the correct design of the incident waveforms this can create gratings with narrow apertures.

To begin, a simple system consisting of a rectangular absorbance grating is modeled (Fig 7.5a and b). This confirms the ability of 400 nm wavelength incident light to excite the plasmonic reflector and demonstrates the plasmonic reflector working without a metal mask interacting with the reflections (c.f. 7.3). The resulting improvement in lateral

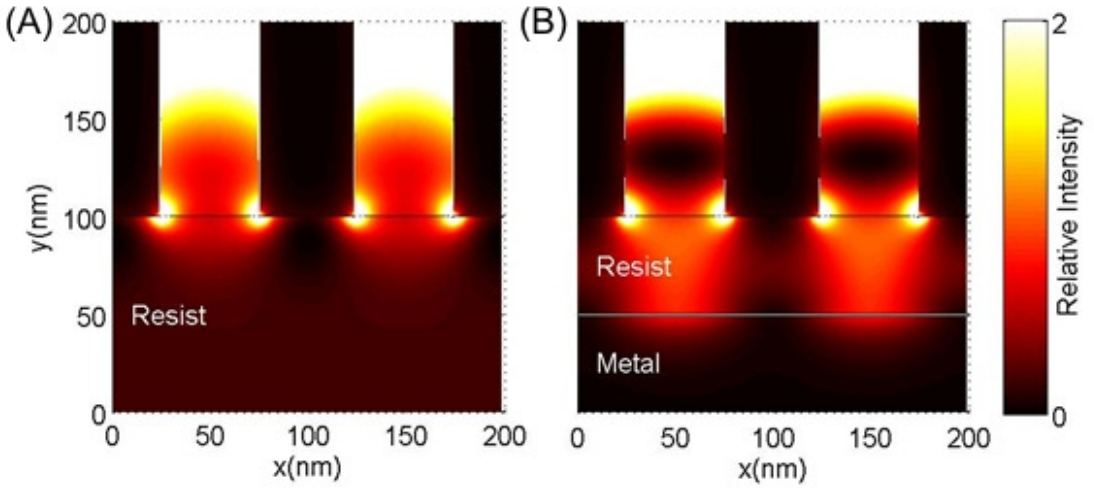

Figure 7.5 Photoresist exposures replicating Fig 7.3 for rectangular absorbance gratings without (a) and with (b) a plasmonic reflector layer. The gratings are 50% duty-cycle, 100 nm period gratings, modeled at 400 nm with 50 nm of photoresist ($n = 1.6 - 0.05j$, $\epsilon_r = 2.5575 - 0.16j$) and either a matched layer or plasmonic layer ($\epsilon_r = -2.5575 - 0.16j$), both semi-infinite. The absorbance grating has permittivity of $\epsilon_r = 1 - 3j$ and 1.

confinement of the intensity waveforms with the introduction of the PRL demonstrates a more confined exposure being possible in an absorbance system; this is due to the change in spatial frequencies present in the intensity profile. The apparent performance of the PRL with this rectangular system varied based upon the geometry used and the permittivity of the PRL, this is likely caused by dispersion in the reflection due to the range of spatial frequencies present. In the AMOL case a very different absorbance aperture shape will be formed and this will affect the transmitted intensity waveforms spatial frequencies and the interaction with the PRL. However these results give confidence that an absorbance type grating can create suitable intensity fields in the resist to allow DOF improvements with the introduction of a PRL.

7.5 IDEAL PRL IN AMOL

Having demonstrated that an absorbance grating is capable of improved DOF through the addition of PRL and the ability of AMOL to create narrow absorbance apertures, the interaction between the AML and a PRL is now studied. The AML is responsive to light

intensity from either the top or bottom surfaces and hence the distinct boundary between mask and photoresist discussed in the previous work [Arnold 2007, McNab 2004] has been removed and reflection from the PRL may act to reduce the ability of the AMOL system to create a narrow aperture. Because in this system λ_1 will be an evanescent field and decay rapidly with distance travelled, any reflections will be limited in their extent thus only shallow resists should see this effect. However the λ_2 standing wave is made from propagating waves and the effect of reflection of this wavelength on system performance is unclear without undertaking a detailed study and analysis.

The AMOL model parameters used for this study are listed in Table 5.1 in Section 5.5.1 except for the photochrome density ($\rho_{conc} = 1$) and thermal constant ($k_{BA} = 8.5 \times 10^{-6}$) which have been adjusted to allow the formation of narrower apertures. A semi-infinite PRL was added at variable depth (d) beneath the AML – this represented a PRL placed on absorbance matched substrate. For the initial simulations an 'ideal' reflector was used where the real part of the electric permittivity was the negative of the photoresist permittivity and the imaginary part constant for both wavelengths, to simulate loss. A nominal photoresist thickness of 50 nm was used for the initial simulations as this is easily in the suggested range $\lambda/8 < \lambda/4$ of λ_1 in the photoresist [Arnold 2007]. Figure 7.6 shows an initial comparison of the aperture in the AML and of the intensity of λ_1 in the photoresist of the AMOL system with and without a PRL and the absorbance in the PML, for the λ_2/λ_1 intensity ratio giving the best normalised intensity log-slope (NILS) performance. These results show considerable difference in maximum λ_1 intensity, the intensity profile transmitted through the photoresist and the absorbance modulation in the AML, and these effects are discussed further here.

7.5.1 EFFECT ON INTENSITY IN RESIST

The addition of the PRL is seen to increase the maximum intensity in the resist and change the confinement of the fields with depth, as shown quantitatively in the line traces in Figs 7.7 and 7.8. The increase in field intensity, by more than a factor of 4

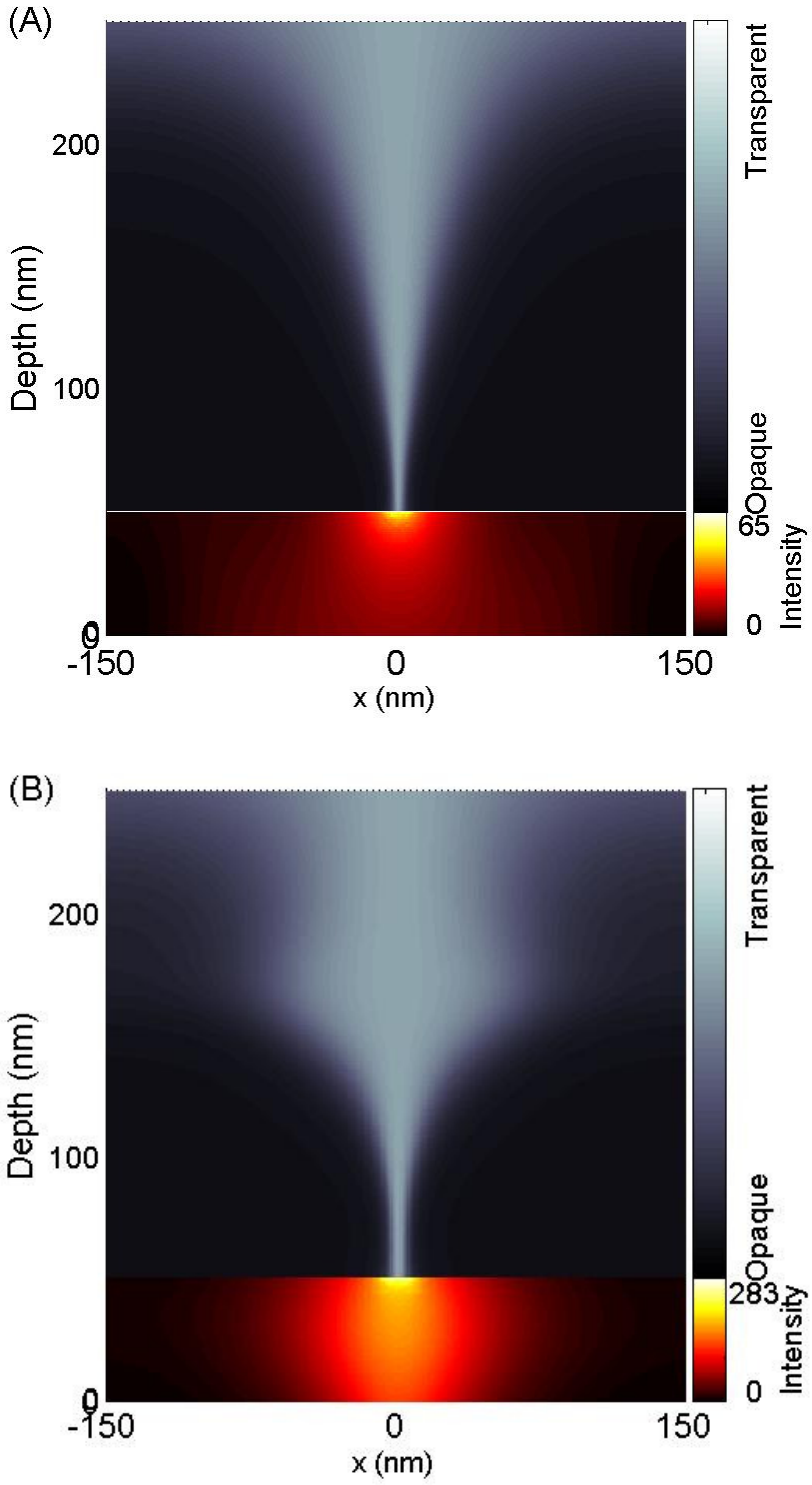

Figure 7.6 AMOL absorbance and λ_1 intensity in the photoresist for AMOL system with (a) matched substrate and (b) an ideal PRL beneath a 50 nm photoresist. The best case results based on NILS are shown which occurred at an λ_2/λ_1 intensity ratio of (a) 19 and (b) 15.

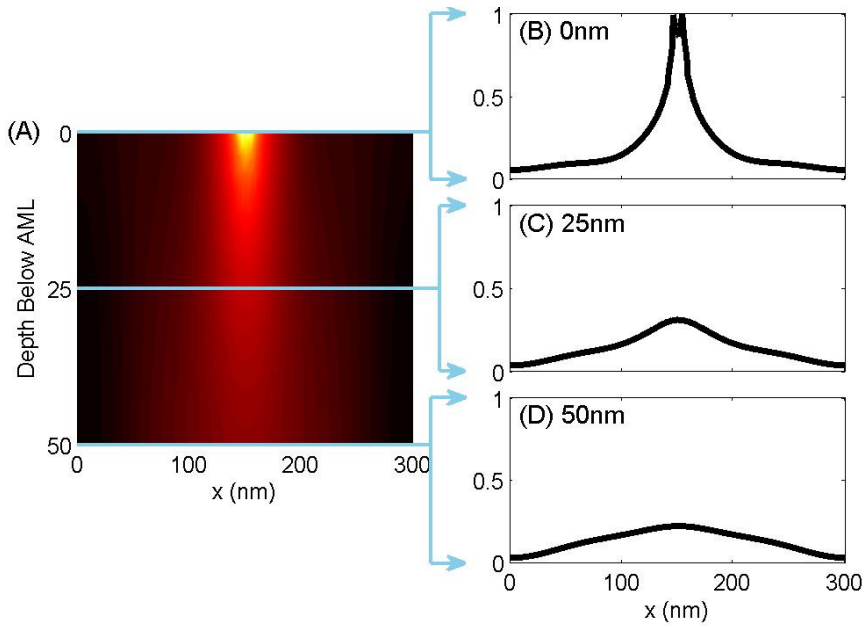

Figure 7.7 The λ_1 intensity in the resist for an AMOL system with a matched substrate (a) and normalised (to I_{max}) intensity waveforms at (b) 0 nm, (c) 25 nm and (d) 50 nm beneath the AML layer.

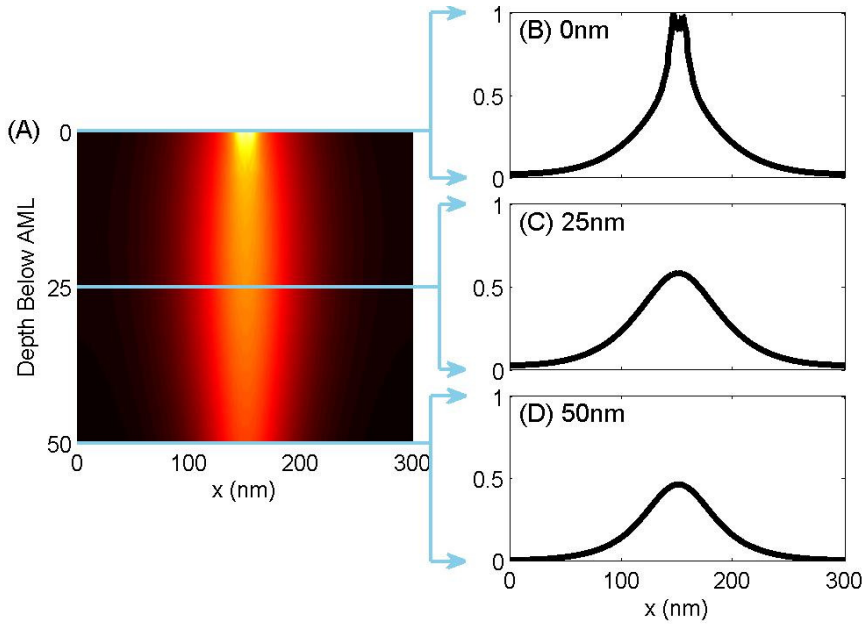

Figure 7.8 The λ_1 intensity in the resist for an AMOL system with an ideal PRL (a) and normalised (to I_{max}) intensity waveforms at (b) 0 nm, (c) 25 nm and (d) 50 nm beneath the AML layer.

($I_{max} = 65$ versus $I_{max} = 283$) can be explained simply by the reflection off the PRL trapping more λ_1 in the photoresist and, although this may reduce the FWHM at some wavelengths, this can be reduced by adjusting the λ_2/λ_1 intensity ratio. If the focus is placed on the intensity waveforms in the resist layers, demonstrated by Figs 7.7 and 7.8, it is observable that there is better lateral confinement of the λ_1 intensity throughout the resist when the PRL is present. In the matched substrate case the initial intensity waveform with a narrow FWHM has decayed strongly to a very flat waveform, thus having limited selectivity available at the base of the resist.

There is a great reduction in the decay of the intensity profile when the PRL is introduced, although there is still decay in the absolute intensity due to loss in the photoresist and loss of the highest spatial frequencies, there is a refocusing of the intensity waveform as the PRL is approached. The worst intensity waveform is now seen around the middle of the photoresist layer which is also improved compared to the similar plot in the matched substrate case. It clearly appears that the FWHM and NILS of the AMOL system are maintained far better throughout the photoresist with the addition of an ideal PRL layer which is studied in more detail next. These results are encouraging for the performance but in order to gain an improved understanding of how the system was being affected and how the system characteristics had changed further investigation was required.

A series of simulations were run for AMOL models with a matched photoresist and a PRL in which, for a constant 50nm photoresist layer the λ_2/λ_1 intensity ratio was increased from $500 — 5000$ in steps of 125 by increasing the intensity of λ_2. At each of these levels the steady-state NILS and FWHM of the intensity waveform in λ_1 were determined in two places, the best performing section of the photoresist (the boundary between the AMOL and photoresist layers) and the ‘worst’ photoresist depth (determined by calculating the depth at which the NILS and FWHM were weakest). Comparing each of the cases (Fig 7.9) demonstrates there is a small degradation of the performance at the AML/resist interface with the addition of the PRL layer. There is also a decrease in the extrema NILS achieved from 2.0 to 1.6 (Fig 7.9a) and an increase in

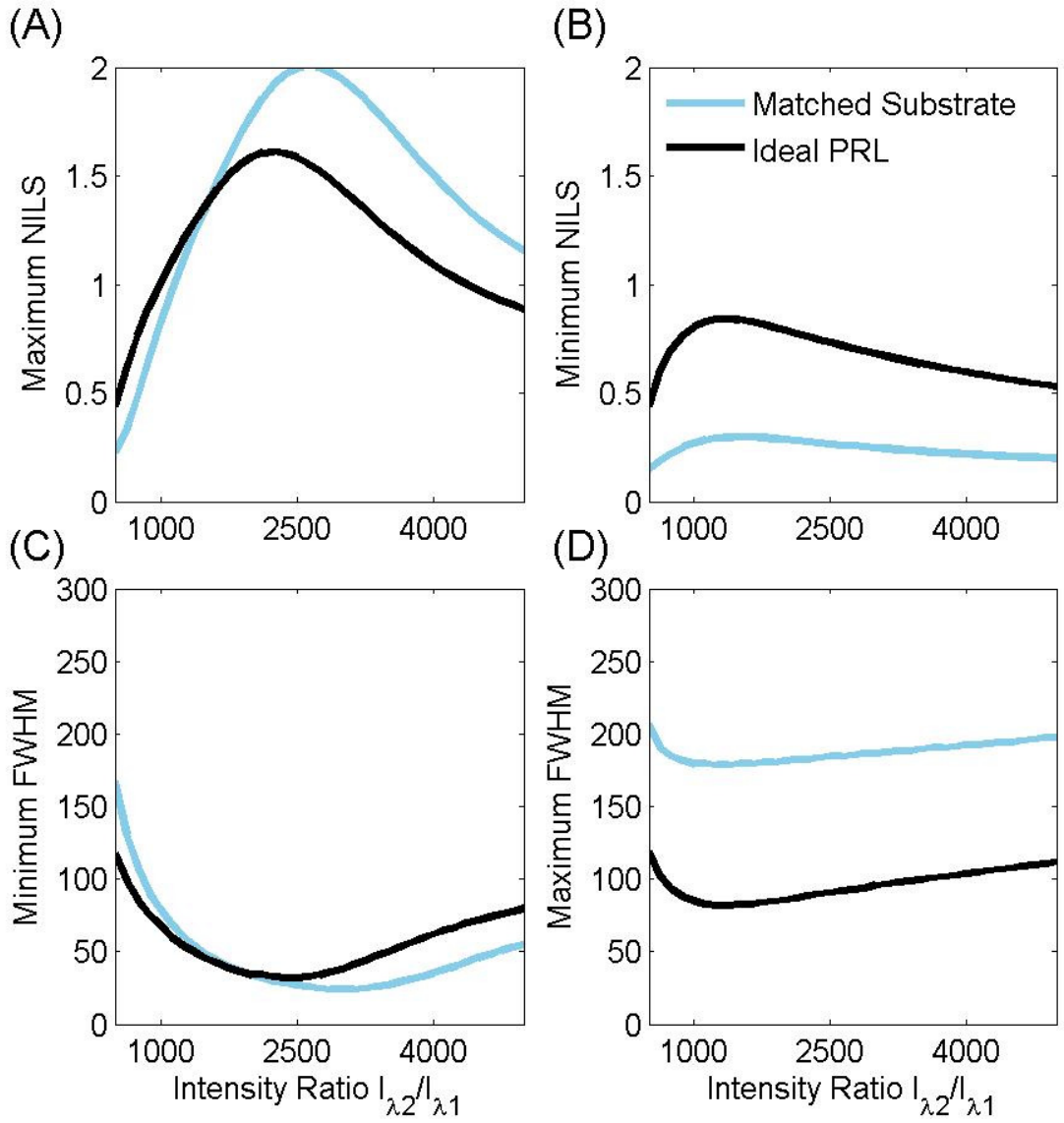

Figure 7.9 Comparison of the maximum and minimum NILS (a,b) and FWHM (d,c) between an AMOL system with a matched layer behind 50 nm of photoresist and a system with 50 nm photoresist followed by semi-infinite ideal reflecting layer. Plots show the results as the input intensity ratio is varied, producing different absorbance profiles.

the minimum FWHM from 24 to 32 nm (Fig 7.9c). There is also a shift of the position at which these maximums take place, with a lower λ_2 intensity giving the best performance in the case of the ideal PRL.

Although there is some loss in peak performance this is limited and the DOF, a key feature able to be improved through the use of the PRL, has shown a considerable increase, as can be seen by the improved transmission of a highly confined λ_1 intensity waveform throughout the resist. The performance is measured by examining the minimum NILS and maximum FWHM that occur at any point in the photoresist. Figure 7.9b demonstrates a clear improvement that adding the PRL has made; before the PRL was added the NILS value fell below 0.30 within the first 50 nm of photoresist; the presence

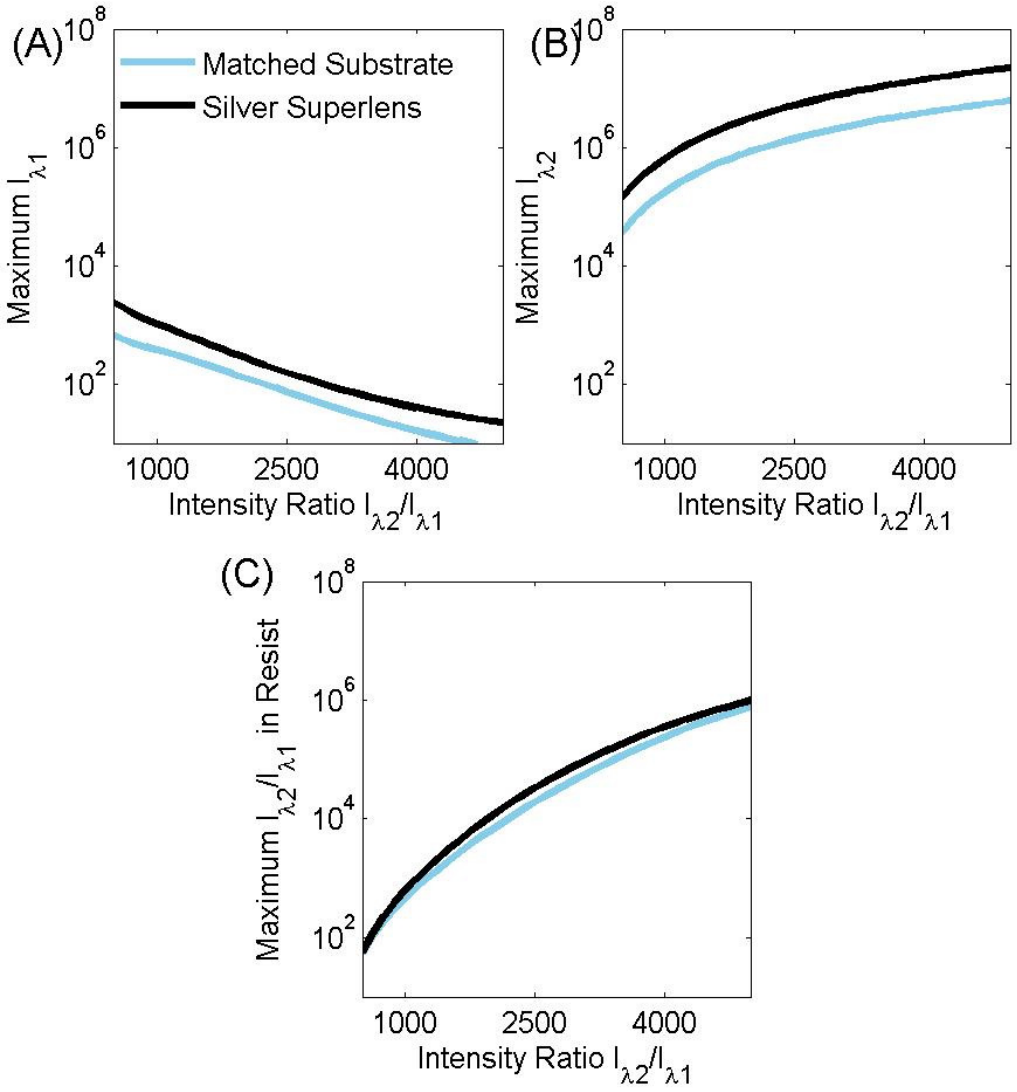

Figure 7.10 Comparison of the maximum intensities of (a) λ_1, (b) λ_2 and (c) λ_2/λ_1 between an AMOL system with a matched substrate or a semi-infinite ideal PRL behind 50 nm of resist as the input intensity ratio is increased.

of an ideal PRL increased this value across all simulations, to a maximum of 0.84.

A similarly dramatic improvement is seen in the maximum FWHM measured (representing the lateral confinement of the image); previously this had increased to 178 nm within the 50 nm of photoresist, and with a PRL this was reduced to 82 nm; the effect of this improvement was also clear to see in Fig 7.6. It is also noted that the intensity of both λ_1 and λ_2 in the photoresist has increased in the AMOL system with a PRL (Fig 7.10) due to the increased reflectivity of the PRL. Although the intensity ratio has changed little (Fig 7.10c) the increase in λ_1 intensity may reduce the necessary exposure time and the formation of the narrow aperture at smaller intensity ratio means a reduced levels of λ_2 and associated problems with unwanted resist exposure.

An alternative view of improvements to the system with a PRL is found by examining some intensity contours across the photoresist depth; Fig 7.11 compares this metric for both the matched layer case and for an ideal reflector. The linewidth is defined here as the distance for which the intensity level exceeds a nominal level ($0.3 \times I_{max}$ at the AMOL, resist boundary) at any depth in the resist; this nominal level is chosen so as to allow for a reasonable comparison throughout the resist depth, especially given the fact that the imaging is taking place with a decay in maximum intensity. In the perfectly matched photoresist case there is, as expected due to evanescent nature of fields, a sharp decay in the linewidth at each nominal level plotted and complete disappearance is seen in less than 30 nm.

The addition of an ideal PRL flattens the contours, although they are initially larger, and remain more constant across the depth of the photoresist. The contour plots also show the effect of increasing/decreasing the contours by $0.1 \times I_{max}$; in the matched case this causes increasingly large differences with depth into the photoresist, whereas the ideal PRL has a much more consistent relationship. This suggests that an AMOL system with a PRL would be less sensitive to fluctuations in the intensity of the controlling light sources, the absorbance properties of the AMOL or sensitivity of the resist, thus along-

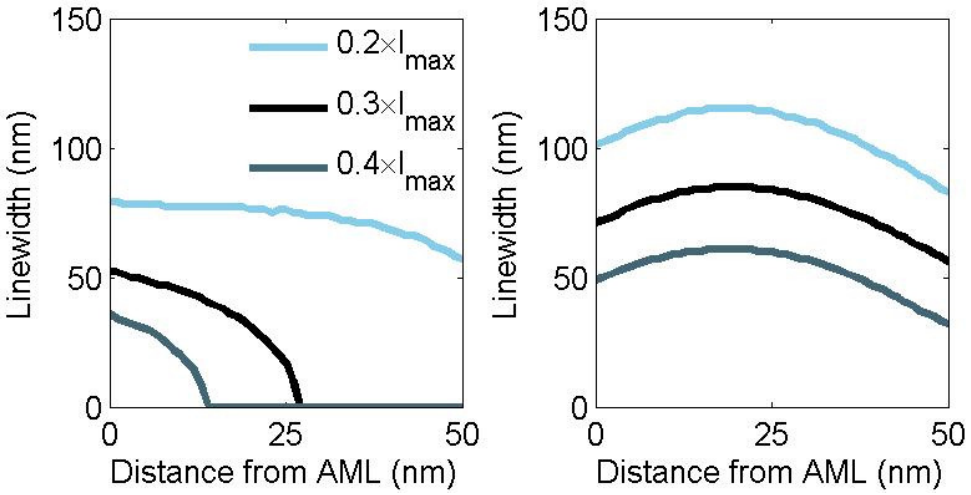

Figure 7.11 Linewidths with depth into photoresist from base of AMOL for (a) index matched substrate and (b) ideal PRL substrate, at $0.2 \times I_{max}$, $0.3 \times I_{max}$ and $0.4 \times I_{max}$ in both pictures. I_{max} is defined as maximum intensity in top intensity waveform.

side improving the lateral confinement of the intensity in the photoresist the process latitude has also been improved.

7.5.2 CHANGE IN ABSORBANCE MODULATION LAYER

Having examined the effects of introducing a PRL to the AMOL system on the intensity waveforms transmitted into the photoresist the effect of the PRL on the AML is now examined, in particular how the changes in the absorption profile effect the AML performance. A comparison of the absorbance profiles in the AML for the AMOL system with a matched photoresist and PRL is shown in Figs 7.12 and 7.13 with some very clear changes. In particular the effect of a standing wave formed in λ_2 interacting with the PRL is seen; this is created because λ_2 is a propagating wave and this wave is being strongly reflected PRL and then interferes with itself. This causes the AML to change from a funnel to an inverted hourglass shape whilst the narrow exit aperture remains. The absorbance waveforms demonstrate clearly the maintained narrow aperture near the interface between the resist and AML (Figs 7.12d and 7.13d) as well as

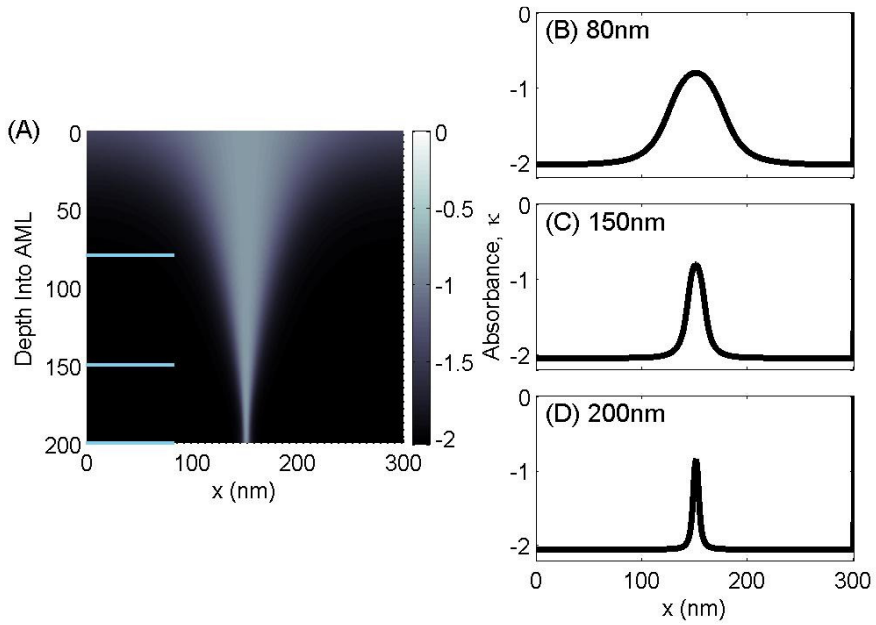

Figure 7.12 AML absorption in the best case matched substrate AMOL system (a). Absorbance is represented by the imaginary refractive index, κ, ranging from 0 to -2.2. Horizontal absorbance waveforms are shown at (b) 80 nm, (c) 150 nm and (d) 200 nm.

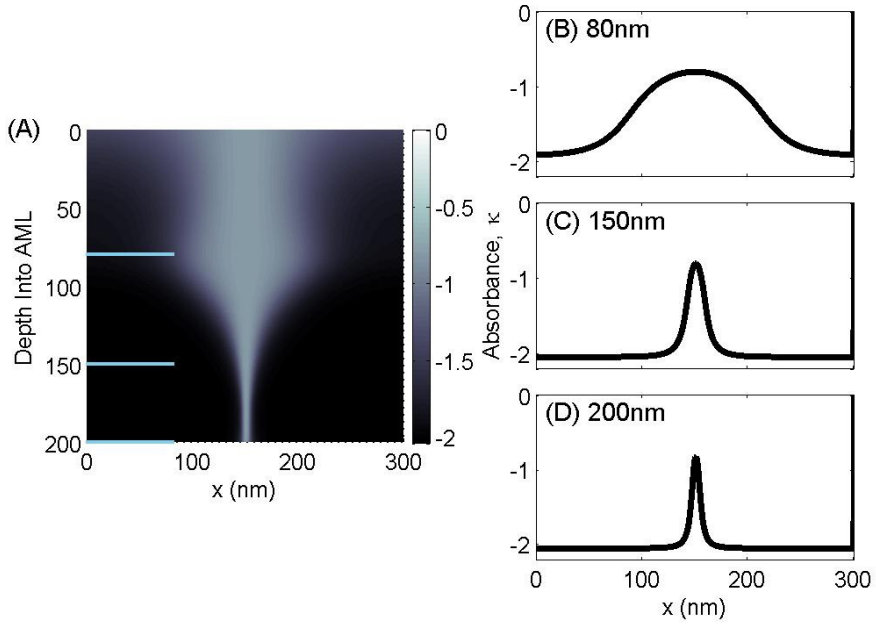

Figure 7.13 AML absorption in the best case AMOL system with PRL (a). Absorbance is represented by the imaginary refractive index, κ, ranging from 0 to -2.2. Horizontal absorbance waveforms are shown at (b) 80 nm, (c) 150 nm and (d) 200 nm.

the large differences created by the standing wave in the higher portion of the PML (Figs 7.12b and 7.13b). This narrow aperture in the AML remains helps to explain why the PRL system is able to create a small intensity waveform in the photoresist, as the initial AMOL system with a matched substrate did, and it is useful to further explore the change in the AML to help understand the effect that changes in this layer have on the λ_1 intensity profiles able to be realised in the photoresist.

It is clear from Figs 7.12 and 7.13 that the ability of the AML to create a narrow aperture is maintained with the addition of a PRL. To examine this aperture more closely a parameter, the aperture width in the AML, is defined as the distance for which the absorbance in the AMOL region is half the maximum absorbance. This enables Fig 7.14 to be plotted, showing the change in aperture width against depth into the AML for both the matched photoresist and ideal reflector models. Figure 7.14 demonstrates that both methods have created comparable aperture width ($\sim$5 nm) at the base of AML next to the photoresist, ($x = 200$ nm) for the cases giving the best NILS performance. The standing wave null in λ_2 occurs approximately 120 nm into the AML (with the inclusion of the 50 nm of photoresist this is approximately equivalent to a half wavelength from the reflecting layer ($n_r \approx 1.6$)) and creates the main differentiating feature between the two aperture width plots.

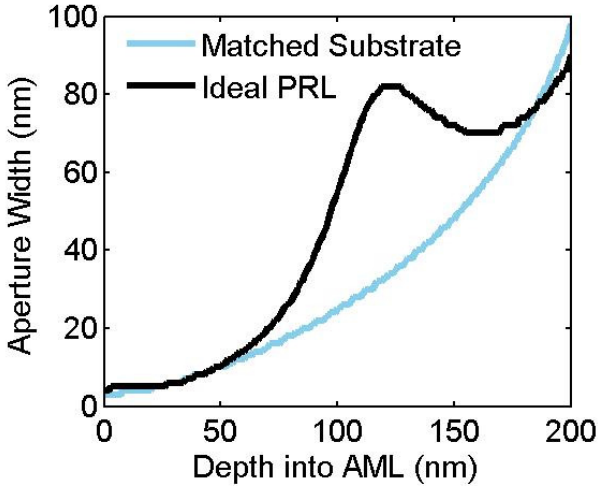

Figure 7.14 Aperture width against depth into AML for matched substrate and for an AMOL system with an ideal PRL after 50 nm of resist.

The aperture in the AMOL system with a matched photoresist case is shaped as a funnel which is constantly narrowing throughout the AML. With the introduction of the PRL the competition between wavelengths in the AML, a standing wave in λ_2, the transmitted λ_1 and the λ_1 from the PRL, has encouraged the aperture to reach a similar narrow size but to broaden faster at a null in the λ_2 standing wave. This change in shape of the AML aperture increases the amount of light transmitted at the edges of the main aperture in the PRL case, hence creating a weaker differentiation between light passing through the more transparent centre of the AML aperture and the aperture fringes. This will reduce the NILS and increase the FWHM of the intensity waveform in the resist as was seen in the metric results (Fig 7.9). A considerable change in the AMOL system has been shown by the introduction of the PRL, in particular in the improvement of the DOF and large differences in both the photoresist and AML. The impacts of the interactions with the PRL of λ_1 and λ_2 are different; these are now modeled separately to allow the different cases to be observed and understood more clearly.

7.6 EFFECTS OF INTRODUCING THE PRL

In this section the effects of the PRL on the AMOL system are discussed through an examination of the role of each of the wavelengths separately, showing that the reflection of λ_1 is much more important to the performance improvement than that of λ_2. This effect can be explained by the propagating nature of λ_2 and the importance of the evanescent field of λ_1 in exposing the photoresist. Here the FEM model of the AMOL system is used to model different reflective parameters for λ_1 and λ_2 in a fictitious PRL placed at 50 nm beneath the photoresist. In each case the comparisons are made at the λ_1/λ_2 intensity ratio giving the best NILS. The two cases which have already examined:

A. λ_1 and λ_2 with a matched substrate (Fig 7.6a, reproduced in Fig 7.15a),

B. λ_1 and λ_2 with a PRL (Fig 7.6b, reproduced in Fig 7.15b),

are compared with two fictitious systems which model part of an AMOL system with a PRL:

C. λ_1 is reflected by a PRL and λ_2 has a matched substrate (Fig 7.15c),

D. λ_1 has a matched substrate and λ_2 is reflected by a PRL (Fig 7.15d).

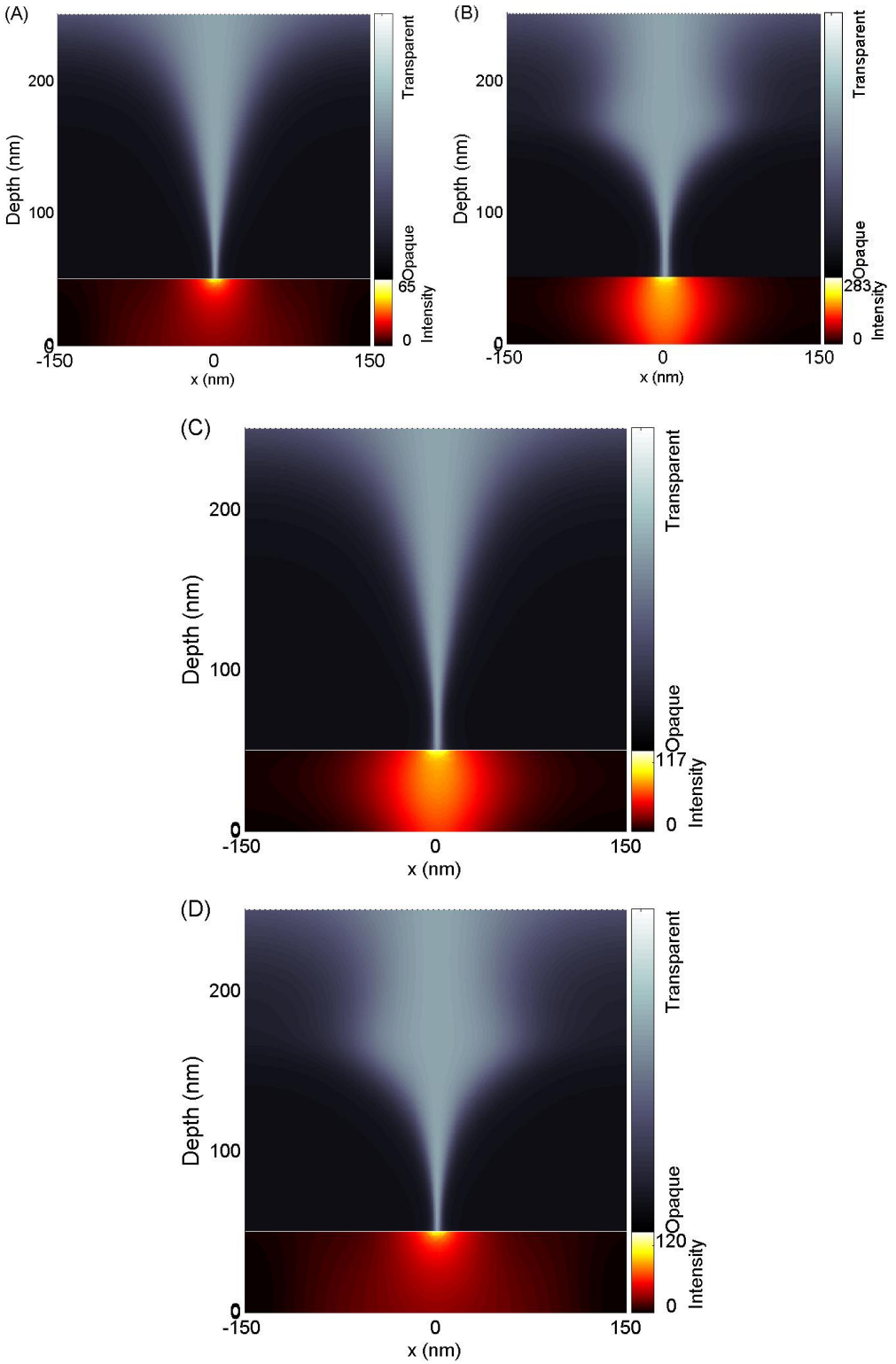

Figure 7.15 Comparison of the four cases for the intensity ratios $\boldsymbol{\lambda_2/\lambda_1}$ giving the best NILS showing (a) A and (b) B from previous considered cases and the fictitious (c) C($\boldsymbol{\lambda_1}$ has a PRL, $\boldsymbol{\lambda_2}$ matched substrate) and (d) D ($\boldsymbol{\lambda_1}$ has a matched substrate, $\boldsymbol{\lambda_2}$ a PRL) showing the absorbance in the AML and the $\boldsymbol{\lambda_1}$ intensity in the photoresist.

7.6 EFFECTS OF INTRODUCING THE PRL

Considering first the new case (C, Fig 7.15c), where λ_1 is reflected by an ideal PRL but λ_2 has a matched substrate; here the reflection of λ_2 in the resist is negligible allowing the focus to be placed on the reflection of λ_1 and how this affects the image. First, comparing the intensity in the photoresist of C to the matched substrate case (A) the most noticeable change is the much improved lateral confinement of λ_1 in the photoresist, combined with a large increase in intensity transmitted into the resist. If the aperture of C is compared to the matched case (A, Fig 7.15a) there is a widening of the aperture near the resist/AML boundary as was noted in the PRL case (B). The aperture widening can be accounted for by considering the reflected λ_1 from the PRL; although λ_1 is an evanescent wave in the resist the closeness of the PRL allows the wave to be partially reflected and the effect of this reflection is to increase the λ_1 intensity in the base of the AML widening the aperture. This effect is noticeable for ~20nm into the photoresist but increased with aperture width as the lower spatial frequencies have slower decay.

Comparing the same case (C) to the ideal PRL case (B, Fig 7.15b) there are also important differences noted. Although the λ_1 intensity remains narrowly confined in the photoresist for both cases the larger aperture of the system without the λ_2 PRL (C) has led to both a wider aperture in the PML and intensity waveform in the photoresist. The lack of any λ_2 reflection is also clear, with no standing wave present in the AML with a funnel shaped aperture being formed. From these comparisons the conclusion may be drawn that it is the λ_1 interaction with the PRL which creates the observed, well confined, aperture in the AMOL system, however without some reflection of λ_2 from the PRL the effect can be less effective due to widening of the aperture at the AMOL/resist boundary. It is also noted that the intensity of λ_1 is reduced when λ_2 is not reflected, this is likely due to the aperture widening causing a reduction in the amplification of λ_1 by the surface plasmons.

The second new case in which λ_1 has a matched substrate and λ_2 has an ideal PRL (D, Fig 7.15d) creates a similar intensity profile in the photoresist as the matched case (A), although with some improvement in intensity, again due to change in optimum intenisty ratio. Without λ_1 interacting with the PRL there is no, or limited, improvement in the

confinement in the photoresist and imaging capability of the system. Comparing D with the ideal PRL case (B, Fig 7.15b) reveals the similarity of the inverted hour-glass pattern created in the AML. The hourglass shape created is even narrower in case D due to the λ_2 being reflected from the PRL and interacting with the AML again, thus narrowing the aperture further; this leads to a lower optimum intensity ratio being able to be used.

Having investigated the two cases in which only one of the two wavelengths in the simulation is affected by the PRL and comparing these to the matched and ideal PRL cases the effect of the PRL on each of the wavelengths is as they are transmitted in the AML and photoresist is seen more clearly. The reflection of λ_2 has a larger effect at longer distances, as it is a propagating wave, and hence creates a strong standing-wave feature in the AML, it also acts to reduce the aperture at the AMOL/resist boundary and reduce the optimum intensity ratio needed. Fortunately this aperture reduction is countered, to allow similar sized apertures to form, by the reflection of λ_1 which leads to a slightly wider aperture, but similar absorbance pattern inside the AML. Most effectively when considering the ability of the system to provide lithographic results the horizontal confinement of the transmitted λ_1 inside the photoresist layer is much improved when a PRL is introduced. It has also become apparent in examining the range of simulations that were run that many of the effects being observed and explained are dependent on the resist depth between the AML and PRL and hence how these differences affect the system are now examined more systematically.

7.7 EFFECT OF PHOTORESIST DEPTH

The thickness of the photoresist is a limiting factor in this lithography system as it is limited by the presence of the PRL beneath it; this places an upper limit on the depth achievable in the resist pattern. The position of the PRL layer beneath the photoresist may be varied, however this will then effect the PRL/AMOL interaction may lead to a reduction in the effectiveness of the reflections as, particularly because they are evanescent, there will be increased loss in the transmission between the base of the AML and the top of the PRL. Arnold [Arnold 2007] suggested improved performance for resist

depths between $\lambda/8 < d < \lambda/4$, which, in the system being considered with λ_1 at 400 nm and a photoresist with a refractive index of $1.6 - 0.05j$ gives an effective $\lambda_{1,eff}$ in the resist of around 250 nm, suggesting improved transmission between 30 and 65 nm. To further investigate how the photoresist depth would affect an AMOL system with a PRL a series of simulations were run which varied the intensity of λ_2 for photoresist depths between 15 and 80 nm, an ideal PRL with the same parameters as the initial work was used.

The performance of the PRL layer with different photoresist depth is first examined by comparing the minimum and maximum NILS and FWHM for the best case scenario at each photoresist depth (Fig 7.16). This shows that the NILS system is able to outperform the matched case for shallow depths, in this case up to ~30 nm in both cases. For cases beyond this distance there is a reduction in the maximum performance, compensated for by the improvements discussed above to the minimum NILS and FWHM occurring in the layer, which easily exceed those seen in a 50 nm photoresist on a matched substrate. Although a shallow photoresist poses increased manufacturing challenges it is interesting to explore the improved performance seen, in particular there is very little loss of intensity confinement of λ_1 throughout the photoresist, this is demonstrated in Fig 7.**17**. Although there remains decay in the maximum intensity with depth in resist there is very good confinement throughout the narrow photoresist layer. The improvement in the NILS and FWHM is likely due to the λ_2 reflection creating a standing wave in the AML; in the case of these shallow resist the standing wave null is further into the AML layer and hence a strong, narrow absorbance aperture may be formed, the closely placed PRL is still functioning well, perhaps because there are limited low-frequency components in the intensity profile due to the low duty-cycle and sharp peak.

Returning to consider the cases of deeper resist layers ($d \sim 60 - 80$ nm), and the ability of the PRL to improve the DOF in these resist layers, an obvious limit in effect is seen to be being reached in which the performance shows negligible improvement on the matched substrate case in maintaining the image transmitted in the resist (FWHM

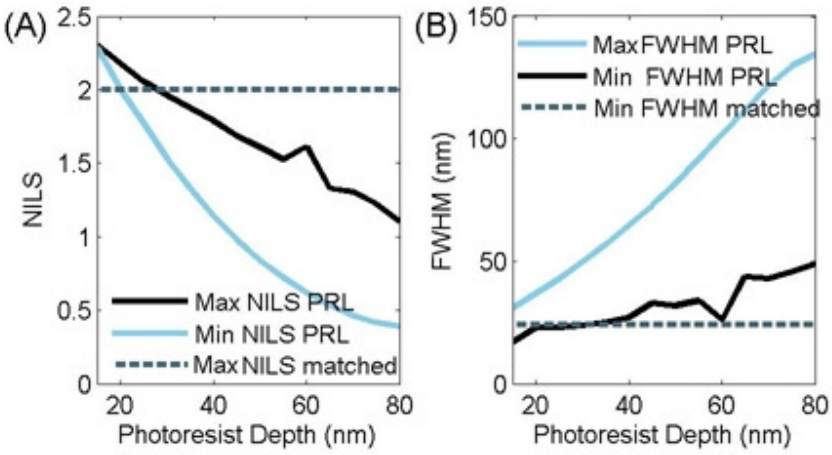

Figure 7.16 Comparing the changes in NILS (a) and FWHM (b) for a PRLs placed at changing depth beneath the AML. Also included for comparison is the best NILS and FWHM performance of an AMOL system with a matched layer. The reason for the kink at 60 nm is unknown but it does not indicate an improvement in the confinement of λ_1.

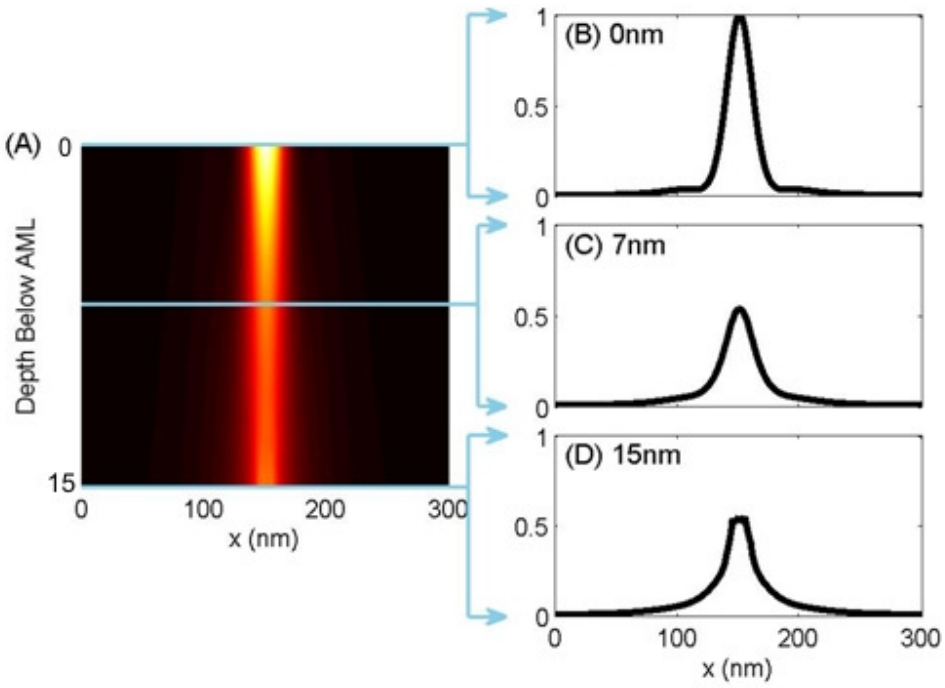

Figure 7.17 λ_1 intensity in the resist for an AMOL system with an ideal PRL at 15 nm beneath the AML (a) and normalised (to I_{max}) intensity waveforms at (b) 0 nm, (c)7 nm and (d)15 nm beneath the AML layer.

approaching 150 nm) and there is also degradation in the best performance for both metrics. Although there is still an improvement of the maximum FWHM to 178 nm for a 50 nm matched substrate case it is difficult to argue a strong confinement is present when the FWHM is half the period of the standing wave and it is likely that a simple reflection is dominating any SP effects. Hence there is a clear trade-off seen when using a PRL system, between performance and resist depth, if a very shallow resist layer can be tolerated then very good and very consistent performance may be achieved, however as the resist depth is increased the PRL is less able to desirably confine the intensity profile.

7.8 SILVER PRL IN AMOL

It is unlikely that for a given photoresist an ideal plasmonic reflector could be easily found and adapted for use. There is however a large range of noble metals that can act as plasmonic reflectors in the optical frequency range and here the replacement of the PRL with an infinite silver layer is considered. The silver layer differs from the ideal case in that the two wavelengths do not experience equal reflection from the surface and the permittivity at each wavelength is much more negative than the ideal case. Here the refractive index used are interpolated from experimental data as $n_r = 0.06 - 3.56i$ at λ_2 (546 nm) and $n_r = 0.05 - 2.17i$ at λ_1 (405 nm) [Johnson 1972]; this may lead to greater dispersion or less effective amplification, depending on the spatial frequencies involved. In particular, as noted by Arnold [Arnold 2007] 405 nm is at the limit of performance improvement for a silver PRL.

Introducing this as a direct replacement for the PRL used previously at a depth of 50nm, and with all other model conditions kept constant produced an optimum NILS image shown in Fig 7.18. This demonstrates a performance between that of the ideal PRL and matched substrate simulated previously, whilst there is clearly improved transmission into the resist layer the lateral confinement is not maintained to the same extent as the ideal PRL was able to achieve. Examining the intensity profiles in the resist layer more

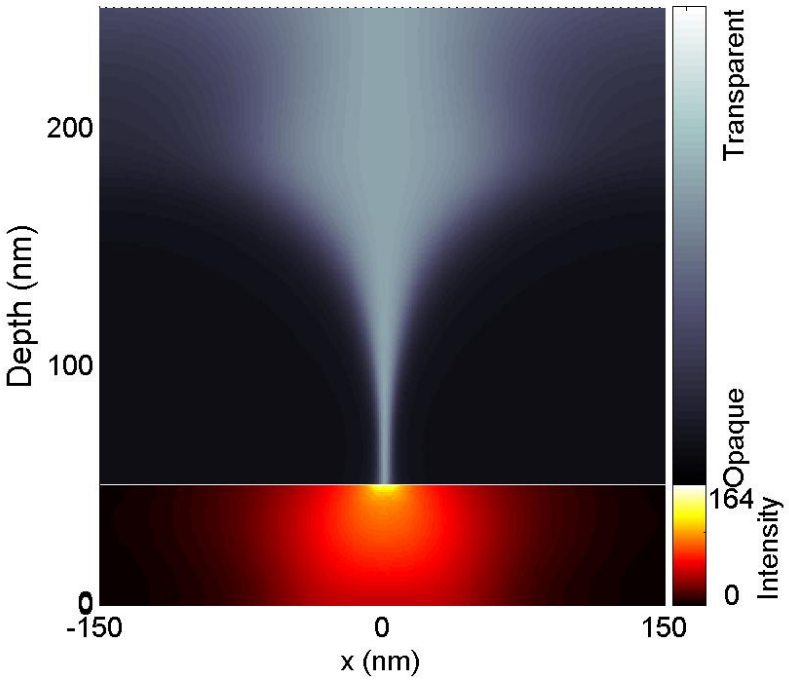

Figure 7.18 AMOL absorbance and λ_1 intensity in the photoresist for silver PRL in an AMOL system separation of 50 nm

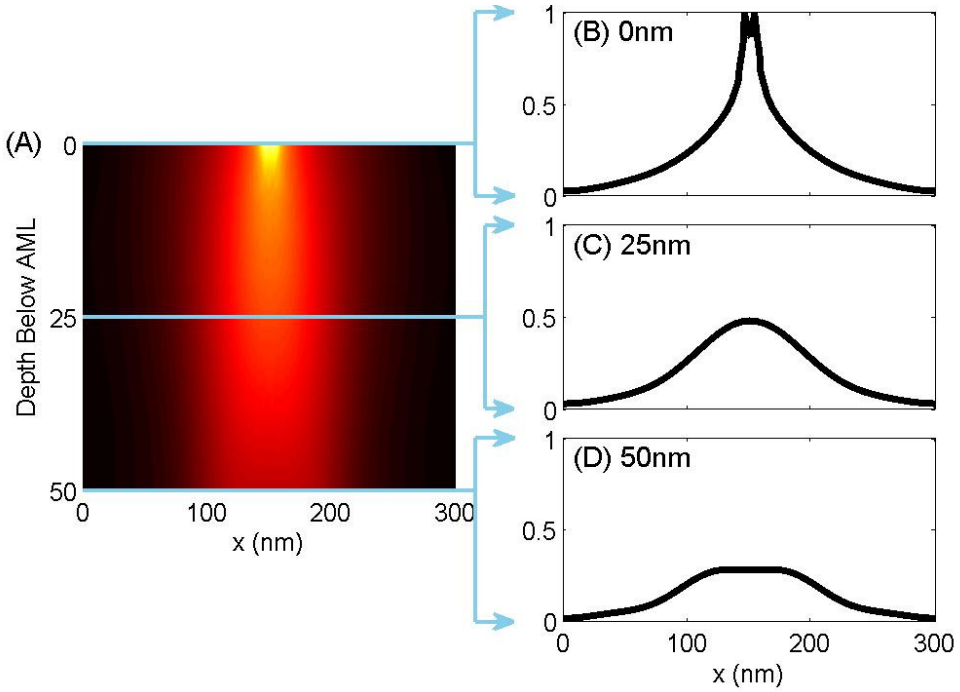

Figure 7.19 The λ_1 intensity in the resist for an AMOL system with a silver PRL (a) and normalised (to I_{max}) intensity waveforms at (b) 0 nm, (c) 25 nm and (d) 50 nm beneath the AML layer.

closely (Fig 7.19) it is seen that the initial intensity profile is similar to that achieved by the matched substrate (Fig 7.7) and ideal PRL cases (Fig 7.8). However in comparison to the ideal PRL case the narrowness of the aperture is not maintained as effectively; there is still improvement in comparison to the matched substrate case as there remains improvement in the lateral confinement, with the intensity peak remaining clearly visible and somewhat confined throughout the resist layer. This flattening is likely due to the decreased ability of 405nm λ_1 to excite plasmons on the silver. Examining the changes in the absorbance layer for the AMOL system with a silver PRL they appear very similar to the ideal PRL case, with an inverted hourglass absorbance profile seen in the AML. To get an improved understanding of the difference between the ideal and real PRLs the results presented earlier (Fig 7.6 and 7.9) for the ideal PRL are compared to those for silver PRL metrics (Fig 7.20).

The metrics plotted in Fig 7.20 show a further reduction in the maximum NILS and a shift back to a higher intensity ratio using a silver PRL, which is somewhat expected because λ_2 will not be being reflected as strongly as in the ideal case. The minimum FWHM achieved is also very similar, so the introduction of the silver PRL has not caused much reduction in the performance of the AML aperture in creating a narrow intensity aperture. Turning to the question of how well the PRL has improved the DOF in the photoresist the minimum NILS shows disappointing performance, with similar values as seen for the matched substrate case. However looking back to the intensity profiles in the photoresist (Fig 7.19c) this is likely because an assumed width of 50nm has been used thus the measurement has been made at the flat top of the intensity waveform. Although this flat top is broader than may be desired it demonstrates improved performance, and with a shallower photoresist, a different PRL or a shorter wavelength for λ_1 it should be possible to increase the DOF.

The maximum FWHM of the silver PRL demonstrates reduced performance compared to the ideal PRL, however the maximum FWHM is still a greater improvement on the matched substrate result, which was ~180 nm at the optimum NILS, as opposed to

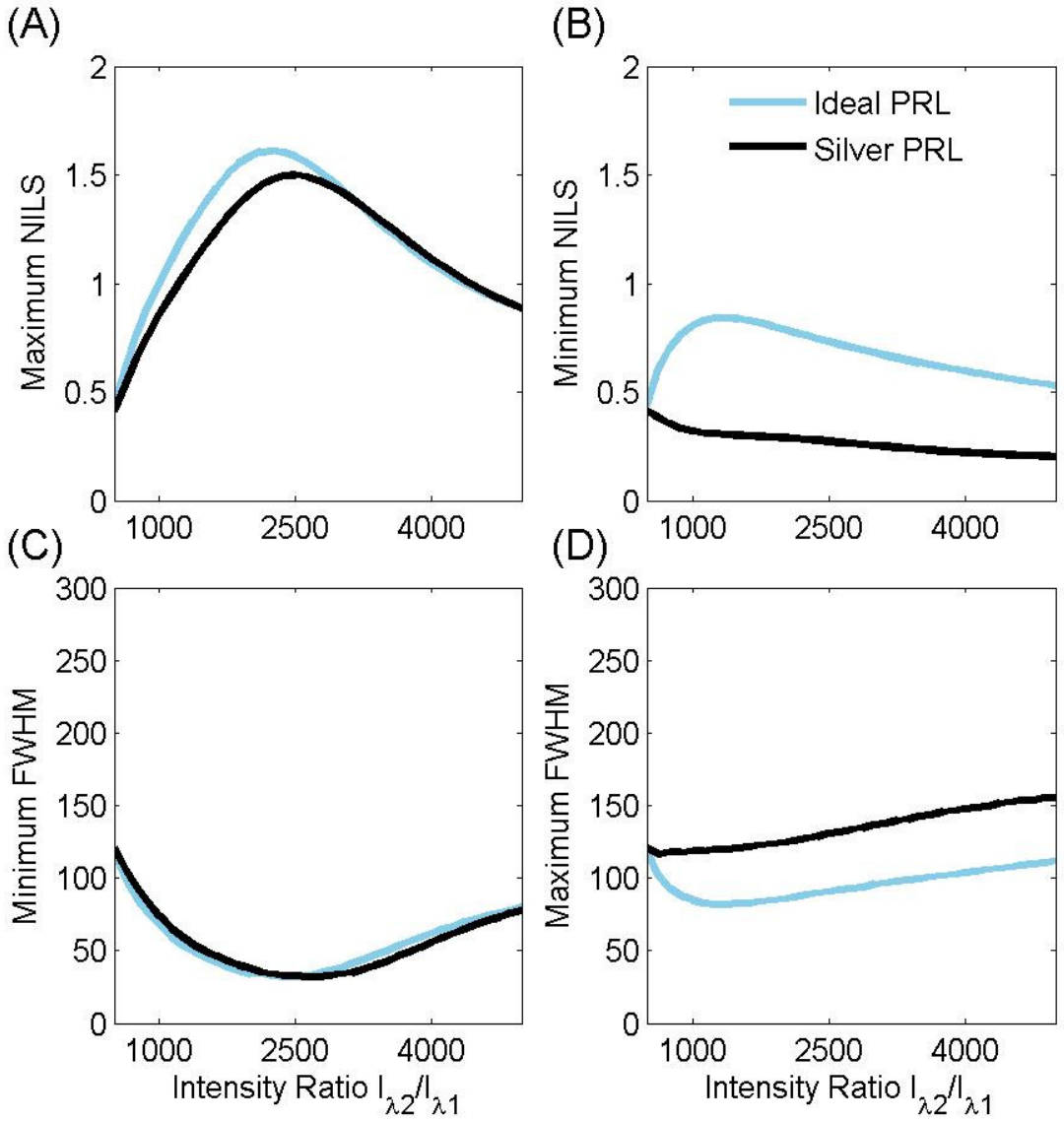

Figure 7.20 Comparison of (a,b) NILS, (c,d) FWHM as the input intensity ratio is varied for an AMOL system with an ideal reflecting layer behind 50 nm of photoresist and a system with 50 nm photoresist followed by semi-infinite silver layer.

~125 nm at the optimum NILS in the silver case. This demonstrates that, although silver is not an ideal PRL for this system, there is still the opportunity for a much improved performance with the introduction of a real PRL into the AML system. These simulation results provide strong evidence of the ability of an underlying silver plasmonic reflector to reduce the blurring of an image transmitted beneath a photoresist in an AMOL

system. The formation of an inverted hourglass figure is retained and although a wider aperture is formed the overall result still allows improved DOF when compared to the matched substrate case.

7.9 CONCLUSIONS

In this chapter the introduction of a PRL has been considered as a way to overcome the lack of DOF and horizontal confinement of an AMOL exposure due to the evanescent decay of the exposing wavelength in the photoresist. The discussed results clearly demonstrate the very positive extension of the DOF within the photoresist due to the introduction of a PRL approximately 60 nm or less beneath of the AML. Investigating the dependence of the performance of the AMOL/PRL system on the distance between the AMOL and PRL it was found that there was increased performance with photoresist depths down to 15 nm (distances below this were not measured as they provide greater manufacturing challenges so are less relevant).

Finally a plasmonic metal was considered as a replacement for the ideal PRL and a system was modeled with a silver PRL, this again demonstrated an improvement in performance when compared to the matched case and the results were not drastically worse than that of the ideal and case; better performance could be expected from alternative plasmonic metals or metamaterials. In summary it has been demonstrated the ability of the DOF of the AMOL system to be increased through the use of a PRL which will allow greater flexibility in the experimentation and manufacture of devices using AMOL. This improvement must, of course, be considered with the fact that these exposure remain in the near-field so there are inevitable limitations. There has been some success in overcoming limitations of near-field exposures using other surface plasmon phenomena such as a superlens.

Chapter 8

PLASMONIC TRANSMISSION WITH AMOL

8.1 MOTIVATION

The ability of AMOL to create near-field images and the transmission of these images into a photoresist have been outlined in the previous chapters. In this chapter the ability of plasmonic layers integrated into an AMOL system to act as a superlens is investigated. This is firstly to confirm and investigate the operation of a superlens with an AML aperture created by AMOL and secondly to explore the ability of the superlens to reduce the intensity of λ_2 in the photoresist, in essence acting as a dichroic filter. There is also a range of phenomena associated with superlensing and lithography that may prove to produce interesting results when combined with an AMOL system.

8.2 INTRODUCTION TO SUPERLENSING

This section will review the development of superlensing, from Veselago's original paper on negative index materials (left-handed materials) [Veselago 1968] through to Pendry's proposal of the superlens [Pendry 2000] and the experimental verification of superlensing effects at microwave [Wiltshire 2006, Shelby 2001a, Shelby 2001] and optical [Melville 2005, Fang 2005] frequencies. Finally a brief overview of the current developments will be included.

8.2.1 NEGATIVE INDEX MATERIALS

In nature the fundamental properties of materials which control the propagation of light - the relative permittivity, ϵ and the relative permeability, μ - are predominantly positive

quantities. Considering the propagation of a monochromatic wave through an isotropic medium the wave vector, k is proportional to the refractive index squared, n^2 which may be expressed as the product of ϵ and μ,

$$n^2 = \epsilon\mu. \tag{8.1}$$

In 1968 Veselago published a paper considering the effect of a simultaneous switch of sign of ϵ and μ, proposing three possibilities: no change would occur, some fundamental law of nature would be contradicted by the switch or new, distinctive properties could be found [Veselago 1968]. Veselago then demonstrated that the third case was the true outcome, and that given the relations

$$\epsilon < 0 \text{ and } \mu < 0 \tag{8.2}$$

the vectors of the electromagnetic wave become a left-handed triplet (as opposed to the 'normal' right-handed triplet), leading to the term left-handed materials.

From this novel development Veselago outlined a series of interesting new phenomena that would arise, first noting that the group velocity would change from positive to negative (and hence the Doppler shift would be reversed). Very interestingly the refraction at two boundaries was considered and to account for the material change Snell's law must be adapted, becoming

$$\frac{\sin(\phi)}{\sin(\gamma)} = \frac{n_1}{n_2} = \frac{p_2}{p_1}\left|\sqrt{\frac{\epsilon_2\mu_2}{\epsilon_1\mu_1}}\right| \tag{8.3}$$

where ϕ and γ represent the incident and refracted ray, p the left ($p = -1$) or right ($p = +1$) handedness of the material and the subscripts 1 and 2 refer to the incident and refracted medium respectively. It is clear from this equation that a negative refraction is possible at a boundary between a left and right-handed material (Fig 8.1). It follows from this negative index of refraction that the effect of concave and convex lenses will be reversed and that a planar slab of negative index material ($n = -1$) can be used to reproduce a radiating point source at some distance less than the thickness of the negative index slab. Importantly there would be no reflection in this case as the magnitude of the refractive indices of the materials are the same (i.e. the wave impedances are matched across the boundary).

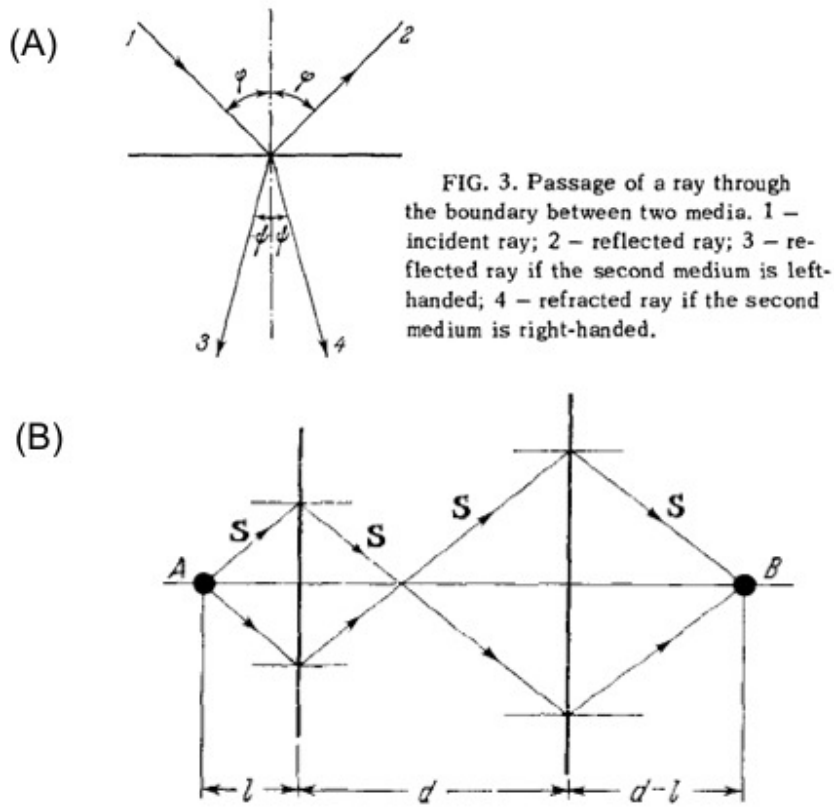

FIG. 3. Passage of a ray through the boundary between two media. 1 – incident ray; 2 – reflected ray; 3 – reflected ray if the second medium is left-handed; 4 – refracted ray if the second medium is right-handed.

FIG. 4. Passage of rays of light through a plate of thickness d made of a left-handed substance. A – source of radiation; B – detector of radiation.

Figure 8.1 (a) Refraction at a boundary between two media and (b) focusing by a planar negative index slab [Vesalego 1968]

After outlining the interesting properties of left-handed materials Veselago offered suggestions for how such materials could be found or manufactured. Considering first the permittivity, it is well known that plasmas may exist in gaseous or solid states and that the permittivity in a plasma is given by

$$\epsilon = 1 - \sum \frac{\omega_0^2}{\omega^2} \tag{8.4}$$

where ω_0 is a material constant for each carrier, ω^2 the frequency of incident radiation and the sum is over all types of carriers; thus it is possible to achieve negative permittivity at low frequencies ($\omega < \omega_0$). Veselago suggested that gyrotropic materials (anistropic

ferroic materials which are able to exhibit a change in material parameters under field or uniaxial stress) are able to have negative ϵ and μ in some direction. One issue raised by Veselago was that a medium having negative ϵ and μ would implicitly require frequency dispersion, so that any negative index material will have frequency dependent parameters, limiting the bandwidth of any negative material. Although the paper raised a series of interesting questions the lack of an easily obtainable negative refractive index material limited any development in this area until the beginning of 2000.

8.2.2 MANUFACTURED LEFT HANDED MATERIALS

There was a return in interest of negative index materials after papers published by Pendry and Smith. Pendry first theorised that it would be possible to create a composite negative index material through creating a periodic structure built from a set of identical unit cells, where, given the unit cell length, a is small enough,

$$a \ll \lambda = \frac{2\pi c_0}{\omega}, \tag{8.5}$$

it would appear to incident illumination at a frequency as a single medium [Pendry 1999]. Pendry uses this idea to propose a series of designs which are able to create negative effective μ, for instance: a split cylinder design in which two cylinders with small gaps (to remove current flow around the cylinder) are nested together. The effective μ is calculated as

$$\mu_{eff} = 1 - \frac{\frac{\pi r^2}{a^2}}{1 + \frac{2\sigma i}{\omega r \mu_0} - \frac{3dc_0^2}{\pi^2 \omega^2 r^3}}, \tag{8.6}$$

where the parametrers are defined in the paper [Pendry 1999], for appropriately chosen values this expression may be negative, with the effective ϵ for the same system being

$$\epsilon_{eff} = \frac{1}{1 - \frac{\pi r^2}{a^2}}, \tag{8.7}$$

where r is the radius of the outer cylinder. Hence a negative index material is possible at certain frequencies using this method. To generalise this to a three dimensional, isotropic

medium Pendry proposes the use split rings instead of cylinders and placing these rings on the surfaces of each unit square.

This theoretical work was then experimentally verified at microwave frequencies by Shultz through the use of copper split ring resonators, demonstrating the first negative index material [Shultz 2000]. A more thorough publication gave further experimental verification and a comparison between a left-handed material and Teflon, clearly showing an angle reversal [Schultz 2001]. The limited wavelength bandwidth at which the material has a negative index and the difficulties in reducing the wavelengths to optical frequencies were noted in these works (these difficulties arise because the periodic structures must be much smaller than the wavelength).

Since these initial papers on the manufacture of negative index materials there has been huge development in the area of metamaterials and a large array of complex structures has been considered [Padilla 2006, Smith 2004]. Although there has been progress on negative index materials at optical frequencies [Valentine 2008, Shalaev 2007, Shalaev 2005] the suggested structures have complex three dimensional geometry and small feature sizes that are difficult to fabricate on a large scale; in particular an efficient method for a negative index layer for a lithography process has not been found.

8.2.3 A PERFECT LENS

In 2000 Pendry published a paper detailing the possibility of using a negative refractive index material to overcome the diffraction limit, as a perfect lens [Pendry 2000]. Pendry begins by considering the propagation from a dipole source in front of a lens, producing an electric field of the form

$$\boldsymbol{E}(\boldsymbol{r},t)=\sum_{\sigma,k_x,k_y}\boldsymbol{E}_{\sigma}\left(k_x,k_y\right)\times e^{-ik_z z-ik_x x-ik_y y+i\omega t}. \tag{8.8}$$

If the axis of the lens is chosen to be in the z direction Pendry states that there are two possible values for k_z depending on the spatial frequency,

$$k_z=\sqrt{\omega^2c^{-2}-k_x^2-k_y^2}\ \text{ for }\ \omega^2c^{-2}>k_x^2+k_y^2 \text{ and} \tag{8.9}$$

$$k_z = -i \times \sqrt{k_x^2 + k_y^2 - \omega^2 c^{-2}} \text{ for } \omega^2 c^{-2} < k_x^2 + k_y^2, \quad (8.10)$$

where Eq 8.9 represents a propagating wave and Eq 8.10 an evanescent wave. In the case of a normal lens the decay in the evanescent components leads to a loss in resolution. Pendry then proposed using a planar slab of negative index material for a lens and demonstrates that if the index has ϵ and μ of -1 then the evanescent propagation (Eq 8.10) must, Pendry states due to causality, become

$$k_z = +i \times \sqrt{k_x^2 + k_y^2 - \omega^2 c^{-2}} \text{ for } \omega^2 c^{-2} < k_x^2 + k_y^2, \quad (8.11)$$

which is an amplification instead of decay; thus Pendry claims that *'with this new lens both propagating and evanescent waves contribute to the resolution of the image'*. Pendry then briefly considers materials that would be able to realise such a system, suggesting the metamaterials described in Section 8.2.2 as well as, for optical frequencies in the near field, considering the electrostatic limit. In such a system, where all the dimensions are much smaller than the wavelength of light, Pendry shows that only the value of ϵ need be negative to allow the approximation of a perfect lens.

The novel nature of the idea and the grandness of the claims presented by Pendry [Pendry 2000] led to vigourous debate over the accuracy of the results and the mathematical derivation of a perfect lens. In comments to the paper ['t Hooft 2001, Williams 2001] there were questions on the impact of loss in the materials and the claims of causality requiring evanescent wave amplification which Pendry replied to [Pendry 2001a, Pendry 2001b]. Later others [Garcia 2002, Valanju 2002] questioned if loss in the negative index material and the requirement of a finite slab thickness would remove any amplification effect.

8.2.4 EXPERIMENTAL VERIFICATION OF A PERFECT LENS

Following the publication of Pendry's paper on a perfect lens and the ensuing debate there was effort by a number of separate groups to verify the perfect lens ideas, both with simulations and experiment. McNab published a multiple multipole program (MMP) simulation of a perfect lens, with particular focus on the possibilities for near-field optical lithography [McNab 2002]; this demonstrated the ability of a silver layer to

project an image a small distance below a resist. Following this, and other simulation work a number of groups attempted experimental results; optical imaging through a silver lens above the evanescent limit was achieved by Melville in agreement with their FDTD simulations [Melville 2004]. Using the same process features below the diffraction limit were achieved by Melville [Melville 2005] (Fig 8.2) and independently with a different experimental setup by Zhang [Zhang 2005], (Fig 8.3); alongside this work metamaterials have allowed lower frequency microwave lenses [Wiltshire 2006]. The experimental proof is a powerful argument for the performance of a perfect lens, although there remains some debate as to whether the performance is simply driven by the presence of surface plasmons [Rao 2003, Fiddy 2010] rather than a 'perfect' lens; whilst this is an interesting debate the results are desirable in either case.

8.2.5 CURRENT STATE OF DEVELOPMENT

Following the initial results progress has been made on refining the superlens techniques, alongside the investigation of related phenomena and how the superlensing effect may best be implemented in lithographical systems. Chaturvedi demonstrates the current state of development with results down to $1/12^{th}$ the exposing wavelength using germanium wetting layers to allow smoother silver, which allows improved performance [Chaturvadi 2010].

Although this performance has been exciting there remain large issues that need to be resolved before superlensing is considered for wider lithography applications, for instance the need for intimate contact between the superlens and the mask which leads to difficulties with dirt residues and consistency. When considering combining plasmonic superlenses with the AMOL process there are two possible gains, firstly the problems surrounding close contact between mask and lens is removed as the AMOL mask can be spun directly onto the silver and secondly the superlens can also be used as a dichroic filter, reducing the transmission of λ_2 into the resist where it may expose the photoresist. However the introduction of a superlens to AMOL will impact on the interaction of the two system wavelengths and hence the system performance.

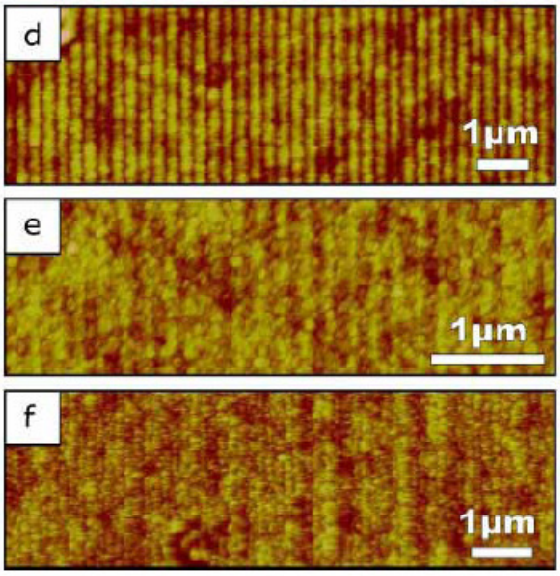

Figure 8.2 AFM images of gratings imaged through a 25 nm/50 nm/10 nm – PMMA/Ag/SiO_2 lens stack, with periods of (d) 250 nm, (e) 200 nm, (f) 170 nm [Melville 2005]

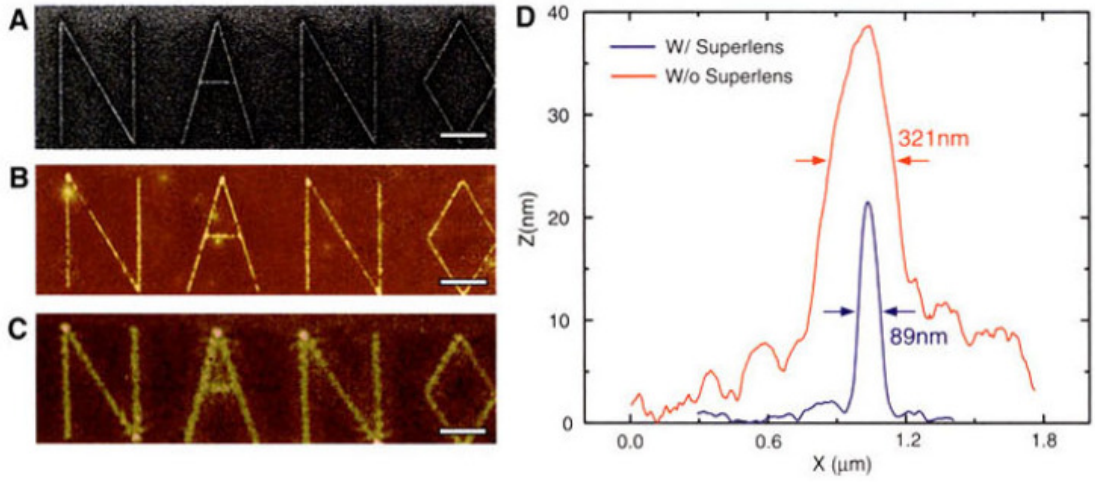

Figure 8.3 Comparison of the effect of introducing a superlens showing (a) an focused ion beam image of an arbitrary object "NANO" with 40 nm linewidth (b) the image result with silver superlens, (c) the image result with silver superlens replaced by PMMA spacer and (d) the average cross-section of letter A. [Zhang 2005]

8.3 SUPERLENSING IN ABSORBANCE MATERIALS

To get an initial gauge of the changes that might be expected from using a superlens with an AMOL system, in particular the interplay between the superlens and the AML, an initial simulation was used to compare the performance of a superlens placed beneath a metal grating to one placed beneath an absorbance grating. This simulation follows the previous simulations for metal and AMOL gratings with and without PRLs (Figs 7.3 and 7.5). Here a 30 nm 'perfect' plasmonic metal layer with loss ($Re\{\varepsilon_{r,prl}\} = Re\{-\varepsilon_{resist}\}$, $Im\{\varepsilon_{r,prl}\} = Im\{\varepsilon_{resist}\}$, where the loss is arbitrarily matched to the resist loss) is placed 10 nm beneath metal and absorbance grating structures (50% duty-cycle, 100 nm period) and a comparison is made of the intensity at 404 nm transmitted into an underlying resist layer (Fig 8.4). This is able to demonstrate that the proposed superlens system is able to interact with an absorbance grating and to allow a comparison of the effects of the change in grating type.

Comparing the two images it is noted that the performance is similar in both cases, with the field intensity peaks created at the edges of the metal gratings being amplified and combined in the superlensing layer to create a more intense, but slightly broader image in the resist layer below the superlens. The intensity is seen to be higher in the absorbance grating case; this is because there is better transmission in this case as the transmitted intensity is slightly wider, due to the increased transmittance through the grating material (absorber versus metal). Although this demonstrates the ability of an absorbance grating to generate surface plasmons for a superlens-type exposure the results demonstrate a strong dependence on the grating edges which are not as clearly present in an AMOL exposure, which may act to reduce the width of the intensity profiles.

Having demonstrated the ability of a superlens to transmit an image from an absorbance grating the performance of the superlens with an AMOL system will now be characterised. This is of interest because it allows the interactions of the two techniques to be

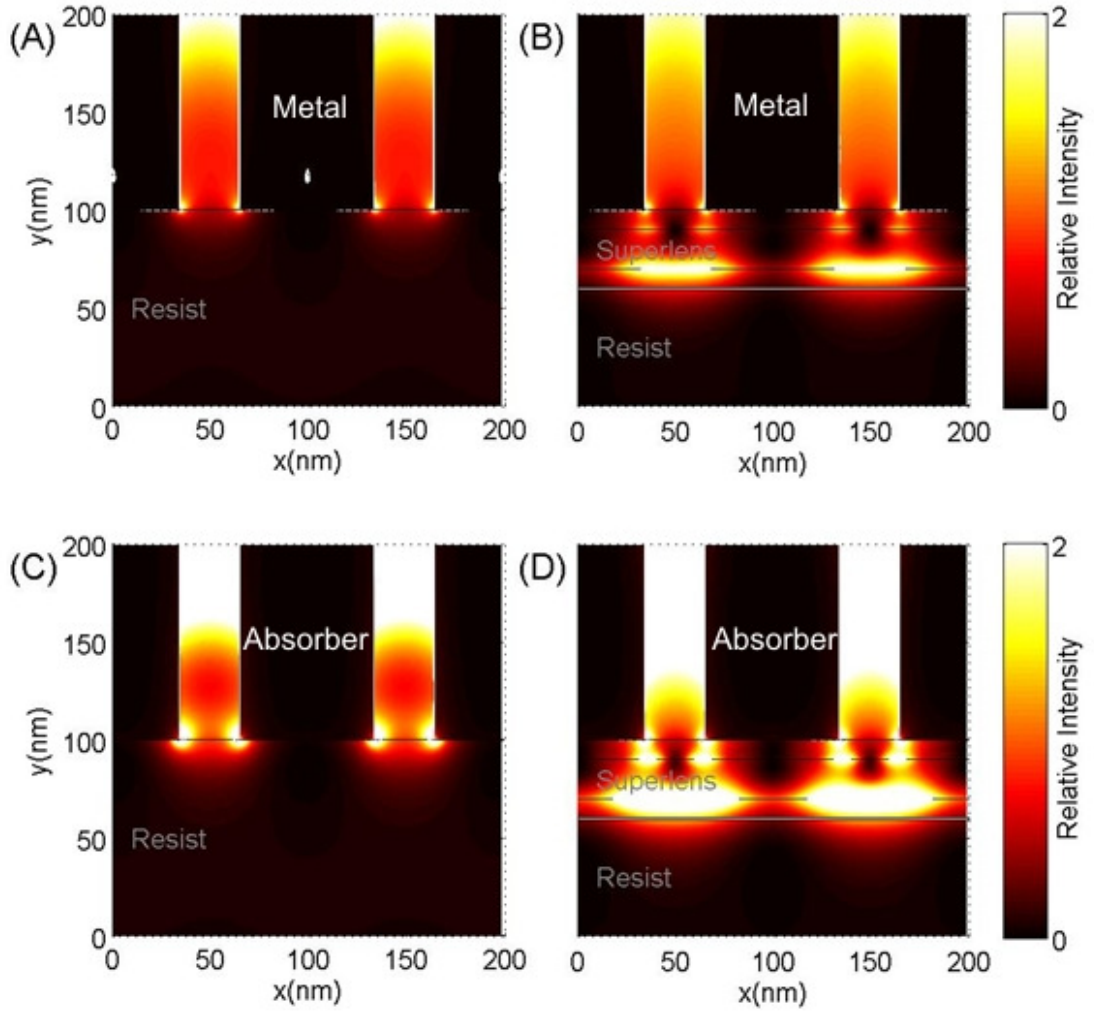

Figure 8.4 Intensity profiles at 400 nm created in a system without (a,c) and with (b,d) a 30 nm superlens with 10 nm spacer into a system with 100 nm gratings of (a,b) metal ($\epsilon_r = -4.4 - 18j$)/air ($\epsilon_r = 1$) and (c,d) absorber($\epsilon_r = 1 - 3j$)/ air ($\epsilon_r = 1$).

seen, firstly to demonstrate the possibility of the superlens to perform when combined with an AML aperture, then to understand how the different reactions of the two wavelengths to a superlens affects performance and whether this may allow dichroic filtering of the unwanted (in the resist layer) wavelength λ_2. It is also expected that, as with the PRL case, the AML layer will be affected by the change in reflections at both wavelengths. These changes will be different from the PRL as there will also be transmission through the superlens layer because it is thinner. The model of the superlens in AMOL

was built from the initial AMOL model in a similar way to the PRL case, with a new layer introduced between the photoresist and the AML (Fig 8.5). The superlens introduced a number of new parameters to the model including the permittivity and permeability of the superlens as well as its positioning and the structure of the superlens and any spacers used.

8.4 INITIAL SIMULATION

Having set up the model and defined the superlens as a single, 30 nm deep layer with permittivity matched to the negative of the photoresist (photoresist permittivity, $\epsilon_{resist} = 2.775 - 0.16i$, superlens permittivity, $\epsilon_{superlens} = -2.775 - 0.16i$) for both incident wavelengths. The AML is 200 nm thick and the photoresist is modeled as infinite, representing a resist perfectly matched to the substrate below. For this initial simulation no spacers were used, as the AMOL system would easily allow a silver layer to be inserted, without the concern with contact to the mask seen in other near-field systems.

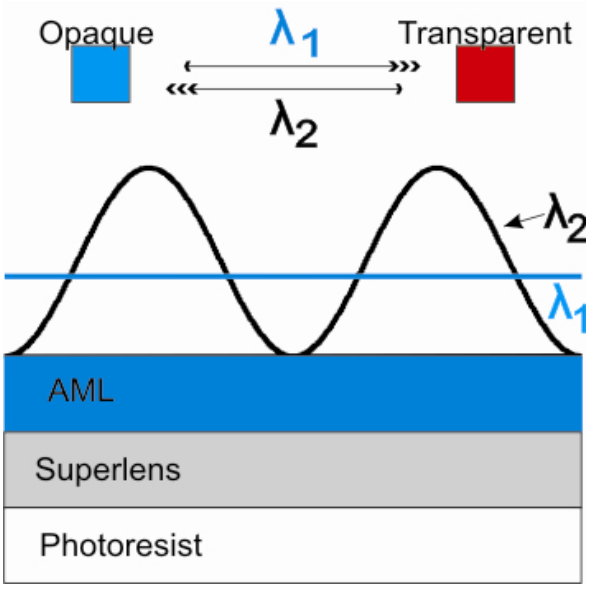

Figure 8.5 Schematic diagram of the AMOL system with included superlens. The superlens may include an additional spacer layer.

The superlens having the same permittivity at both wavelengths is a non-real situation as any plasmonic material is dispersive; however it allows an initial simulation to investigate the limits that may be expected from a superlens when combined with AMOL. The properties of the AMOL layer are the same as used in the PRL simulations, with these values taken from Table 5.1 except that $\rho_{conc} = 1$ and $k_{ba} = 8.5 \times 10^{-6}$ to allow for sub-diffraction limited effects to be more easily explored. The simulations that return the maximum NILS value for an intensity sweep of λ_2/λ_1 are shown in for the AMOL system before (Fig 8.6a) and after (Fig 8.6b) the introduction of the superlens with the corresponding intensity profile shown in Figs 8.7 and 8.8.

There are clear differences seen in these results. The superlens has been able to propagate λ_1 into the resist, however there has been substantial broadening of the intensity waveform after the superlens. This is partially due to the transmission through the superlens, but also because of a widening of the aperture in the AML; the cause of the widening is probably due to the surface plasmons induced on the superlens broadening the λ_1 intensity profile at the AML/superlens interface and thus opening up the aperture, detrimental to the imaging taking place.

8.4.1 INTRODUCTION OF A SPACER

The superlens was introduced as a single 30 nm layer, the resulting λ_1 intensity in the resist demonstrated two intensity peaks from the grating edges being transmitted through the superlens; this had the effect of widening the intensity waveform in the resist. The image transmitted by the superlens is dominated by the images closest to the superlens, hence the introduction of a spacer layer between the AML and the superlens may allow an improved image. This is because in the small spacer layer a single narrow peak will form in the intensity profile (as it does in the matched substrate case) and this image will be transmitted by the superlens, also any surface plasmons induced on the superlens will have less effect on the AML. The result of introducing a 10 nm spacer layer ($\epsilon_{spacer} = \epsilon_{resist} = 2.775 - 0.16i$) above a 30 nm superlens is shown in Figs 8.9 and 8.10.

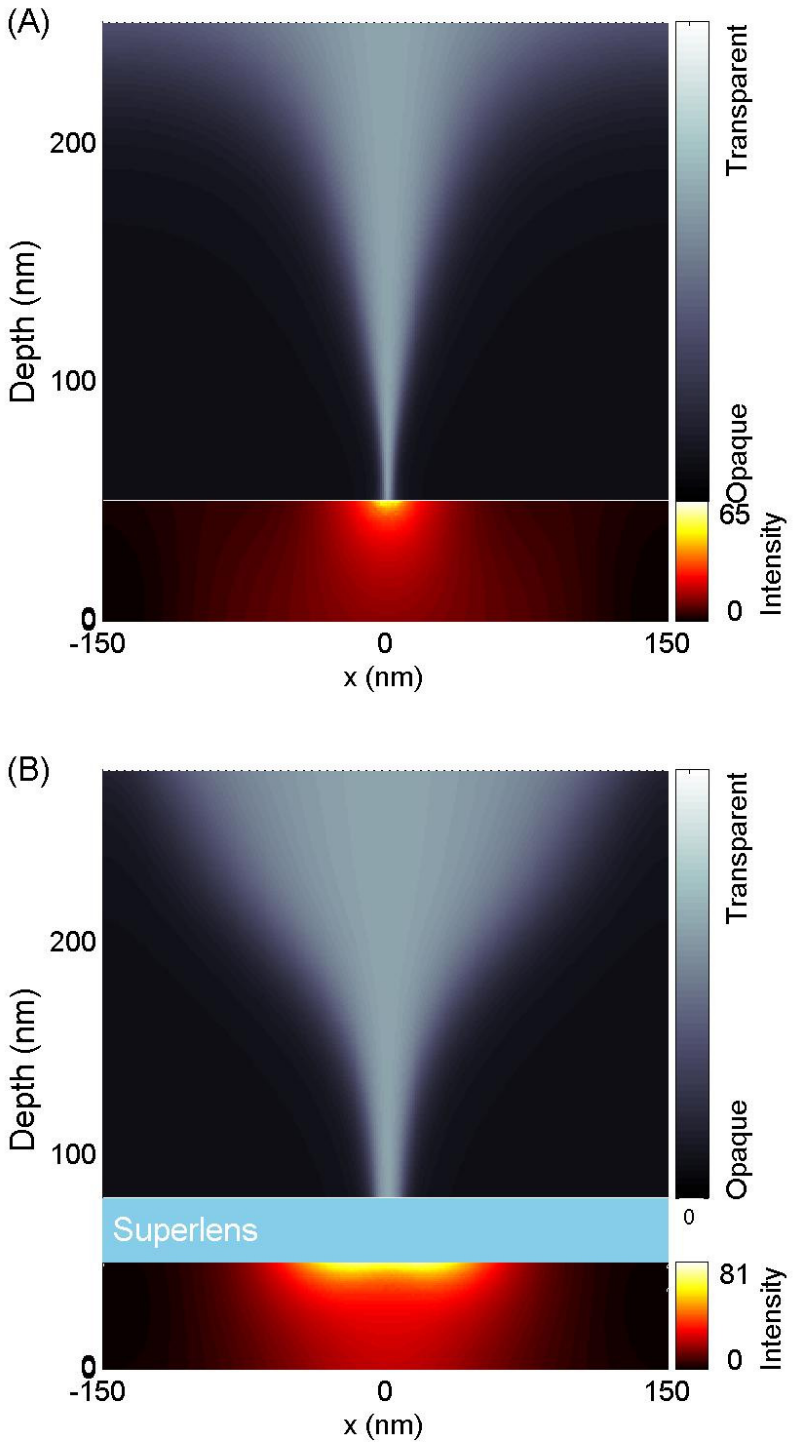

Figure 8.6 Absorbance in the AML and λ_1 intensity in the resist layer for an AMOL system with (a) the resist with a matched substrate directly beneath the AML and (b) with a 30 nm superlens directly between the AML and resist with matched substrate

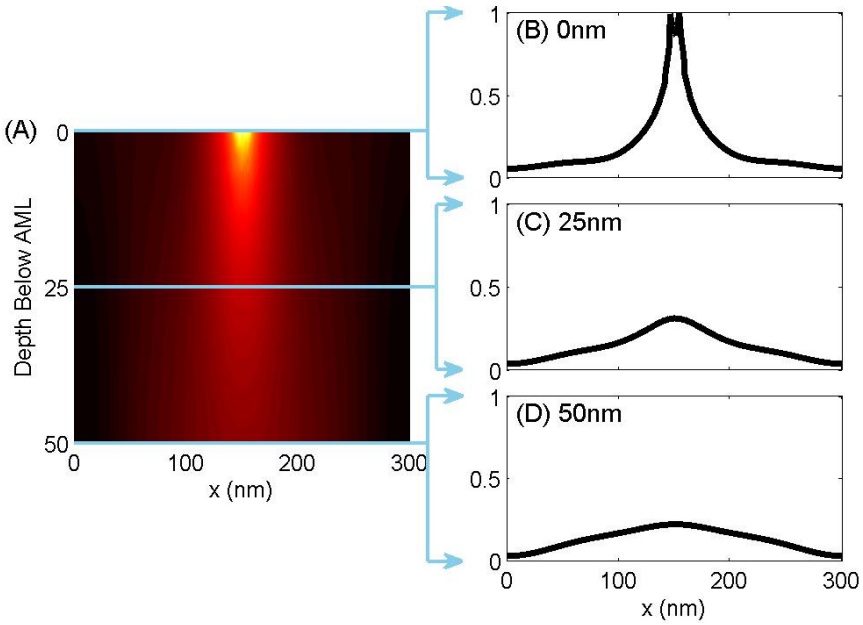

Figure 8.7 (a) Intensity profile for the transmission of λ_1 50 nm beneath an AMOL system with matched substrate. Intensity profiles relative to I_{max} are shown at (b) 0 nm, (c) 25 nm and (d) 50 nm depths.

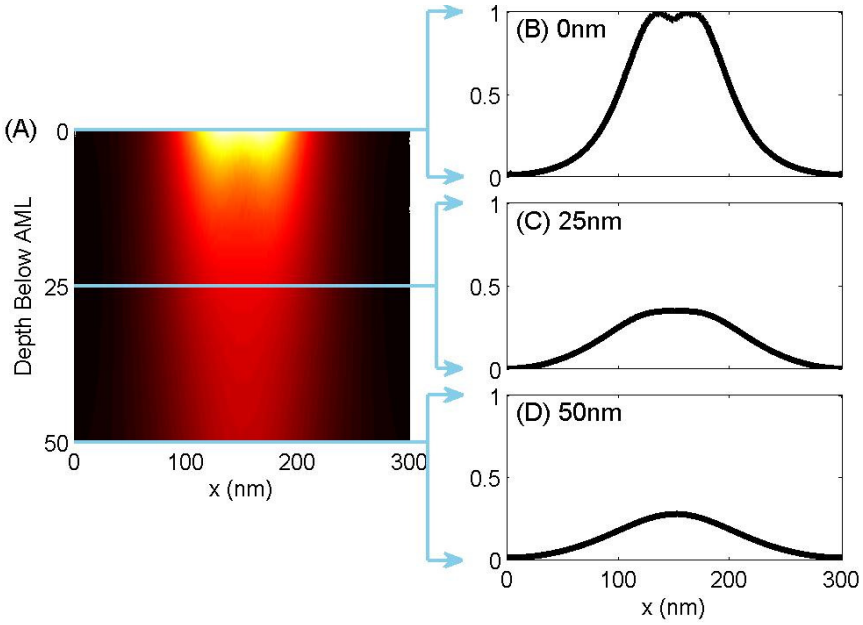

Figure 8.8 (a) Intensity profile for the transmission of λ_1 50 nm beneath an AMOL system with 30 nm ideal superlens sandwiched between the AML and resist with matched substrate. Intensity profiles relative to I_{max} are shown at (b) 0 nm, (c) 25 nm and (d) 50 nm depths.

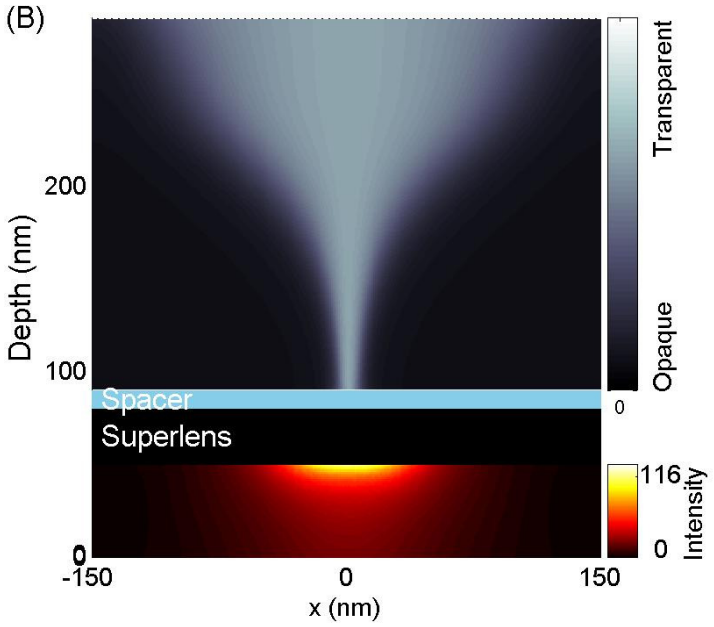

Figure 8.9 Absorbance in the AML and λ_1 intensity in the resist layer for an AMOL system and one with a 10 nm spacer layer and 30 nm superlens directly between AML and resist

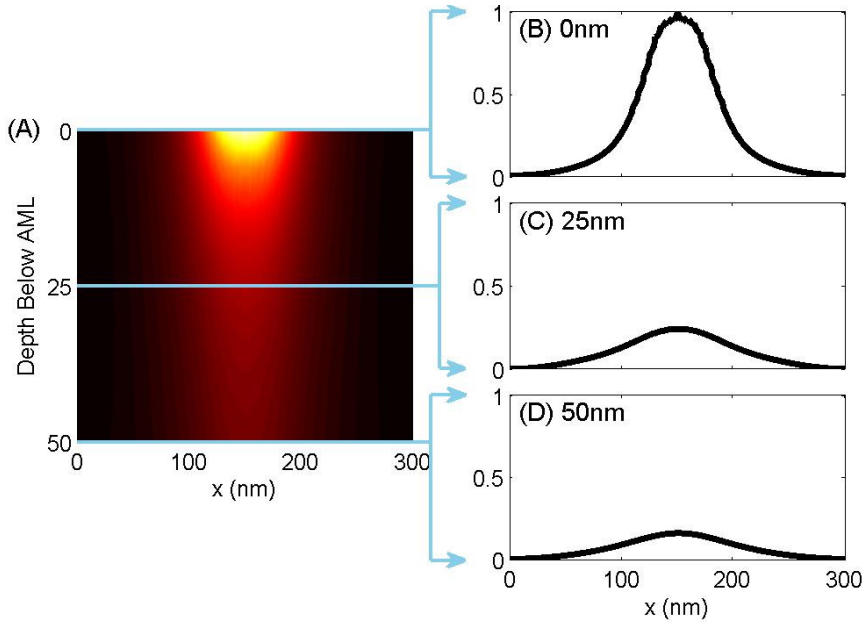

Figure 8.10 (a) Intensity profile for the transmission of λ_1 50 nm beneath an AMOL system with 10 nm spacer layer and 30 nm ideal superlens sandwiched between the AML and resist with matched substrate. Intensity profiles relative to I_{max} are shown at (b) 0 nm, (c) 25 nm and (d) 50 nm depths.

In comparison to the superlens without the spacer layer the absorbance layer shows slightly narrower aperture, although still wider than the matched substrate case, again likely due to the surface plasmons interactions between the superlens and AML. The intensity profile in the resist has also narrowed, with the twin peaks becoming less obvious. This result poses the question of what the optimal thickness of the spacer is, as, at some distance, the decay will be too much and all the desirable features of the intensity profile will be lost. A simulation investigating spacer depths between 5 and 30 nm was run for a 30 nm case (Fig 8.11) demonstrating the optimal distance between 10 and 30 nm for both NILS and FWHM.

8.4.2 FOCUSING EFFECT

In some of the simulations there is a weak focusing effect seen, in which image quality improves with depth into the image for a small distance from the interface between the superlens and resist; as opposed to the matched substrate case in which the best performance will be seen at the interface. For instance, with a 60 nm superlens in contact with the AML intensity plots show improvement with depth (Fig 8.12 and Fig 8.13), although the overall performance is weaker than that achieved with a thinner superlens. This follows from theory, as the superlens should act to focus the image at a distance approximately equal to the spacer depth subtracted from the lens depth [Pendry 2000] (i.e. the

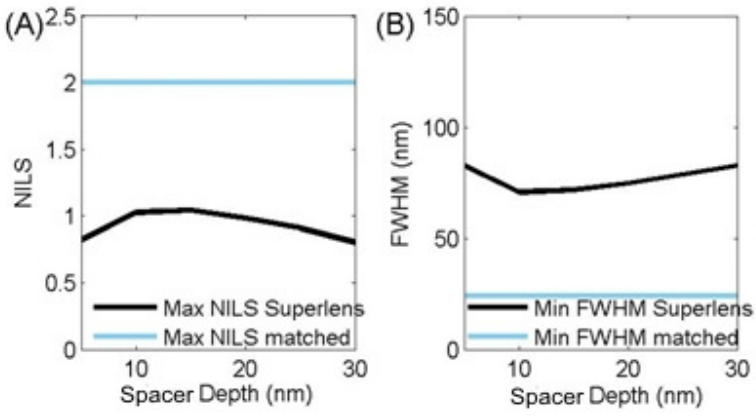

Figure 8.11 Affect on (a) NILS and (b) FWHM of increasing the spacer thickness for a 30 nm superlens.

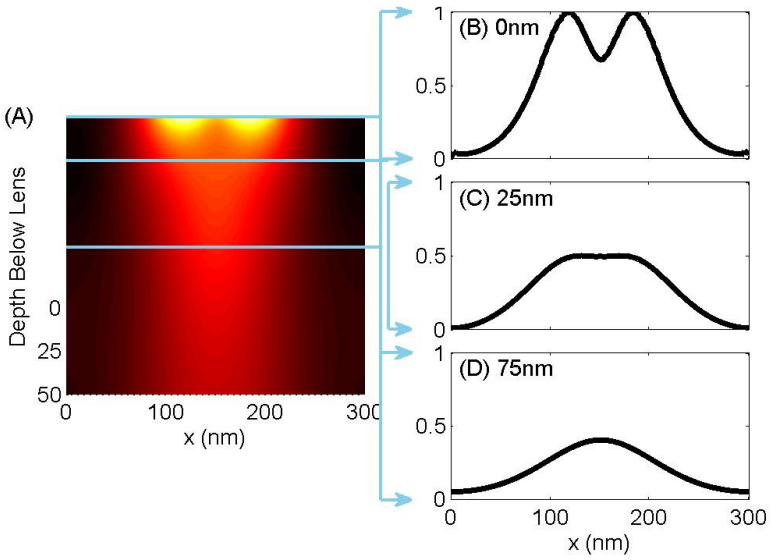

Figure 8.12 (a) Intensity profile for the transmission of $\boldsymbol{\lambda_1}$ 50 nm beneath an AMOL system with a 60 nm ideal superlens sandwiched between the AML and resist with matched substrate. Intensity profiles relative to $\boldsymbol{I_{max}}$ are shown at (b) 0 nm, (c) 25 nm and (d) 50 nm depths.

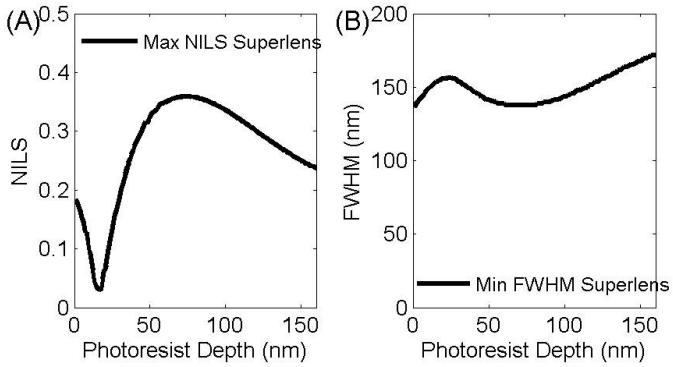

Figure 8.13 (a) NILS and (b) FWHM measured with photoresist depth for the intensity profile shown in Fig 8.12 demonstrating a focusing effect occurring at a depth of ~60-70 nm.

effect is only noticeable when wider apertures are used, with intensity profiles approaching 50% duty-cycle). This focusing effect is examined in Fig 8.13, in which the NILS is measured at 1 nm intervals for the first 160 nm into the resist. The peak NILS is seen at a distance of 60~70 nm into the resist, a similar distance to the minimum FWHM. Although interesting the overall performance of exposures exhibiting this effect is poor; narrower apertures cause strong confinement of light and without additional material parameters causing this to happen any additional focusing seems difficult to achieve.

8.4.3 SUPERLENS THICKNESS

An important question regarding the introduction of a superlens in the AMOL system is how thick the superlens should be to allow the best performance, in terms of a narrow λ_1 intensity exposure being able to be transmitted into the resist layer. An upper limit on thickness is created by the electrostatic approximation needed to ensure that a material with only negative permittivity can act as 'perfect lens'; this restricts the width to something less than the wavelength of λ_1 [Pendry 2000]. An experimental lower limit is also present as it becomes increasing difficult to deposit thin silver films accurately. Here a set of simulations, using the same model as previously detailed, investigate superlenses between 10 and 60 nm thick with a 10 nm spacer layer used. The maximum NILS and minimum FWHM are calculated and plotted in Fig 8.14 against the best case performance of an AMOL system with a matched substrate. This shows that above 20 nm there is a marked increase of the FWHM of the intensity profile and that the NILS peaks for a superlens between 15 and 20 nm thick. The superlens is able to produce some form of image for all the lens depths but as the depth increases the confinement is reduced, producing an image that is closer to 50% duty-cycle of the λ_2 standing wave than the desired subwavelength image. As the superlens depth is reduced the performance gain is limited by the lack of depth of superlens to amplify the intensity.

8.4.4 METRICS OF A SUPERLENS IN AMOL

To improve the analysis of how well the superlens can transmit an image into an underlying resist a 15 nm ideal superlens with a 10 nm spacer is examined. Firstly a sweep is made of the intensity ratio λ_2/λ_1 and the NILS and FWHM metrics are compared to an AMOL system with a substrate perfectly matched to the resist (Fig 8.15) for the first 50 nm of the resist. The results demonstrate how well a superlens may be able to interact with an AMOL system. The metrics show two important features: the overall performance has been reduced slightly but interestingly there is also some improvement in the DOF as seen by improvement in the minimum NILS and Maximum FWHM.

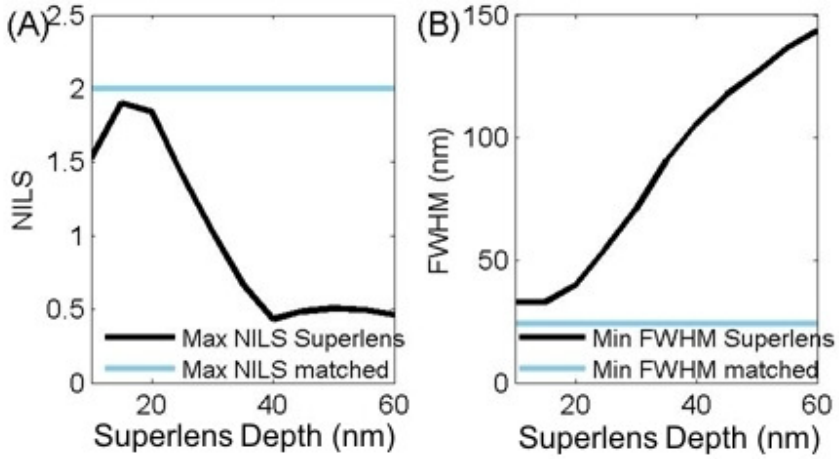

Figure 8.14 Effect of changing superlens depth on the transmission of $\boldsymbol{\lambda_1}$ as measured by (a) NILS and (b) FWHM

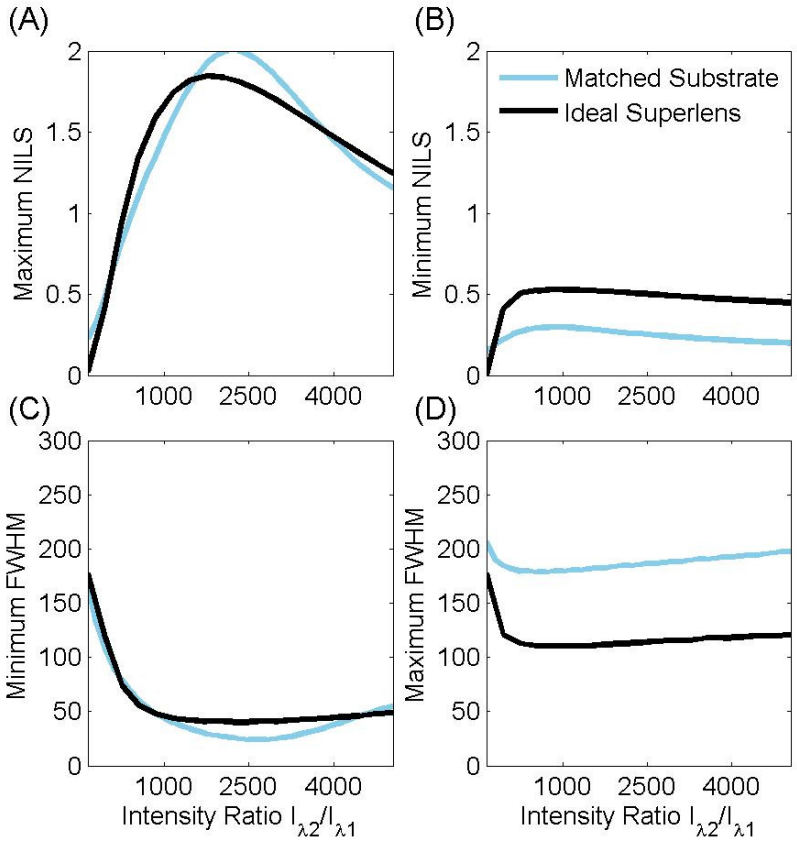

Figure 8.15 Comparison of the maximum and minimum NILS (a,b) and FWHM (d,c) between AMOL systems with and without a 15 nm ideal superlens with 10nm spacer layer as the incident intensity ratio λ_2/λ_1 is varied

The reduction in peak performance is reasonable as the superlens using a plasmonic metal is only an approximation of a 'perfect lens' and hence some losses in high-frequency components and the loss in the simulated ideal lens should be expected to degrade the performance of the system. The increase in the minimum FWHM can be attributed to the surface plasmons not being perfectly localized and then being amplified by the superlens layer, broadening the intensity waveform. The lensing effect of the superlens explains the improvement in the DOF as there is some focusing of the fields passing through the superlens, unfortunately the evanescent nature of the fields ensures that they decay in the resist, hence it is unlikely to be useful to add a spacer layer beneath the superlens to improve the initial NILS. The intensity ratio which gives the best case NILS is used to show the absorbance in the AML and intensity ratio in the resist (Fig 8.16), clearly showing very good lateral confinement close to the interface between superlens and resist.

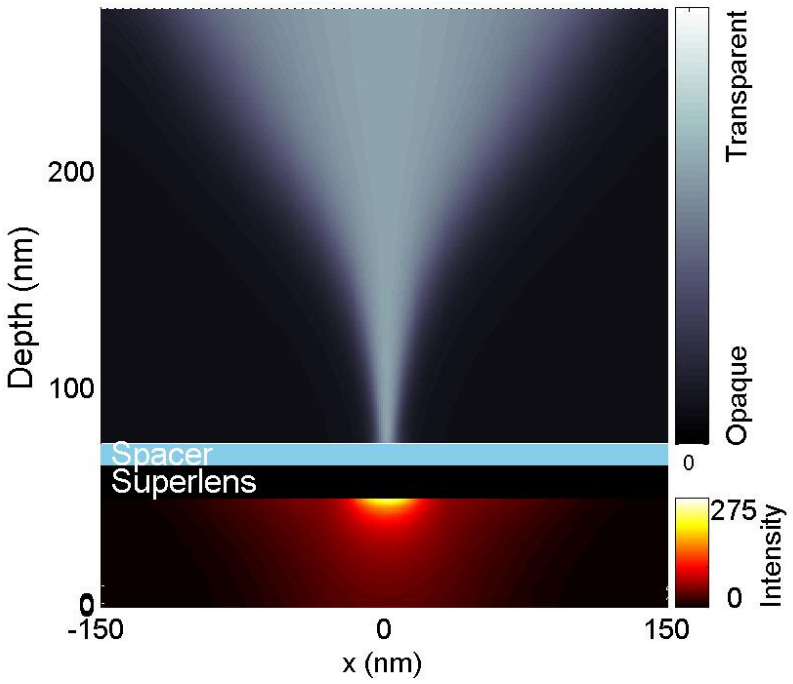

Figure 8.16 AML absorbance and resist intensity plots for the best case NILS AMOL system and an AMOL system with a 10 nm spacer layer and 15 nm superlens directly between AML.

8.4.5 INTENSITY PROFILES WITH SUPERLENS

Continuing from the previous analysis it is interesting to explore how the intensity profiles in the resist have changed with the introduction of the superlens. Here the best case intensity ratio from the 15 nm superlens with 10 nm spacer is explored (Fig 8.17); the matching figure for the matched substrate case reproduced here to allow for comparison (Fig 8.18). Comparing first the intensity profiles at the top of the resist layers (Figs 8.17b and 8.18b) the highest spatial frequency components, the two peaks generated by the aperture edges, have been lost in the transmission by the superlens and are not visible in Fig 8.17b. The peak intensity at λ_1 for the best NILS result in the resist has increased markedly with the introduction of the superlens, from 65a.u (Fig 8.6) to 275a.u (Fig 8.16). The increased λ_1 intensity transmitted into the resist in the case of the superlens is due to amplification of the evanescent fields [Liu 2003], and leads to the improved contrast as the minimum intensities stay reasonably similar.

The intensity profile at the top of the resist layer for the superlens shows strong confinement in the central region, with a sudden broadening below a relative intensity of ~0.2. As the image propagates through the resist layer the central peak decays rapidly, however the reason for the decreased maximum FWHM noted earlier is seen to be that λ_1 remains confined to a broad peak. In comparison to the matched substrate case the intensity nulls at the edges of the intensity profiles are stronger (Figs 8.17c and 8.18c); unfortunately the overall decay in comparison to the initial intensity is more severe, which is undesirable assuming a simple resist model, such as a threshold level. From this examination of the intensity profiles in the resist it has been shown that the superlens transmits λ_1 differently from an AMOL system with a matched substrate. Although the initial intensity profiles provided somewhat similar metrics there are large differences in the profiles, due to loss of the highest spatial frequencies and the focusing of the superlens.

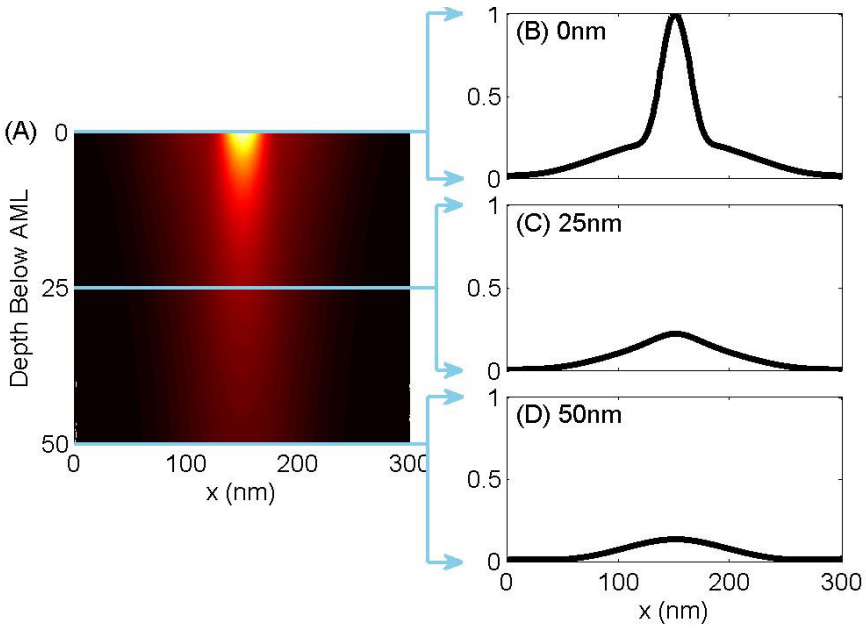

Figure 8.17 (a) Intensity profile for the best NILS case for transmission of λ_1 50 nm into a resist layer by an AMOL system with a 10 nm spacer and 15 nm ideal superlens sandwiched between the AML and resist with matched substrate. The intensity profiles are relative to I_{max} in the resist and are shown at (b) 0 nm, (c) 25 nm and (d) 50 nm depths.

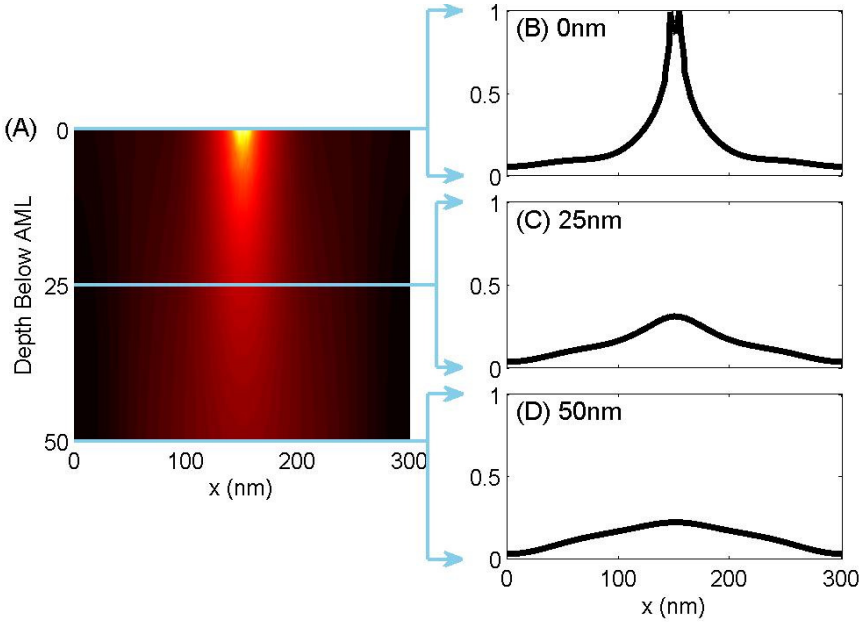

Figure 8.18 (a) Intensity profile for the best NILS case for transmission of λ_1 50 nm into a resist layer by an AMOL system with a matched substrate. The intensity profiles are relative to I_{max} in the resist and are shown at (b) 0 nm, (c) 25 nm and (d) 50 nm depths.

8.4.6 TRANSMISSION OF λ_2 THROUGH THE SUPERLENS

The superlens will transmit the two wavelengths differently, even when modeled as an ideal superlens, because the λ_2 intensity waveform does not contain the same high spatial frequencies as those present in λ_1. This is because the absorbance modulation of the modeled system does not affect the longer λ_2 wavelength as strongly. Hence it is expected that there should be a decrease in λ_2 due to loss in the superlens and alongside the increase in λ_1 due to surface plasmon effects this should result in a reduced λ_2/λ_1 intensity ratio. In this section the focus is placed on the intensity levels of both of these wavelengths because it is desirable that the amount of λ_2 reaching the resist should be reduced, as a non-ideal resist will have a range of sensitivity to a bandwidth of wavelengths and the sinusoidal waveform of λ_2 peaks at the points desired to be nulls (Fig 8.5). The ability of the superlens to act as a dichroic filter would increase the usefulness of the superlens. To examine this effect more closely the intensity of λ_1 and λ_2 and the ratio λ_2/λ_1 are examined in the resist layer

Using the same model as previously used to calculate the systems performance metrics, a 15 nm superlens with a 10 nm spacer layer, the maximum values of the intensities at both wavelengths and their ratio were calculated. The results (Fig 8.19a), plotted on a log scale, demonstrate a strong increase in the magnitude of λ_1 into the resist, this effect had been seen earlier when examining the intensity of λ_1 in the resist layers. The maximum λ_1 intensity occurred at an intensity ratio of ~5, this is the point at which the best coupling between the surface plasmons and the spatial frequencies created by the light passing through the AML aperture occurs. Unfortunately the filtering effect of the superlens layer is reduced by the thinness of the layer and limits the decay in λ_2 when transmitted through the superlens (Fig 8.19b). Loss is, however, clearly visible in the simulation results and this loss is reasonably constant across the intensity range. A thicker lens would increase this loss, but at the cost of imaging performance; this relation will be explored further using a real superlens material which is likely to have more loss at λ_2. The intensity ratio, λ_2/λ_1, is of central importance to this discussion as this shows how selective the resist layer needs to be to adequately resolve λ_1 features without

exposing λ_2. Here a decrease by an order of magnitude is seen for intensities above ~5 (Fig 8.19c), mainly driven by the increased transmission of λ_1; this is a good improvement and suggests that it is plausible that even a very thin superlens can allow reasonable imaging alongside dichroic filtering ability if that is required.

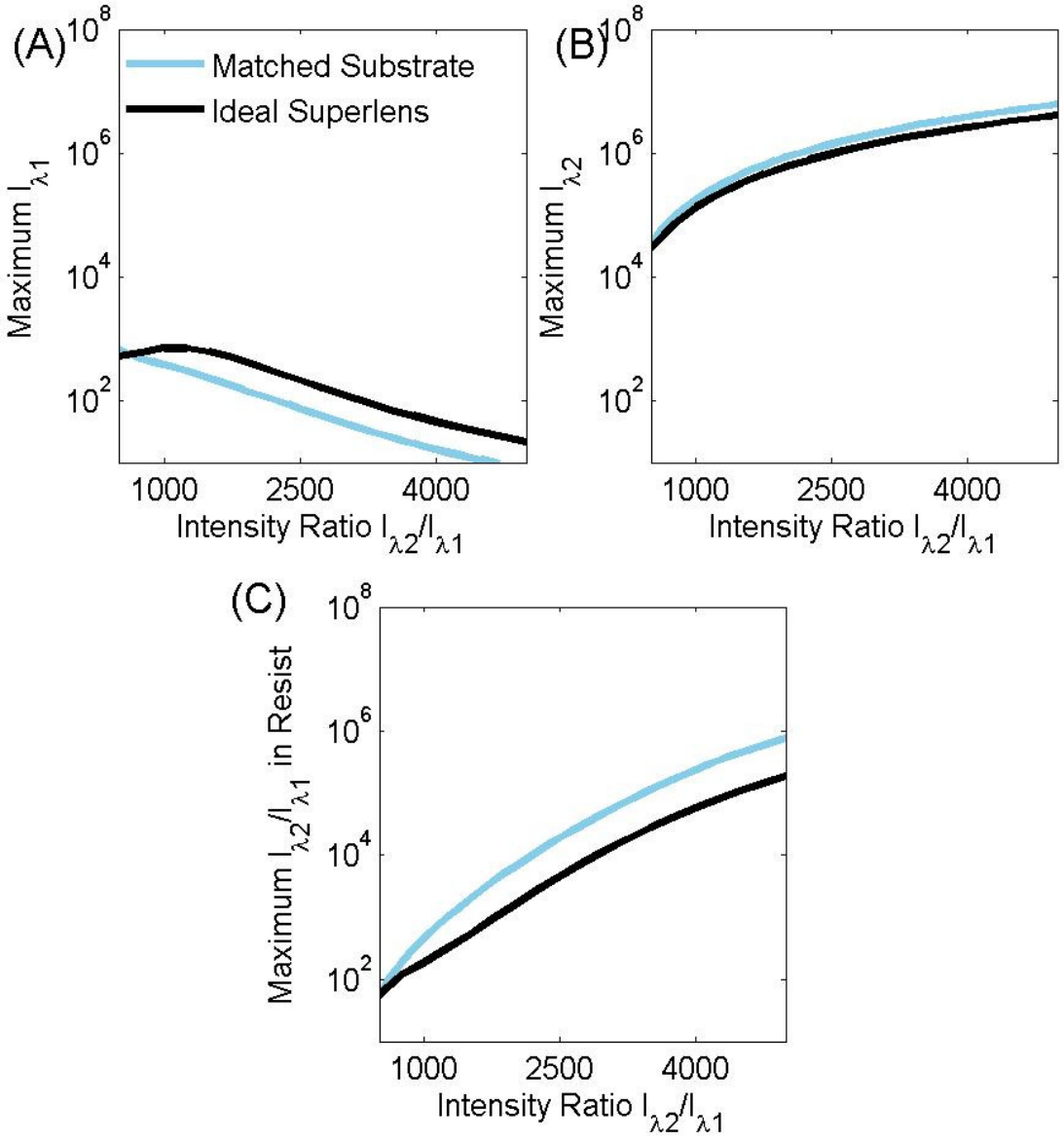

Figure 8.19 Comparison of the maximum intensities of (a) λ_1, (b) λ_2 and (c) λ_2/λ_1 between an AMOL system with a matched substrate and an AMOL system with an ideal 15 nm superlens ($\epsilon_r = -2.775 - 0.16i$) with 10 nm spacer.

8.4.7 ABSORBANCE IN THE AML

The introduction of the superlens has also affected the AML with distinct changes in the absorbance patterns compared to the AMLs of AMOL systems with a matched substrate and a PRL (Figs 7.12 and 7.13). The absorption profile in the AML, and a set of horizontal absorbance profiles are reproduced for the matched case in Fig 8.20 and shown for a 15 nm superlens with 10 nm spacer case in Fig 8.21. As in the case of the PRL the introduction of the superlens has created a standing wave in λ_2 due to the propagating nature of the standing wave at this wavelength and reflection by the superlens. The effect of this is visible in the AML, as there is a sharp narrowing of the absorbance aperture 80 nm into the layer. The two major changes are that the superlens is now closer to the AMOL (the spacer is only 10 nm thick) which causes the standing wave to be higher in the AML and there is now transmission of both wavelengths through the superlens layer because it is suitably thin.

The transmission of λ_1 through the superlens enhances the surface plasmon effects on both surfaces and if high spatial frequencies are present in λ_1 this acts to widen the aperture in the AML. The transmission of λ_2 through the superlens reduces the reflectance and hence the strength of the standing wave, reducing the ability of the AML aperture to be tightly confined. The impact of these changes is to increase the width of the aperture, explaining why the aperture size, and partially why the FWHM of λ_1 in the resist, are larger than in an AMOL system with a matched substrate for the case giving the best NILS value. Increasing λ_2 will, of course, close the aperture further, but the transmitted image quality will deteriorate. The changes taking place in the absorbance layer do not encourage the formation of apertures as narrow as those seen in either the matched or PRL cases; the standing wave pattern in the resist is slightly longer but this does not appear to have significant compensating affect on the system's ability to define the narrowest of apertures. However the apertures created are still narrow enough to allow the transmission of tightly confined intensity profiles through the superlens, as was demonstrated earlier.

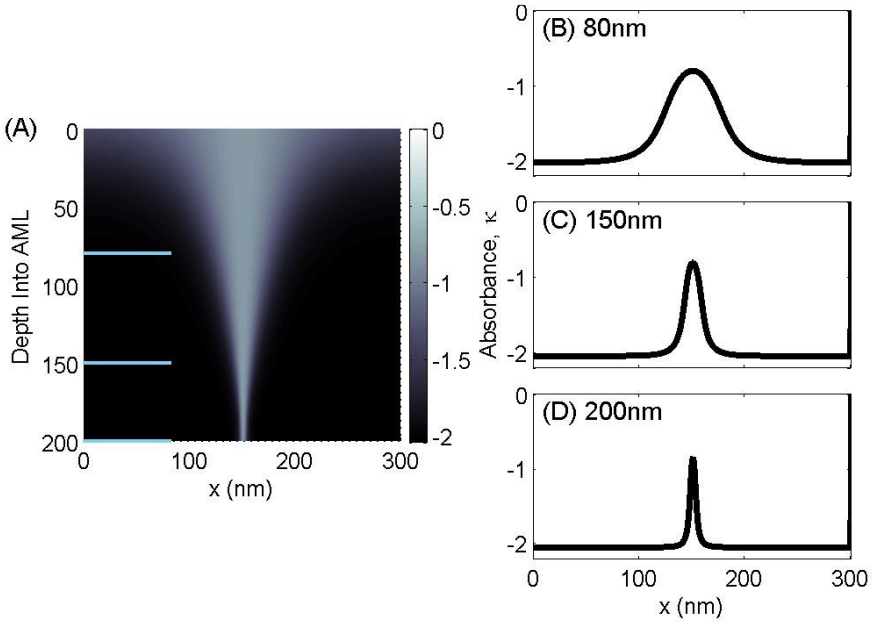

Figure 8.20 (a) AML absorption in the best NILS case for a matched substrate AMOL system. Absorbance is represented by the imaginary part of the refractive index, κ, ranging from 0 to 2. Horizontal absorbance profiles are shown at (b) 80 nm (c) 150 nm and (d) 200 nm into the AML

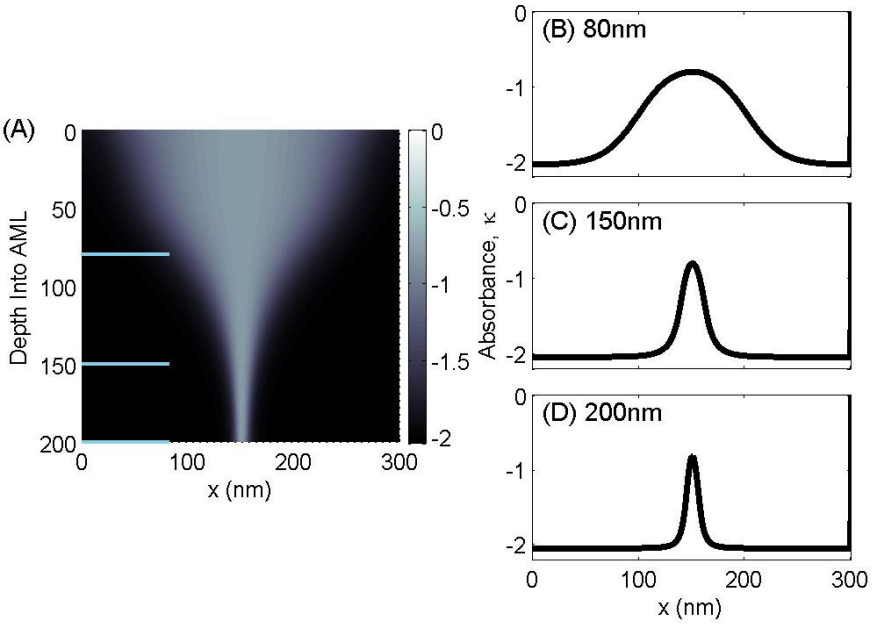

Figure 8.21 (a) AML absorption in the best NILS case for an AMOL system with a 15 nm ideal superlens and 10 nm spacer. Absorbance is represented by the imaginary part of the refractive index, κ, ranging from 0 to 2. Horizontal absorbance profiles are shown at (b) 80 nm (c) 150 nm and (d) 200 nm into the AML

8.5 A SILVER SUPERLENS

In order to examine the performance of the introduction of a superlens into a real system the ideal lens values need to be replaced by real material parameters, in the case of the superlens the most common choice is silver, given its low absorption at optical frequencies, although other possibilities have been reported including gold and the alkali metals [West 2010]. Here the superlens previously modeled using an ideal lens (with loss) will be replaced by a silver layer to investigate the possible performance from a real material, the silver layer is modeled with a permittivity of $\epsilon_r = -4.70 - 0.22i$ at 405 nm and $\epsilon_r = -12.6 — 0.42i$ at 546 nm. It is expected that there will be some degradation in performance due to worse coupling to the surface plasmons on the silver surface and increased losses, as well as a reduced bandwidth of spatial frequencies which are enhanced by the superlens.

8.5.1 INTENSITY PROFILES

The substitution of the ideal superlens layer by a silver plasmonic layer led to large changes in the performance of the superlens. The simulations used the same model as the ideal superlens but substituted in the silver permittivity values. The height of the silver layer was varied between 10 and 60 nm and the best NILS and FWHM results were calculated (Fig 8.22). A drastic drop in performance is seen, with limited plasmonic transmission being seen except for the thinnest silver layers. The maximum NILS, 1.4, is for the 10 nm silver superlens, as is the minimum FWHM, 51 nm, a rise is seen in the NILS for higher depths but this is erroneous due to the formation of two wide peaks and the NILS being calculated for the inside slope.

Examining the intensity profile for the best NILS result, occurring for a 10 nm silver superlens (Fig 8.23) some similarities are seen in comparison to the ideal superlens case (Fig 8.17) as there is a reasonably sharp central peak and a wider base intensity. Unfortunately unlike the ideal superlens case the image deteriorates quickly, with decay in the central peak and the formation of undesirable side-lobes; thus even for the best case the

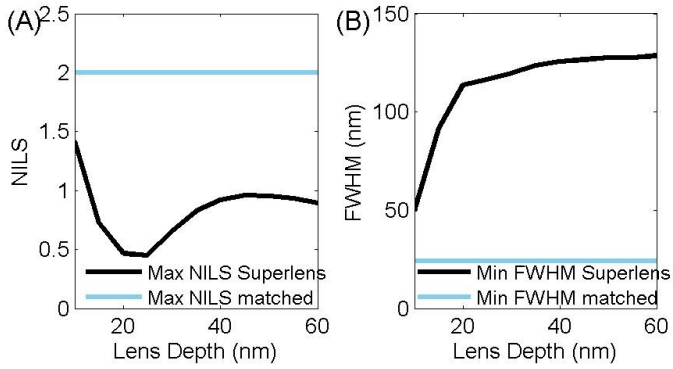

Figure 8.22 (a) NILS and (b) FWHM for λ_1 as the thickness of a silver superlens is increased (at 405 nm)

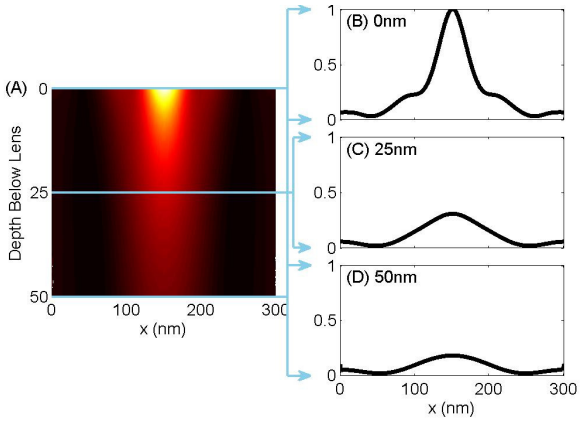

Figure 8.23 (a) Intensity profiles having the best NILS for transmission of λ_1 50 nm beneath an AMOL system with a 10 nm spacer and 10 nm silver superlens sandwiched between the AML and resist. Intensity profiles relative to I_{max} are shown at (b) 0 nm, (c) 25 nm and (d) 50 nm depths.

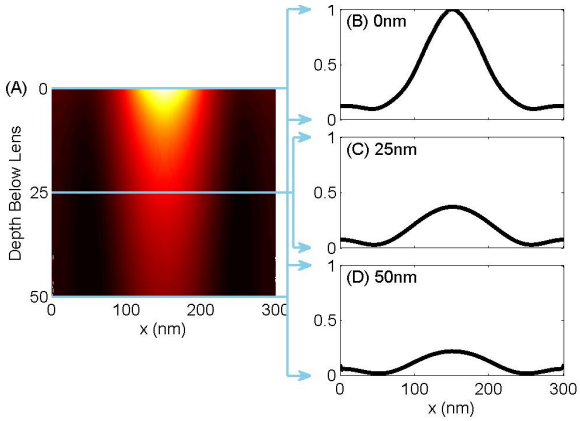

Figure 8.24 (a) Intensity profiles having the best NILS for transmission of λ_1 50 nm beneath an AMOL system with a 10 nm spacer and 15 nm silver superlens sandwiched between the AML and resist. Intensity profiles relative to I_{max} are shown at (b) 0 nm, (c) 25 nm and (d) 50 nm depths.

intensity profiles are poor. Investigating the resist intensity for the best case 15 nm superlens enables some clarification of the problems with the silver superlens. There is very little amplification of the high spatial frequencies, thus the narrow intensity peak decays rapidly. There is, however, increased transmission at lower frequencies and these produce the wide intensity profile and sidelobes. It is not unexpected for a real superlens to have limited bandwidth over which enhancement is seen [Fang 2003], nor is the enhancement always uniform [Moore 2008] however it suggests that a change to the system may improve performance, either a change of the wavelength, changing the plasmonic metal, or increasing the permittivity of the spacer should act to alleviate the problems.

Taking the refractive index as that of silver at the mercury I-line (365 nm) the permittivity is changed to $\epsilon_r = -2.6 - 0.4i$ whilst keeping the simulation wavelength at 405 nm and the permittivity at 546 nm as $\epsilon_r = -12.6 — 0.42i$ results in the expected improvements in the intensity profile in the resist (Fig 8.25) where the high spatial frequencies

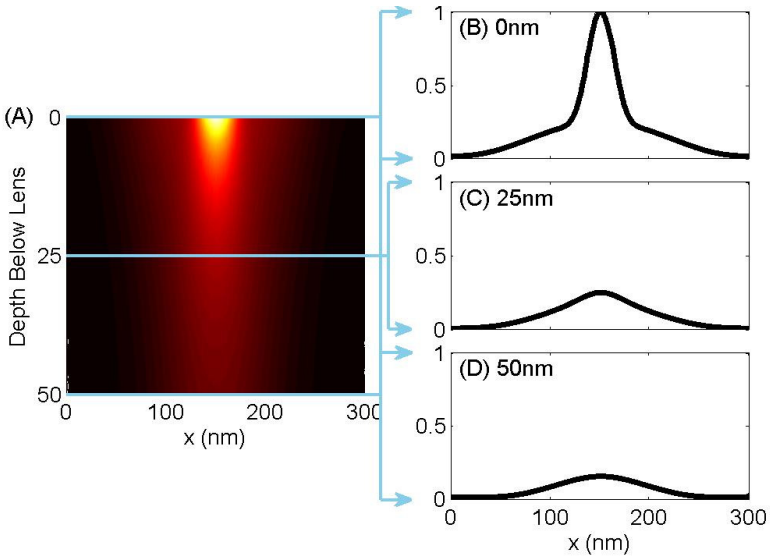

Figure 8.25 (a) Intensity profile for the best NILS case for transmission of λ_1 50 nm beneath an AMOL system with a 10 nm spacer and 15 nm silver (at 365nm) superlens sandwiched between the AML and resist with matched substrate. Intensity profiles relative to I_{max} are shown at (b) 0 nm, (c) 25 nm and (d) 50 nm depths.

are again being amplified and successfully transmitted by the superlens. Thus the choice of exposing wavelength is particularly important if the silver superlens is going to be considered experimentally as otherwise it will be extremely difficult to see any improvement.

8.5.2 TRANSMISSION OF λ_2 IN A REAL SUPERLENS

Previously the ideal superlens demonstrated a drop in the transmission of λ_2, here the study is repeated using a silver layer which has a permittivity $\epsilon_r = -12.6 — 0.42i$ at 546 nm. Using a silver superlens thickness of 15 nm and performing a sweep of the intensity ratio λ_2/λ_1 allows comparison with the earlier data for the matched case (Fig 8.26). Similar to the perfect reflector case there is a peak in the λ_1 transmission created by the superlens effects and a decrease in the λ_2 transmission due to the silver layer. However with the silver superlens the λ_1 enhancement has decreased there has been increased suppression of λ_2 due to increased losses at both wavelengths.

In comparison to the ideal superlens case λ_2 has been more strongly attenuated by the lens due to the increased reflectance of the lens with the change in permittivity and increased loss in the silver layer. Reducing the impact of this desired reduction there has also been a reduction in the intensity of λ_1 caused by weaker coupling to the surface plasmons and increased loss in the silver layer at 405 nm, however the effects of this reduction are smaller. The ratio of λ_2/λ_1, Fig 8.26c, demonstrates the capability of a superlens system to provide a dichroic filtering effect, reducing the transmission of the undesirable λ_2 peaks by approximately an order of magnitude. This effect would be increased by increasing the depth of the silver superlens layer or by going to tuned silver-dielectric multi-layers; but as detailed previously this would come at the cost of a loss in performance. Further changes, such as changing the spacer layer materials or increasing the duty-cycle may also improve the silver superlens performance. Any experimental work introducing a silver superlens to AMOL would need to work with material imperfections such as surface roughness that can cause further problems [Schøler 2010, Schøler 2009] but have not been considered here.

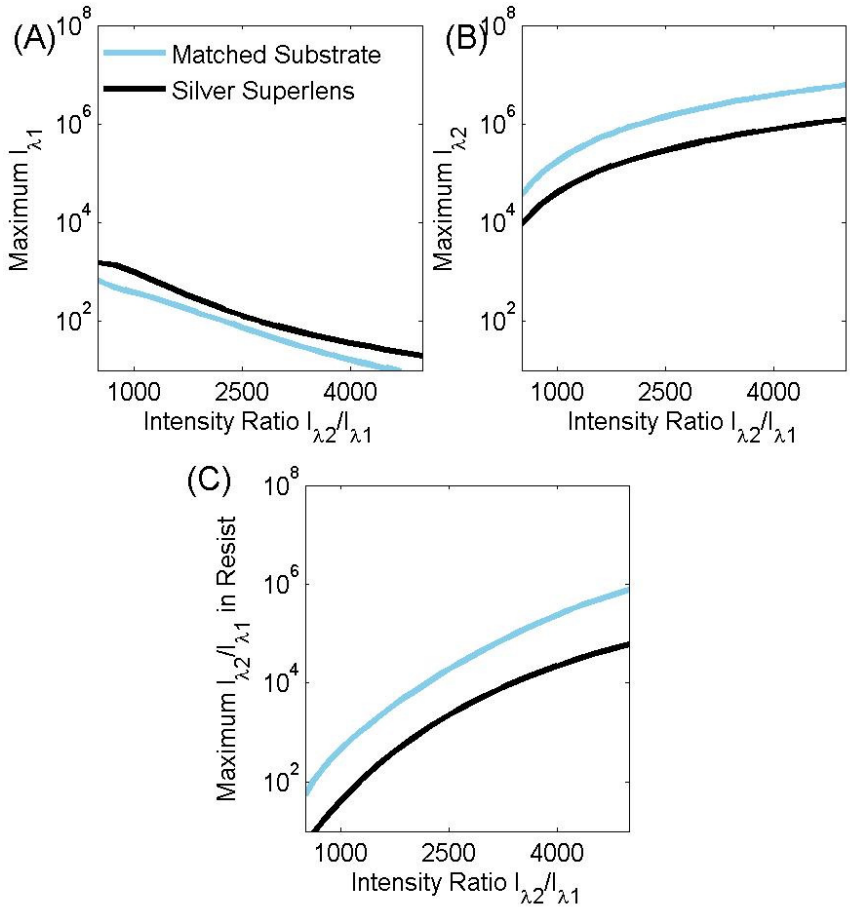

Figure 8.26 Comparison of the maximum intensities of (a) λ_1, (b) λ_2 and (c) λ_2/λ_1 between an AMOL system with a matched substrate and an AMOL system with an silver type, 15 nm superlens ($\lambda_1, \epsilon_r = -2.6 - 0.4i, ; \lambda_2, \epsilon_r = -12.6 — 0.42i$) and 10 nm spacer.

8.6 CONCLUSIONS

In this chapter the idea to use a superlens to project a near-field image has been introduced to an AMOL system with an adaptive absorbance mask, using the full-vector FEM model developed in this thesis. The change in superlens performance between a metal and absorbance grating was first, briefly, compared using a rectangular grating, clearly showing evanescent field enhancement but not great confinement. Then using the AMOL model an ideal superlens ($\epsilon_r = -2.775 - 0.16i$) was used to indicate the performance that could be expected from a well matched superlens, with both the

transmission of λ_1 into the resist and the shape of the intensity profiles in the resist being examined. The reduction in the level of λ_2 in the resist due to increased reflection and absorption by the silver layer was also detailed. Finally the system was modeled using real material parameters for the superlens to indicate how the simulations could be realised experimentally.

The introduction of a superlens into an AMOL system allowed the image profile in λ_1 to be successfully transmitted into a resist with only limited decay in performance for short lens thicknesses in the ideal case modeled here and demonstrated good confinement of the surface plasmons was possible in this system. Examination of the intensity profiles revealed the amplification of some of the high spatial frequency components and some improvement in the DOF due to this amplification. Although this performance is interesting and demonstrates the ability of an absorbance type mask to generate the required fields for the superlens the performance gain is unlikely, by itself, to warrant the additional fabrication complexity of introducing a silver lens to the system as the PRL has shown greater ability in increasing the DOF without reduction in performance. The second feature of the superlens in the AMOL system, which sets it apart from a typical lithographic system, is that the superlens can have a useful function as a dichroic filter, enhancing λ_1 and absorbing λ_2. This would be useful in an AMOL system because a real resist will have absorbencies across the wavelength spectrum and the high incident intensities at λ_2 can detriment the resist exposure. The introduction of the superlens was shown to allow, for thin lenses, reasonably well maintained performance and a reduction in the λ_2 intensity reaching the resist by an order of magnitude.

The final section of this chapter examined how the ideal superlens could be replaced by a real material, with the first choice being a silver superlens due to its low loss and previous use in metal systems. Unfortunately the wavelength used to model the system did not allow a large bandwidth of high spatial frequencies to be transmitted and there was a large drop in performance except for very thin silver layers. It was demonstrated that the use of an alternative, shorter, wavelength such as the mercury I-line could

overcome this problem but this would change the system parameters also used (an alternative AML material with λ_1 of 322 nm has been described [Andrew 2009]).

This chapter has demonstrated the effect that the introduction of a superlens could have on an AMOL system, including projection of the image and the ability to partially filter λ_2. Although there is some loss of performance with the superlens the addition of the filtering aspects suggest a superlens could make a useful contribution in some situations. It has also been shown that, as with other superlens work there is strong dependence on the material used for the superlens and its ability to interface with the mask and resist layers, here silver at 405 nm performed poorly but it was shown that a wavelength change could reduce this problem. The concept of a superlens in a near-field lithography system, implemented though a thin plasmonic metal layer, is an interesting one and has shown advantages to an AMOL system, when the material parameters can be matched.

Chapter 9

CONCLUSIONS AND FUTURE WORK

9.1 REVIEW OF THESIS

This thesis has used FEM simulations to explore AMOL, the effects of polarisation and the interaction between AMOL and surface plasmons. AMOL uses a photochromic material as an adaptive masking layer and because this can be placed in intimate contact with a resist layer allows imaging using the near field. The work in this thesis furthered the understanding of AMOL as well as investigating proposed improvements to AMOL to allow easier imaging. The background material explaining lithography's goal to allow continual reduction in feature size was outlined in Chapters 1 and 2, as were the obstacles facing conventional projection lithography. These obstacles continue to encourage the development of alternative techniques, such as AMOL, and the complex challenges involved in understanding them.

The major contribution of this thesis has been the development of a full vector-field finite element method (FEM) model of the AMOL system and the use of this model to explore AMOL, as introduced in Chapters 3 to 5. The vector nature of the simulation allows for additional insights, not available with the scalar approaches, due to effects such as diffraction inside the apertures and the polarisation of the incident illumination. The model of AMOL described in this thesis encompasses the interactions of two separate wavelengths (λ_1 and λ_2) in the AML layer to determine the appropriate absorbance of the apertures and the transmission through the system. The absorbance state of the AML is central to the operation and effectiveness of AMOL. The complex effects of light propagation through the AML apertures define the image in the resist layer. The

model of AMOL has allowed an understanding of the abilities and limitations of the AMOL and demonstrated system constraints.

The use of an AML as an adaptive mask differentiates AMOL from other near-field lithography systems which are based on dielectric or metal masks. This difference in masking layer was explored in Chapter 6, with particular examination of the polarisation effects. This showed clearly that TM polarised λ_1 allowed the best system performance and importance of strongly differentiated opaque and transparent mask regions. This was explained by considering the fields involved; in TM polarisation there are electric fields in the plane of the AML and these interact strongly with the change of absorbance at the aperture to create a tightly confined intensity profile. This section of the thesis showed that AMOL is able to produce sub-diffraction limited intensity profiles, but these are weaker than for a comparative metal mask. The importance of material parameters was also discussed, in particular the thermal constant (k_{BA}) and photochrome density (ρ) had large effects on the system and set limits on the FWHM able to be achevied.

An important feature of any lithography system is the transmission of the created intensity profile into a reasonable thickness of underlying photoresist to allow easier fabrication. The industry goals for a ~66 nm DOF for 22-nm half-pitch features are demanding for near-field systems. Near-field systems struggle with DOF because of the inherent exponential decay in the images formed, and AMOL is no exception to the trend, in fact due to less distinction between 'opaque' and 'transparent' regions there was a deterioration of the DOF as measured by contrast with respect to metal gratings shown in Chapter 6. Chapter 7 introduced a PRL to AMOL to explore whether this could improve performance as it had done in other near-field systems. The high spatial frequencies created by the narrow AMOL aperture were able to couple to surface plasmons on the underlying PRL and the interference between these surface plasmons and the incident λ_1 intensity lead to an improvement in the DOF of the system. Importantly the AMOL system remained able to form narrow apertures with the much improved DOF, although there was deterioration of the smallest apertures. The addition of a PRL introduced a trade-off between the maintenance of the desired intensity profile and the resist

depth between the AML and PRL; as the resist depth increased the coupling to the surface plasmons weakened and the FWHM increased. Modeling the PRL as a silver layer caused further loss but the DOF still improved considerably. The modeling in this thesis has shown the introduction of a PRL is a very useful addition to AMOL when imaging sub-diffraction limited features.

This thesis also explored the addition of a superlens to the AMOL system. The superlens concept had previously been applied to near-field lithography systems with metal masks, where difficulties due to mask contamination, dust and intimate contact limited performance. AMOL overcame both these limits and simulations demonstrated that it was possible to interface a superlens with AMOL and created a weak filtering effect, although imaging performance deteriorated. The best results used a small spacer layer (10 nm) and a thin superlens (15 nm) and were able to reduce λ_2 by a factor of ten, whilst still enabling a FWHM of 50 nm and a reduction in NILS by ~10%. Unfortunately the modeling of a silver superlens sharply degraded performance, due to the difficulty of broadband coupling to surface plasmons at 405 nm. A change in wavelength λ_1 or a change in superlens material are suggested to overcome these issues; similarly the use of a multilayer superlens may increase the filtering strength. The introduction of a superlens in AMOL has been modeled and demonstrated some usefulness, however future work, mainly in materials, is needed to realise an effective system.

This thesis has contributed to understanding in three major areas; the creation of a simulation to allow substantial exploration of the propagation of light through an AMOL system; the exploration of absorbance gratings including those created by AMOL, and the interactions between AMOL and surface plasmon effects for improved DOF and as a dichroic filter. The development of the full-wave vector FEM simulation for AMOL was central to this thesis and provided the engine with which to explore AMOL. It was found that, given appropriate material parameters AMOL was able to create narrow apertures and that these apertures could tightly confine an exposing wavelength. However there are obstacles to this performance, particularly in material parameters but also in the limited DOF. The introduction of a PRL is able to extend this DOF, but with the FWHM

widening with resist depth. A superlens is able to act as a dichroic filtering reducing undesired transmission of λ_2 but at a cost of reduced performance. Overall the abilities of AMOL for sub-diffraction limited lithography have been thoroughly explored and the complexities of using an AML for a mask have been demonstrated, whilst the possibility for improvements using surface plasmons effects have been investigated.

9.2 CURRENT AMOL DEVELOPMENT

The simulations performed in this thesis have focused on the ability of AMOL to create sub-diffraction limited features and transmit these features into an underlying resist. The simulations have shown that AMOL has the ability to create narrow apertures and that these apertures allow sub-diffraction limited exposures in an underlying resist. It is, however, important to note that these results are weaker than a corresponding metal grating and are limited by the available material parameters. In particular the AML requires a low thermal constant (k_{BA}), the difference between opaque and transparent regions absorbance must be as large as possible (affected by ρ_{conc}) and appropriate wavelengths must be available. Outside the scope of this thesis there are issues such as efficiency and exposure time that may restrict AMOLs use; appropriately powerful illumination sources and the time taken for exposures are important considerations. The material obstacles provide a serious challenge for AMOL and although progress has been made [Andrew 2009] the material parameters used in AMOL will always struggle to compete with a metallic masking system although it does have the benefits of being adaptive and overcoming intimate contact problems.

The transmission of the exposing wavelength, λ_1, into the underlying resist is of importance to any fabrication using the optical near-field, as without sufficient DOF the fabrication becomes more difficult and less reliable. The AMOL system has no demonstrated advantage over conventional near-field systems for extending this DOF, in fact the simulation results in this thesis show poorer DOF results for absorbance gratings. A PRL has been demonstrated as an effective way to partially overcome these limitations in AMOL. The PRL improves the process latitude and DOF but widens the exposures

for larger DOFs; to the region of ~50 nm for a ~50 nm FWHM. This is a definite improvement and a useful addition to AMOL for small features sizes, however the industry aims are tougher still (~66 nm DOF at 22 nm half pitch [ITRS 2010]). The further extension of the DOF of an AMOL exposure is clearly an important objective.

AMOL is a novel technique for optical lithography and the modeling has demonstrated the ability of AMOL to create very tightly confined exposures in some cases (Fig 9.1). However, there remain performance limitations due to obstacles such as; finding appropriate photochromic materials, and extending the DOF. The list of material requirements: a large absorbance change, low thermal constant, fast reaction kinetics and appropriate wavelengths make the selection or creation of a better photochrome difficult, but necessary, aim if fast and efficient sub-diffraction lithography is the desired goal. The DOF problem is common among all near-field lithography systems and no obvious solution exists; although plasmonic layers have the ability to improve the DOF further

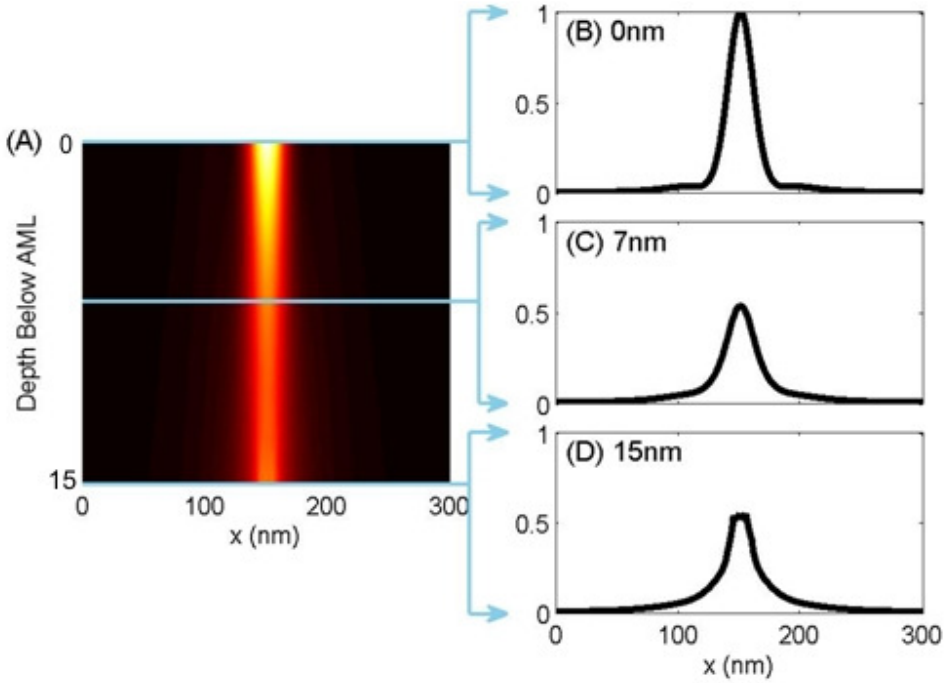

Figure 9.1 $\boldsymbol{\lambda_1}$ intensity in the resist for an AMOL system with an ideal PRL at 15 nm beneath the AML (a) and normalised (to $\boldsymbol{I_{max}}$) intensity waveforms at (b) 0 nm, (c) 7 nm and (d) 15 nm beneath the AML layer.

ideas and/or improved resist techniques are needed before suitable process latitude will be possible. Although AMOL shows promise because it is able to create near-field apertures directly on top of a resist layer, reducing contact and masking problems and allowing multiple exposures, the weaker nature of the adaptive mask and the requirements for improved materials are major obstacles that must be overcome before small feature sizes can be achieved.

9.3 FUTURE WORK

There have been numerous proposals for optical lithography systems, in particular for methods to achieve sub-diffraction limited feature sizes. AMOL was proposed relatively recently, in 2006 [Menon 2006], and there remain many intricacies that have not been thoroughly explored. In particular there are challenges involving further simulation work, for experimentation based on this work, for the AMOL materials and chemicals and for adaptations to AMOL. There is no clear path to an industrial system but AMOL allows the exploration of an easy to use adaptive absorbance masking system with the potential for sub-diffraction limited imaging.

The AMOL model developed in this thesis was the first vector model to examine how narrow apertures can form in a two wavelength absorbance system and how light would propagate through this system. As with any model there are additional features that could be incorporated, here some possibilities are briefly discussed. Firstly the time-dependence of the AMOL has not been included (as a steady state was assumed), although there are some complications including multiple time scales (wave propagation versus aperture formation) the addition of this would provide some useful information, particularly regarding the speed of imaging and aperture formation. Secondly photochromic layers have also shown a range of other phenomena alongside absorbance change, such as surface deformation and changing real permittivity; given appropriate experimental results or models these could also be included in the simulation to make it more realistic. Finally the simulations could also be extended by incorporating a model of the resist development process; this would allow a greater understanding of the effect of

changes in the intensity profiles. Each of these extensions to the simulations would allow a better understanding of AMOL and help guide experiment.

Perhaps the pertinent issue for AMOL is the challenge, discussed previously, of materials; are there photochromic compounds that can act suitably fast and create opaque and transparent regions which allow narrow apertures? Until these goals are achieved there will be great difficulty in achieving the desired narrow profiles experimentally. There is a clear need here for additional chemical research outlining the expected ranges of material parameters possibly and any trade-offs that need to be made. The model, and results presented in this thesis, can be used to decide on the viability of any new photochromic compound. If a suitable compound was found then a comparison between experimental results and the model would allow a deeper understanding of AMOL.

A second important issue is whether, even in an ideal AMOL system the DOF would be sufficient for industrial fabrication? This is currently unlikely to be the case, as demonstrated in this thesis, but this is a major drawback, both for AMOL and other near-field techniques. The two major proposals to overcome this are improved resists (multistage or chemically enhanced resist layers) and the PRLs discussed here. The PRL has shown an ability to get a DOF of ~60 nm but with a widening of the FWHM, can this performance be improved by changing the PRL material? Any improvement to the DOF would be a great step forward for near-field lithography as a whole, but working with evanescent decay does not make this easy.

The superlens work discussed in this thesis used a single layer of silver and one spacer and was able to achieve, for an ideal case, reasonable image projection and some filtering. The performance did deteriorate, and reduced further using a silver layer, but this poses the question of how further improvements might be enabled with a superlens structure? In terms of real materials there has been exploration of a wide range of materials [West 2010] that provide more options for an AMOL system, alternatively a photochromic system could be used with lower wavelength. The superlens itself has also been widely explored, particularly looking at multi-layer lenses [Moore 2008] which

may prove useful in AMOL. In particular the multi-layer lenses have the possibility of improving the image projection whilst also improving the filtering of λ_2, both by increased loss, boundary reflections and resonances. The confirmation of the superlens demonstrated in this thesis suggests that there may be future work in modeling a rangeof superlens designs to improve filtering effects.

To speculate on a possibility closely linked to AMOL and the competition between two wavelengths; the absorbance plots in this thesis show the system is able to create narrow aperturess and these can be reasonable consistent for tens of nanometers (when plasmonic reflectors are used beneath the AML). If, for instance, a photochrome with a solubility change was used there is the possibility of using the photochrome for imaging, similar to suggestions by Hell [Hell 2004]. This would not suffer from the same limits of evanescent decay at resist exposures. Techniques of this type, in which the resist is not a separate layer but part of the masking material, could offer a solution to the DOF problems of near-field lithography. The obvious issues with ideas of this type are the even more challenging material problems and the shape of the apertures, but an investigation of available materials would be interesting.

Near-field lithography is an intensely challenging discipline, even with the best case scenario there remains only a shallow resist depth to capture the image. However, the potential to overcome the resolution limit encourages further developments and the exploration of new ideas. The modeling of AMOL has allowed exploration of absorbance masks and light competition in a photochromic layer as well as near-field exposures. There are limits to the current AMOL systems which have been discussed here but increasing the understanding of what these limitations are provides new ideas for lithography and continues the challenge of fabricating ever smaller features.

Appendix A

UNITS OF ABSORBANCE

A.1 INTRODUCTION

There are a variety of variables and units that may specify the ability of a photoresist to absorb light, here a brief overview is given to clarify the relations and usage in this thesis. Considering a TE plane wave propagating in the y direction through a lossy material, having a complex refractive index

$$\tilde{n} = n(1 - ik_n) = n - i\kappa. \tag{A.1}$$

Representing the plane wave in phasor form;

$$\boldsymbol{E} = Ae^{-iky}, \tag{A.2}$$

where k is the propagation constant. Then through the substitution of the relation

$$k = \frac{2\pi\tilde{n}}{\lambda}, \tag{A.3}$$

the real and imaginary parts of the field may be separated,

$$\boldsymbol{E} = Ae^{iky} = Ae^{\frac{-i2\tilde{n}\pi}{\lambda}y} = Ae^{\frac{-i2n\pi}{\lambda}y}e^{\frac{-2\kappa\pi}{\lambda}y}, \tag{A.4}$$

which, substituted into the intensity equation gives

$$I = S = \frac{1}{2}Re\left(\sqrt{\frac{\varepsilon}{\mu}}\right)|\boldsymbol{E}|^2 = \frac{1}{2}\sqrt{\frac{\varepsilon}{\mu}}A^2e^{\frac{-4\kappa\pi}{\lambda}y}. \tag{A.5}$$

Given the definition of absorbance α, from the change in intensity,

$$I = I_0e^{-\bar{\alpha}} = I_0e^{-\alpha y}, \tag{A.6}$$

where y is the distance travelled, then by comparison with Eq.A.5 the absorbance may be related to the complex part of the refractive index;

$$\alpha = \frac{4\pi\kappa}{\lambda}. \tag{A.7}$$

It is also possible to define the material parameters in terms other than a complex refractive index, commonly in lithography a complex permittivity is used. From the Helmholtz equation for wave propagation in absorbing media we have [Born 1999]

$$k^2 = \omega^2\varepsilon\mu - i\omega\mu\sigma = \omega^2\mu_0\mu_r\varepsilon_0\tilde{\varepsilon_r} \tag{A.8}$$

where a complex permittivity

$$\tilde{\varepsilon} = \varepsilon - i\frac{\sigma}{\omega} = \varepsilon_0(\tilde{\varepsilon_r}) = \varepsilon_0\left(\varepsilon_r^{'} - i\varepsilon_r^{''}\right) = \varepsilon^{'} - i\varepsilon^{''}, \tag{A.9}$$

has been introduced. Using this relationship the complex refractive index, $n\tilde{n}$ may be rewritten as

$$\begin{aligned}\tilde{n}^2 = \left(\frac{\lambda k}{2\pi}\right)^2 = \frac{\lambda^2\omega^2\varepsilon\mu}{4\pi^2} - i\frac{\lambda^2\omega}{4\pi^2} &= \mu_0\mu_r c^2\left(\varepsilon^{'} - i\varepsilon^{''}\right)\\ &= \mu_0\mu_r c^2\varepsilon_0\left(\varepsilon_r^{'} - i\varepsilon_r^{''}\right)\\ &= (n - i\kappa)^2.\end{aligned} \tag{A.10}$$

Equation A.9 combined with the approximations that

$$\mu_r \approx 1 \; and \; c = \frac{1}{\sqrt{\varepsilon_0\mu_0}} \tag{A.11}$$

allows the permittivity to be represented as

$$\varepsilon_r' = Re\{\sqrt{n - i\kappa}\} \; and \; \varepsilon_r'' = Im\{\sqrt{n - i\kappa}\}. \tag{A.12}$$

These may be expressed in reversed as

$$\begin{aligned}n^2 &= \frac{1}{2}\varepsilon_r'\left(\sqrt{1 + \left(\frac{\varepsilon_r''}{\varepsilon_r'}\right)^2} + 1\right), \text{and}\\ \kappa^2 &= \frac{1}{2}\varepsilon_r'\left(\sqrt{1 + \left(\frac{\varepsilon_r''}{\varepsilon_r'}\right)^2} - 1\right),\end{aligned} \tag{A.13}$$

which, for weakly absorbing media approximate as

$$\begin{aligned}n &\approx \sqrt{\varepsilon_r^{'}} \; and\\ \kappa &\approx \frac{1}{2}\left(\frac{\varepsilon_r''}{n}\right).\end{aligned} \tag{A.14}$$

Thus the relationships between the different ways of expressing the absorbance of a medium; absorbance, α the refractive index, $\tilde{n}$ and the refractive index, $\tilde{\varepsilon}$ have been

explained. All of these parameters can be used in a model of the system and the choice is arbitrary, although particular areas often make use of one representation. In this work the absorbance, permittivity and refractive index will be widely used.

Appendix B

INTRODUCTION TO THE FINITE ELEMENT METHOD

This appendix introduces the details behind the Finite Element Method (FEM). It begins by covering the basic mathematical derivations required before outlining the solution methods, how Maxwell's equations are interpreted and the appropriate boundary conditions.

B.1 VARIATIONAL FORM

In the case of many differential equation (DE) systems it is possible use a known relationship to a minimised value, such as energy or time, to create an alternative form of the DE in which the problem has become the minimisation of a particular variable. For instance, in the case of a light ray in a medium with changing index of refraction, Fermat's principle states that an equivalent problem is to consider the minimum time taken for the light to traverse the material. In many cases an obvious minimising variable is not present, however it is possible to reorganise a general DE to create an equivalent variational form [Henwood 1996]. If our initial DE is represented (in two dimensions, x and y) as

$$L\big(u(x,y)\big) = f(x,y) \tag{B.1}$$

for (x,y) in R and $u = u^*$ on some part of S, the boundary of R, where L is an operator representing the DE, u the solving function and R the region on which the problem is defined; the general variational form (VF) is of the form

$$B\big(u(x,y), v(x,y)\big) = C(v(x,y)) \tag{B.2}$$

such that u satisfies $u = u^*$ on part of the boundary S for any function v on S, where B and C are functionals and v a selected function. The VF of Eq B.2 obscures the actual functionals involved and the mathematics taking place, so the next step expands the process of deriving functional form.

B.1.1 DERIVATION OF VARIATIONAL

Beginning with the initial DE, Eq B.1 it is possible to create an unknown trial function, say $g(x,y)$ which may then be substituted into the DE. As the actual solution, $u(x,y)$ solves the equation exactly an error (residual, $r(x,y)$) may be defined as the difference between the two sides of the equation;

$$r(x,y) = L\big(g(x,y)\big) - f(x,y). \tag{B.3}$$

As the trial function is varied such that the value of $r(x,y)$ approaches zero across the region of the model, *R*, then the function $g(x,y)$ approaches a solution to the DE, thus the problem can be expressed as the minimisation of the Eq B.3.

It is possible to develop a more useful form using a relation such as that if a function $h(x,y)$ is continuous, and if

$$\iint_R h(x,y)v(x,y)dx = 0 \tag{B.4}$$

for all continuous functions *v*, then $h(x,y) = 0$ for $x,y \in R$ [Henwood 1996]. If the residual function $r(x,y)$ is substituted for $h(x,y)$ in this equation (as $r(x,y)$ should be minimised) the variational form is created in two dimensions, becoming;

$$\iint_R (\nabla^2 g(x,y) + f(x,y)) * v(x,y)dA = 0 \tag{B.5}$$

for all continuous functions *v*, where $v = 0$ on S (or part of S). The resulting equation now expresses the solution to our DE as the sum over the region of the residual vector, multiplied by some other, unspecified function $v(x,y)$ which may be chosen so as to simplify the finding of the solution. Of course, for any DE system the boundary conditions must also be considered.

B.1.2 BOUNDARY CONDITIONS

The initial VF implicitly includes only boundary conditions where the result (u) is specified on the boundary, S, of the region, which are known as essential (Dirichlet) boundary conditions. A second class of boundary conditions (natural boundary condi-

tions) involves derivatives of the function along the boundary condition and model movement across the boundary and more complex cases. In general natural boundary conditions require an additional term to be added to the system, in order to force the solution to match the required boundary flows; FEM will only approximate natural boundary conditions. A brief example of the inclusion of natural boundary conditions follows.

If the Laplacian term of g in Eq B.5 (where the (x, y) symbols have been dropped for clarity) is integrated by parts giving,

$$\iint_R v\nabla^2 g \, dA = \int_S \frac{\partial g}{\partial n} v \, dS - \iint_R (\nabla g) \cdot (\nabla v) \, dA \tag{B.6}$$

where *n* is the outward normal at the boundary, there are two major effects. Firstly the differentiability required of the function *g* is reduced to a first differential (as instead of $\ddot{u}v$ there is instead a term $\dot{u}\dot{v}$) allowing greater flexibility in choosing *g*. There is also a new term directly involving the boundary of R, an integral of the change in u normal to *S*. This new term may be considered as the combination of all of the boundary conditions; the boundary integral along *S* may be rewritten as a sum of the integrals along each boundary section, including sections specified with different conditions.

This allows the natural boundaries conditions along each section to be inserted into the model. As the essential boundary conditions are already in the model it is not surprising that they integrate to 0 in this section if present (as *v* would be zero across the entire surface). If this form of the second differential term is substituted back into Eq B.5 then the equation becomes

$$\int_S \frac{\partial g}{\partial n} v \, dS - \iint_R (\nabla g) \cdot (\nabla v) \, dA = -\iint_R fv \, dA, \tag{B.7}$$

where terms in *v* only have been moved to the right hand side. With comparison to the general variation form (Eq B.2) it is seen that the functionals *B* and *C* are given by

$$B(u, v) = \int_S \frac{\partial u}{\partial n} v \, dS - \iint_R (\nabla u) \cdot (\nabla v) \, dA \tag{B.8}$$

and

$$C(v) = \iint_R fv\, dA \tag{B.9}$$

where u and g have been exchanged. At this point the equation has been rewritten in variational form and the boundary conditions introduced, but the solution still needs to be found.

B.2 FINITE ELEMENTS

It is possible to solve Eq B.5 directly, however this is normally computationally excessive and the resulting function complex due to the variability in the result with the selection of $v(x, y)$ [Evans 2000]. More commonly a FEM approach is used, in which the region is spanned by a set of finite elements where each element is defined by piecewise functions, which are only non-zero inside that element. The solution is then found through a piecewise summation across all of the finite elements.

B.2.1 CREATING THE FINITE ELEMENTS

FEM solves for the solution $u(x, y)$ by systematically breaking the region into small areas (lines in 1-D, triangles or quadrilaterals in 2-D) and solving the DE, expressed in variational form, in each small area with independent variables (such as permittivity) held constant. Although many methods exist to divide and solve the problem the most common involves defining functions on each of the finite elements which are 1 at one of the nodes and linearly reduce to 0 at each of the others, being defined at zero outside the given element. Example functions for each of the nodes on a 2-dimensional triangular finite element are shown in Fig B.1. For example, the surface in Fig B.1a may be describe by the equations

$$W_a(x, y) = \begin{cases} 1 - x - y, & if\ x, y \in \varphi \\ 0, & Otherwise \end{cases} \tag{B.10}$$

where φ is the finite element region; similar equations are possible for the other regions. Each basis function is then assigned a multiplier variable, α, so that the complete surface of each finite element, for the triangular case, is described by the sum of the three basis functions which are non-zero in that element,

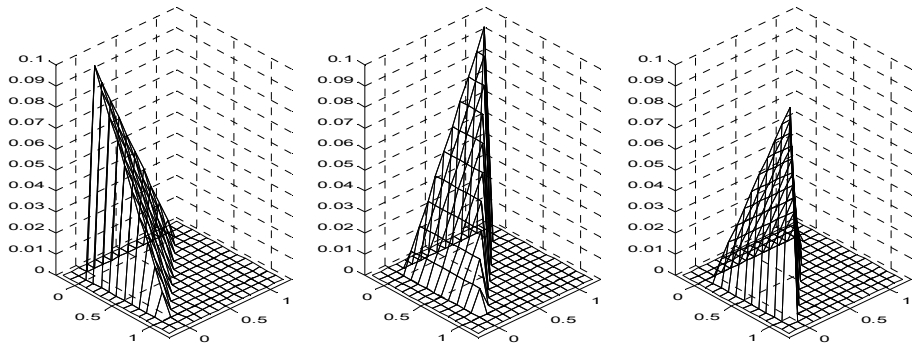

Figure B**.1** Basis functions for a 2-Dimensional triangular finite element, with the function defined as zero anywhere outside the element.

$$\varphi(x,y) = \alpha_a W_a(x,y) + \alpha_b W_b(x,y) + \alpha_c W_{ac}(x,y), \tag{B.11}$$

creating a plane between the three points. In some case higher order elements may allow a more accurate surface.

B.2.2 SUMMATION OF FINITE ELEMENTS

Having defined each of the finite elements they must be combined to express the solution across the region. As each finite element equation consists of functions defined only on the finite element they may be combined simply as long as the constants (α) are the same for nodes shared by multiple finite elements. Thus the solution, u is represented as

$$u = \alpha_1 W_1 + \alpha_2 W_2 + \cdots + \alpha_N W_N \tag{B.12}$$

where N is the number of elements in the region. The constants α may then be found through solving the equation

$$\sum_{c=1}^{N} B(W_c, v)\alpha = L(v) \tag{B.13}$$

for all v, where $v = 0$ on the boundary, which, once the test function v is chosen, will become a linear equation as B and L will be constant. This has reduced the complexity of the integration to an algebraic summation, given an appropriate selection of v.

B.2.3 SOLUTION OF THE FINITE ELEMENTS

Now that the equation has been expressed in terms of an N-dimensional set of basis functions, the unspecified function $v(x, y)$ needs to be selected to solve, and hopefully simplify the calculations. To ensure this N dimensional equation set is solvable the test function v must also be N dimensional, it also must agree with the conditions defined on the boundary. There remains flexibility in the choice of the test function and different techniques have been suggested to reduce the complexity of the problem. The Galerkin method reintroduces for v the basis functions used for u, hence giving the form

$$\sum_{\mathrm{r}=1}^{\mathrm{N}} \sum_{c=1}^{N} B(W_c, W_r)\alpha = L(W_r), \tag{B.14}$$

which may be rewritten as

$$K\alpha = f, \tag{B.15}$$

where the matrices K and f are represented by

$$K_{rc} = B(W_c, W_r) \text{ and } f_r = L(W_r). \tag{B.16}$$

The original problem has now been reduced to a set of equations, written in matrix form which may be solved to find α. The total solution may then be calculated by summing up across all of the elements, remembering they are defined as zero outside their own element, thus

$$u = \alpha_1 W_1 + \alpha_2 W_2 + \cdots + \alpha_N W_N = \sum_{1}^{N} u_c \, \varphi_c. \tag{B.17}$$

Once the equation is in this form it may be solved through Gaussian elimination, although in general more complex methods are used to exploit symmetries and computation efficient methods, such that both the memory required and system complexity are reduced.

B.3 BOUNDARY CONDITIONS

The main boundary conditions used in the simulations used in this thesis: continuity conditions, periodic boundary conditions, scattering boundary conditions and perfectly

matched layers (PMLs) must also be considered. Continuity conditions are used for all internal boundaries; they specify that all tangential fields must be continuous,

$$\boldsymbol{n} \times (\boldsymbol{E}_1 - \boldsymbol{E}_2) = 0 \text{ and} \tag{B.18}$$

$$\boldsymbol{n} \times (\boldsymbol{H}_1 - \boldsymbol{H}_2) = 0. \tag{B.19}$$

For a system solving for the electric field Eq B.18 must already fulfilled by a FEM solution, Eq B.19 is the natural boundary condition contained implicitly in the FEM equations. The grating features which are considered here are modeled by a single grating (or half grating with symmetry) with periodic (or aperiodic) boundary conditions, representing infinite gratings. In periodic conditions the fields on either side must be the same, COMSOLs periodic boundaries are thus set

$$\boldsymbol{E}_{Source} = \boldsymbol{E}_{Destination} \tag{B.20}$$

where the source and destination are defined as the opposing sides of the simulations.

The simulations also require an incident wave to be specified, an incident plane wave is set along an edge (normally the top edge) and scattering boundary conditions ensure that any reflected fields are ignored (since there is no real boundary here) as well as allowing the incident wave to pass into the domain with a specified propagation angle. Finally the base of our simulations – acting as our substrate – is modelled as an effectively infinite depth; improved performance encourages the choice of a PML over a simpler matched boundary.

A PML was first proposed by Berenger [Berenger 1994] and requires an increased modeling region. This additional region is lossy, thus any wave present in the region decays, yet there is no reflection at the boundary between the regions. There are many ways to consider this; Jin [Jin 2002] repeats a derivation by Sacks [Sacks 1995] where specific forms of the diagonally anisotropic dielectric permittivity and permeability are found such that the interface is reflection-less - this requires non-real material values. The properties of the PML may then be defined by two values which determine the wavelength in the absorbing region and the rate of decay in that region. Care must be taken that the PML region is of adequate length to sufficiently reduce any remaining reflections from the back surface.

Appendix C

DIELECTRIC BOUNDARY

C.1 ANALYTICAL DERIVATION

The consideration of a dielectric boundary is a common problem and is documented in most general optics books [Born and Wolf, Hecht]. Beginning by considering a propagating plane wave of amplitude A (which is complex to represent the phase), shown in Fig C.1 the fields may be written as

$$\boldsymbol{E} = Ae^{-ik_1 y} \; and \; \boldsymbol{H} = Ae^{-ik_1 y}, \tag{C.1}$$

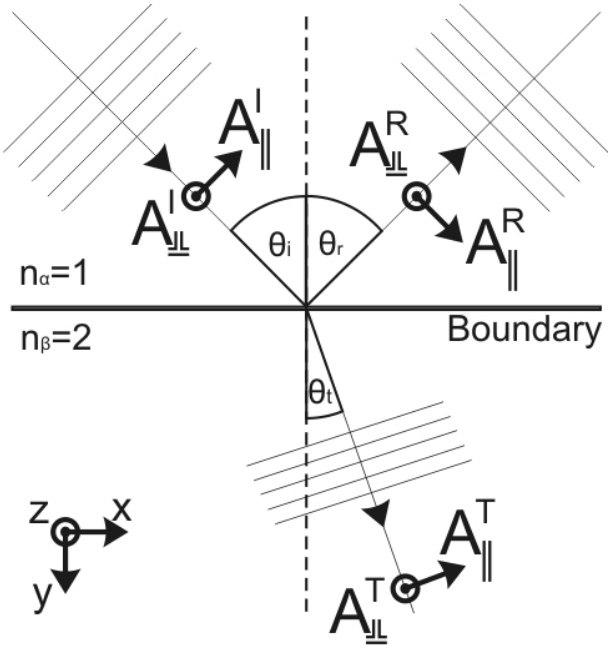

Figure C.1 Schematic of plane of incidence for the dielectric boundary showing the axis and the incident (***I***), reflected (***R***) and transmitted (***T***) amplitudes parallel (∥) and perpendicular (⊥) to the plane of incidence. This may be applied to either the TE (⊥=***E***, ∥ =***H***) or TM (∥=***E***, ⊥ =***H***) polarisations.

where the waves are travelling in the x, y plane and $\boldsymbol{k_1}$ is the wavevector in the region where $n = n_1$. The fields may be resolved into x, y and z components as well as splitting the amplitude into parallel, $A_{\parallel}$ and perpendicular, $A_{\perp}$ components. Here for compactness only the TM case is considered, however a similar analysis can be performed for TE. The field equations may be written for three different sections; the incident field

$$\begin{aligned} E_z^I &= A_{\perp} e^{-i\boldsymbol{k_1}\cdot\boldsymbol{r_i}}, \\ H_x^I &= -A_{\perp} \times \sqrt{\varepsilon_1}\cos(\theta_i) \times e^{-i\boldsymbol{k_1}\cdot\boldsymbol{r_i}}, \\ H_y^I &= A_{\perp} \times \sqrt{\varepsilon_1}\sin(\theta_i) \times e^{-i\boldsymbol{k_1}\cdot\boldsymbol{r_i}} \cdot, \end{aligned} \tag{C.2}$$

the transmitted field

$$\begin{aligned} E_z^T &= T_{\perp} e^{-i\boldsymbol{k_2}\cdot\boldsymbol{r_t}}, \\ H_x^T &= -T_{\perp} \times \sqrt{\varepsilon_2}\cos(\theta_t) \times e^{-i\boldsymbol{k_2}\cdot\boldsymbol{r_t}}, \\ H_y^T &= T_{\perp} \times \sqrt{\varepsilon_2}\sin(\theta_t) \times e^{-i\boldsymbol{k_2}\cdot\boldsymbol{r_t}}, \end{aligned} \tag{C.3}$$

and the reflected field

$$\begin{aligned} E_z^R &= R_{\perp} e^{-i\boldsymbol{k_1}\cdot\boldsymbol{r_r}}, \\ H_x^T &= R_{\perp} \times \sqrt{\varepsilon_1}\cos(\theta_r) \times e^{-i\boldsymbol{k_1}\cdot\boldsymbol{r_r}}, \\ H_y^T &= R_{\perp} \times \sqrt{\varepsilon_1}\sin(\theta_r) \times e^{-i\boldsymbol{k_1}\cdot\boldsymbol{r_r}}, \end{aligned} \tag{C.4}$$

where $\boldsymbol{r_m}$ represents the direction of the m field. The magnetic components are derived from the electric components through Eqs 4.2 and 4.3 with assumptions about the plane waves.

Considering the boundary, the continuity boundary conditions require that the components of the fields tangential to the boundary, E_z and H_x must be continuous, implying that

$$E_z^I + E_z^R = E_z^T \quad and \quad H_x^I + H_x^R = H_x^T. \tag{C.5}$$

Substitution the formulae for the field components, Eq C.2-C.4 into Eq C.5 then gives two equations at the boundary;

$$A_{\perp} + R_{\perp} = T_{\perp}, \tag{C.6}$$

$$-A_{\perp} \times \sqrt{\varepsilon_1}\cos(\theta_i) + R_{\perp} \times \sqrt{\varepsilon_1}\cos(\theta_r) = -T_{\perp} \times \sqrt{\varepsilon_2}\cos(\theta_t), \tag{C.7}$$

and using the relation that $\cos(\theta_i) = \cos(\theta_r)$ these may solved for the ratios of the reflected and transmitted fields to the incident field;

$$\frac{R_\perp}{A_\perp} = \frac{\sqrt{\varepsilon_1}\cos(\theta_i) - \sqrt{\varepsilon_2}\cos(\theta_t)}{\sqrt{\varepsilon_1}\cos(\theta_i) + \sqrt{\varepsilon_2}\cos(\theta_t)}, \tag{C.8}$$

$$\frac{T_\perp}{A_\perp} = \frac{2\sqrt{\varepsilon_1}\cos(\theta_i)}{\sqrt{\varepsilon_1}\cos(\theta_i) + \sqrt{\varepsilon_2}\cos(\theta_t)} \tag{C.9}$$

A similar derivation for TE plane waves [Born 2002] gives

$$\frac{R_\parallel}{A_\parallel} = \frac{\sqrt{\varepsilon_2}\cos(\theta_t) - \sqrt{\varepsilon_1}\cos(\theta_i)}{\sqrt{\varepsilon_1}\cos(\theta_i) + \sqrt{\varepsilon_2}\cos(\theta_t)}, \tag{C.10}$$

$$\frac{T_\parallel}{A_\parallel} = \frac{2\sqrt{\varepsilon_1}\cos(\theta_i)}{\sqrt{\varepsilon_1}\cos(\theta_i) + \sqrt{\varepsilon_2}\cos(\theta_t)}. \tag{C.11}$$

Consider normally incident fields, as these will be the fields used in the later simulations; Eqs C.8 and C.9 reduce to

$$\frac{R_\perp}{A_\perp} = \frac{\sqrt{\varepsilon_1} - \sqrt{\varepsilon_2}}{\sqrt{\varepsilon_1} + \sqrt{\varepsilon_2}} = \frac{n_1 - n_2}{n_1 + n_2}, \tag{C.12}$$

$$\frac{T_\perp}{A_\perp} = \frac{2n_1}{n_1 + n_2}. \tag{C.13}$$

These analytical forms for the transmitted and reflected waveforms allow for easy comparison with, and validation of, the FEM simulation results.

Appendix D

MATLAB CODE

D.1 RUN SIMULATION

This function is called once all the simulation variables have been set. It iterates until the desired tolerance is met and saves the data required to rerun the simulation.

```
function[] = RunSimulation(fem,femDimensions,var1String,var2String,...
    folderPath,endsFolderPath,tol,conductionValues,simWidth,lambdas)

      ...
% Run first iteration to set initial values etc
      ...

for numIts = 2:maxIterations+1;

    % For each simulation wavelength run FEM
    for femCount = 1:2
        % Run Iteration
        [fem,fieldIntensity] = runIteration(fem,femCount,...
        femDimensions,fieldIntensity,0);
    end

    % Save Information
       ...
    % Saves data used to run last simulation and results
       ...

    % Calculation of new Conduction Values
    [conductionValuesL1 conductionValuesL2] = ...
        kCalculation(fieldIntensity,lambdas);

    % Update Conduction Arrays - No longer needed
    % conductionValuesL1 and conductionValuesL2 are set as global
    % variables as this improves code speed compared to reloading.

    % Check for convergence,
    normsc_old = normsc;
    normsc = norm(conductionValuesL1,2);
    difference = abs((normsc_old-normsc)/normsc)
    if difference < tol
        ...
```

```
    %%% Save and Exit for next iteration
        ...
        break
    end
end
```

D.2 RUN ITERATION

This code is used to run each individual FEM simulation used in the Matlab routine.

```
function
[fem,fieldIntensity]=runIteration(fem,femCount,femDimensions,...,
    fieldIntensity,extend)
% Run an iteration of the FEM
% Also calculates the new field Intensity
% John Foulkes

% Set up the Mesh
fem{femCount}.mesh = meshinit...
(fem{femCount},'hauto',5,'hpnt',10,'jiggle','on');
fem{femCount}.mesh = meshsmooth...
(fem{femCount}.mesh,'jiggleiter',7,'Qualoptim','min');
fem{femCount}.mesh = meshrefine(fem{femCount},'rmethod','longest');

% If greater accuracy desired improve mesh
if extend == 1
    fem{femCount}.mesh = meshrefine(fem{femCount});
    fem{femCount}.mesh = meshre-
fine(fem{femCount},'sdl',[2],'rmethod','regular');
end

% Update mesh
fem{femCount}.xmesh = meshextend(fem{femCount});

% Solver routine
fem{femCount}.sol=femstatic(fem{femCount},...
    'nonlin','on',...
    'linsolver','spooles',...
    'complexfun','on', ...
    'solcomp',{'Hz','Ez'}, ...
    'outcomp',{'Hz','Ez'}, ...
    'blocksize','auto');

% Calculate Field Intensity in AML for both wavelengths
% PostInterp E field then calculate Intensity, e.g ...
% intensity = 0.5*sqrt(real(e0r/u0r))*absESquared;
fieldIntensity{femCount} =...
    FieldIntensityInterpolation(fem{femCount},femDimensions);
```

D.3 KCALCULATION

This code takes the intensity values for both wavelengths and calculates the appropriate absorbance values.

```
function [nL1 nL2] = ...
    kCalculation(fieldIntensity,lambdas)
% First Order Photochromic Kinetics Used to calculate the desired
% absorbance values, as detailed in Chapter 2
% Field Intensity is given for both lambda1, lambda2
% lambda1 = fieldIntensity{1}; % Lambda 1  Exposing wavelength
% lambda2 = fieldIntensity{2}; % Lambda 2  Aperture wavelength
% Intensity given in W/m^2
% Matches Menon and Warner
% John Foulkes

% Set variables
% n is state of lambda2
nold=1.6;

lambda1 = lambdas(1);
lambda2 = lambdas(2);

% Intensity in W/m^2 to mol/m^2
hplanck = 6.626e-34;
PhotonEnergy1 = 3e8./lambda1;
fieldIntensity{1} = fieldIntensity{1}./(PhotonEnergy1*hplanck);
PhotonEnergy2 = 3e8./lambda2;
fieldIntensity{2} = fieldIntensity{2}./(PhotonEnergy2*hplanck);

% Quantum Efficiencies
phi1AB = 28.5e-3;
phi1BA = 24.5e-3;
phi2AB = 2.1e-3;
phi2BA = 7.2e-3;

% Absorption cross section
Gamma1A = 1.1473e-19;
Gamma1B = 2.6770e-020; % (Trey) % Rajesh = 4.7804e-020; %
Gamma2A = 4.78e-21;
Gamma2B = 1.1473e-20;

% Global knBA
knBA = 8.5e-6;

% Number density of chomophores
NA = 6.02e23;

dens = 1; % Actual 0.395;
numDens = dens*1000*NA; % Menon - 0.395*1000*NA; % [num per m^3]
rhoAlambda1 = numDens; %
rhoBlambda1 = numDens;
```

```
rhoAlambda2 = numDens;
rhoBlambda2 = numDens;

% Absorbance - Beer's Law
absorbanceAlamb1 = rhoAlambda1.*Gamma1A;
absorbanceBlamb1 = rhoBlambda1.*Gamma1B;
absorbanceAlamb2 = rhoAlambda2.*Gamma2A;
absorbanceBlamb2 = rhoBlambda2.*Gamma2B;

% Calculate fraction
numN = phi1BA*Gamma1B*fieldIntensity{1}...
      +phi2BA*Gamma2B*fieldIntensity{2}+knBA;
denomN = numN+phi1AB*Gamma1A*fieldIntensity{1}+...
      phi2AB*Gamma2A*fieldIntensity{2};
n = numN./denomN;

% Absorption_total = Absorp_trans*(#trans)+Absorp_cis*(#cis)
absorption1 = (absorbanceAlamb1.*n+...
    absorbanceBlamb1.*(1-n));

absorption2 = absorbanceAlamb2.*n+...
    absorbanceBlamb2.*(1-n);

% Convert Absorbance to Conductance
% Complex refractive Index
k1 = -1*absorption1.*lambda1/(4.*pi); %% Negative as Comsol e^jwt
k2 = -1*absorption2.*lambda2/(4.*pi); %% Negative as Comsol e^jwt
%Kappa = k./refractiveIndex;

nL1 = nold+i*k1;
% LAMBDA2
nL2 = nold+i*k2;
```

D.4 INPUTWAVE

This sets the field at the top edge of the simulation to represent the formation of the standing wave.

```
function [fem,femDimensions] = InputWave(fem,femDimensions,...
      simWidth,multi,lambda)
% This function takes the fem model and updates the lambda2 sections so
% that a different period grating is formed. This requires both a
% change in the incidence angle of the lambda2 to create the desired
% spacing, and changing the simulation width.

% The intensity is set as half the sum of two waves in exponential form
% arriving from opposite directions

% Calculate the angle required to get desired standing wave
x = simWidth;
```

D.4 INPUTWAVE

```
cosTheta = lambda/(2*x);
theta1 = acos(cosTheta);
theta1Str = num2str(theta1);

% Update string of wave specified at top of simulation
xmove = num2str(xmovePt*simWidth);
E0iz_rfweh_Lambda2 = strcat(multi,'*.5*(exp(-j*k0_rfweh*(cos(-
',theta1Str,...
    ')+y*sin(-',theta1Str,')))+exp(-j*k0_rfweh*(cos(-pi+',theta1Str,...
    ')+y*sin(-pi+',theta1Str,'))))');

% Example update to Incidend field variable
    ...
[fem,success] = ...
        updateVariable(fem,'E0iz_rfweh',E0iz_rfweh_Lambda2,'fem')
    ...
% Resize FEM so that whole number of periods is seen
fem = resizeHorizontal(fem,femDimensions,simWidth,repeats);
```

REFERENCES

Alkaisi, MM, Blaikie, RJ, McNab, SJ, Cheung, R & Cumming, DRS 1999, 'Sub-diffraction-limited patterning using evanescent near-field optical lithography', *Applied Physics Letters*, vol. 75, no. 22, pp. 3560-2.

Anderson, A & Peters, K 2009, 'Finite element simulation of self-writing waveguide formation through photopolymerization', *Journal of Lightwave Technology*, vol. 27, no. 24, pp. 5529-36.

Andrew, TL, Tsai, HY & Menon, R 2009, 'Confining light to deep subwavelength dimensions to enable optical nanopatterning', *Science*, vol. 324, no. 5929, pp. 917-21.

Babu, SV & Barouch, E 1986, 'Exact solution of Dill's model-equations for positive photoresist kinetics', *IEEE Electron Device Letters*, vol. 7, no. 4, pp. 252-3.

Babu, SV & Barouch, E 1987, 'Exposure bleaching of nonlinear resist materials - exact solution', *IEEE Electron Device Letters*, vol. 8, no. 9, pp. 401-3.

Babu, SV, Barouch, E & Bradie, B 1988, 'Calculation of image profiles for contrast enhanced lithography', *Journal of Vacuum Science & Technology B*, vol. 6, no. 2, pp. 564-8.

Baird, WE, Moharam, MG & Gaylord, TK 1983, 'Diffraction characteristics of planar absorption gratings', *Applied Physics B-Photophysics and Laser Chemistry*, vol. 32, no. 1, pp. 15-20.

Barnes, WL 2006, 'Surface plasmon-polariton length scales: a route to sub-wavelength optics', *Journal of Optics a-Pure and Applied Optics*, vol. 8, no. 4, pp. S87-S93.

Barnes, WL 2009, 'Comparing experiment and theory in plasmonics', *Journal of Optics a-Pure and Applied Optics*, vol. 11, no. 11.

Barnes, WL, Dereux, A & Ebbesen, TW 2003, 'Surface plasmon subwavelength optics', *Nature*, vol. 424, no. 6950, pp. 824-30.

Barrett, C, Natansohn, A & Rochon, P 1995, 'Cis-trans thermal-isomerization rates of bound and doped azobenzenes in a series of polymers', *Chemistry of Materials*, vol. 7, no. 5, pp. 899-903.

Barrett, CJ, Mamiya, JI, Yager, KG & Ikeda, T 2007, 'Photo-mechanical effects in azobenzene-containing soft materials', *Soft Matter*, vol. 3, no. 10, pp. 1249-61.

Berenger, JP 1994, 'A perfectly matched layer for the absorption of electromagnetic-waves', *Journal of Computational Physics*, vol. 114, no. 2, pp. 185-200.

Blaikie, RJ, Alkaisi, MM, McNabt, SJ & Melville, DOS 2004, 'Nanoscale optical patterning using evanescent fields and surface plasmons', in HC Kang & WS Chin (eds), *International Journal of Nanoscience, Vol 3, Nos 4 and 5*, vol. 3, pp. 405-17.

Blaikie, RJ & McNab, SJ 2002, 'Simulation study of 'perfect lenses' for near-field optical nanolithography', *Microelectronic Engineering*, vol. 61-2, pp. 97-103.

Bockelmann, U 1991, 'Polarization-dependent optical-wave fields in grating structures', *Europhysics Letters*, vol. 16, no. 6, pp. 601-6.

Borderie, B, Lavabre, D, Micheau, JC & Laplante, JP 1992, 'Nonlinear dynamics, multiple steady-states, and oscillations in photochemistry', *Journal of Physical Chemistry*, vol. 96, no. 7, pp. 2953-61.

Born, M & Wolf, E 1999, *Principles of optics: electromagnetic theory of propagation, interference and diffraction of light*, 7th expanded edn, Cambridge University Press, Cambridge ; New York.

Bouas-Laurent, H & Durr, H 2001, 'Organic photochromism', *Pure and Applied Chemistry*, vol. 73, no. 4, pp. 639-65.

Bratton, D, Yang, D, Dai, JY & Ober, CK 2006, 'Recent progress in high resolution lithography', *Polymers for Advanced Technologies*, vol. 17, no. 2, pp. 94-103.

Bublitz, D, Fleck, B & Wenke, L 2001, 'A model for surface-relief formation in azobenzene polymers', *Applied Physics B-Lasers and Optics*, vol. 72, no. 8, pp. 931-6.

Burger, S, Köhle, R, Zschiedrich, L, Gao, W, Schmidt, F, März, R & Nölscher, C 2005, *Benchmark of FEM, waveguide and FDTD algorithms for rigorous mask simulation*, Proceedings of SPIE , vol 5992, pp. 378-389

Campion, A & Kambhampati, P 1998, 'Surface-enhanced Raman scattering', *Chemical Society Reviews*, vol. 27, no. 4, pp. 241-50.

REFERENCES

Chaturvedi, P, Wu, W, Logeeswaran, VJ, Yu, ZN, Islam, MS, Wang, SY, Williams, RS & Fang, NX 2010, 'A smooth optical superlens', *Applied Physics Letters*, vol. 96, no. 4.

Cole, DC, Barouch, E, Conrad, EW & Yeung, M 2001, 'Using advanced simulation to aid microlithography development', *Proceedings of the IEEE* vol. 89, no. 8, pp. 1194-213.

COMSOL 2010, *COMSOL MULTIPHYSICS 3.5*, (http://www.comsol.com/products/rf/), viewed 10/11/2010.

Corbett, D, van Oosten, CL & Warner, M 2008, 'Nonlinear dynamics of optical absorption of intense beams', *Physical Review A*, vol. 78, no. 1, p. 4.

Corbett, D & Warner, M 2007, 'Linear and Nonlinear photoinduced deformations of cantilevers', *Physical Review Letters*, vol. 99, no. 17, p. 4.

Corbett, D & Warner, M 2008, 'Polarization dependence of optically driven polydomain elastomer mechanics', *Physical Review E*, vol. 78, no. 6, p. 13.

Crano, JC, Flood, T, Knowles, D, Kumar, A & VanGemert, B 1996, 'Photochromic compounds: Chemistry and application in ophthalmic lenses', *Pure and Applied Chemistry*, vol. 68, no. 7, pp. 1395-8.

Cummer, SA, Popa, BI, Schurig, D, Smith, DR & Pendry, J 2006, 'Full-wave simulations of electromagnetic cloaking structures', *Physical Review E*, vol. 74, no. 3.

Dantsker, D 1996, 'Photoinduced nonlinear effects in organic photochromics', *Journal of Nonlinear Optical Physics & Materials*, vol. 5, no. 4, pp. 775-88.

Dantsker, D & Persoons, A 1998, 'Two-wave two-wavelength mixing in photochromic molecular systems', *Physical Review A*, vol. 58, no. 2, pp. 1567-73.

Dantsker, D & Speiser, S 1994, 'Utilization of photoreversible optical nonlinearities in trans-cis photochromic molecules for spatial light-modulation', *Applied Physics B-Lasers and Optics*, vol. 58, no. 2, pp. 97-104.

Davidson, DB 2010, *Computational electromagnetics for RF and microwave engineering*, 2nd edn, 1 vols., Cambridge University Press, Cambridge.

Delaire, JA & Nakatani, K 2000, 'Linear and nonlinear optical properties of photochromic molecules and materials', *Chemical Reviews*, vol. 100, no. 5, pp. 1817-45.

Diamond, JJ & Sheats, JR 1986, 'Simple algebraic description of photoresist exposure and contrast enhancement', *IEEE Electron Device Letters*, vol. 7, no. 6, pp. 383-6.

Dill, FH 1975, 'Optical lithography', *IEEE Transactions on Electron Devices*, vol. 22, no. 7, pp. 440-4.

Dill, FH, Hornberger, WP, Hauge, PS & Shaw, JM 1975a, 'Characterization of positive photoresist', *IEEE Transactions on Electron Devices*, vol. 22, no. 7, pp. 445-52.

Dill, FH, Neureuther, AR, Tuttle, JA & Walker, EJ 1975b, 'Modeling projection printing of positive photoresists', *IEEE Transactions on Electron Devices*, vol. ED22, no. 7, pp. 456-64.

Ercole, F, Davis, TP & Evans, RA 2010, 'Photo-responsive systems and biomaterials: photochromic polymers, light-triggered self-assembly, surface modification, fluorescence modulation and beyond', *Polymer Chemistry*, vol. 1, no. 1, pp. 37-54.

Evans, G, Blackledge, JM & Yardley, P 2000, *Numerical methods for partial differential equations*, Springer undergraduate mathematics series, Springer, London ; New York.

Fang, N, Lee, H, Sun, C & Zhang, X 2005, 'Sub-diffraction-limited optical imaging with a silver superlens', *Science*, vol. 308, no. 5721, pp. 534-7.

Fang, N & Zhang, X 2003, 'Imaging properties of a metamaterial superlens', *Applied Physics Letters*, vol. 82, no. 2, pp. 161-3.

Fay, B 2002, 'Advanced optical lithography development, from UV to EUV', *Microelectronic Engineering*, vol. 61-2, pp. 11-24.

Fikri, R, Barchiesi, D, H'Dhili, F, Bachelot, R, Vial, A & Royer, P 2003, 'Modeling recent experiments of apertureless near-field optical microscopy using 2D finite element method', *Optics Communications*, vol. 221, no. 1-3, pp. 13-22.

Fischer, J, von Freymann, G & Wegener, M 2010, 'The Materials Challenge in Diffraction-Unlimited Direct-Laser-Writing Optical Lithography', *Advanced Materials*, vol. 22, no. 32, pp. 3578.

Flack, WW, Nguyen, HA, Buchanan, J, Capsuto, E & Marks, A 2004, 'Contrast enhancement materials for thick photoresist applications', in JL Sturtevant (ed.), *Advances in Resist Technology and Processing XXI, Pts 1 and 2*, vol. 5376, pp. 1190-205.

Flagello, D & Mack, C 2009, 'COMPUTATIONAL LITHOGRAPHY', *Journal of Micro-Nanolithography Mems and Moems*, vol. 8, no. 3, p. 1.

Foulkes, J & Blaikie, R 2008, 'Finite Element Simulation of Absorbance Modulation Optical Lithography', Melbourne, Australia: 2008 International Conference on

Nanoscience and Nanotechnology (ICONN 2008), Feb 25-29 2008. *Proceedings International Conference on Nanoscience and Nanotechnology* 2008, 184-187

Foulkes, JE & Blaikie, RJ 2009, 'Influence of polarization on absorbance modulated subwavelength grating structures', *Journal of Vacuum Science & Technology B*, vol. 27, no. 6, pp. 2941-6.

Fourkas, JT 2010, 'Nanoscale photolithography with visible light', *Journal of Physical Chemistry Letters*, vol. 1, no. 8, pp. 1221-7.

French, RH & Tran, HV 2009, 'Immersion lithography: photomask and wafer-level materials', *Annual Review of Materials Research*, vol. 39, pp. 93-126.

Fritzsche 1867, Comptes Rendus Acad. Sci.,, Paris.

Garcia, N & Nieto-Vesperinas, M 2007, 'Theory of electromagnetic wave transmission through metallic gratings of subwavelength slits', *Journal of Optics a-Pure and Applied Optics*, vol. 9, no. 5, pp. 490-5.

Gaylord, TK & Moharam, MG 1985, 'Analysis and applications of optical diffraction by gratings', *Proceedings of the IEEE*, vol. 73, no. 5, pp. 894-937.

Goodman, JW 2005, *Introduction to Fourier optics*, 3rd edn, Roberts & Co. Publishers, Englewood, Colo.

Griffing, BF & West, PR 1983, 'Contrast enhanced photoresists - processing and modeling', *Polymer Engineering and Science*, vol. 23, no. 17, pp. 947-52.

Griffing, BF & West, PR 1985, 'Contrast enhanced lithography', *Solid State Technology*, vol. 28, no. 5, pp. 152-7.

Guo, LJ 2007, 'Nanoimprint lithography: methods and material requirements', *Advanced Materials*, vol. 19, no. 4, pp. 495-513.

Hell, SW 2004, 'Strategy for far-field optical imaging and writing without diffraction limit', *Physics Letters A*, vol. 326, no. 1-2, pp. 140-5.

Hell, SW, Jakobs, S & Kastrup, L 2003, 'Imaging and writing at the nanoscale with focused visible light through saturable optical transitions', *Applied Physics a-Materials Science & Processing*, vol. 77, no. 7, pp. 859-60.

Hell, SW & Wichmann, J 1994, 'Breaking the diffraction resolution limit by stimulated-emission - stimulated-emission-depletion fluorescence microscopy', *Optics Letters*, vol. 19, no. 11, pp. 780-2.

Henwood, D & Bonet, J 1996, *Finite elements : a gentle introduction*, Macmillan, Basingstoke, Hampshire.

Holzwarth, T 2010, *Private Correspondence*.

Huo, FW, Zheng, GF, Liao, X, Giam, LR, Chai, JA, Chen, XD, Shim, WY & Mirkin, CA 2010, 'Beam pen lithography', *Nature Nanotechnology*, vol. 5, no. 9, pp. 637-40.

Ito, T, Takahashi, S, Okano, S, Sugimoto, A & Kobayashi, M 1992, '3-dimensional analysis for contrast enhancement lithography by a 3-dimensional photolithography simulator', *Journal of Vacuum Science & Technology B*, vol. 10, no. 1, pp. 126-32.

ITRS 2009, *International Technology Roadmap for Semiconductors.*, viewed 12/11 2010, (http://www.itrs.net/Links/2009ITRS/Home2009.htm)

Jin, J-M 2002, *The finite element method in electromagnetics*, 2nd edn, Wiley, New York.

Johnson, PB & Christy, RW 1972, 'Optical-constants of noble metals', *Physical Review B*, vol. 6, no. 12, pp. 4370-9.

Kawata, S 2001, *Near-field optics and surface plasmon polaritons*, Topics in applied physics, Springer, Berlin ; New York.

Kawata, S & Kawata, Y 2000, 'Three-dimensional optical data storage using photochromic materials', *Chemical Reviews*, vol. 100, no. 5, pp. 1777-88.

Kim, RH & Levinson, HJ 2007, 'Application of contrast enhancement layer to 193 nm lithography', *Journal of Vacuum Science & Technology B*, vol. 25, no. 6, pp. 2466-70.

KLATencor 2010, *Prolith X3.2*, viewed 10/11 2010. (http://www.kla-tencor.com/lithography-modeling/chip-prolith.html)

Kumar, GS & Neckers, DC 1989, 'Photochemistry of azobenzene-containing polymers', *Chemical Reviews*, vol. 89, no. 8, pp. 1915-25.

Lakowicz, JR 1999, *Principles of fluorescence spectroscopy*, 2nd edn, Kluwer Academic/Plenum, New York.

Lalanne, P & Lemercier-Lalanne, D 1997, 'Depth dependence of the effective properties of subwavelength gratings', *Journal of the Optical Society of America a-Optics Image Science and Vision*, vol. 14, no. 2, pp. 450-8.

REFERENCES

Latimer, P & Crouse, RF 1992, 'Talbot effect reinterpreted', *Applied Optics*, vol. 31, no. 1, pp. 80-9.

Lee, S, Jen, K, Willson, CG, Byers, J, Zimmerman, P & Turro, NJ 2009, 'Materials modeling and development for use in double-exposure lithography applications', *Journal of Micro-Nanolithography Mems and Moems*, vol. 8, no. 1.

Lee, W & Degertekin, EL 2004, 'Rigorous coupled-wave analysis of multilayered grating structures', *Journal of Lightwave Technology*, vol. 22, no. 10, pp. 2359-63.

Li, LJ, Gattass, RR, Gershgoren, E, Hwang, H & Fourkas, JT 2009, 'Achieving lambda/20 Resolution by One-Color Initiation and Deactivation of Polymerization', *Science*, vol. 324, no. 5929, pp. 910-3.

Lin, BJ 2006, 'Optical lithography - present and future challenges', *Comptes Rendus Physique*, vol. 7, no. 8, pp. 858-74.

Lin, BJ 2006a, 'The ending of optical lithography and the prospects of its successors', *Microelectronic Engineering*, vol. 83, no. 4-9, pp. 604-13.

Liu, ZW, Fang, N, Yen, TJ & Zhang, X 2003, 'Rapid growth of evanescent wave by a silver superlens', *Applied Physics Letters*, vol. 83, no. 25, pp. 5184-6.

Mack, C 2006, 'Accuracy, speed, new physical phenomena: The future of litho simulation', *Solid State Technology*, vol. 49, no. 2, pp. 38-+.

Mack, C 2008, Seeing Double, *IEEE Spectrum*, vol. 11,

Mack, CA 1987, 'Contrast enhancement techniques for submicron optical lithography', *Journal of Vacuum Science & Technology a-Vacuum Surfaces and Films*, vol. 5, no. 4, pp. 1428-31.

Mack, CA 2001, 'Lithographic simulation: a review', in EB Kley & HP Herzig (eds), *Lithographic and Micromachining Techniques for Optical Component Fabrication*, Spie-Int Soc Optical Engineering, Bellingham, vol. 4440, pp. 59-72.

Mack, CA 2007, *Fundamental principles of optical lithography : the science of microfabrication*, Wiley, Chichester, West Sussex, England ; Hoboken, NJ, USA.

Maier, SA & Atwater, HA 2005, 'Plasmonics: Localization and guiding of electromagnetic energy in metal/dielectric structures', *Journal of Applied Physics*, vol. 98, no. 1, p. 10.

Mathworks 2010, *Matlab*, viewed 10/11 2010, (http://www.mathworks.com/products/matlab/).

McNab, SJ 2001, 'Evanescent near-field optical lithography : overcoming the diffraction limit: a thesis presented for the degree of Doctor of Philosophy in Electrical and Electronic Engineering at the University of Canterbury, Christchurch, New Zealand', Ph D thesis, University of Canterbury.

McNab, SJ & Blaikie, RJ 2000, 'Contrast in the evanescent near field of lambda/20 period gratings for photolithography', *Applied Optics*, vol. 39, no. 1, pp. 20-5.

Mechau, N, Saphiannikova, M & Neher, D 2005, 'Dielectric and mechanical properties of azobenzene polymer layers under visible and ultraviolet irradiation', *Macromolecules*, vol. 38, no. 9, pp. 3894-902.

Melville, DOS 2006, 'Planar lensing lithography : enhancing the optical near field : a thesis presented for the degree of Doctor of Philosophy in Electrical and Electronic Engineering at the University of Canterbury, Christchurch, New Zealand', Ph D thesis, University of Canterbury.

Melville, DOS & Blaikie, RJ 2005, 'Super-resolution imaging through a planar silver layer', *Optics Express*, vol. 13, no. 6, pp. 2127-34.

Menon, R & Smith, HI 2006, 'Absorbance-modulation optical lithography', *Journal of the Optical Society of America a-Optics Image Science and Vision*, vol. 23, no. 9, pp. 2290-4.

Menon, R, Tsai, HY & Thomas, SW 2007, 'Far-field generation of localized light fields using absorbance modulation', *Physical Review Letters*, vol. 98, no. 4.

Michelson, AA 1995, *Studies in optics*, Dover ; Constable, New York. London.

Microchemicals 2010, *Photoresist Optical Parameters*, viewed 10/11 2010.

Moharam, MG & Gaylord, TK 1981, 'Rigorous coupled wave analysis of surface gratings with arbitrary profiles', *Journal of the Optical Society of America*, vol. 71, no. 12, pp. 1573-.

Moharam, MG & Gaylord, TK 1981a, 'Rigorous coupled-wave analysis of planar-grating diffraction', *Journal of the Optical Society of America*, vol. 71, no. 7, pp. 811-8.

Moharam, MG & Gaylord, TK 1986, 'Rigorous coupled-wave analysis of metallic surface-relief gratings', *Journal of the Optical Society of America a-Optics Image Science and Vision*, vol. 3, no. 11, pp. 1780-7.

Moharam, MG, Grann, EB, Pommet, DA & Gaylord, TK 1994, 'Formulation for stable and efficient implementation of the rigorous coupled-wave analysis of binary

gratings', *Optical Society of America 2nd Topical Meeting on Diffractive Optics*, Rochester, Ny, Jun 06-09.

Moore, CP., Arnold, MD., Bones, PJ. & Blaikie, RJ. 2008. 'Image fidelity for single-layer and multi-layer silver superlenses', *Journal of the Optical Society of America a-Optics Image Science and Vision,* Vol 25**,** pp 911-918.

Moore, GE 1998, 'Cramming more components onto integrated circuits (Reprinted from Electronics, pg 114-117, April 19, 1965)', *Proceedings of the IEEE*, vol. 86, no. 1, pp. 82-5.

Novotny, L & Hecht, B 2006, *Principles of nano-optics*, Cambridge University Press, Cambridge.

Novotny, L, Pohl, DW & Regli, P 1994, 'Light-propagation through nanometer-sized structures - the 2-dimensional-aperture scanning near-field optical microscope', *Journal of the Optical Society of America a-Optics Image Science and Vision*, vol. 11, no. 6, pp. 1768-79.

Oldham, WG 1987, 'The use of contrast enhancement layers to improve the effective contrast of positive photoresist', *IEEE Transactions on Electron Devices*, vol. 34, no. 2, pp. 247-51.

Otoole, MM 1985, 'Simulated performance of a contrast-enhancement material', *Ieee Electron Device Letters*, vol. 6, no. 6, pp. 282-4.

Ottavi, G, Ortica, F & Favaro, G 1999, 'Photokinetic methods: A mathematical analysis of the rate equations in photochromic systems', *International Journal of Chemical Kinetics*, vol. 31, no. 4, pp. 303-13.

Ozbay, E 2006, 'Plasmonics: Merging photonics and electronics at nanoscale dimensions', *Science*, vol. 311, no. 5758, pp. 189-93.

Padilla, WJ, Basov, DN & Smith, DR 2006, 'Negative refractive index metamaterials', *Materials Today*, vol. 9, no. 7-8, pp. 28-35.

Pease, RF & Chou, SY 2008, 'Lithography and other patterning techniques for future electronics', *Proceedings of the IEEE*, vol. 96, no. 2, pp. 248-70.

Pedersen, TG, Johansen, PM & Pedersen, HC 2000, 'Characterization of azobenzene chromophores for reversible optical data storage: molecular quantum calculations', *Journal of Optics A-Pure and Applied Optics*, vol. 2, no. 4, pp. 272-8.

Pendry, J 2001, 'Comment on "Negative refraction makes a perfect lens" - Reply', *Physical Review Letters*, vol. 87, no. 24, p. 1.

Pendry, J 2001a, 'Some problems with negative refraction - Reply', *Physical Review Letters*, vol. 87, no. 24, p. 1.

Pendry, JB 2000, 'Negative refraction makes a perfect lens', *Physical Review Letters*, vol. 85, no. 18, pp. 3966-9.

Pendry, JB, Holden, AJ, Robbins, DJ & Stewart, WJ 1999, 'Magnetism from conductors and enhanced nonlinear phenomena', *IEEE Transactions on Microwave Theory and Techniques*, vol. 47, no. 11, pp. 2075-84.

Pepper, DW & Heinrich, JC 2006, *The finite element method : basic concepts and applications*, 2nd edn, Series in computational and physical processes in mechanics and thermal sciences, Taylor & Francis, New York.

Pilozzi, L, Dandrea, A & DelSole, R 1996, 'Electromagnetic properties of a dielectric grating .1. Propagating, evanescent, and guided waves', *Physical Review B*, vol. 54, no. 15, pp. 10751-62.

Pitarke, JM, Silkin, VM, Chulkov, EV & Echenique, PM 2005, 'Surface plasmons in metallic structures', *Journal of Optics A-Pure and Applied Optics*, vol. 7, no. 2, pp. S73-S84.

Rittweger, E, Han, KY, Irvine, SE, Eggeling, C & Hell, SW 2009, 'STED microscopy reveals crystal colour centres with nanometric resolution', *Nature Photonics*, vol. 3, no. 3, pp. 144-7.

Ronse, K 2006, 'Optical lithography - a historical perspective', *Comptes Rendus Physique*, vol. 7, no. 8, pp. 844-57.

Ronse, K, Jansen, P, Gronheid, R, Hendrickx, E, Maenhoudt, M, Wiaux, V, Goethals, AM, Jonckheere, R & Vandenberghe, G 2009, 'Lithography Options for the 32 nm Half Pitch Node and Beyond', *IEEE Transactions on Circuits and Systems I-Regular Papers*, vol. 56, no. 8, pp. 1884-91.

Rytov, SM 1956, 'Electromagnetic properties of a finely stratified medium', *Soviet Physics Jetp-USSR*, vol. 2, no. 3, pp. 466-75.

Saavedra, HM, Mullen, TJ, Zhang, PP, Dewey, DC, Claridge, SA & Weiss, PS 2010, 'Hybrid strategies in nanolithography', *Reports on Progress in Physics*, vol. 73, no. 3, p. 40.

Sacks, ZS, Kingsland, DM, Lee, R & Lee, JF 1995, 'A perfectly matched anisotropic absorber for use as an absorbing boundary condition', *IEEE Transactions on Antennas and Propagation*, vol. 43, no. 12, pp. 1460-3.

REFERENCES

Sanders, DP 2010, 'Advances in Patterning Materials for 193 nm Immersion Lithography', *Chemical Reviews*, vol. 110, no. 1, pp. 321-60.

Sasaki, K & Nagamura, T 1997, 'Ultrafast air-optical switch using complex refractive index changes of thin films containing photochromic dye', *Applied Physics Letters*, vol. 71, no. 4, pp. 434-6.

Scholer, M. & Blaikie, RJ.,2009. 'Simulations of surface roughness effects in planar superlenses', *Journal of Optics a-Pure and Applied Optics,* vol 11**,** no 6.

Scholer, M. & Blaikie, RJ, 2010. 'Resonant surface roughness interactions in planar superlenses', *Microelectronic Engineering,* vol 87**,** pp 887-889.

Scott, TF, Kowalski, BA, Sullivan, AC, Bowman, CN & McLeod, RR 2009, 'Two-Color Single-Photon Photoinitiation and Photoinhibition for Subdiffraction Photolithography', *Science*, vol. 324, no. 5929, pp. 913-917.

Serra, F & Terentjev, EM 2008, 'Nonlinear dynamics of absorption and photobleaching of dyes', *Journal of Chemical Physics*, vol. 128, no. 22, p. 6.

Shalaev, VM 2007, 'Optical negative-index metamaterials', *Nature Photonics*, vol. 1, no. 1, pp. 41-8.

Shalaev, VM, Cai, WS, Chettiar, UK, Yuan, HK, Sarychev, AK, Drachev, VP & Kildishev, AV 2005, 'Negative index of refraction in optical metamaterials', *Optics Letters*, vol. 30, no. 24, pp. 3356-8.

Shao, DB & Chen, SC 2005, 'Surface-plasmon-assisted nanoscale photolithography by polarized light', *Applied Physics Letters*, vol. 86, no. 25, p. 3.

Shelby, RA, Smith, DR, Nemat-Nasser, SC & Schultz, S 2001, 'Microwave transmission through a two-dimensional, isotropic, left-handed metamaterial', *Applied Physics Letters*, vol. 78, no. 4, pp. 489-91.

Shelby, RA, Smith, DR & Schultz, S 2001, 'Experimental verification of a negative index of refraction', *Science*, vol. 292, no. 5514, pp. 77-9.

Silverman, JP 1997, 'X-ray lithography: Status, challenges, and outlook for 0.13 mu m', *Journal of Vacuum Science & Technology B*, vol. 15, no. 6, pp. 2117-24.

Smith, B 2009, Alternative optical technologies - More than curiosities?, *Proceedings of SPIE*, vol 7274.

Smith, DR, Pendry, JB & Wiltshire, MCK 2004, 'Metamaterials and negative refractive index', *Science*, vol. 305, no. 5685, pp. 788-92.

Statman, D & Janossy, I 2003, 'Study of photoisomerization of azo dyes in liquid crystals', *Journal of Chemical Physics*, vol. 118, no. 7, pp. 3222-32.

Stoykovich, MP, Kang, H, Daoulas, KC, Liu, G, Liu, CC, de Pablo, JJ, Mueller, M & Nealey, PF 2007, 'Directed self-assembly of block copolymers for nanolithography: Fabrication of isolated features and essential integrated circuit geometries', *ACS Nano*, vol. 1, no. 3, pp. 168-75.

Strong, FC 1952, 'Theoretical basis of the Bouguer-Beer law of radiation absorption', *Analytical Chemistry*, vol. 24, no. 2, pp. 338-42.

Stulen, RH & Sweeney, DW 1999, 'Extreme ultraviolet lithography', *IEEE Journal of Quantum Electronics*, vol. 35, no. 5, pp. 694-9.

t'Hooft, GW 2001, 'Comment on "Negative refraction makes a perfect lens"', *Physical Review Letters*, vol. 87, no. 24, p. 1.

Taflove, A & Hagness, SC 2000, *Computational electrodynamics : the finite-difference time-domain method*, 2nd edn, Artech House antennas and propagation library, Artech House, Boston.

Tejeda, R, Frisque, G, Engelstad, R, Lovell, E, Haugeneder, E & Loschner, H 1999, 'Finite element simulation of ion-beam lithography mask fabrication', *Microelectronic Engineering*, vol. 46, no. 1-4, pp. 485-8.

Teng, SY, Tan, YG & Cheng, CF 2008, 'Quasi-Talbot effect of the high-density grating in near field', *Journal of the Optical Society of America a-Optics Image Science and Vision*, vol. 25, no. 12, pp. 2945-51.

Tsai, H-Y 2007, 'Absorbance modulation Optical Lithography', Master's Thesis, Massachusetts Institute of Technology.

Tsai, HY, Smith, HI & Menon, R 2008, 'Reduction of focal-spot size using dichromats in absorbance modulation', *Optics Letters*, vol. 33, no. 24, pp. 2916-8.

Tsai, HY, Thomas, SW & Menon, R 2010, 'Parallel scanning-optical nanoscopy with optically confined probes', *Optics Express*, vol. 18, no. 15, pp. 16014-24.

Tsai, HY, Wallraff, GM & Menon, R 2007, 'Spatial-frequency multiplication via absorbance modulation', *Applied Physics Letters*, vol. 91, no. 9.

Valanju, PM, Walser, RM & Valanju, AP 2002, 'Wave refraction in negative-index media: Always positive and very inhomogeneous', *Physical Review Letters*, vol. 88, no. 18, p. 4.

REFERENCES

Valentine, J, Zhang, S, Zentgraf, T, Ulin-Avila, E, Genov, DA, Bartal, G & Zhang, X 2008, 'Three-dimensional optical metamaterial with a negative refractive index', *Nature*, vol. 455, no. 7211, pp. 376-U32.

Veselago, VG 1968, 'Electrodynamics of substances with simultaneously negative values of sigma and mu', *Soviet Physics Uspekhi-USSR*, vol. 10, no. 4, pp. 509-&.

Vieu, C, Carcenac, F, Pepin, A, Chen, Y, Mejias, M, Lebib, A, Manin-Ferlazzo, L, Couraud, L & Launois, H 2000, 'Electron beam lithography: resolution limits and applications', *Applied Surface Science*, vol. 164, pp. 111-7.

Warner, M & Blaikie, RJ 2009, 'Two-color nonlinear absorption of light in dye layers', *Physical Review A*, vol. 80, no. 3, p. 6.

Webb, JP 1995, 'Application of the finite-element method to electromagnetic and electrical topics', *Reports on Progress in Physics*, vol. 58, no. 12, pp. 1673-712.

West, P, Ishii, S, Naik, G, Emani, N, Shalaev, V & Boltasseva, A 2010, *Searching for Better Plasmonic Materials*, 6, Laser and photonics reviews.

West, PR & Griffing, BF 1983, 'Contrast enhancement - a route to sub-micron optical lithography', *Proceedings of the SPIE*, vol. 394, pp. 33-8.

White, LK & Meyerhofer, D 1986, 'Process latitude in contrast enhancement layer lithography', *RCA Review*, vol. 47, no. 2, pp. 117-37.

Williams, JM 2001, 'Some problems with negative refraction', *Physical Review Letters*, vol. 87, no. 24, p. 1.

Wilson, AEJ 1984, 'Applications of photochromic polymer-films', *Physics in Technology*, vol. 15, no. 5, pp. 232-8.

Wiltshire, MCK, Pendry, JB & Hajnal, JV 2006, 'Sub-wavelength imaging at radio frequency', *Journal of Physics-Condensed Matter*, vol. 18, no. 22, pp. L315-L21.

Wua, BQ & Kumar, A 2007, 'Extreme ultraviolet lithography: A review', *Journal of Vacuum Science & Technology B*, vol. 25, no. 6, pp. 1743-61.

Wurm, S 2009, 'EUV Lithography Development and Research Challenges for the 22 nm Half-pitch', *Journal of Photopolymer Science and Technology*, vol. 22, no. 1, pp. 31-42.

Xie, Y, Zakharian, AR, Moloney, JV & Mansuripur, M 2004, 'Transmission of light through slit apertures in metallic films', *Optics Express*, vol. 12, no. 25, pp. 6106-21.

Yager, KG & Barrett, CJ 2006, 'Novel photo-switching using azobenzene functional materials', *Journal of Photochemistry and Photobiology a-Chemistry*, vol. 182, no. 3, pp. 250-61.

Yamashita, S, Ono, H & Toyama, O 1962, 'The cis-trans photoisomerization of azobenzene', *Bulletin of the Chemical Society of Japan*, vol. 35, no. 11, pp. 1849-53.

Yang, XF, Fang, LA, Zeng, BB, Wang, CT, Feng, Q & Luo, XG 2010, 'Deep subwavelength photolithography based on surface plasmon polariton resonance with metallic grating waveguide heterostructure', *Journal of Optics*, vol. 12, no. 4, p. 6.

Yee, KS 1966, 'Numerical solution of initial boundary value problems involving Maxwell's equations in isotropic media', *IEEE Transactions on Antennas and Propagation*, vol. AP14, no. 3, pp. 302-8.

Yuan, CM 1993, 'Calculation of one-dimensional lithographic aerial images using the vector theory', *IEEE Transactions on Electron Devices*, vol. 40, no. 9, pp. 1604-13.

Zakharian, AR, Moloney, JV & Mansuripur, M 2007, 'Surface plasmon polaritons on metallic surfaces', *Optics Express*, vol. 15, no. 1, pp. 183-97.